



2016

Ceria Based Catalysts for Low Temperature NO_x Storage and Release

Samantha Jones

University of Kentucky, jones.samantha80@gmail.com

Digital Object Identifier: <http://dx.doi.org/10.13023/ETD.2016.379>

[Right click to open a feedback form in a new tab to let us know how this document benefits you.](#)

Recommended Citation

Jones, Samantha, "Ceria Based Catalysts for Low Temperature NO_x Storage and Release" (2016). *Theses and Dissertations--Chemistry*. 67.

https://uknowledge.uky.edu/chemistry_etds/67

This Doctoral Dissertation is brought to you for free and open access by the Chemistry at UKnowledge. It has been accepted for inclusion in Theses and Dissertations--Chemistry by an authorized administrator of UKnowledge. For more information, please contact UKnowledge@lsv.uky.edu.

STUDENT AGREEMENT:

I represent that my thesis or dissertation and abstract are my original work. Proper attribution has been given to all outside sources. I understand that I am solely responsible for obtaining any needed copyright permissions. I have obtained needed written permission statement(s) from the owner(s) of each third-party copyrighted matter to be included in my work, allowing electronic distribution (if such use is not permitted by the fair use doctrine) which will be submitted to UKnowledge as Additional File.

I hereby grant to The University of Kentucky and its agents the irrevocable, non-exclusive, and royalty-free license to archive and make accessible my work in whole or in part in all forms of media, now or hereafter known. I agree that the document mentioned above may be made available immediately for worldwide access unless an embargo applies.

I retain all other ownership rights to the copyright of my work. I also retain the right to use in future works (such as articles or books) all or part of my work. I understand that I am free to register the copyright to my work.

REVIEW, APPROVAL AND ACCEPTANCE

The document mentioned above has been reviewed and accepted by the student's advisor, on behalf of the advisory committee, and by the Director of Graduate Studies (DGS), on behalf of the program; we verify that this is the final, approved version of the student's thesis including all changes required by the advisory committee. The undersigned agree to abide by the statements above.

Samantha Jones, Student

Dr. Jack Selegue, Major Professor

Dr. Mark Lovell, Director of Graduate Studies

CERIA BASED CATALYISTS FOR LOW TEMPERATURE NO_x STORAGE
AND RELEASE

DISSERTATION

A dissertation submitted in partial fulfillment of the
requirements for the degree of Doctor of Philosophy in the
College of Arts and Sciences
at the University of Kentucky

By
Samantha Jones

Lexington, Kentucky

Director: Dr. Jack Selegue, Professor of Chemistry

Lexington, Kentucky

2016

Copyright © Samantha Jones 2016

ABSTRACT OF DISSERTATION

CERIA BASED CATALYST FOR LOW TEMPERATURE NO_x STORAGE AND RELEASE

Model ceria catalysts were evaluated for NO_x storage and desorption performance under lean conditions. Three different storage temperatures (80 °C, 120 °C, and 160 °C) were utilized to evaluate NO_x storage. Higher temperatures resulted in higher NO_x storage. It was observed that storage of platinum promoted ceria resulted in higher NO_x storage compared to promotion with palladium. NO_x desorption behavior of platinum promoted ceria indicated that the majority of NO_x is released at high temperatures (> 350 °C), comparatively palladium promotion released more of the stored NO_x at lower temperatures. Diffuse Reflectance Infrared Fourier Transform Spectroscopy (DRIFTS) indicated that platinum promotion results in NO_x storage as thermally stable nitrates, while palladium promotion results in NO_x storage as thermally labile nitrites.

Doping ceria with trivalent rare earth oxides has been shown to improve NO_x storage by generating lattice oxygen vacancies. Ceria doped with Pr, Y, La, Sm, and Nd at two different concentrations (5 and 20 mol%) and promoted with Pt were evaluated. Doping ceria with 5% Sm, Nd, and Pr improved the amount of NO_x stored while the addition of Sm and La did not improve storage. Upon increasing dopant concentration, NO_x storage decreased in all cases but Pr. However, increasing Pr concentration was found to increase NO_x storage as well as low temperature NO_x release. Ceria doped with Pr promoted with Pd increased the amount of NO_x released at lower temperatures compared to Pt promotion, although palladium promotion resulted in lower storage. Similar DRIFTS spectra were obtained with Ce-Pr when promoted with Pt or Pd compared to model catalysts. Platinum promotion results in the storage of NO_x at nitrates, which require high temperatures for removal. Comparatively, Pd promotion results in NO_x stored at nitrites requiring lower temperatures for removal.

Ceria doped with Pr proved to be promising, although not thermally stable when exposed to high temperatures as may be seen during a DPF clean up. Therefore, stabilizing Ce-Pr catalysts with Zr were evaluated. It was found that stabilizing Ce-Pr with Zr was not found to be beneficial to the catalyst performance.

KEYWORDS: NO_x, Low temperature NO_x storage, Passive NO_x Adsorbers, PNA, DRIFTS, Ce-Pr, and doped ceria.

Samantha Jones

July 26, 2016

CERIA BASED CATALYSTS FOR LOW TEMPERATURE NO_x STORAGE
AND RELEASE

By

Samantha Jones

Dr. Jack Selegue
Director of Dissertation

Dr. Mark Lovell
Director of Graduate Studies

July 26, 2016

To my family.

ACKNOWLEDGEMENTS

First and foremost I would like to thank Dr. Mark Crocker, whom I deeply appreciate having had as an advisor.

I would also like to express my gratitude to Dr. Jack Selegue, for being my co-advisor.

I also recognize and credit the other members of my advisory committee: Dr. Mark Lovell and Dr. Yang Tse Cheng, both for their time and their helpful insight.

Thanks to Dr. Agustín Bueno-López for his help with XPS and Raman analyses performed at the Department of Inorganic Chemistry of the University of Alicante.

Many thanks to the faculty and staff at the Chemistry Department, the Center for Applied Energy Research, and the Electron Microscopy Center of the University of Kentucky. Many thanks to Dennis Sparks and Will Shafer, for their endless help and support throughout my time at CAER.

I would like to thank my father and late mother for their endless support and dedication to my education. Without them I would not be where I am today. My mother wanted nothing more than for me to finish my PhD and go on to do great things. Although she passed before the completion of my PhD she supported me through the whole process.

To my brother and sister, thank you for your support and putting up with your baby sister.

To my loving fiancé, Andrew Jackson, thank you for your endless support, late nights of listening to presentations while attempting to follow my train of thought, and mostly for your continual encouragement.

Lastly, I would like to acknowledge my very dear friends Sarah Thompson and Nikki Lynn for their continual support through out the majority of my adult life.

Table of Contents

ACKNOWLEDGEMENTS	iii
Chapter 1. General Introduction.....	1
1.1. Causes of Emission Regulation.....	2
1.2. Atmospheric Sources of NO _x	3
1.3. Clean Air Act.....	5
1.4. EPA Emission Standards.....	6
1.4.1. FTP-75 Drive Cycle.....	6
1.4.2. Tier 1 Emission Standards.....	7
1.4.3. Tier 2 Emission Standards.....	7
1.4.4. Tier 3 Emission Standards.....	8
1.5. Solutions to Meet Stringent Emission Standards.....	9
1.6. Diesel Emission Control.....	10
1.7. Use of Passive NO _x Adsorbers.....	11
1.8. Scope of Dissertation.....	12
Chapter 2. Development of Passive NO _x Adsorbers.....	14
2.1. Patent Literature.....	15
2.2. Ceria-based PNAs.....	16
2.3. Non-rare earth doped ceria-based PNAs.....	22
2.4. Aluminum-based PNAs.....	25
2.5. NO _x Storage and Release Mechanisms.....	28
2.6. Summary.....	29
Chapter 3. Electron Microscopy Study of LNT and SCR catalysts.....	30
3.1. Introduction.....	30
3.2. Experimental.....	32
3.2.1. Aging protocol.....	32
3.2.2. Microscopy Methods.....	34
3.3. Results and Discussion.....	35
3.4. Conclusions.....	41
Chapter 4. Ceria-based Catalysts for Low-Temperature NO _x Storage and Release ...	42
4.1. Introduction.....	42
4.2. Experimental Methods.....	44
4.2.1. Catalyst Preparation.....	44
4.2.2. Catalyst Characterization.....	44
4.2.3. NO _x storage and desorption measurements.....	45
4.2.4. DRIFTS measurements.....	46
4.3. Results and Discussion.....	47
4.3.1. Sample characterization.....	47
4.3.2. NO _x adsorption.....	48
4.3.3. NO _x desorption.....	49
4.3.4. Effect of CO ₂ and H ₂ O on NO _x adsorption/desorption.....	52
4.3.5. Adsorption/desorption cycling.....	54
4.3.6. DRIFTS measurements.....	56
4.4. Conclusions.....	60
Chapter 5. CeO ₂ -M ₂ O ₃ Passive NO _x Adsorbers for Cold Start Applications.....	62
5.1. Introduction.....	62

5.2. Experimental Methods.....	65
5.2.1. Catalyst preparation.....	65
5.2.2. Catalyst Characterization.....	65
5.2.3. NO _x storage and desorption measurements.....	66
5.2.4. DRIFTS Measurements.....	67
5.3. Results and Discussion.....	68
5.3.1. Sample Characterization.....	68
5.3.2. NSE and NDE for Pt-Promoted Catalysts.....	76
5.3.3. NSE and NDE for Pd-Promoted Catalysts.....	80
5.3.4. Cycling Studies.....	84
5.3.5. Aging Studies.....	87
5.3.6. NSE and NDE in the absence of CO ₂ and H ₂ O.....	89
5.3.7. DRIFTS Studies.....	91
5.4. Conclusions.....	95
Chapter 6. Doped CZO Catalysts for Passive NO _x Adsorber Applications.....	96
6.1. Introduction.....	96
6.2. Experimental Methods.....	99
6.2.1. Catalyst preparation.....	99
6.2.2 Catalyst Characterization.....	100
6.2.3. NO _x storage and desorption measurements.....	101
6.2.4. DRIFTS Measurements.....	102
6.3. Results and Discussion.....	103
6.3.1. Sample Characterization.....	103
6.3.2. Effect of CeO ₂ content on NSE.....	109
6.3.3. NO _x -TPD and NDE results.....	110
6.3.4. Cycling Studies.....	112
6.3.5. Effect of Zr on Content Aging.....	114
6.3.6. Affects of CO ₂ and H ₂ O on NSE and NDE.....	117
6.3.7. DRIFTS Studies.....	118
6.4. Conclusions.....	120
Chapter 7. Significant Findings and Recommendations.....	122
7.1. Significant Findings.....	122
7.1.1. Electron Microscopy of LNT and SCR Catalysts.....	122
7.1.2. NO _x Storage and Desorption Behavior of Model Ceria Catalysts.....	122
7.1.3. Effects of NO _x Storage Behavior upon Doping CeO ₂ with Rare Earth Oxides.....	123
7.1.4. Doping Ce-Pr mixed oxides with ZrO ₂	124
7.2. Suggestions for Future Work.....	124
Appendix – List of Abbreviations.....	125
Appendix A.2. Supplemental Figures and Graphs.....	128
BIBLIOGRAPHY.....	135
VITA.....	145

List of Tables

TABLE 1.1. TIER 2 EMISSION STANDARDS AS DETERMINED BY FTP-75 DRIVE CYCLE, G/MI [26]. SOURCE: DIESELNET.COM. REPRINTED WITH PERMISSION.	8
TABLE 1.2. TIER 3 EMISSION STANDARDS AS DETERMINED BY FTP-75 DRIVE CYCLE [24]. SOURCE: DIESELNET.COM.	9
TABLE 2.1. COMPARISON OF DECOMPOSITION TEMPERATURES FOR DIFFERENT METAL NITRATES [27-31].	19
TABLE 2.2. COMPARISON OF DECOMPOSITION TEMPERATURES FOR DIFFERENT METAL NITRITES [27, 32-33].	21
TABLE 3.1. COMPOSITION OF FEED GAS USED FOR LNT-SCR SYSTEM AGING. SOURCE: APPL. CATAL. B. ENV. REPRINTED WITH PERMISSION.	32
TABLE 4.1. SUMMARY OF CeO_2 PARTICLE SIZE CALCULATED FROM X-RAY DIFFRACTION DATA, BET SURFACE AREA (SA), PORE VOLUME, PORE DIAMETER, AND METAL PARTICLE SIZE DIAMETER DETERMINED BY CO CHEMISORPTION.	47
TABLE 5.1. PHYSICAL PROPERTIES OF $\text{Pt/CeO}_2\text{-M}_2\text{O}_3$ USED IN THIS WORK.	71
TABLE 5.2. PHYSICAL PROPERTIES OF $\text{Pd/CeO}_2\text{-Pr}_2\text{O}_3$ USED IN THIS WORK.	71
TABLE 5.3. ATOMIC CONCENTRATIONS DETERMINED BY XPS FOR FRESH SAMPLES (*DENOTES NOMINAL VALUES).	74
TABLE 5.4. ATOMIC CONCENTRATIONS DETERMINED BY XPS FOR AGED SAMPLES (*DENOTES NOMINAL VALUES).	75
TABLE 6.1. PHYSICAL PROPERTIES OF FRESH PR-DOPED CeO_2 AND $\text{CeO}_2\text{-ZrO}_2$ CATALYSTS USED IN THIS WORK.	104
TABLE 6.2. ATOMIC CONCENTRATIONS DETERMINED BY XPS FOR FRESH SAMPLES (*DENOTES NOMINAL VALUES).	107
TABLE A.2.1. BET SURFACE AREA (SA) OF CATALYST SUPPORTS PREPARED AT THE UNIVERSITY OF KENTUCKY CENTER FOR APPLIED ENERGY RESEARCH AND SUPPORT DIAMETERS AS DETERMINED BY X-RAY DIFFRACTION.	129

LIST OF FIGURES

FIGURE 1.1. REDUCTION OF NO _x EMISSIONS BETWEEN 1960-2010 [1]. SOURCE: AIR QUALITY MANAGEMENT IN THE UNITED STATES. REPRINTED WITH PERMISSION.....	2
FIGURE 1.2. SMOG COMING FROM THE STACKS OF ZINC WORKS OF AMERICAN STEEL & WIRE CO. IN DONORA, PA IN 1948 [8]. SOURCE: POST-GAZETTE.COM. REPRINTED WITH PERMISSION.	3
FIGURE 1.3. NATIONAL pH DISTRIBUTIONS FROM 2002 [12]. SOURCE: WATER.USGS.GOV. REPRINTED WITH PERMISSION.	4
FIGURE 1.4. FTP-75 DRIVE CYCLE [21]. SOURCE: DIESELNET.COM. FIGURE REPRINTED WITH PERMISSION.	6
FIGURE 2.1. EXHAUST GAS TEMPERATURES OBSERVED DURING THE FTP-75 DRIVE CYCLE ON A 4.4 L DIESEL TRUCK. SOURCE: SAE 2012-01-0371 [1]. REPRINTED WITH PERMISSION.	14
FIGURE 2.2. NO _x CONCENTRATIONS PRE- AND POST-SCR CATALYST DURING THE FTP-75 DRIVE CYCLE. SOURCE: DIESELNET.COM [2]. REPRINTED WITH PERMISSION.....	15
FIGURE 2.3. PROCESS OF FORMING OXYGEN VACANCIES IN THE CERIA LATTICE THROUGH THE REMOVAL OF OXYGEN FROM THE LATTICE LEAVING BEHIND TWO ELECTRONS. SOURCE: PHYS. REV. LETT. [9]. REPRINTED WITH PERMISSION.	17
FIGURE 2.4. OUTLET NO _x CONCENTRATION COMPARISONS FOR PBA AND PBAC BEFORE AND AFTER SULFATION. SOURCE: CATAL. LETT. [21]. REPRINTED WITH PERMISSION.	18
FIGURE 2.5. PERCENTAGE OF NO _x STORED AFTER ONE MINUTE AS A FUNCTION OF TEMPERATURE ON VARIOUS LNT SUPPORTS PROMOTED WITH 1 WT.% PT. SOURCE: TOP. IN CATAL. [26]. REPRINTED WITH PERMISSION.....	19
FIGURE 2.6. HOW DIFFERING RATIOS OF CE-CO-CR AFFECT NO CONVERSION. SOURCE: ASIA PACIFIC ENGINEERING [40]. REPRINTED WITH PERMISSION.	24
FIGURE 2.7. THE USE OF AG PROMOTED CATALYSTS RESULTED IN NO TO NO ₂ OXIDATION AT LOWER TEMPERATURES COMPARED TO A SUPPLIER DOC CATALYST. SOURCE: CAT. TODAY. [46] REPRINTED WITH PERMISSION.....	27
FIGURE 2.8. ADSORPTION AND REDUCTION OF NO ON Pd/ZSM-5. SOURCE: SAE 2012-01-1002 [48]. REPRINTED WITH PERMISSION.	28
FIGURE 3.1. SUMMARY OF PROTOCOL USED FOR ACCELERATED CATALYST AGING. SOURCE: APPL. CATAL. B. REPRINTED WITH PERMISSION.....	33
FIGURE 3.2. LNT CATALYST INLET AND MID-BED TEMPERATURES DURING AGING (ONE AGING CYCLE DEPICTED). SOURCE: APPL. CATAL. B. ENV. REPRINTED WITH PERMISSION.	34
FIGURE 3.3. STEM OF FRESH LNT CATALYST SHOWING ROD-LIKE STRUCTURES OF ALUMINA.	36
FIGURE 3.4. EDS LINE-SCAN ON AGED LNT CATALYST INDICATING THE PRESENCE OF SULFUR ON THE THREE SINTERED PLATINUM PARTICLES IN THE UPPER RIGHT CORNER OF THE AGED STEM IMAGE. SOURCE: APPL. CATAL. B. ENV. REPRINTED WITH PERMISSION.	37
FIGURE 3.5. STEM IMAGE OF AGED LNT CATALYST SHOWING SMALL PLATINUM PARTICLES ON THE ALUMINA SUPPORT, WHILE PLATINUM DENSITY INCREASES ON BARIUM RICH AREAS. SOURCE: APPL. CATAL. B. ENV. REPRINTED WITH PERMISSION.	38

FIGURE 3.6. STEM IMAGE OF AGED LNT CATALYST SHOWING THE DIFFERENT SUPPORTS CAN BE DISTINGUISHED FROM ONE ANOTHER IN STEM BECAUSE OF THE DIFFERENCES IN ATOMIC MASS OF CE, BA, AND AL. A) CeO_2 APPEARS MUCH BRIGHTER IN COMPARISON TO BA. B) Al_2O_3 APPEARS MUCH DARKER THAN SUPPORTED BA. SOURCE: APPL. CATAL. B. ENV. REPRINTED WITH PERMISSION.	39
FIGURE 3.7. TEM IMAGES OF THE FRESH SCR CATALYST WERE FOUND TO HAVE WELL-DEFINED STRUCTURES (FIGURE A). AGED STRUCTURES EXHIBIT LESS WELL-DEFINED EDGES AND CONTAIN CU NANOPARTICLES (HIGHLIGHTED, FIGURE B). SOURCE: APPL. CATAL. B. ENV. REPRINTED WITH PERMISSION.	40
FIGURE 3.8. EDS SPECTRA INDICATED THE PRESENCE OF ZR IN THE FRESH SCR CATALYST AS WELL AS THE AGED (NOT PICTURED). TEM INSET IS OF THE AREA ON WHICH EDS ANALYSIS WAS PERFORMED.	40
FIGURE 4.1. COMPARISON OF NO_x STORAGE EFFICIENCY AT 80, 120, AND 160 °C FOR PT/ CeO_2 AND PD/ CeO_2 . FEED: 300 PPM NO , 5% O_2 , 5% CO_2 , 3.5% H_2O AND HE BALANCE.	49
FIGURE 4.2. NO_x RELEASE PROFILES DURING TEMPERATURE PROGRAMMED DESORPTION (TPD) AFTER NO_x STORAGE AT 120 °C FOR 5 MIN.	50
FIGURE 4.3. COMPARISON OF NO_x DESORPTION EFFICIENCY FOR TWO DIFFERENT TEMPERATURE RANGES: < 350 °C AND 350-500 °C.	51
FIGURE 4.4. EFFECT OF NO_x STORAGE TEMPERATURE ON THE AMOUNT OF NO_x DESORBED DURING TPD.	52
FIGURE 4.5. COMPARISON OF NO_x STORAGE EFFICIENCY AT 120 °C IN THE ABSENCE OF H_2O AND CO_2	53
FIGURE 4.6. COMPARISON OF NO_x DESORPTION EFFICIENCY AFTER STORAGE 120 °C FOR 5 MIN IN THE ABSENCE OF H_2O AND CO_2	54
FIGURE 4.7. COMPARISON OF NO_x STORAGE EFFICIENCY DURING STORAGE AT 120 °C FOR 5 MIN FOR FIVE CONSECUTIVE ADSORPTION-DESORPTION CYCLES. FEED GAS SAME AS FOR FIG. 3.1.	55
FIGURE 4.8. COMPARISON OF NO_x DESORPTION EFFICIENCY BELOW 250 °C AND 350 °C DURING TPD FOR FIVE CONSECUTIVE ADSORPTION-DESORPTION CYCLES.	56
FIGURE 5.1. X-RAY DIFFRACTION PATTERNS OF PT-PROMOTED CeO_2 - M_2O_3 CATALYSTS.	69
FIGURE 5.2. X-RAY DIFFRACTION PATTERNS OF PD- AND PT-PD-PROMOTED CeO_2 - Pr_2O_3 CATALYSTS.	70
FIGURE 5.3. RAMAN ANALYSIS OF UNDOPED AND PR-DOPED CeO_2 CATALYSTS.	73
FIGURE 5.4. EFFECT OF PR DOPING ON THE RAMAN SHIFT OF THE CeO_2 F_{2g} BAND.	74
FIGURE 5.5. H_2 -TPR PROFILES OF FRESH CATALYSTS FROM THE Ce20Pr SERIES.	76
FIGURE 5.6. COMPARISON OF NO_x STORAGE EFFICIENCY AT 120 °C FOR PtCe5-20M. FEED: 300 PPM NO , 5% O_2 , 5% CO_2 , 3.5% H_2O AND HE BALANCE.	77
FIGURE 5.7. NO_x -TPD PROFILES OF PtCe(5-20)M AFTER NO_x STORAGE AT 120 °C FOR 5 MINUTES.	78
FIGURE 5.8. COMPARISON OF NO_x DESORPTION EFFICIENCY AFTER STORAGE AT 120 °C FOR TWO DIFFERENT TEMPERATURE RANGES: < 350 °C AND 350-500 °C.	79
FIGURE 5.9. COMPARISON OF AMOUNT OF NO_x DESORBED AFTER STORAGE AT 120 °C FOR TWO DIFFERENT TEMPERATURE RANGES: < 350 °C AND 350-500 °C.	80
FIGURE 5.10. COMPARISON OF NO_x STORAGE EFFICIENCY AT 120 °C FOR PTPD OR PdCe5-20Pr. FEED: 300 PPM NO , 5% O_2 , 5% CO_2 , 3.5% H_2O AND HE BALANCE.	81

FIGURE 5.11. COMPARISON OF NO _x DESORPTION EFFICIENCY AFTER STORAGE AT 120 °C FOR PdCePr CATALYSTS AT TWO DIFFERENT TEMPERATURE RANGES: < 350 °C AND 350-500 °C.....	82
FIGURE 5.12. COMPARISON OF AMOUNT OF NO _x DESORBED AFTER STORAGE AT 120 °C FOR TWO DIFFERENT TEMPERATURE RANGES: < 350 °C AND 350-500 °C.....	83
FIGURE 5.13. NO _x -TPD PROFILES OF PdCe(5-20)Pr AFTER NO _x STORAGE AT 120 °C FOR 5 MINUTES.....	83
FIGURE 5.14. COMPARISON OF NO _x STORAGE EFFICIENCY AT 120 °C FOR 5 MINUTES AND NO _x DESORPTION EFFICIENCY BELOW 250 °C AND 350 °C FOR FIVE CONSECUTIVE ADSORPTION-DESORPTION CYCLES FOR Pt AND PdCe20Pr.....	86
FIGURE 5.15. COMPARISON OF NO _x STORAGE EFFICIENCY STORAGE AT 120 °C FOR 5 MINUTES AND NO _x DESORPTION EFFICIENCY BELOW 250 °C AND 350 °C FOR FIVE CONSECUTIVE ADSORPTION-DESORPTION CYCLES FOR PdPtCe20Pr.....	86
FIGURE 5.16. NSE COMPARISON OF Ce20Pr SERIES AFTER AGING FOR 16 HOURS UNDER LEAN CONDITIONS (5% CO ₂ , 5% O ₂ , AND 3.5% H ₂ O WITH HE BALANCE).....	88
FIGURE 5.17. COMPARISON OF NDE FOR Ce20Pr SERIES AFTER AGING FOR 16 HOURS.....	89
FIGURE 5.18. COMPARISON OF NSE FOR Ce20Pr SERIES MEASURED WITHOUT CO ₂ AND WATER IN THE FEED.....	90
FIGURE 5.19. COMPARISON OF NDE FOR Ce20Pr SERIES WITHOUT CO ₂ AND WATER IN THE FEED.....	90
FIGURE 5.20. DRIFT SPECTRA ACQUIRED DURING NO STORAGE AT 100 °C FOR (A) PtCe20Pr (B) PdCe20Pr AND (C) PtPdCe20Pr. FEED: 300 PPM NO, 5% O ₂ , AR BALANCE.....	93
FIGURE 5.21. DRIFT SPECTRA ACQUIRED DURING TPD AFTER NO STORAGE AT 100 °C FOR (A) PtCe20Pr (B) PdCe20Pr AND (C) PtPdCe20Pr. FEED: 300 PPM NO, 5% O ₂ , AR BALANCE.....	95
FIGURE 6.1. X-RAY DIFFRACTION PATTERNS OF Pr-DOPED CeO ₂ AND CeO ₂ -ZrO ₂ CATALYSTS.....	105
FIGURE 6.2. RAMAN ANALYSIS OF Pr-DOPED CeO ₂ AND CeO ₂ -ZrO ₂ CATALYSTS.....	106
FIGURE 6.3. EFFECT OF Pr DOPING ON THE RAMAN SHIFT OF THE CeO ₂ F _{2g} BAND.....	107
FIGURE 6.4. H ₂ -TPR PROFILES OF FRESH CATALYSTS FROM THE Ce20Pr AND 64Ce16Pr20Zr SERIES.....	108
FIGURE 6.5. COMPARISON OF NO _x STORAGE EFFICIENCY AT 120 °C FOR Pr-DOPED CeO ₂ AND CeO ₂ -ZrO ₂ CATALYSTS. FEED: 300 PPM NO, 5% O ₂ , 5% CO ₂ , 3.5% H ₂ O AND HE BALANCE.....	110
FIGURE 6.6. NO _x -TPD PROFILES OF Pr-DOPED CeO ₂ AND CeO ₂ -ZrO ₂ AFTER NO _x STORAGE AT 120 °C FOR 5 MINUTES.....	111
FIGURE 6.7. COMPARISON OF NO _x DESORPTION EFFICIENCY AFTER STORAGE AT 120 °C FOR TWO DIFFERENT TEMPERATURE RANGES: < 350 °C AND 350-500 °C.....	111
FIGURE 6.8. COMPARISON OF AMOUNT OF NO _x DESORBED AFTER STORAGE AT 120 °C FOR TWO DIFFERENT TEMPERATURE RANGES: < 350 °C AND 350-500 °C.....	112
FIGURE 6.9. COMPARISON OF NO _x STORAGE EFFICIENCY AT 120 °C FOR 5 MINUTES FOR FIVE CONSECUTIVE ADSORPTION CYCLES FOR Pd64Ce16Pr20Zr AND PdCe20Pr.....	113
FIGURE 6.10. COMPARISON OF NO _x DESORPTION EFFICIENCY BELOW 250 °C AND 350 °C FOR FIVE CONSECUTIVE DESORPTION CYCLES FOR Pd64Ce16Pr20Zr AND PdCe20Pr.....	113

FIGURE 6.11. COMPARISON OF NO _x STORAGE AND DESORPTION WITH EACH CYCLE FOR Pd64Ce16Pr20Zr AND PdCe20Pr.	114
FIGURE 6.12. NSE COMPARISON OF PdCe20Pr AND Pd64Ce16Pr20Zr AFTER AGING FOR 16 HOURS UNDER LEAN CONDITIONS (5% CO ₂ , 5% O ₂ , AND 3.5% H ₂ O WITH HE BALANCE).	115
FIGURE 6.13. COMPARISON OF NDE FOR PdCe20Pr AND Pd64Ce16Pr20Zr AFTER AGING FOR 16 HOURS.	116
FIGURE 6.14. CUMULATIVE NO _x RELEASE OF FRESH AND AGED PdCe20Pr AND Pd64Ce16Pr20Zr.	116
FIGURE 6.15. COMPARISON OF NSE FOR PdCe20Pr AND Pd64Ce16Pr20Zr MEASURED WITH AND WITHOUT CO ₂ AND WATER IN THE FEED.	117
FIGURE 6.16. COMPARISON OF NDE FOR PdCe20Pr AND Pd64Ce16Pr20Zr WITH AND WITHOUT CO ₂ AND WATER IN THE FEED.	118
FIGURE 6.17. DRIFT SPECTRA ACQUIRED DURING NO STORAGE AT 100 °C FOR Pd64Ce16Pr20Zr. FEED: 300 PPM NO, 5% O ₂ , AR BALANCE.	119
FIGURE 6.18. DRIFT SPECTRA ACQUIRED DURING TPD AFTER NO STORAGE AT 100 °C FOR Pd64Ce16Pr20Zr. FEED: 300 PPM NO, 5% O ₂ , AR BALANCE.	120
FIGURE A.2.1. NO _x EMISSIONS ARE STORED ON THE PNA UNTIL THE DOWNSTREAM SCR CATALYST HAS REACHED OPERATIONAL TEMPERATURES (>180 °C).	128
FIGURE A.2.2. STEM IMAGE OF AGED LNT CATALYST DISPLAYING Pt PARTICLE WITH A SIZE OF 27 NM.	128
FIGURE A.2.3. CO-PRECIPITATION PROCEDURE UTILIZED TO MAKE CeO ₂ -M ₂ O ₃ SUPPORTS. NITRATE PRECURSORS WERE COMBINED WITH AMMONIUM HYDROXIDE (NH ₄ OH) AND ALLOWED TO STIR OVER NIGHT TO PRECIPITATE. FOLLOWED BY VACUUM FILTRATION AND HEATING OF THE CATALYST IN AIR FOR 1 HOUR AT 80 °C AFTER WHICH THE CATALYST IS PLACED IN A VACUUM OVEN TO COMPLETELY DRY OVER NIGHT AT 80 °C. ONCE THE CATALYST IS COMPLETELY DRY IT IS CALCINED IN A MUFFLER FURNACE AT 500 °C FOR 3 HOURS TO REMOVE NITRATES.	129
FIGURE A.2.4. TOTAL AMOUNT OF NO _x RELEASED (mmol) PER GRAM OF CATALYSTS FOLLOWS THE SAME TREND AS NSE DATA FOR PtCeXM. INCREASING Pr CONTENT INCREASES NO _x STORAGE, BUT DECREASES STORAGE WHEN INCREASING THE CONTENT OF Y, La, Nd, AND Sm.	130
FIGURE A.2.5. NSE AT 120 °C FOR 5 MINUTES WERE PERFORMED IN TRIPLICATES FOR CATALYSTS THAT HAD INITIAL NDE GREATER THAN 100%. PERCENT ERROR WAS FOUND TO BE LARGEST FOR Pd/20Pr-80Zr AT 1 MINUTE WITH A PERCENT ERROR OF 7.70% AND SMALLEST FOR Pd/16Ce-4Pr-80Zr AT ONE MINUTE WITH A PERCENT ERROR OF 5.00%.	131
FIGURE A.2.6. NDE OF STORAGE PERFORMED IN TRIPLICATES AT 120 °C FOR 5 MINUTES INDICATED THAT Pd/16Ce-4Pr-80Zr HAD THE LARGEST TOTAL NDE PERCENT ERROR OF 8.07% AND Pd/80Ce-20Pr HAD THE SMALLEST TOTAL NDE PERCENT ERROR OF 5.00%.	132
FIGURE A.2.7. NITRITE SPECIES THAT MAY APPEAR ON THE CATALYST SURFACE DURING NO _x STORAGE AND THE BAND RANGES.	133
FIGURE A.2.8. NITRATE SPECIES THAT MAY APPEAR ON THE CATALYST SURFACE DURING NO _x STORAGE AND THE BAND RANGES.	134

Chapter 1. General Introduction.

For over 40 years automotive companies have been striving to produce vehicles that meet ever tightening Environmental Protection Agency (EPA) emission standards. As seen in Figure 1.1, national NO_x emission standards have dropped from ~ 6 g/mi in 1960 to 0.07 g/mi in 2010 [1]. Not only does the EPA regulate nitrogen oxides (NO_x), they regulate the emission of carbon monoxide (CO), particulate matter (PM), and hydrocarbons (HC).

CO is a poisonous gas that is colorless and odorless. HCs have been linked to cancer in humans as well as contributing to the greenhouse gas effect. PM are fine particles found in aerosols that are produced during combustion processes, some of which have been linked to heart disease and lung cancer [2]. Most NO_x is produced by several different combustion processes: fuel combustion for electrical utility operation, high temperature industrial operations (cement kilns), and operation of vehicles [3]. It's estimated that 1% of NO_x is produced in nature [4] through bacterial processes, lightening resulting in the oxidation of N_2 to NO_x , or biomass burning, i.e. forest fires where nitrogen is oxidized, producing NO_x [5]. The other 99% of NO_x emissions are generated by man made sources, including vehicle emissions [4].

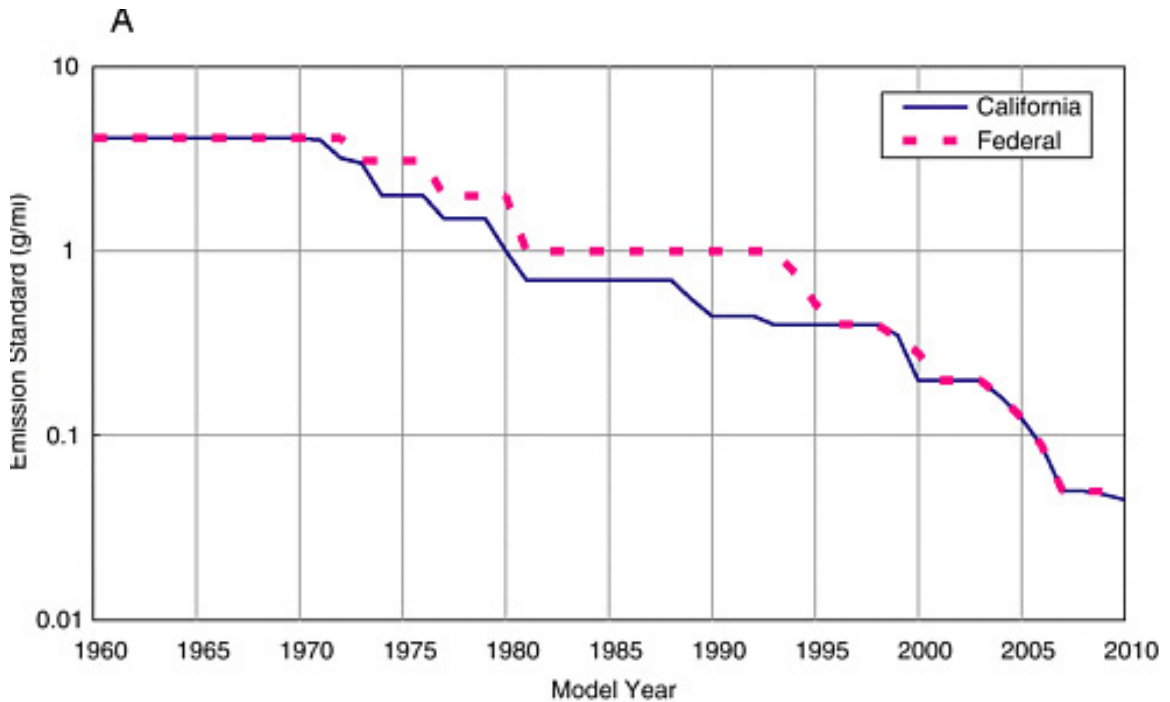


Figure 1.1. Reduction of NOx emissions between 1960-2010 [1]. Source: Air Quality Management in the United States. Reprinted with permission.

1.1. Causes of Emission Regulation.

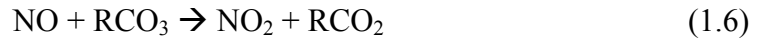
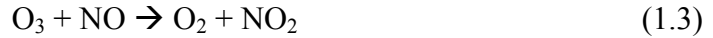
In October of 1948 in the town of Donora, Pennsylvania, a thick cloud of smog formed over the town and lingered for 5 days (Figure 1.2). During those 5 days 20 people were killed and almost half of the town’s population became sick [6]. Four years later in December 1952, thick smog emerged over London, England, becoming known as London’s “killer fog.” In the aftermath of the smog it was reported that 4,000 people died due to bronchitis and pneumonia caused by the smog. All transportation in London was crippled (except the underground) because people were unable to see, and it was reported that buses could only function with guides walking in front of the buses holding lanterns in front of them [7]. Events like these, prompted emission regulations in the U.S. as well as globally.



Figure 1.2. Smog coming from the stacks of Zinc Works of American Steel & Wire Co. in Donora, PA in 1948 [8]. Source: post-gazette.com. Reprinted with permission.

1.2. Atmospheric Sources of NO_x .

Increasing regulations on NO_x emissions have been prompted by increases in photochemical smog, greenhouse gases, and acid rain produced by NO_x reactions with atmospheric gases. On warm sunny days, especially in urban areas, smog warnings have become commonplace due to increased emissions and optimal conditions for smog production. Photochemical smog is produced through numerous reactions (1.1-1.6) [9]. When NO_2 is struck by u.v. sunlight, NO_2 is broken down to radical oxygen (O^*) and NO , which begins the formation of photochemical smog. O^* reacts further with O_2 to form ozone (O_3). After the formation of ozone, O_3 will scavenge NO to form NO_2 and O_2 dropping the ozone concentration. However, radical oxygens can also further react with volatile organic compounds (VOCs), denoted as RC in reaction 1.4, to form aldehydes and ketones (RCO). These aldehydes and ketones can be further oxidized to form peroxide radicals (RCO_3). Oxygen can react with RCO_3 to form more ozone and VOCs. RCO_3 can form more NO_2 by reacting with NO , which will go on to form more ozone, further contributing to global warming. A summary of the reactions previously discussed is presented below.



In addition to increasing ozone concentrations, NO_x forms nitric acid (HNO_3), which typically comprises 32% of acid rain [10]. Normal rainwater has a pH slightly less than 6, where as acid rain has a pH of 5.0-5.5 and as low as 4.5 in some areas (Figure 1.3), making it harmful to the environment (i.e. killing marine life and crops) [11].

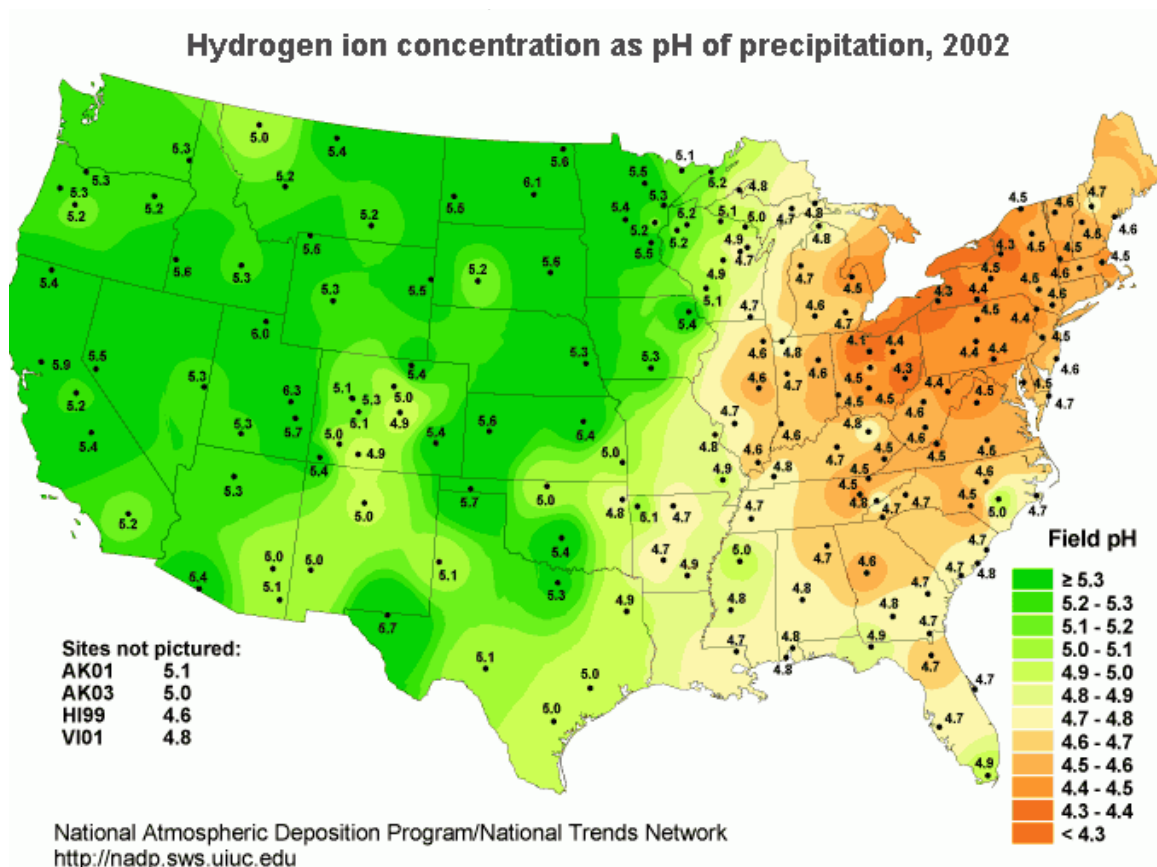


Figure 1.3. National pH distributions from 2002 [12]. Source: Water.USGS.gov.

Reprinted with permission.

It is worth noting that nitric acid is also formed (steps 1.7-1.9) during lightening storms by the reaction of N_2 and O_2 to produce NO that can be further oxidized to NO_2 thus promoting acid rain through means of NO_2 reacting with water forming nitric acid and NO [13].



Nitrous oxide (N_2O) is a type of greenhouse gas. According to the EPA, 40% of N_2O is produced through human activities [14]. Although NO and NO_2 emissions are regulated by the EPA, N_2O has a much longer half-life (+100 years) than NO or NO_2 [15]. N_2O also has the largest impact towards global warming compared to other greenhouse gases (CO_2 , methane and F-containing gases) [16]. One pound of N_2O compared to one pound of CO_2 impacts global warming almost 300 times more than CO_2 , and hence N_2O emissions are increasingly being subject to regulation [17].

1.3. Clean Air Act.

Events like those in Donora, PA and London led to government regulations on emission control. The first federal legislation passed on emission control in the United States was the Clean Air Act (CAA) of 1963. This was followed by the passing of the CAA of 1970 [18]. The CAA of 1970 required that emissions in 1975 model year cars be reduced by 90% or more [19], with new emission requirements leading the way for the first practical catalytic convertor design and lead-free gasoline. Amendments were made to the CAA throughout the 70s and important additions were made in the 90s regarding automobile exhaust emissions, resulting in programs like the Acid Rain Program created to control acid rain in 1990, followed by the introduction of National Ambient Air Quality Standards lowering levels of ground level ozone and the quantity of particulate matter that make up soot.

1.4. EPA Emission Standards.

1.4.1. FTP-75 Drive Cycle.

To certify that a vehicle meets emission standards set forth by the EPA, the FTP-75 drive cycle is utilized. The FTP-75 mimics urban driving through 4 different phases (Figure 1.4). The first phase is known as the cold start transient phase, that lasts for 505 seconds. During the cold start transient phase the engine is started at ambient temperatures (20-30 °C). The second phase, the-called stabilized phase, is where the engine has had time to warm up and reach typical operating conditions, this lasting for 866 seconds. After stabilization the engine is turned off for a minimum of 540 seconds to a maximum of 660 seconds for the hot soak phase. This phase mimics someone running a quick errand, i.e. going into a store for 10 minutes. Following the hot soak is the hot start transient phase, which lasts 505 seconds. Throughout the drive cycle there are constant stops and starts as there would be in an urban driving environment. Several basic parameters are set forth during the drive cycle: the duration is 1877 seconds, with a total distance traveled of 11.04 miles, an average speed of 21.2 mph, and a maximum speed of 56.7 mph [20].

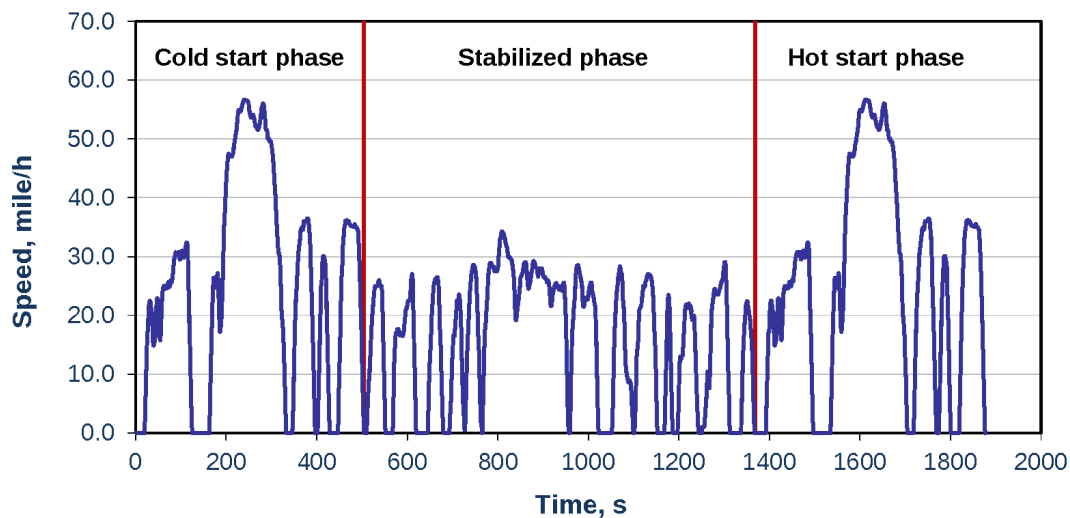


Figure 1.4. FTP-75 Drive Cycle [21]. Source: DieselNet.com. Figure reprinted with permission.

In addition to the FTP-75 drive cycle two supplemental tests may be run as well: US06 and SC03. US06 simulates high-speed driving and/or high acceleration with rapid speed fluctuations. US06 is representative of a 8.01 mile route that averages 48.4 mph, doesn't exceed a speed of 80.3 mph, and has a total duration of 596 seconds [22]. SC03 is used to simulate conditions similar to the FTP-75 with the use of air conditioning. The drive cycles occurs in a lab with the temperature set to 35 °C, a 3.6 mile driving loop, with average speeds of 21.6 mph (max of 54.8 mph), and totaling 596 seconds [23].

1.4.2. Tier 1 Emission Standards.

Emission standards established with the Clean Air Act of 1990 led to more stringent criteria set forth by the EPA in Tier 1 and these guidelines began phasing-in throughout the mid-90's. Tier 1 requirements were applied to all light duty vehicles (LDV) possessing a gross vehicle weight ratio (GVWR) of 8500 pounds or less. LDV vehicles are classified as passenger vehicles such as: cars, light-duty trucks, sport utility vehicles (SUV), mini-vans, and pick-up trucks. Emissions standards were broken into two types of mileage standards set forth by Tier 1 (miles or years—depending which milestone occurred first): 50,000 miles or 5 years and 100,000 miles or 10 years. Emission standards also varied depending on the type of fuel, i.e. diesel engines had different standards than gasoline engines [24].

1.4.3. Tier 2 Emission Standards.

With the goal of further decreasing vehicle emissions, Tier 2 standards were phased in from 2004 to 2009. Differing from Tier 1, Tier 2 emission standards are the same for all LDV, regardless of fuel type. Emission levels are organized by bins in Tier 2, as shown in Table 1.1. The reduction of NO_x emissions will be the focus of this dissertation due to lower HC and CO emissions in diesel engines compared to stoichiometric gasoline engines, i.e. NO_x emissions represent the main challenge. Tier 2 mandates that manufacturers have an average fleet NO_x emission of 0.07g/mile during the FTP-75 for the vehicles' "usable lifetime" (10 years or 120,000 miles). Sulfur contents in gasoline and diesel fuels are also mandated by Tier 2. Gasoline is to have an average sulfur content of 30 ppm with no more than 80 ppm, while diesel fuel is to have a

maximum sulfur content of 15 ppm due to the ability of sulfur to deactivate diesel emission control catalysts [25].

Table 1.1. Tier 2 Emission Standards as determined by FTP-75 drive cycle, g/mi [26]. Source: DieselNet.com. Reprinted with permission.

Bin #	Intermediate Life (5 years/50,000 miles)					Full Life (10 years/120,000 miles)				
	NMOG	CO	NO _x	PM	HCHO	NMOG	CO	NO _x	PM	HCHO
8	0.1	3.4	0.14	--	0.015	0.125	4.2	0.2	0.02	0.018
7	0.075	3.4	0.11	--	0.015	0.09	4.2	0.15	0.02	0.018
6	0.075	3.4	0.08	--	0.015	0.09	4.2	0.1	0.01	0.018
5	0.075	3.4	0.05	--	0.015	0.09	4.2	0.07	0.01	0.018
4	--	--	--	--	--	0.07	2.1	0.04	0.01	0.011
3	--	--	--	--	--	0.055	2.1	0.03	0.01	0.011
2	--	--	--	--	--	0.01	2.1	0.02	0.01	0.004
1	--	--	--	--	--	0	0	0	0	0

1.4.4. Tier 3 Emission Standards.

The final set of emission standards arising from the Clean Air Act of 1990, Tier 3, is set to begin phasing in during 2017, the phase in period ending in 2025. There are several differences between Tier 2 and Tier 3, the first being the fact that non-methane organic gases (NMOG) and NO_x categories are combined into one, and the second involving the extension of total emission certification life to 150,000 miles. Lastly, gasoline vehicles will be tested with gasoline containing 10% ethanol. With the new emission group of NMOG and NO_x, manufacturer fleets must average 30 mg/mile for both gases combined (Table 1.2). Sulfur content in gasoline is lowered in Tier 3 from 30 ppm to 10 ppm [27].

Table 1.2. Tier 3 Emission Standards as determined by FTP-75 drive cycle [24]. Source: DieselNet.com. Reprinted with permission.

Bin	NMOG + NO _x	PM	CO	HCHO
	mg/mi	mg/mi	g/mi	mg/mi
Bin 160	160	3	4.2	4
Bin 125	125	3	2.1	4
Bin 70	70	3	1.7	4
Bin 50	50	3	1.7	4
Bin 30	30	3	1.0	4
Bin 20	20	3	1.0	4
Bin 0	0	0	0	0

1.5. Solutions to Meet Stringent Emission Standards.

In response to the CAA of 1970 automotive manufacturers developed the first practical catalytic convertor. The three way catalytic (TWC) converter was designed to convert nitrogen oxides (NO_x), carbon monoxide (CO), and unburned hydrocarbons (HC) into nitrogen gas (N₂), carbon dioxide (CO₂), and water [28]. Within the first 25 years of use of catalytic convertors, 56 million tons of HC, 118 million tons of NO_x, and 464 billion tons of CO emissions were prevented [29].

TWCs needed to be able to withstand high temperatures because of large temperature gradients caused by exothermic catalytic reactions and high exhaust temperatures. They also needed to have large surface areas and be produced at low cost; because of these requirements car manufacturers considered using alumina beads and ceramic monoliths with a honeycomb structure as catalyst supports [30]. The catalyst also needed to be resistant to poisons, like sulfur, and have high mechanical strength [31].

Through the evolution of TWCs, ceramic monoliths made of cordierite, (Mg,Fe)₂Al₄Si₅O₁₈, were used as catalyst supports because of their low thermal expansion coefficient [32]. The extrusion of clay, talc, alumina, water, and organic additives was used to generate cordierite, which allowed for control of the geometry, size, and contour of the honeycomb [33]. The catalyst was applied by wash-coating the

monolith to generate a washcoat thickness of 20-150 μm depending on the application of the monolith [26].

TWCs also saw the addition of rhodium and platinum to improve NO reduction activity. For later era TWCs palladium became a major component because of its lower cost, while ceria was employed for oxygen storage to reduce fluctuations in air/fuel ratios for stoichiometric engines (air: fuel = 14.7:1 by weight). Minimizing fluctuations allowed for balanced conversions of HC, CO, and NO_x . In contrast, while lean burn engines (air: fuel = 20-50:1) are more efficient than stoichiometric engines, they produce excess oxygen in the exhaust that consumes reductants, making it difficult to convert NO_x to N_2 [34].

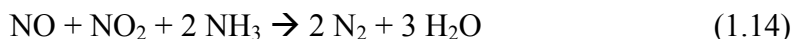
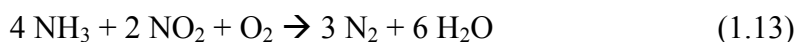
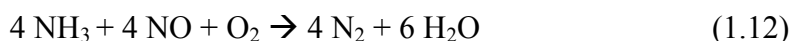
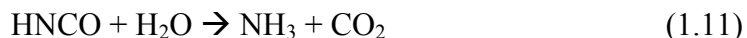
1.6. Diesel Emission Control.

The use of diesel engines over gasoline spark-ignited engines is attractive primarily due to their increased fuel efficiency. Diesel engines have increased fuel efficiency primarily due to extremely lean operating conditions and better combustion efficiency. The combustion of diesel fuel results in lower emissions of NO_x , CO, and HC than stoichiometric engines due to lower combustion temperatures, but lower temperatures result in higher particulate matter (PM) [35]. To prevent PM emissions, manufacturers developed diesel oxidation catalysts (DOC) and diesel particulate filters (DPF). DOCs promote the oxidization of HC and CO to CO_2 and H_2O [36]. DPFs are utilized to store PM matter to be subsequently oxidized during periodic DPF regeneration events [37].

Advancing to modern lean-burn engines, lean NO_x trap (LNT) and selective catalytic reduction (SCR) catalysts are used in place of TWCs. To optimize LNT NO_x conversions while using minimal amounts of fuel, NO_x is stored on an alkaline earth metal or alkali metal oxide. NO_x storage is found to be more effective if NO is first oxidized to NO_2 , traditionally performed by a precious group metal (PGM) like platinum between 200 $^\circ\text{C}$ and 350 $^\circ\text{C}$ [38-40]. NO_2 is then stored in the form of nitrates under lean conditions until NO_2 breakthrough (\sim 1-2 minutes) [41]. When breakthrough occurs, fuel is injected into the exhaust for regeneration of the storage capacity, during which metal nitrates and nitrites decompose to metal carbonates, oxides, and hydroxides. The released

NO_x is subsequently reduced to N₂ by the fuel-derived reductant species present (CO, H₂, and HCs). Although N₂ is the desired product from lean-rich cycling, N₂O and NH₃ are generated as by-products during cycling under certain conditions [32, 42].

SCR represents the main alternative to the use of LNT catalysts. Effective reduction of NO_x by NH₃ using SCR catalysts was first discovered in 1957 [43]. NH₃ is reduced NO_x to N₂ through standard SCR (reaction 1.12-1.13) or fast SCR reactions (reaction 1.14) [44]. NH₃ can be generated in-situ by the thermal decomposition of urea (reactions 1.10-1.11) which is injected into the exhaust.



SCR catalysts were discovered in the 50s, however few applications for them existed until the 70s. In the 70s SCR catalysts were used on power plants in Japan to reduce NO_x [43]. Early SCR catalysts utilized Pt technology, but weren't effective in the desired temperature range (> 250 °C). Following the use of Pt catalysts, V₂O₅/Al₂O₃ catalysts were studied for SCR use, however, they were not resistant to sulfur poisoning. Alumina reacts with SO₃ to form Al₂(SO₄)₃, deactivating the catalyst. To resist sulfur poisoning Al₂O₃ was replaced with TiO₂ [45-46]. V₂O₅/TiO₂ catalysts also operate at higher temperatures than Pt catalysts (300-400 °C) [47]. For even higher temperature operation zeolite based catalysts were found to perform the best [48].

1.7. Use of Passive NO_x Adsorbers.

While typical LNT and SCR catalysts do not become active until ~200 °C, FTP-75 testing begins under ambient conditions. Therefore, NO_x can pass through the exhaust unreacted during the first 200 seconds of vehicle use before catalyst operating temperatures are reached [49-50]. The EPA Tier 3 standards which are set to start phasing in beginning in 2017 call for a 46% reduction in emissions from the Tier 2

standards (which requires that light duty trucks have an average fleet NO_x emission of 0.07g/mi) [51-53]. Hence to meet these more stringent emission standards it is important to decrease cold start emissions. To this end, the concept of a passive NO_x adsorber (PNA) closely coupled to an urea-SCR catalyst has been suggested; the PNA is designed to store NO_x as a nitrate and/or nitrite below 200 °C and to readily release the NO_x above 200 °C to be reduced downstream by the urea-SCR catalyst.

1.8. Scope of Dissertation.

The research reported in this dissertation will discuss the use of PNAs to improve low temperature NO_x mitigation to meet upcoming Tier 3 standards. Combining NMOG and NO_x into one emission category in Tier 3 reduces NO_x emissions compared to Tier 2 standards. Moreover, Tier 3 requires that the emission control lifetime of an engine be increased from 120,000 miles to 150,000. To meet Tier 3 emissions standards it is imperative to reduce cold start NO_x slip. In this study this is done by evaluating the use of ceria based mixed oxides for NO_x storage below 200 °C and NO_x release above 200 °C. The effect of different precious metals (Pt v. Pd) in NO_x storage and release is studied and to understand how NO_x is stored and released, Diffuse Reflectance Infrared Fourier Transform Spectroscopy (DRIFTS) is utilized to probe NO_x storage and release mechanisms.

The next chapter of this dissertation will focus on the essential background information involving PNAs and the mechanism of NO_x storage and release.

Chapter 3 will focus on Microscopy work performed on LNT and SCR catalysts.

Chapter 4 will focus on the use of model ceria catalysts promoted with Pt or Pd.

Chapter 5 evaluates the effect of doping ceria with other trivalent rare earth oxides. Doping ceria is known to generate vacancies in the lattice, therefore increasing oxygen mobility and potentially increasing NO_x storage.

Chapter 6 focuses on the addition of zirconium to praseodymium-doped ceria to reduce catalyst sintering under the high temperatures experienced in exhaust systems (e.g. during DPF regeneration).

Lastly, Chapter 7 will focus on all of the significant findings from the work discussed in previous chapters along with suggestions for future work regarding PNAs. The most common abbreviations used throughout the dissertation will be included in Appendix 1.

Chapter 2. Development of Passive NO_x Adsorbers.

The EPA began regulating vehicle emissions (CO, HC, PM, and NO_x) in the 1970s. Since then automotive manufacturers have continually developed and improved exhaust aftertreatment systems. For aftertreatment systems to meet evolving pollutant emission targets, the improvement of catalytic activity at low temperatures has become a key objective due to low the temperatures observed for diesel engines during the first 200 seconds of the FTP-75 drive cycle (see Figure 2.1). Even with the use of an SCR catalyst, tailpipe NO_x emissions are at their highest during the first 200 seconds of the drive cycle (see Figure 2.2). To overcome this problem, the use of a PNA closely coupled to an SCR catalyst has been suggested, see Figure A.2.1.

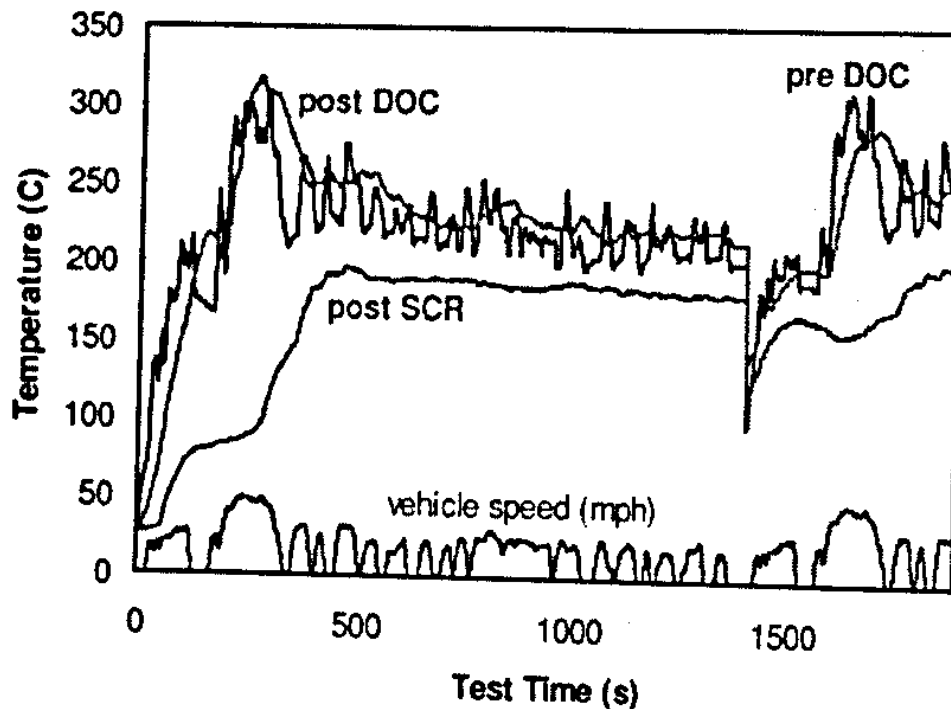


Figure 2.1. Exhaust gas temperatures observed during the FTP-75 drive cycle on a 4.4 L diesel truck. Source: SAE 2012-01-0371 [1]. Reprinted with permission.

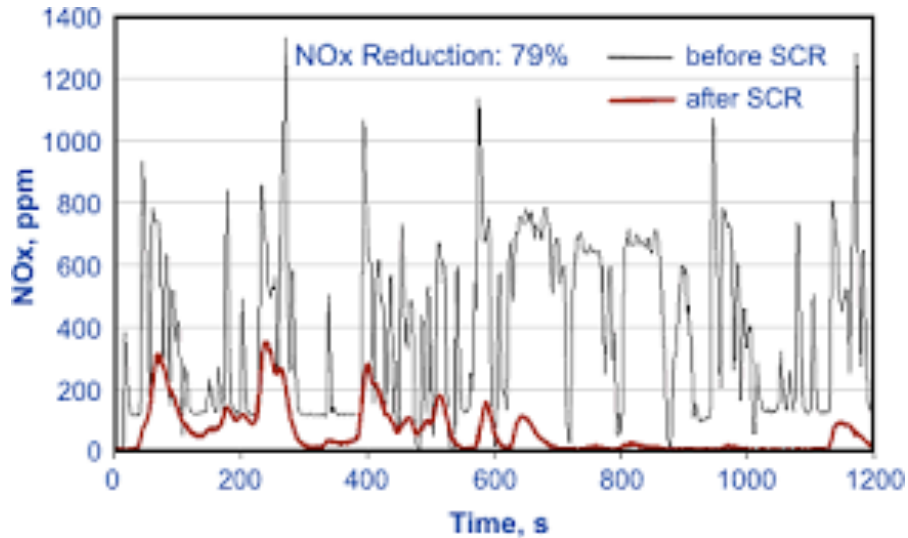


Figure 2.2. NO_x concentrations pre- and post-SCR catalyst during the FTP-75 drive cycle. Source: Dieselnet.com [2]. Reprinted with permission.

2.1. Patent Literature.

A 1998 patent from Energy and Environmental Research Corporation first mentioned the use of a passive NO_x adsorber, in conjunction with a TWC. The NO_x storage component was claimed to store NO_x below 180 °C, which was followed by release of NO_x to the downstream TWC once operational temperatures were reached [3]. Subsequently, the use of a PNA closely coupled to an SCR catalyst appeared in a patent issued to Ford in 2001, which claimed the use of platinum-promoted γ -Al₂O₃ as the PNA. Under lean conditions Pt/Al₂O₃ stores NO_x, although when hydrocarbons are present during lean conditions the catalyst simultaneously stores and reduces NO_x via HC-SCR reactions. The addition of a urea-SCR component allows the stored NO_x to be reduced to the desired N₂ product as the temperature increases and NO_x is desorbed from the PNA. The use of 2 wt.% of Pt loaded onto a γ -Al₂O₃ support achieves maximum NO_x storage of 80% at 160 °C for ~200 seconds [4].

A subsequent US patent application submitted by GM incorporates an external fuel injection system and air pump to insure that the PNA catalyst is regenerated if the engine is shut off before regeneration is achieved. To do so, fuel and air are injected into the exhaust to raise the temperature of the catalyst, releasing any remaining NO_x on the

PNA that is then reduced by residual NH_3 on the surface of the downstream SCR catalyst [5].

In a 2012 patent issued to Johnson Matthey, it is claimed that the use of Pd supported on CeO_2 as a PNA results in NO_x storage at nitrites, therefore avoiding the need for NO to be oxidized to NO_2 during storage [6]. Similarly, in a report by Chen et al. [7], Johnson Matthey's diesel Cold Start Catalyst (dCSCTM) is reported to have the ability to store NO_x as nitrite instead of nitrate, making it easier to desorb NO_x at relatively low temperatures and thereby regenerate the catalyst. The dCSCTM incorporates the previously mentioned PNA from Johnson Matthey along with a hydrocarbon trap. In the first report concerning the application of a PNA to a diesel vehicle, Cummins researchers showed that the use of a PNA closely coupled with an SCR catalyst was able to greatly reduce NO_x emissions on a light duty V8 truck that occurred during cold starts compared to an SCR-only catalyst system [8]. However, while the use of a PNA can be beneficial, the Cummins researchers concluded that more research was needed to develop the technology.

2.2. Ceria-based PNAs.

Ceria is often used in exhaust aftertreatment systems because of its ability to readily store and release oxygen [9-10]; this has been attributed to the non-stoichiometric fluorite structure of ceria. The non-stoichiometric form contains Ce^{3+} ions in addition to Ce^{4+} ions that lead to anionic vacancies—that can function as NO_x storage sites—in the crystal lattice as demonstrated in Figure 2.3 [4, 11-12]. It has been demonstrated that 17% of CeO_2 can be reduced without changing the fluorite structure to the hexagonal form, Ce_2O_3 [13]. In a study of Pd/ CeO_2 by Cordatos and Gorte [14], it was found that oxygen, as well as NO, has the potential to move freely between Ce and Pd. Lattice oxygen from CeO_2 can be transferred to the PGM at the PGM-ceria interface for oxidation reactions. The transfer of oxygen at the metal-ceria interface creates a reduced site on ceria, generating an adsorption site for NO. The adsorption of NO re-oxidizes the site to release N_2 and complete the oxidation-reduction cycle. The high oxygen mobility and favorable redox properties of ceria make ceria an ideal candidate for applications requiring NO_x storage and/or reduction.

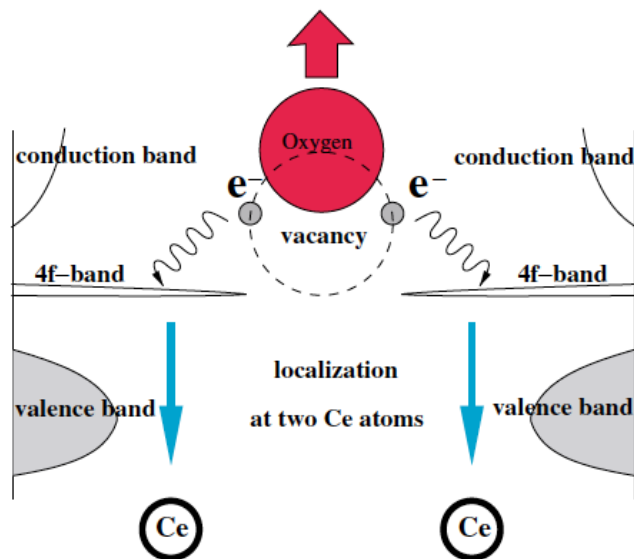


Figure 2.3. Process of forming oxygen vacancies in the ceria lattice through the removal of oxygen from the lattice leaving behind two electrons. Source: Phys. Rev. Lett. [9].

Reprinted with permission.

The fact that ceria is readily able to store and release oxygen due to its redox properties (e.g., through the creation of lattice oxygen vacancies by reduction of Ce^{4+} to Ce^{3+}), aids NO_x storage as shown in a number of recent studies [15-19]. Moreover, ceria has also been found to stabilize high dispersions of Pt [20] and reduce sulfur-induced deactivation of the active phase in LNT catalysts by acting as a sulfur sink [21-22]. Figure 2.4 compares NO_x storage over $\text{BaO}/\text{Al}_2\text{O}_3$ promoted with platinum (PBA) to a physical mixture of $\text{Pt}/\text{BaO}/\text{Al}_2\text{O}_3$ and Pt/CeO_2 (74:26 weight ratio), the mixture being denoted as PBAC. In the case of PBAC, little difference was observed in outlet NO_x concentrations before and after catalyst sulfation, as well as desulfation.

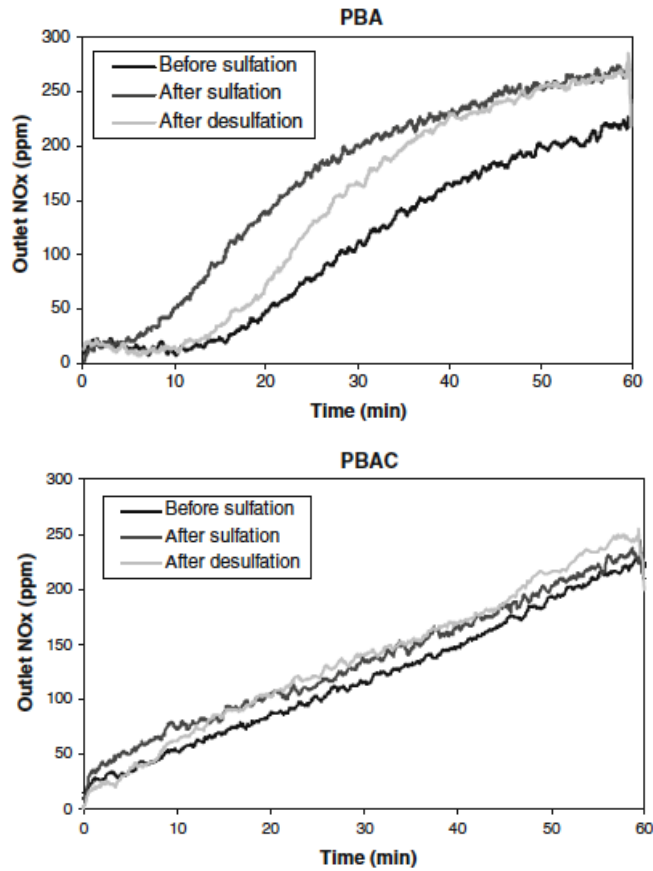


Figure 2.4. Outlet NO_x concentration comparisons for PBA and PBAC before and after sulfation. Source: Catal. Lett. [21]. Reprinted with permission.

Moreover, when Pt/CeO₂ is physically mixed with Pt/BaO/Al₂O₃ in a powder as well as in a monolith washcoat, NO_x conversions below 400 °C are improved during NO_x adsorption-reduction cycling [23-25]. Similarly, the addition of ceria to a Ba LNT catalyst improved NO_x storage capacity at low temperatures and high temperature catalyst durability in findings by Rohart et al. [26]. Rohart also investigated the use of rare earth (RE) oxides in place of Ba in LNT catalysts and found that use of various Ce-Pr, Ce-Nd and Ce-La oxides resulted in substantial NO_x storage at low temperatures (< 350 °C), whereas a BaO/Al₂O₃ reference catalyst showed poor storage in this temperature range (Figure 2.5).

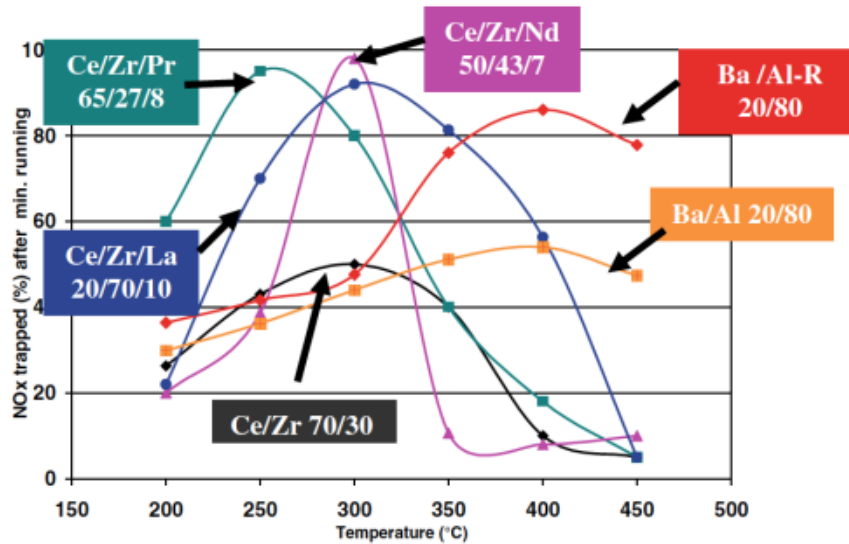


Figure 2.5. Percentage of NO_x stored after one minute as a function of temperature on various LNT supports promoted with 1 wt.% Pt. Source: Top. in Catal. [26]. Reprinted with permission.

The Ce-Pr derivative stored over 90% of the NO_x fed after 1 minute of storage at 250 °C, while the Ce-La derivative stored about 70% of the NO_x, and the Ce-Nd sample stored less than 40% of the NO_x. These results paralleled catalyst ability to oxidize NO to NO₂ at 250 °C [26]. Doping with rare earth oxides is also appealing due to their lower nitrate (Table 2.1) and nitrite (Table 2.2) decomposition temperatures compared to other metals. While group I and II metals have been evaluated for use in lean NO_x trap catalysts, they aren't viable options for low temperature operation under continuous lean conditions due to the high decomposition temperatures of the nitrates (e.g., bulk Ba nitrate decomposes at 645 °C). Alternatively, transition metals may be a viable option although not as appealing as rare earths because of their higher nitrate decomposition temperatures; nevertheless, the thermostability of their nitrates is generally lower than that of group I and II metals.

Table 2.1. Comparison of decomposition temperatures for different metal nitrates [27-31].

Metal	Decomposition Temperature (°C)
Ag	450
Al	167
Ba	645
Ca	575
Ce	297
Co	310
Cs	406
Cu	290
Dy	280
Fe	167
Ga	202
Gd	367
K	850
La	240-420
Li	640
Lu	230
Mg	450
Mn	200
Na	750
Nd	280-350
Ni	300
Pd	177
Pr	220
Pt	237
Rb	600
Rh	197
Sm	200
Sr	645
Ti	217-339

Y	376
Yb	270
Zn	337
Zr	300-600

Table 2.2. Comparison of decomposition temperatures for different metal nitrites [27, 32-33].

Metal	Decomposition Temperature (°C)
Ba	90-150
Ca	267-315
Li	220-270
Ni	260
K	410
La	240
Pr	220
Nd	200
Sm	200
Dy	110
Yb	90
Sr	264
Co	100
Rb	450
Tl	182

In a recent article, Wang et al. discussed the use of Nd, La, and Y in a Pt/Ba/Ce_{0.6}Zr_{0.4}O₂-Al₂O₃ LNT catalyst. The addition of La to the Ce-Zr mixed oxide improved NO_x storage capacity at 200 °C compared to the non-RE containing counterpart, while the addition of Y and Nd did not improve storage [34]. Stakheev et al.

[35] studied NO_x storage at low temperatures over Pt/CeO₂-ZrO₂. In their study it was confirmed that NO_x storage occurs in two phases: nitrite storage (100-180 °C) and nitrate storage (> 200 °C). Under isothermal conditions (200 ppm NO, 10% O₂, 6% H₂O, and N₂ balance) the catalyst was found to store ~0.18 mmol/g NO after saturating it with NO at 120 °C. Upon simulating NO_x storage during a cold start (100-200 °C) only a small amount of NO was stored: ~0.049 mmol/g, indicating that the full capacity of the catalyst to store NO_x isn't utilized during cold starts. Reducing Pt/CeO₂-ZrO₂ under 5% H₂/Ar at 450 °C was found to increase NO_x storage in the range of 100-150 °C. However, comparing storage after reduction to storage after oxidation over the 100-200 °C range, overall storage was found to be almost identical. NO_x storage drastically decreased over the 100-200 °C range when adding CO₂ to the gas feed due to competitive formation of surface carbonates with unstable surface nitrites.

The activity of Ce-Pr mixed oxides has also been examined [36]. Researchers observed an increase in NO₂ yield during NO oxidation from 24% for pure ceria to 39% for ceria doped with 20% Pr. Continuing to increase Pr content increased NO oxidation, indicating that Pr is a very active oxidation catalyst. Interestingly, increasing Pr content does not increase BET surface area but decreases it, indicating that NO oxidation activity is not as dependent upon surface area as generally reported for other catalysts. However, H₂-TPR indicated that increasing Pr content lowers the reduction temperatures of the catalyst, further supporting the high activity of Pr toward NO oxidation. Additionally, TG-MS data indicated that pure CeO₂ was not able to release O₂ under inert conditions, whereas Ce-Pr mixed oxides were. Upon performing CO₂-TPD it was observed that increasing Pr content increased surface carbonates, however, the carbonates did not affect NO oxidation ability.

2.3. Non-rare earth doped ceria-based PNAs.

Manganese-based catalysts have been studied as NO_x adsorbers due to their excellent NO oxidation activity at low temperatures. Fe-Mn based catalysts were evaluated for NO adsorption at room temperature by Yang et al. [37]. Fe-Mn-Ti and Fe-Mn-Zr oxides were found to be the best storage materials with a maximum NO storage capacity of 42-45 mg NO/g catalyst at 25 °C. Upon evaluating the effect of different

gases in the feed, it was observed that water greatly hinders NO storage, while SO₂ and CO₂ only slightly decreased storage. It was concluded that the high NO storage on the Fe mixed oxides can be attributed to their high surface areas as well as their ability to oxidize NO to NO₂. In a later study by Yoshida et al., Cu-Mn based catalysts were used for NO_x reduction by non-thermal plasma (NTP) and temperature swing adsorption (TSA) of engine NO_x emissions fueled by waste heat from the engine [38]. TSA generates a mixture of N₂ and NO_x that is reduced by NTP. Improved performance was achieved by reinjecting the gas treated by NTP into the engine intake. When the catalyst was incorporated in the aftertreatment system, the NTP energy efficiency was higher (200 g NO₂/kwh), as was the NO_x conversion.

Sun et al. [39] found that incorporating Ce into Mn-Sn catalysts improved NO_x storage at 100 °C, Mn_{0.4}Sn_{0.5}Ce_{0.1} exhibiting the best NO_x storage capacity. Through DRIFTS and other experimentation Sun et al. were able to conclude that the added CeO₂ plays two important roles during NO_x storage. The first is its ability to oxidize NO to NO₂. XPS results indicated the presence of increased defect concentrations in the trimetallic system compared to the bimetallic system, explaining the trimetallic system's better oxidation activity. Secondly, through NO- and NO₂-TPD as well as DRIFTS measurements, NO_x storage was found to be higher with increasing Sn/Ce interactions. This was attributed to the trimetallic system's ability to expose more NO_x storage sites on the surface.

Mixed metal oxide catalysts of the type Ce-Co-Cr-O were evaluated for NO oxidation capabilities by Cao et al. [40] They observed a correlation between NO oxidation and Co³⁺ concentration (Figure 2.6). XRD and BET analysis indicated little change in the structure of the catalysts even with varying Co/Cr concentrations and doping with Ce. Higher Ce concentrations resulted in better dispersion of Co, thereby increasing the Co/Cr interactions (e.g., benefiting the interaction of Ce with Co and Cr), which should benefit adsorption of reactant gases (leading to higher catalytic activity) due to the redox properties of Ce. In doing so NO oxidation was greatly enhanced, thus increasing NO_x storage. However, Cr-rich samples possessed low surface areas and hence comparatively lower NO_x storage.

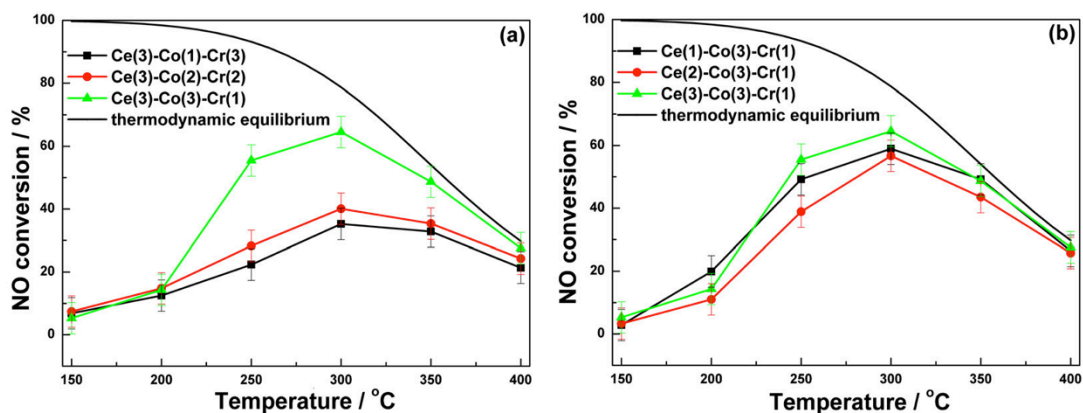


Figure 2.6. How differing ratios of Ce-Co-Cr affect NO conversion. Source: Asia Pacific Engineering [40]. Reprinted with permission.

Theis et al. [41] reported the use of Pt and Pd promoted catalysts (obtained from commercial catalyst suppliers) as low temperature NO_x adsorbers (LTNAs). In their studies (which used aged catalysts) it was found that Pt- only and Pt-rich (Pt/Pd) catalysts exhibited low NO_x storage and low NO oxidation activity during simulated cold starts. Following a rich pretreatment, Pt-only formulations exhibited better NO_x storage attributed to improved NO oxidation activity. Pd-rich samples had high ethene and NO_x storage during cold starts after aging. Additionally, most of the stored NO_x was released as NO, suggesting NO_x storage occurred as nitrites. Nitrite storage at low temperatures for Pd-rich samples resulted in improved robustness to SO_2 poisoning as opposed to NO_x stored as nitrates due to poisoning of nitrate storage sites. Upon NO adsorption-desorption cycling, Pd-rich LTNAs lost NO_x storage efficiency with each subsequent cycle due to the gradual reduction of Pd (present as PdO) by NO and ethene to form NO_2 and CO at low temperatures. CH_4 oxidation tests confirmed that Pd was partially reduced after only 2 transient tests.

In another recent study by researchers at Ford Motor Company, Pt and Pd on Al_2O_3 or ceria-zirconia (CZO) washcoats were evaluated for low temperature NO_x storage and desorption under lean conditions [42]. NO_x storage and release was studied in a reactor simulating the FTP-75 followed by US06 test cycle on a Ford Super Duty diesel truck. After aging at 700 °C under lean conditions, NO storage below 100 °C was greatly hindered on Pd/CZO by the presence of water in the feed. However, in the presence of

ethene with and without water, NO_x storage improved due to beneficial interactions between ethene and NO during the cold start, although not through HC-SCR reactions (which are observed at higher temperatures). When reduced under rich conditions at 350 °C, Pd/CZO showed higher NO_x storage during the first cycle of the simulated FTP-75 and US06 tests, but lower NO_x storage on the subsequent cycles due to incomplete desorption of NO_x during the US06 test. While storage gradually improved during cycling of Pd/CZO under lean conditions, the same behavior was not observed for Pd/Al₂O₃, indicating that Ce plays an important role in NO_x storage. Reducing Pd/Al₂O₃ resulted in higher NO_x storage, similar to Pd/CZO, indicating that reduced Pd is an effective NO_x storage component. In the case of Pt/Al₂O₃, water and ethene were found to severely hinder NO_x storage and high concentrations of NO₂ and N₂O were formed. Rich reduction improved the catalyst's tolerance to water and improved NO oxidation activity, although performance was still hindered by ethene. Pt/CZO produced lower amounts of NO₂ and N₂O after reduction and oxidation compared to Pt/Al₂O₃, but more than the Pd/CZO counterpart. Overall, Pd/CZO provided the best performance for NO_x storage, while most of the NO_x was released by 400 °C, and low NO₂ and N₂O formation was observed.

2.4. Aluminum-based PNAs.

Ji et al. [43] recently studied Pt/Al₂O₃ and Pt/La-Al₂O₃ for PNA use. They found that the addition of 1 wt.% La to Al₂O₃ increased NO_x storage through the creation of new NO_x storage sites. Although NO_x storage was increased with the addition of La, most of the stored NO_x was released above 250 °C compared to the non-La containing counterpart. Increased high temperature desorption with the addition of La is attributed to higher nitrate concentrations as confirmed by DRIFTS. Upon cycling of the catalysts, decreases in NO_x storage and low temperature release (below 250 °C) continued with each subsequent cycle (La-doped Al₂O₃ being affected more). DRIFTS spectra indicated that the majority of NO_x was stored on the Al₂O₃ support when pretreated under lean conditions. However, when pretreated under rich conditions NO_x storage increased and the presence of NO_x stored on Pt was observed.

Millo et al. [44] reported the use of an Advanced-Diesel Oxidation Catalyst (A-DOC) to store NO_x at low temperatures for the NEDC test (New European Drive Cycle, the European equivalent of the FTP-75 for passenger cars). Fresh catalysts exhibited high NO_x storage, but aging under lean conditions significantly decreased NO_x storage. Most of the stored NO_x was released at temperatures above 200 °C, which is the minimum operating temperature for SCR catalysts. Upon analysis of NO/NO_2 concentrations at low temperatures downstream of the DPF (e.g., at the inlet of the SCR catalyst), NO conversion over the closely coupled A-DOC was found to be negative, while NO_2 conversion was high, indicating that most NO_2 was converted to NO . Therefore, NO_2/NO_x ratios entering the SCR were low throughout the entire EUDC test, thus hindering high NO_x conversions. Evidently, the use of A-DOC with a downstream SCR catalyst must be optimized because high NO_2 concentrations are needed to facilitate SCR reactions at low temperatures.

Researchers at Toyota [45] explored the use of Ag on Al_2O_3 and TiO_2 for NO_x Storage Reduction (NSR). They found that NO_x could be stored at 150 °C on Ag/ Al_2O_3 , temperatures where traditional NSR catalysts lose activity. By adding TiO_2 to Ag/ Al_2O_3 , storage at 150 °C was improved and required desulfation temperatures were lowered to 600 °C or less due to the presence of titania's acid sites which suppress the support's basicity and therefore decrease sulfur poisoning while increasing the Ag dispersion. To further improve the performance of Ag/ $\text{TiO}_2/\text{Al}_2\text{O}_3$, a small amount of palladium was added. In doing so, NO_x release under rich conditions was greatly increased. The palladium promoted catalyst was also able to release NO_x at 250 °C or lower. Building on the work by Toyota, researchers at General Motors evaluated the use of silver in place of platinum on Al_2O_3 [46-47]. Ren et al. found that the use of Ag resulted in higher NO to NO_2 conversions below 200 °C compared to supplier DOCs. However, Ag requires the presence of H_2 for NO_x storage to keep Ag in its metallic state. Moreover, complete thermal desorption of stored NO_x was not achieved until temperatures in excess of 400 °C were reached. A minimum $\text{H}_2:\text{NO}$ ratio of 5 was found to maximize NO to NO_2 conversion when varying H_2 and NO ratios. A silver loading of 1.3 wt% resulted in the best NO_x storage, Figure 2.7.

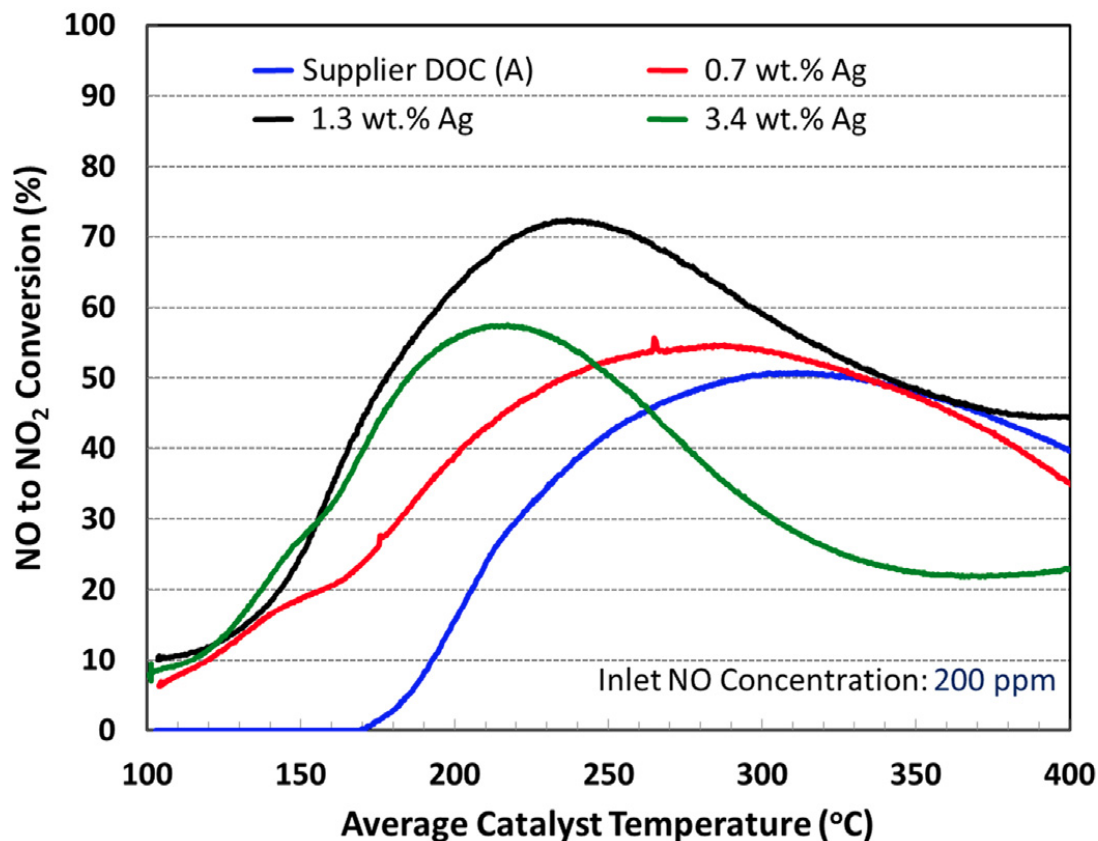


Figure 2.7. The use of Ag promoted catalysts resulted in NO to NO₂ oxidation at lower temperatures compared to a supplier DOC catalyst. Source: Cat. Today. [46] Reprinted with permission.

While the presence of H₂ is needed to ensure efficient NO oxidation and higher temperatures are needed to completely regenerate the catalyst, N₂O formation was not observed over any of the catalysts studied. However, Ag is subject to deactivation by sulfur poisoning and poor recovery of catalytic activity after desulfation. Moreover, while promising as an upstream PNA, Ag/Al₂O₃ will not be able to replace supplier DOCs due to poor CO and HC oxidation activity.

Researchers at Honda [48] have found that Pd/ZSM-5, as a NO_x-trap Three Way Catalyst (N-TWC), has the ability to reduce HC and NO_x emissions which have proven to be problematic for TWC catalysts. Pd/ZSM-5 exhibited NO_x storage capability at room temperature and during cold starts NO_x emissions were reduced from 200 ppm to under 50 ppm. The catalyst is believed to store NO as a nitrosyl group (Pd-NO), and also stores

HCs during cold starts. As the catalyst heats up, CO and HC in the exhaust (or adsorbed HC) are used to reduce stored NO_x (Figure 2.8).

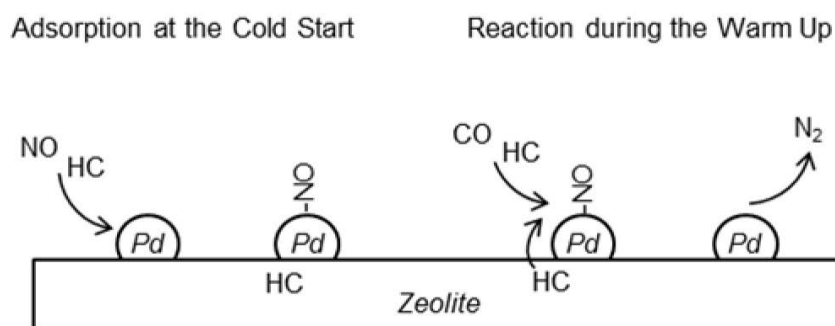


Figure 2.8. Adsorption and reduction of NO on Pd/ZSM-5. Source: SAE 2012-01-1002 [48]. Reprinted with permission.

2.5. NO_x Storage and Release Mechanisms.

Although NO_x is generally stored in the form of nitrites and nitrates, the details of the specific mechanisms of adsorption and desorption are not well known. However, Diffuse Reflectance Infrared Fourier Transform Spectroscopy (DRIFTS) has been used in some cases to gain insight into NO_x storage mechanisms. A study by Luo and co-workers established different NO_x storage routes for Al₂O₃- and CeO₂-containing catalysts during the adsorption of NO with O₂ at 200 °C. The appearance of nitrite and nitrate bands was observed for Pt/Al₂O₃ and Pt/CeO₂/Al₂O₃, while nitrite bands first appeared for Pt/CeO₂ with the appearance of nitrate bands over time. DRIFTS studies conducted during temperature programmed desorption (TPD) saw a decrease in intensity of nitrite bands with increasing temperature for all catalysts [49].

A DRIFTS study conducted by Philipp et al. for unpromoted CeO₂ found similar results to Luo et al. Experiments involving only the adsorption of NO resulted in nitrite bands and no nitrate bands. However, when NO was adsorbed in the presence of O₂ a bridged nitrate band appeared over time suggesting that the NO is adsorbed and then oxidized [50]. A 2007 study published by Symalla et al. for CeO₂ and BaO/CeO₂ found storage to be through a nitrite route, which is oxidized to form nitrates when oxygen is present. It was also found that oxidation to form nitrates decreases with increasing

amounts of BaO [51]. In summary, all three studies suggest that NO is stored through a nitrite route in CeO₂-containing catalysts. These studies also suggest that the addition of different supports and promoters to the CeO₂ can affect storage mechanisms.

Finally, when Pd/CeO₂-ZrO₂-Pr₂O₃ was exposed under stoichiometric CO + HC + NO_x + O₂ reaction conditions, Yang et al. [52] observed the formation of nitrite surface species on ceria-rich catalysts at 50 °C, while zirconia-rich catalysts favored the formation of nitrates. Higher Zr content afforded a higher concentration of active oxygen species, facilitating the oxidation of nitrites to nitrates and explaining why Zr-rich catalysts favor NO_x storage as nitrates at 50 °C.

Different authors have suggested different mechanisms for nitrite and nitrate formation on CeO₂ and CeO₂-ZrO₂ [53-58]. The occurrence of nitrite storage has been suggested to proceed through interactions of NO with Ce⁴⁺ sites to form nitrites (-NO₂⁻). Oxygen vacancies have also been found to play an important role in NO_x storage. Nitrites can form by adsorption of NO onto an oxygen vacancy site, which is then oxidized through the interaction of neighboring lattice oxygens. Nitrates have been found to form through similar methods. Nitrite and nitrate formation on CeO₂-containing catalysts will be discussed in more detail in Chapter 4.

2.6. Summary.

Diesel emission control is advancing to meet upcoming Tier 3 and LEV VIII standards by focusing on the mitigation of cold start emissions. To meet more stringent emission control targets researchers are focusing on the type of precious metals used, i.e., the use of Pt which promotes the formation of nitrates (that require higher temperatures to be removed) versus the use of Pd that promotes the formation of nitrites requiring lower temperatures for removal compared to nitrates. NO_x storage materials are also a focus of research. Doping CeO₂ with other rare earth metals has been found to increase NO_x storage at low temperatures (below 350 °C) by increasing lattice oxygen vacancies, doping with Pr appearing to be particularly promising for low temperature operations. Palladium promoted zeolites have also been found to be promising for PNA applications.

Chapter 3. Electron Microscopy Study of LNT and SCR catalysts.

Note—This chapter was preprinted from:

Wang, J.; Ji, Y.; Jacobs, G.; Jones, S.; Kim, D.J.; Crocker, M. Effect of aging on NO_x reduction in coupled LNT-SCR systems. *Appl. Catal. B: Env.* 2014, 148-149, 51-61.

This article appears in this dissertation with permission from Elsevier.

Note: Catalyst aging (description in section 3.2.1) was not performed by the author.

3.1. Introduction

While lean burn engines are more efficient than traditional stoichiometric engines, affording better fuel economy and producing lower CO emissions, they produce larger NO_x emissions. Two approaches have been developed commercially to reduce NO_x emissions: Lean NO_x Trap (LNT) and Selective Catalytic Reduction (SCR) catalysts. LNT catalysts are designed to store NO_x under lean conditions, the stored NO_x being reduced to N₂ by periodic operation under rich conditions. SCR catalysts effectively reduce NO_x to N₂ with NH₃ (from an external source) in the presence of excess O₂. Coupling LNT and SCR catalysts has been found to improve NO_x removal and afford lower NH₃ slip (generated over the LNT during rich purging) compared to the use of a LNT catalyst alone because the SCR catalyst is able to reduce NO_x slip using the NH₃. Moreover, when using a commercial Cu-chabazite catalyst as the SCR component it has been shown that a second NO_x reduction pathway can operate. In this second reduction pathway, HCs that slip through the LNT catalyst during the rich phase of cycling can act as NO_x reductants over the Cu-CHA (chabazite) catalyst [1-2]. The addition of the SCR catalyst also helps to reduce N₂O emissions formed over the LNT catalyst [3]. Given that the SCR catalyst can contribute to the overall NO_x reduction achieved by the system, a lower PGM loading can be used on the LNT to reduce NO_x when coupled with a SCR catalyst, lowering the overall cost [2, 4].

Commercially available LNT catalysts have exhibited durability problems. By coupling LNT and SCR catalysts the durability of the system should be enhanced compared to the LNT-only case since the SCR catalyst can compensate, to a degree, for the decreased NO_x conversion over the LNT. Deactivation of LNT catalysts has been

found to occur through two routes, the first being the sintering of the PGM resulting in phase segregation of the PGM and the NO_x storage component (in this case Ba). The second deactivation route occurs through the accumulation of sulfur in the NO_x storage phase that is not completely removed during periodic desulfation [5-8]. In contrast, Cu-chabazite SCR catalysts are generally found to have high durability with respect to hydrothermal aging [9-10]. However, deactivation of Cu-chabazite catalysts can occur at high temperatures through dealumination of the zeolite, leading to the collapse of the zeolite framework, as well as Cu sintering [11].

Seo et al. [12] evaluated the de-NO_x performance of an LNT-SCR system after hydrothermal aging and sulfur poisoning. NO_x conversion was found to be lower after aging for both the LNT only and LNT-SCR systems. However, the LNT-SCR system displayed increased NO_x conversion of 10-30% compared to only the LNT. Combining the LNT and SCR catalysts also resulted in a decrease in NH₃ emissions due to the consumption of NH₃ (produced over the LNT) downstream by the SCR catalyst (via reaction with NO_x). Although the LNT-SCR system did not recover its initial NO_x conversion level after sulfur poisoning, the system was considered promising due to decreases in NH₃ and N₂O emissions compared to the LNT only. Researchers at Ford [13-14] reported numerous advantages of using Fe-zeolite or Cu-zeolite catalysts as the SCR component in LNT-SCR systems. The use of ion exchanged zeolites as the SCR catalyst was found to compensate for the decreased NO_x reduction activity of the LNT after aging. It was also reported that lower desulfation temperatures were achieved and lower PGM loadings could be used for the LNT catalyst. Alternate NO_x reduction pathways utilizing adsorbed HC species in place of NH₃ were suggested and improved HC oxidation efficiency due to the SCR catalyst was reported.

Ford also evaluated the addition of a Cu-CHA (chabazite) SCR catalyst to an LNT catalysts for HC conversion after aging [15]. The Cu-CHA catalyst converts significant amounts of HC by utilizing stored HC species during rich regeneration of the LNT catalyst. Stored HCs are released or react over the SCR catalyst during subsequent lean operation. The longer the SCR catalyst was aged, the lower the ability of the catalyst to store HCs during rich operation. However, absolute NO_x and NMHC conversions over the Cu-CHA catalyst are increased when the upstream LNT catalyst is heavily aged due

to the increases HC and NO_x slip from the LNT. Although it is not beneficial for fuel economy, the addition of the SCR catalyst significantly increases NO_x and NMHC conversions compared to only the LNT catalyst. Placing the Cu-CHA catalyst both upstream and downstream of the LNT catalyst increased NMHC conversions. It is found to be most effective when placed upstream of the LNT, however, NO_x conversion is lowered in this configuration. This is due to either the upstream SCR catalyst delaying warm up of the LNT or the SCR withholding HCs necessary for the LNT to be effectively regenerated under rich conditions.

The following study utilizes transmission electron microscopy (TEM) and scanning transmission electron microscopy (STEM) to understand the effect aging has on the LNT-SCR system. The LNT (Pt/BaO/CeO₂) and SCR catalysts (Cu-chabazite) were provided by BASF. The aging protocol employed for these catalysts followed that disclosed in a recent publication (reference 18).

3.2. Experimental.

3.2.1. Aging protocol.

Catalyst aging was performed on a synthetic gas bench using a rapid aging protocol which has been detailed in earlier papers [16-17]. The LNT and SCR catalysts were placed in the same reactor, the SCR catalyst being placed downstream of the LNT. Each aging cycle was composed of three modes: sulfation, desulfation, and simulated DPF regeneration, the corresponding feed gas compositions being shown in Table 3.1. Fig. 3.1 summarizes the protocol used for the accelerated catalyst aging.

Table 3.1. Composition of feed gas used for LNT-SCR system aging. Source: Appl. Catal. B. Env. Reprinted with Permission.

Parameter	Sulfation		Desulfation		DPF Regeneration
	Lean	Rich	Lean	Rich	
Duration (s)	60	5	5	15	1800
Temperature (°C)	300	300	700	700	650
NO (ppm)	300	300	300	300	0
O ₂ (%)	8	0	8	0	8
CO (%)	--	5	0	4	0
H ₂ (%)	0	1.3	0	1.3	0

SO ₂ (ppm)	45	45	0	0	0
CO ₂ (%)	5	5	5	5	5
H ₂ O (%)	5	5	5	5	5
N ₂ (%)	Balance	Balance	Balance	Balance	Balance
Space velocity (h ⁻¹)	60,000	60,000	60,000	60,000	60,000

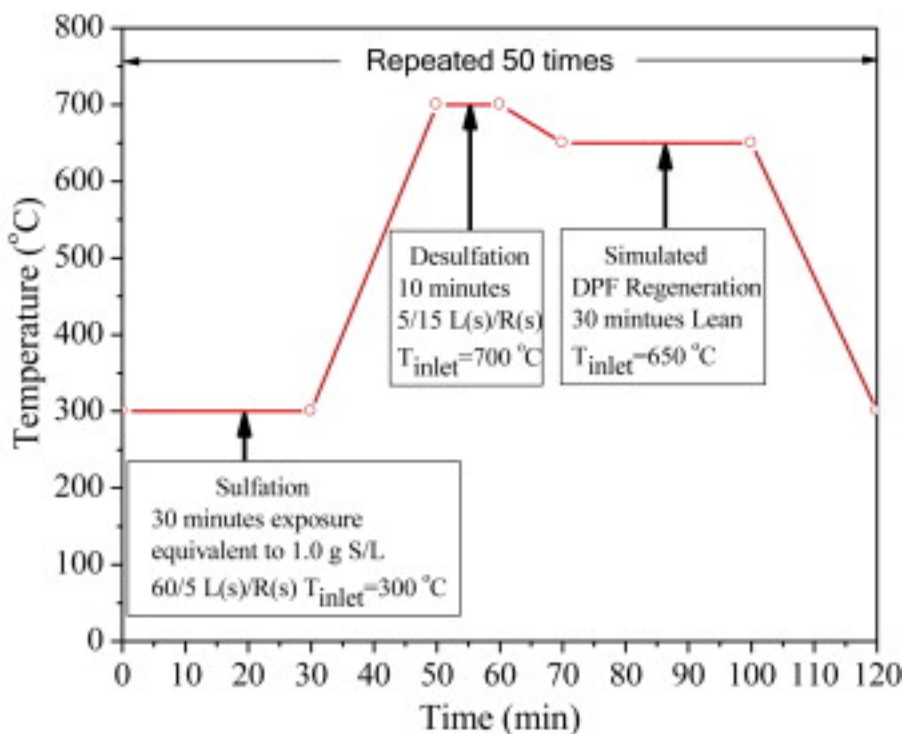


Figure 3.1. Summary of protocol used for accelerated catalyst aging. Source: Appl. Catal. B. Reprinted with Permission.

As described previously [17], the maximum mid-bed temperature experienced by the LNT catalyst occurs during the desulfation mode of the aging cycle and typically corresponds to 770 ± 10 °C, this being higher than the 700 °C set-point due to the exotherm created by lean-rich cycling. This is illustrated in Figure 3.2, which depicts LNT catalyst inlet and mid-bed temperatures for one aging cycle.

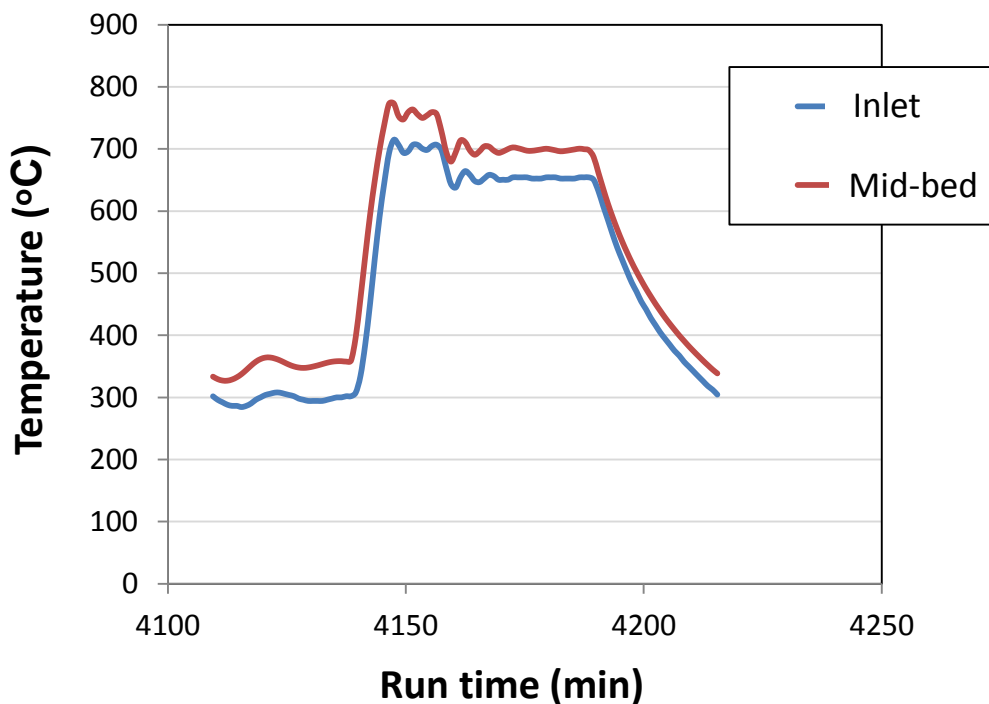


Figure 3.2. LNT catalyst inlet and mid-bed temperatures during aging (one aging cycle depicted). Source: Appl. Catal. B. Env. Reprinted with permission.

The corresponding maximum temperature experienced by the SCR catalyst downstream of the LNT was 750 ± 10 °C (inlet temperature). Depending on actual fuel sulfur levels, one aging cycle is estimated to be the equivalent to 1000-1500 miles of road aging. In total, 50 cycles were used for the aging, requiring a total aging time of ca. 100 hours. At the end of each aging run a final desulfation was performed under constant rich conditions, corresponding to 2% H₂ in the presence of 5% CO₂ and 5% H₂O at 750 °C for 10 min, in order to remove as much residual sulfur as possible.

3.2.2. Microscopy Methods.

Materials for electron microscopy analysis (TEM, STEM, and EDS) were collected by scraping a small amount of washcoat from the catalyst samples and supporting the material on TEM grids obtained from Electron Microscopy Sciences. TEM and STEM investigations were conducted using a field emission JEOL 2010F

STEM outfitted with a URP pole piece, GATAN 2000 GIF, GATAN DigiScann II, Fischione HAADF STEM detector, Oxford energy-dispersive X-ray detector and EmiSpec EsVision software. STEM measurements were acquired for fresh and aged samples using a high-resolution probe at 2 Å. For the SCR catalyst samples, nickel grids purchased from Electron Microscopy Sciences (EMS) were used in addition to the copper grids.

3.3. Results and Discussion.

Considering first the LNT catalyst samples, the alumina support appeared as spear shaped agglomerates in both fresh and aged LNT samples as displayed in Figure 3.3. Platinum particles appeared within the alumina support regions of the sample, measuring 2 nm or smaller in size in both fresh and aged samples. Platinum density appeared to be higher in barium rich areas. The size of the platinum particles was found to increase in aged samples (ranging from 13 nm to 27 nm in size—see figure A.2.2.), as confirmed by EDS in Figure 3.4, suggesting that Pt particle sintering occurred during aging.

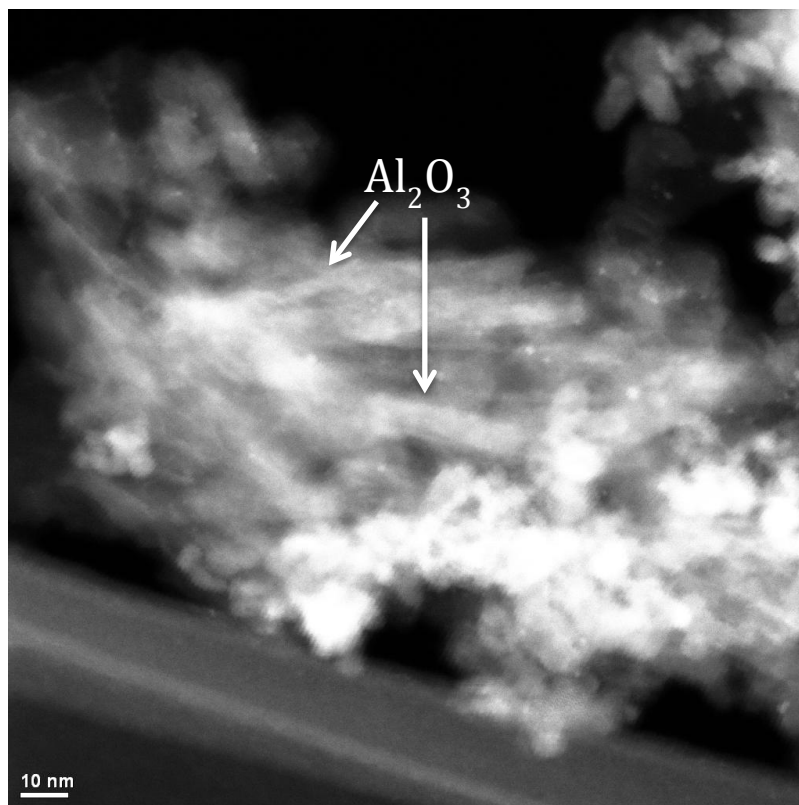


Figure 3.3. STEM of fresh LNT catalyst showing rod-like structures of alumina.

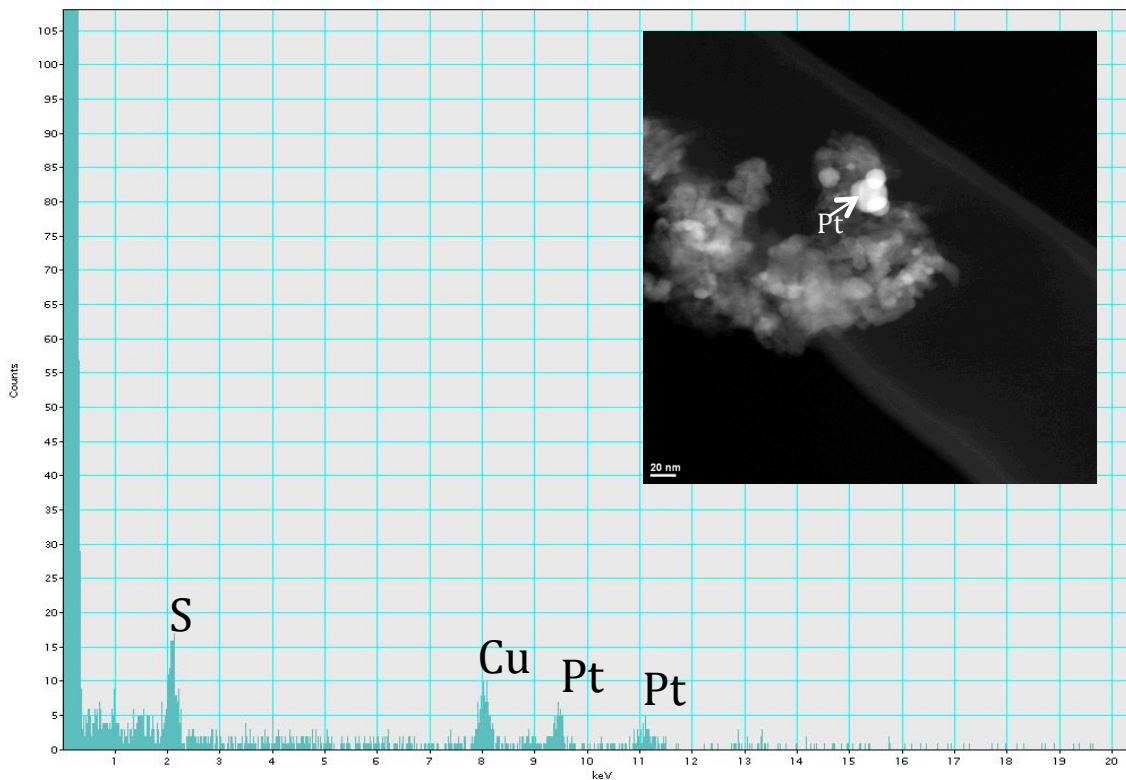


Figure 3.4. EDS line-scan on aged LNT catalyst indicating the presence of sulfur on the three sintered platinum particles in the upper right corner of the aged STEM image.

Source: Appl. Catal. B. Env. Reprinted with permission.

In Figure 3.5, EDS also indicated the presence of sulfur associated with platinum particles in aged samples. Note that heavier supports appeared brighter in coloration than lighter supports, i.e. the CeO_2 support appeared brighter than the BaO , which appeared brighter than the Al_2O_3 support, as pictured in Figure 3.5.

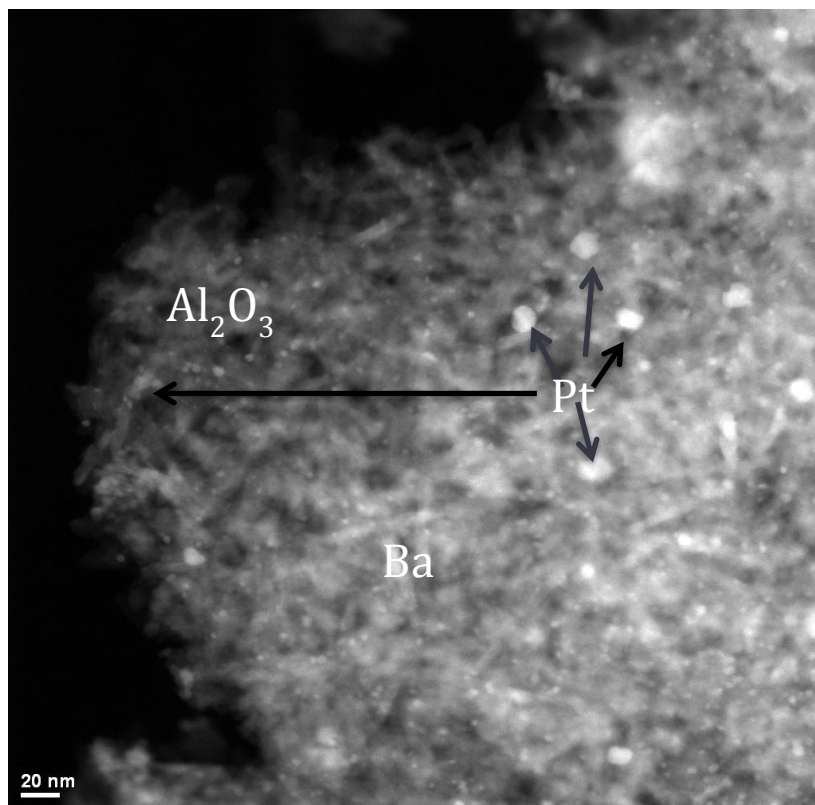


Figure 3.5. STEM image of aged LNT catalyst showing small platinum particles on the alumina support, while platinum density increases on barium rich areas. Source: Appl. Catal. B. Env. Reprinted with permission.

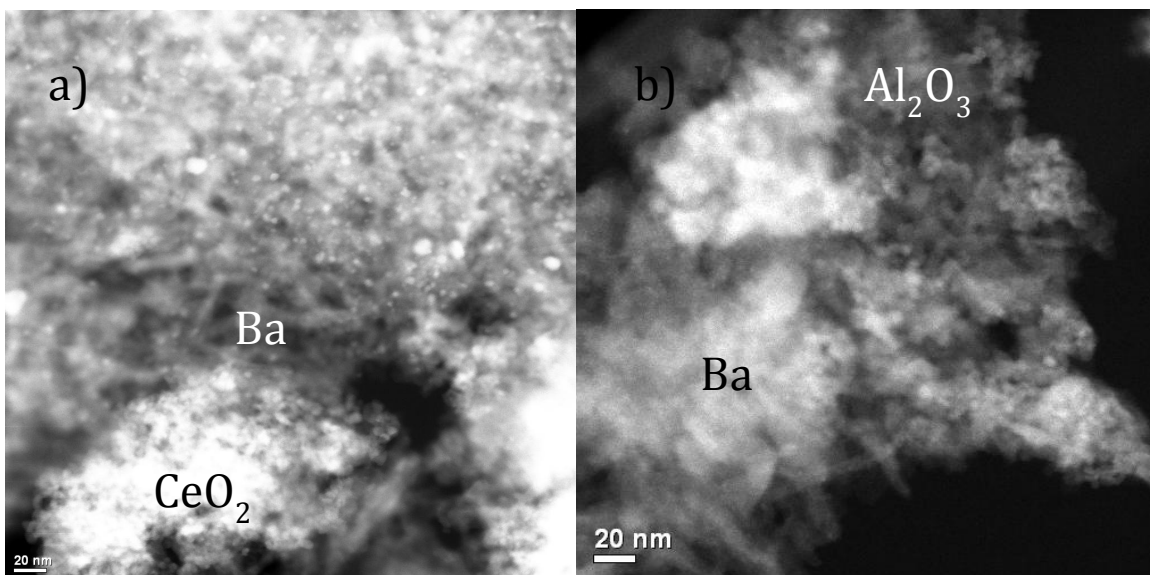


Figure 3.6. STEM image of aged LNT catalyst showing the different supports can be distinguished from one another in STEM because of the differences in atomic mass of Ce, Ba, and Al. a) CeO_2 appears much brighter in comparison to Ba. b) Al_2O_3 appears much darker than supported Ba. Source: Appl. Catal. B. Env. Reprinted with permission.

Structural changes in the fresh and aged SCR catalyst were observed through TEM. The aged sample showed the presence of structures with less well-defined edges (Figure 3.7), while the fresh sample showed the presence of structures with generally well-defined edges. Though this suggests loss of crystallinity after aging, this was not confirmed through powder x-ray diffraction (XRD). This is potentially due to the fact that XRD is a measure of the crystallinity of the bulk sample (indicating that the sample maintained a large degree of crystallinity), while TEM analyzes only a small amount of sample. The presence of Zr was also observed in both fresh and aged catalysts as confirmed by EDS in Figure 3.8. This suggests that the manufacturer added ZrO_2 to the washcoat, possibly as a binder and/or diluent. TEM also indicated the presence of CuO structures on the zeolite surface after aging [18]. This occurrence is consistent with observations published in *Catalysis Today* by Schmiege and coworkers on Cu-SZM-13 after aging. It was reported that Cu^{2+} originally located in the zeolite migrated to the outer zeolite surface and underwent agglomeration to form CuO during aging [19].

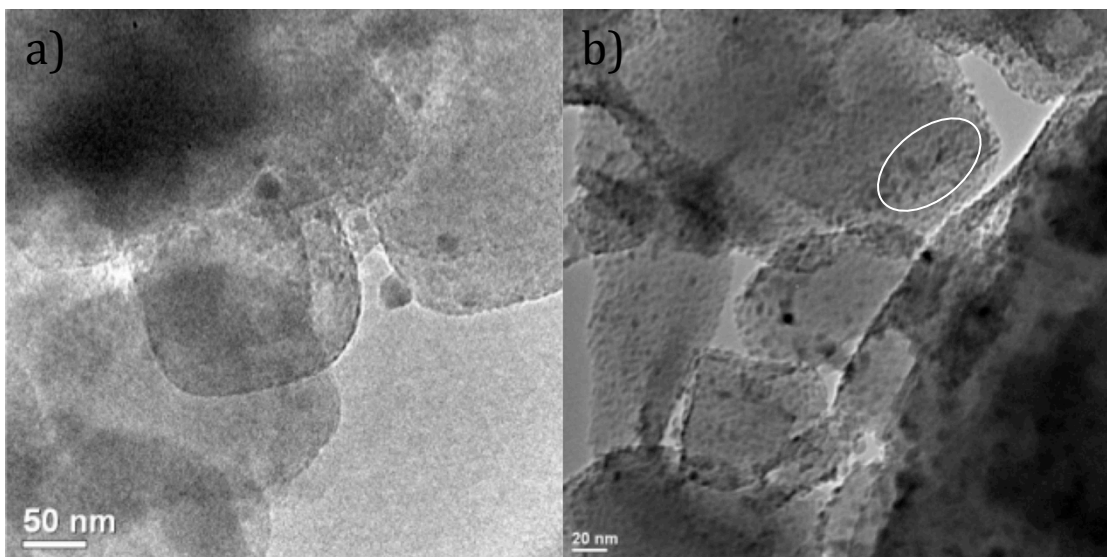


Figure 3.7. TEM images of the fresh SCR catalyst were found to have well-defined structures (Figure a). Aged structures exhibit less well-defined edges and contain Cu nanoparticles (highlighted, Figure b). Source: Appl. Catal. B. Env. Reprinted with permission.

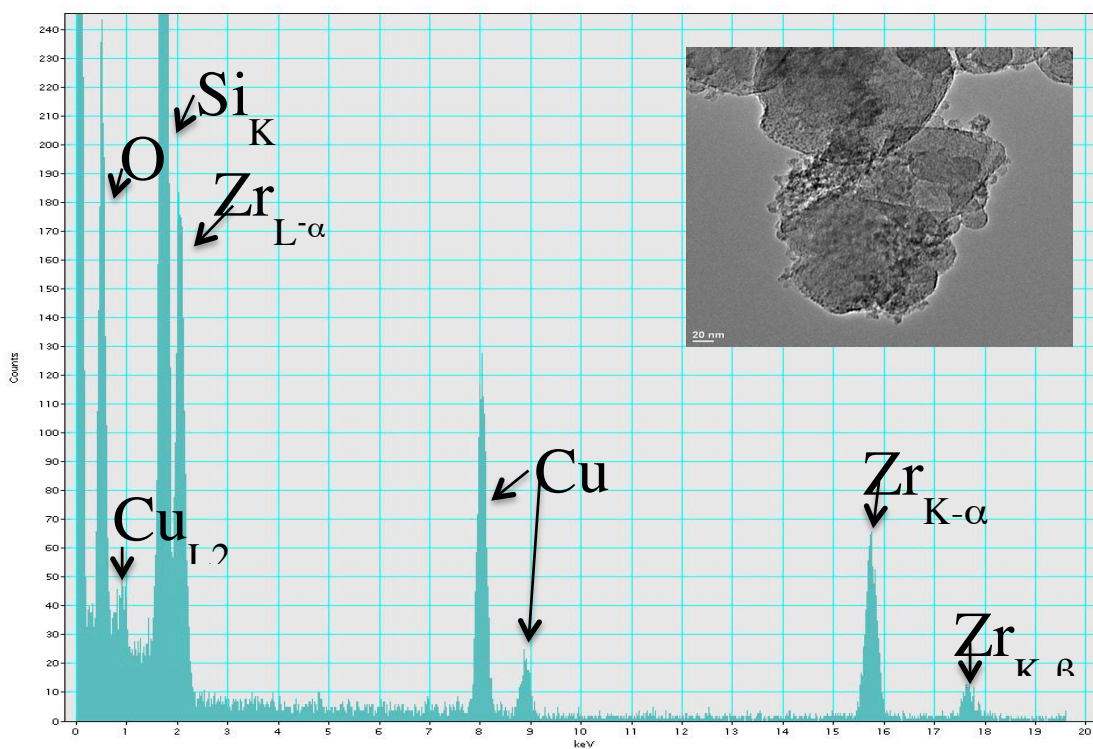


Figure 3.8. EDS spectra indicated the presence of Zr in the fresh SCR catalyst as well as the aged (not pictured). TEM inset is of the area on which EDS analysis was performed.

3.4. Conclusions.

Analysis of LNT and SCR catalysts subjected to simulated road aging revealed, in the case of the LNT, two main physico-chemical changes which contributed to catalyst deactivation: the accumulation of sulfur associated with the Pt, and sintering of the precious metals, resulting in decreased contact between the Pt and Ba phases. In the case of the SCR catalyst, upon aging some fraction of the Cu^{2+} species initially located in the zeolite migrated to the outer surface and underwent agglomeration to form CuO nanoparticles, although the catalyst maintained a high degree of activity in the NH_3 -SCR reaction (data not shown). The appearance of Zr was observed in both fresh and aged SCR catalysts, with no apparent change in structure after aging.

Chapter 4. Ceria-based Catalysts for Low-Temperature NO_x Storage and Release
Note—This chapter was reprinted from:

Jones, S.; Ji, Y.; Crocker, M. Ceria-based Catalysts for Low-Temperature NO_x Storage and Release. *Catalysis Letters*. 2015, 146, 909-917.

This article appears in this dissertation with permission from Elsevier.

4.1. Introduction.

If automotive manufacturers are to meet future emission standards, reducing cold start emissions is imperative. This is particularly true for lean burn engines, for which the mitigation of NO_x emissions is especially challenging. Current technology for NO_x mitigation in lean burn systems is based on the use of Lean NO_x Trap (LNT) and Selective Catalytic Reduction (SCR) catalysts that display limited activity below 200 °C. Moreover, in the case of urea-SCR, the slow rate of urea decomposition limits the ability to deploy this technology at low operating temperatures. Urea decomposition occurs in two steps [1-2]: in the first, the urea releases one equivalent of NH₃ and one equivalent of isocyanic acid (HNCO); the latter is then hydrolyzed to NH₃ and CO₂. However, at low temperatures deposits can accumulate on the catalyst, in the form of undecomposed urea, or compounds (such as melamine complexes) which result from side reactions of the HNCO [3]. Given that the accumulation of these compounds can poison the SCR catalyst at low temperatures, in practice urea injection is typically ramped in the temperature range ~150-200 °C, i.e., sub-stoichiometric amounts of urea are injected (to minimize catalyst poisoning at the expense of unconverted NO_x), stoichiometric urea injection beginning at ca. 200 °C [4]. This, in turn, limits the achievable NO_x conversion.

To address this problem, the use of passive NO_x adsorbers (PNAs) has been suggested as a solution for the NO_x slip emitted during cold starts [5]. The use of a passive NO_x adsorber (PNA) coupled with an SCR catalyst was first mentioned by Ford Motor Company in a 2001 patent in which a PNA consisting of γ -Al₂O₃ promoted with platinum was claimed [6]. Ji et al. [7] recently studied Pt/Al₂O₃ and Pt/La-Al₂O₃ for PNA applications, finding that the addition of 1 wt% La to Al₂O₃ resulted in the creation of new NO_x storage sites and improved NO_x storage efficiency. However, according to TPD measurements, Pt/La-Al₂O₃ exhibited slightly lower NO_x desorption efficiency below

250 °C than Pt/Al₂O₃. DRIFTS measurements indicated that during NO_x-TPD, nitrites and weakly bound nitrate species were initially removed from the surface of Pt/Al₂O₃ and Pt/La-Al₂O₃, NO_x desorption at higher temperatures (>250 °C) being mainly associated with nitrate decomposition. The use of Ag/Al₂O₃ for low temperature NO_x storage has also been reported [8,9], albeit the presence of H₂ is required for NO oxidation and adsorption below 200 °C. In a recent report by Honda, the use of a NO_x trap three-way catalyst (N-TWC) consisting of Pd on ZSM-5 was able to reduce NO_x and hydrocarbon emissions during cold starts which has proven to be a problem for traditional TWC catalysts [10].

Ceria and ceria-containing systems also represent interesting candidates for PNA applications given that anionic vacancies in the crystal lattice [11-14] have been found to facilitate NO_x adsorption [15-17]. Information concerning the mechanism of NO_x storage on ceria has been provided by the results of several studies employing Diffuse Reflectance Infrared Fourier Transform Spectroscopy (DRIFTS) measurements. Philipp et al. found that the adsorption of O₂ and NO on bare ceria at 50 °C resulted in the adsorption of NO as a nitrite which subsequently underwent oxidation to nitrate [18]. In the case of NO/O₂ adsorption on Pt/CeO₂, Ji et al. [19] observed the formation of nitrites at 25 °C, while at 200 °C nitrates were formed almost exclusively. Luo et al. [20] also studied NO/O₂ adsorption on Pt/CeO₂ in the presence of O₂ and concluded that NO_x is initially stored as nitrite. In a similar vein, a 2012 patent claims the use of Pd supported on CeO₂ as a PNA [21] and indicates that NO does not need to be oxidized to NO₂ for storage to occur. Subsequently, Chen et al. [22] reported that a diesel Cold Start Catalyst (dCSCTM) incorporating the PNA from the aforementioned patent (together with a hydrocarbon trap), has the ability to store NO_x as a nitrite, as opposed to nitrate, thereby making it easier to regenerate the NO_x storage function of the catalyst. Recently, Yang et al. [23] reported DRIFTS data for Pd/CeO₂-ZrO₂-Pr₂O₃ catalysts exposed to stoichiometric CO+HC+NO_x+O₂ reaction conditions. For ceria-rich catalysts, nitrites were the main surface species formed at 50 °C, while zirconia-rich compositions favored the formation of nitrates; this was attributed to the increased concentration of active oxygen species at higher Zr content, facilitating nitrite oxidation to nitrate.

Herein we report a comparison of 1 wt% Pt and Pd supported on ceria for PNA use. Although ceria is typically stabilized with other metals for automotive applications [24], in this study we used an unstabilized ceria support in order to simplify data interpretation. The NO_x storage and desorption efficiencies of the catalysts were evaluated at several temperatures, in both the presence and absence of CO₂ and H₂O, and the ability of the catalysts to store and release NO_x upon repeated adsorption-desorption cycling was ascertained. DRIFTS measurements were utilized to understand the surface species present during NO_x adsorption and desorption.

4.2. Experimental Methods.

4.2.1. Catalyst Preparation.

CeO₂ was prepared by precipitation from aqueous Ce(NO₃)₃ [25] and calcined in air at 500 °C for 3 h (Figure A.2.3.). 1 wt% Pt or Pd was loaded onto the CeO₂ by means of incipient wetness impregnation using aqueous solutions of [Pt(NH₃)₄](NO₃)₂ or Pd(NO₃)₂*xH₂O. The resulting samples were calcined at 500 °C for 3 h in a muffle furnace.

4.2.2. Catalyst Characterization.

X-ray powder diffraction analysis was conducted on a Phillips X'Pert diffractometer using Cu-Kα radiation ($\lambda=1.540598 \text{ \AA}$). Diffractograms were recorded between 5° and 90° (2θ) with a step size of 0.02°. Brunauer-Emmett-Teller (BET) surface area and pore volume measurements were performed by nitrogen physisorption at -196 °C using a Micromeritics Tri-Star 3000 system. Catalyst samples were outgassed overnight at 160 °C under vacuum prior to measurements.

Pt and Pd dispersions were determined by means of pulsed CO chemisorption at -78 °C using a Micromeritics AutoChem II Analyzer. Samples (250 mg) were loaded into the reactor and reduced in 10% H₂/Ar at 300 °C for 10 min. In each case the sample was then purged with Ar for 20 min at the same temperature to remove residual H₂ and then cooled to -78 °C prior to CO chemisorption. During the measurements 100 μl of CO was pulsed into the reactor every 2 min, the CO signal being monitored with a thermal conductivity detector (TCD). CO pulsing was terminated when the TCD signal reached a

constant value, i.e., the precious metal sites were saturated with CO. Assuming a 1:1 ratio of CO to surface Pt and Pd atoms, the metal dispersion was calculated based on the amount of CO adsorbed. The Pt dispersion was also measured for Pt/CeO₂ using H₂ chemisorption at -78 °C, the value obtained (42%) showing good agreement with that obtained by CO chemisorption at -78 °C (46%).

Materials for electron microscopy were supported on Cu grids purchased from Electron Microscopy Sciences. Transmission electron microscopy (TEM) and scanning transmission electron microscopy (STEM) studies were conducted using a field emission JEOL 2010F with a URP pole piece, GATAN 200 GIF, GATAN DigiScann II, Fischione HAADF STEM detector, Oxford energy-dispersive X-ray detector and EmiSpec EsVision software. STEM measurements were acquired for 1%Pd/CeO₂ using a high-resolution probe at 2 Å.

4.2.3. NO_x storage and desorption measurements.

NO_x storage and desorption efficiencies of the catalysts were determined in a quartz microreactor with a Pfeiffer Thermostar GSD301 mass spectrometer as the detector. Prior to measurements samples (170 mg) were pretreated at 550 °C for 10 min under a flow of 5% O₂ in He (120 sccm) and then cooled to room temperature under flowing Ar. Samples were then equilibrated under a flow of 3.5% H₂O, 5.0% CO₂ and 5% O₂ (bal. He, 120 sccm) at the designated storage temperature; typically, this took 15 min, at which point the feed and effluent H₂O and CO₂ concentrations were equivalent. NO_x storage was initiated by adding 300 ppm NO to the feed. Storage experiments were conducted at 80 °C, 120 °C and 160 °C using a 5 min storage time. In all cases, a total flow rate of 120 sccm was used, corresponding to a gas hourly space velocity (GHSV) of ca. 30,000 h⁻¹. At the completion of the storage period the feed gas was switched to bypass mode and the NO flow was switched off. When the NO concentration had dropped to zero, the gas was re-directed to the reactor and temperature programmed desorption (TPD) was carried out to study NO_x desorption behavior using a ramp rate of 10 °C/min from the storage temperature up to 500 °C.

To understand the effect of multiple storage-desorption cycles, cycling experiments were also performed. Catalyst pretreatment and NO_x storage were performed

as described above (using a storage temperature of 120 °C), after which TPD was performed up to 350 °C at a ramp of 10 °C/min under the same lean feed gas with the exclusion of NO. Subsequently, the temperature was lowered to 120 °C for the next NO_x adsorption-desorption cycle. A total of five cycles were performed for both Pt/CeO₂ and Pd/CeO₂.

NO_x storage efficiency (hereafter denoted as NSE) is defined as the percentage of NO_x passed over the catalyst that is stored, while NO_x desorption efficiency (hereafter denoted as NDE) is defined as the percentage of stored NO_x desorbed during TPD, i.e.:

$$\text{NSE} = \left(1 - \frac{\int_0^t ([\text{NO}_x]_{\text{out}}) dt}{\int_0^t ([\text{NO}]_{\text{in}})} \right) \times 100\%$$

$$\text{NDE} = \left(\frac{\int_{t(T_0)}^{t(T)} ([\text{NO}_x]_{\text{out}}) dt}{\text{NSE} \times t \times [\text{NO}]_{\text{in}}} \right) \times 100\%$$

in which t is the NO_x storage time; $[\text{NO}]_{\text{in}}$ is the inlet NO_x concentration during NO_x storage; $[\text{NO}_x]_{\text{out}}$ is the outlet NO_x concentration during either NO_x storage or the subsequent NO_x desorption period; $t(T_0)$ is the start time of NO_x-TPD corresponding to the NO_x storage temperature before the temperature is raised; $t(T)$ is the end time of NO_x-TPD corresponding to the desired NO_x desorption temperature.

4.2.4. DRIFTS measurements.

DRIFTS measurements were performed to monitor the surface species involved in NO_x adsorption and desorption. Measurements were performed using a Nicolet 6700 IR spectrometer equipped with a Harrick Praying Mantis accessory and MCT detector. The reaction cell was sealed with a dome equipped with two ZnSe windows and one SiO₂ observation window. The temperature of the reactor cell was controlled and monitored by a K-type thermocouple placed beneath the reaction chamber. For each DRIFT spectrum an average of 115 scans was collected (requiring ca. 1 min) with a resolution of 4 cm⁻¹. The spectrometer as well as the outside of the reaction cell were continuously purged with dry nitrogen to avoid diffusion of air into the system. Catalyst samples (~50 mg)

were pretreated in situ in 5% O₂/Ar (120 sccm) at 500 °C for 1 h in order to remove moisture and carbonates, after which background spectra were collected (using the same feed gas) in the range 500-100 °C at intervals of 50 °C. NO_x storage was carried out at 100 °C for 30 min using a feed consisting of 5% O₂/Ar and 300 ppm NO (120 sccm). During NO_x storage, spectra were collected as a function of time. After 30 min of NO_x storage, TPD was performed in flowing 5% O₂/Ar flow (120 sccm), the temperature being raised from 100 °C to 500 °C at a rate of 10 °C/min. DRIFT spectra were recorded during TPD at intervals of 50 °C. Absorbance spectra were obtained by subtracting background spectra from the spectra collected during NO_x storage and desorption.

4.3. Results and Discussion.

4.3.1. Sample characterization.

Analytical data for the two PNA samples prepared in this work are collected in Table 1. After calcination at 500 °C the powder X-ray diffractogram of the CeO₂ support contained diffraction lines corresponding to (111), (200), (220), (311), (222), (400), (331), (420) and (422) crystal planes (data not shown), characteristic of the fluorite crystal structure of CeO₂. The average CeO₂ particle size calculated using the Scherrer equation was 13.2 nm. From N₂ physisorption data a BET surface area of 75.1 m²/g was obtained, which is typical of CeO₂ prepared by precipitation methods [24]. Upon loading with 1 wt% Pt and 1 wt% Pd (followed by calcination) the specific surface area decreased to 71.7 m²/g and 71.3 m²/g, respectively, indicative of minimal pore filling of the support. CO chemisorption results indicated an average Pt particle size of 1.92 nm for the Pt/CeO₂, the average Pd particle size being 2.41 nm in the Pd/CeO₂ sample (Table 4.1). Consistent with the highly dispersed nature of the Pt and Pd in these samples, diffraction lines for Pt and Pd were not observed in their X-ray diffractograms. TEM analysis of 1 wt% Pd/CeO₂ revealed that the CeO₂ crystals possessed a rod-like structure (data not shown). Individual Pd particles could not be imaged.

Table 4.1. Summary of CeO₂ particle size calculated from x-ray diffraction data, BET surface area (SA), pore volume, pore diameter, and metal particle size diameter determined by CO chemisorption.

Catalyst	CeO ₂ particle size (nm)	BET SA (m ² /g)	Pore Diameter (nm)	Pore Volume (cm ³ /g)	Metal particle size (nm)
CeO ₂	12.2	75.1	4.4	0.17	--
Pt/CeO ₂	12.6	71.7	4.4	0.16	2.71
Pd/CeO ₂	13.0	71.3	4.4	0.16	2.83

4.3.2. NO_x adsorption.

NO_x storage temperatures of 80 °C, 120 °C, and 160 °C were utilized during NO_x storage-desorption studies. The minimum temperature of 80 °C was chosen based on published data from Ford Motor Co. [26] showing that for a 4.4 L diesel engine the exhaust gas temperature behind a diesel oxidation catalyst (DOC), upstream of an SCR catalyst, reaches ~60 °C after the first ~10 s of a cold start, whereas temperatures greater than 180 °C are not obtained for ~180 seconds. Five minute NO_x storage efficiency (NSE) data for CeO₂, 1 wt% Pt/CeO₂, and 1 wt% Pd/CeO₂ are shown in Figure 4.1. Notably, the addition of Pt to CeO₂ improved the NSE by more than a factor of two at 120 °C at all times during the 5 min storage experiment. In comparison, the addition of Pd produced an increase of only 37.4% in the 5 min NSE compared to the bare CeO₂ sample. Both Pt/CeO₂ and Pd/CeO₂ exhibited similar storage trends with respect to temperature, i.e., higher storage temperatures resulted in higher NSE (and hence higher amounts of stored NO_x), this effect being most prominent for Pt/CeO₂. As described below, this can be attributed to the increase in oxygen mobility at the CeO₂ surface at higher temperatures. Additionally, in the case of Pt/CeO₂, an increase in the rate of NO oxidation can be expected in this temperature span, given that NO oxidation on Pt typically lights-off at temperatures in the range 100-200 °C [27]. Hence, increase of the temperature in this range should result in significantly enhanced rates of nitrate formation, with an accompanying increase in NSE. In the case of Pd, NO oxidation activity is comparatively low, even at high temperatures [28-29]. Consequently, at each

temperature Pt/CeO₂ stored significantly more NO_x than Pd/CeO₂, as exemplified by 1 min NSE values at 160 °C of 78.7 % for Pt/CeO₂ and 31.1 % for Pd/CeO₂.

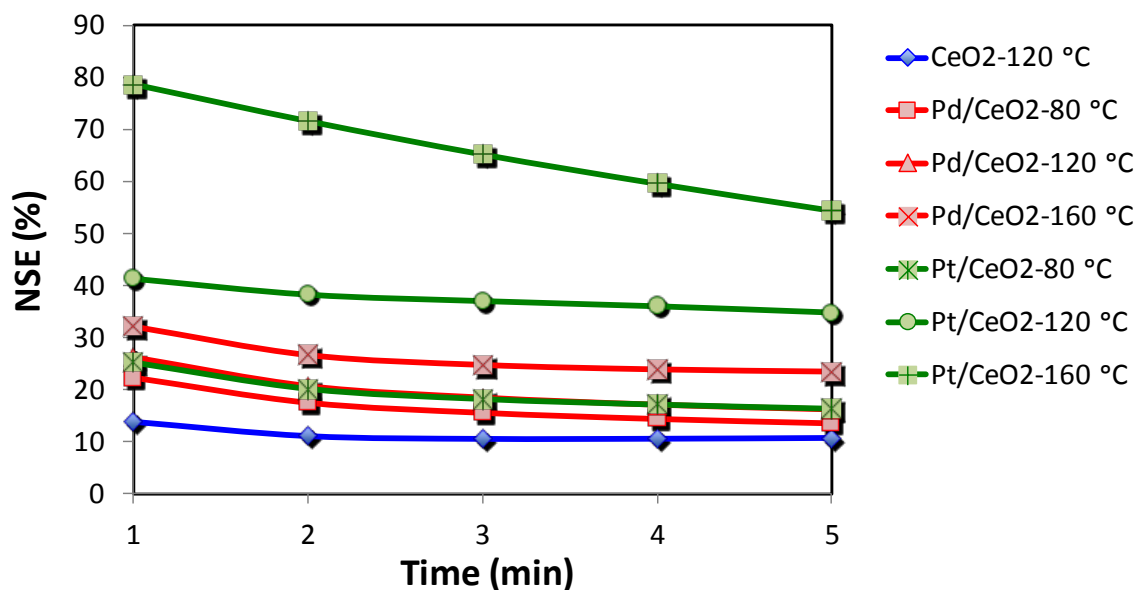


Figure 4.1. Comparison of NO_x storage efficiency at 80, 120, and 160 °C for Pt/CeO₂ and Pd/CeO₂. Feed: 300 ppm NO, 5% O₂, 5% CO₂, 3.5% H₂O and He balance.

4.3.3. NO_x desorption.

NO_x-TPD profiles obtained after NO_x storage at 120 °C are shown in Figure 4.2. In each case two NO_x desorption events were evident. The first occurred below 300 °C, while the second was characterized by a desorption maximum in the range 300-500 °C. The addition of Pt shifted both desorption peaks to lower temperatures compared to bare CeO₂, while the addition of Pd to CeO₂ shifted only the high temperature desorption peak to lower temperature. Both Pd/CeO₂ and the CeO₂ support released relatively more NO_x at lower temperatures (compared to the higher temperature desorption peak) in comparison with Pt/CeO₂; for the latter, the vast majority of the stored NO_x was released at temperatures in excess of 300 °C.

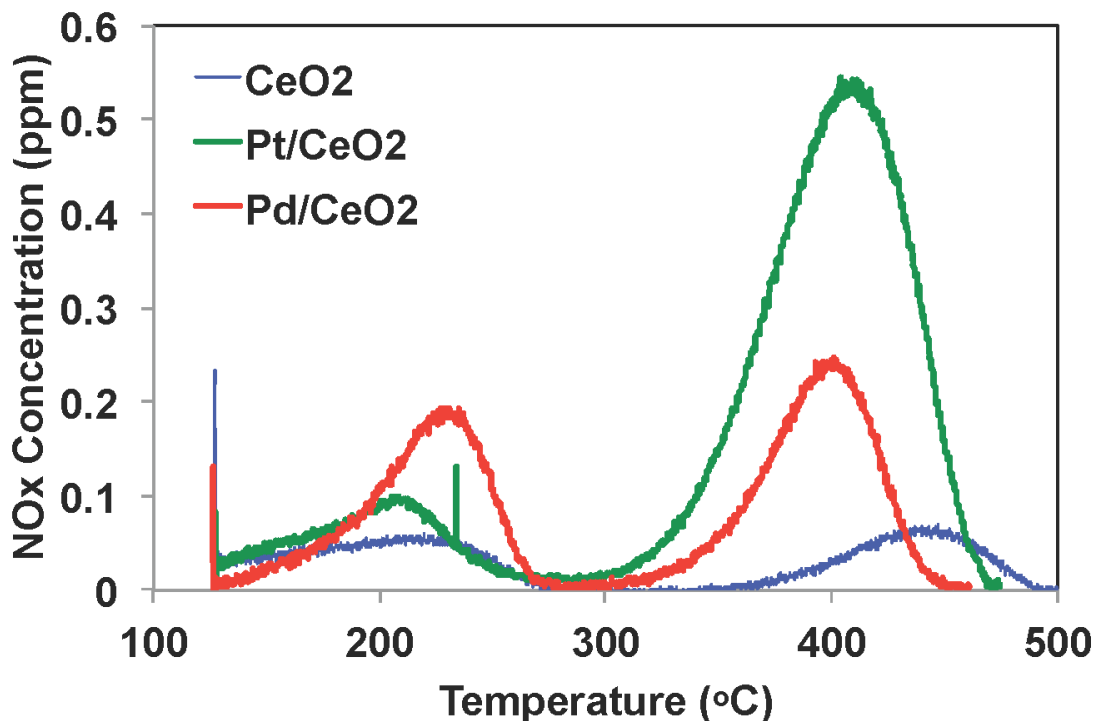


Figure 4.2. NO_x release profiles during temperature programmed desorption (TPD) after NO_x storage at 120 °C for 5 min.

The calculated NO_x desorption efficiency (NDE) values for CeO₂, Pd/CeO₂ and Pt/CeO₂ during thermal ramping to 500 °C are displayed in Figure 4.3; results are shown for three cases, corresponding to NO_x storage at 80 °C, 120 °C and 160 °C. From the figure it is evident that the bare CeO₂ and Pd/CeO₂ samples consistently release a greater percentage of their NO_x below 350 °C – the highest temperature the catalysts would see in an exhaust during the US06 cycle [5] – as compared to the Pt/CeO₂ sample, which is in line with the higher NO oxidation activity of Pt/CeO₂. In a previous study of NO_x desorption from Al₂O₃ and Pt/Al₂O₃ samples we observed that NDE below 250 °C was greater for the bare Al₂O₃ support as compared to the Pt-containing sample [7]. This was attributed to the fact that NO oxidation results in the formation of nitrate species which are more thermally stable than the products of NO adsorption (nitrites). Moreover, NO which desorbs from Pt/Al₂O₃ can in principal be oxidized to NO₂ and re-adsorbed to form

thermally stable nitrates. Similar reasoning can be applied to the samples studied in the present work.

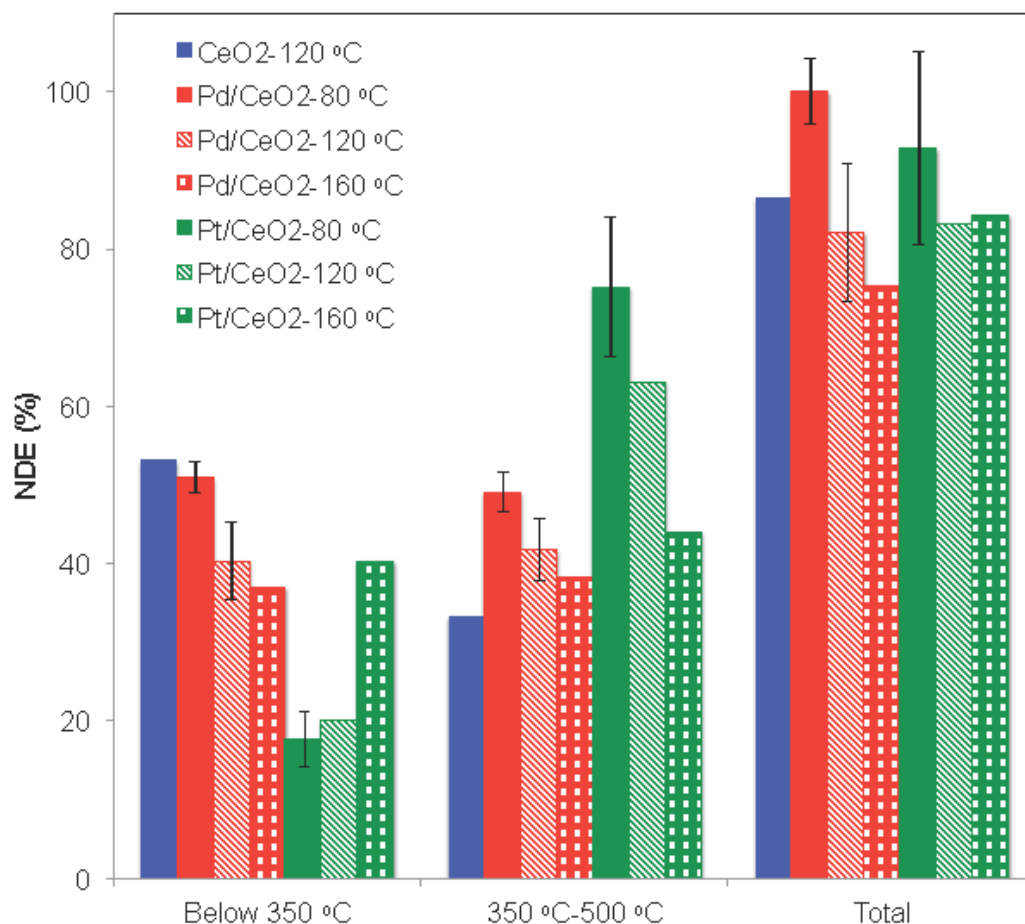


Figure 4.3. Comparison of NO_x desorption efficiency for two different temperature ranges: < 350 °C and 350-500 °C.

Figure 4.4 summarizes the absolute amount of NO_x desorbed during TPD. Both Pt/CeO₂ and Pd/CeO₂ released increasing amounts of NO_x with increasing NO_x storage temperature. This trend was previously observed for Pt/Al₂O₃ and is a consequence of the increased amount of NO_x stored at higher temperatures. Pt/CeO₂ released significantly more NO_x upon ramping to 500 °C than the Pd analog for all storage temperatures, again reflecting the greater amount of NO_x stored. Notably, however, Pd/CeO₂ released more NO_x below 350 °C than Pt/CeO₂ for the 80 °C and 120 °C storage temperatures as a

consequence of its superior NDE at lower temperatures. This suggests that Pd-based PNAs may offer advantages over their Pt analogs, particularly at lower temperatures.

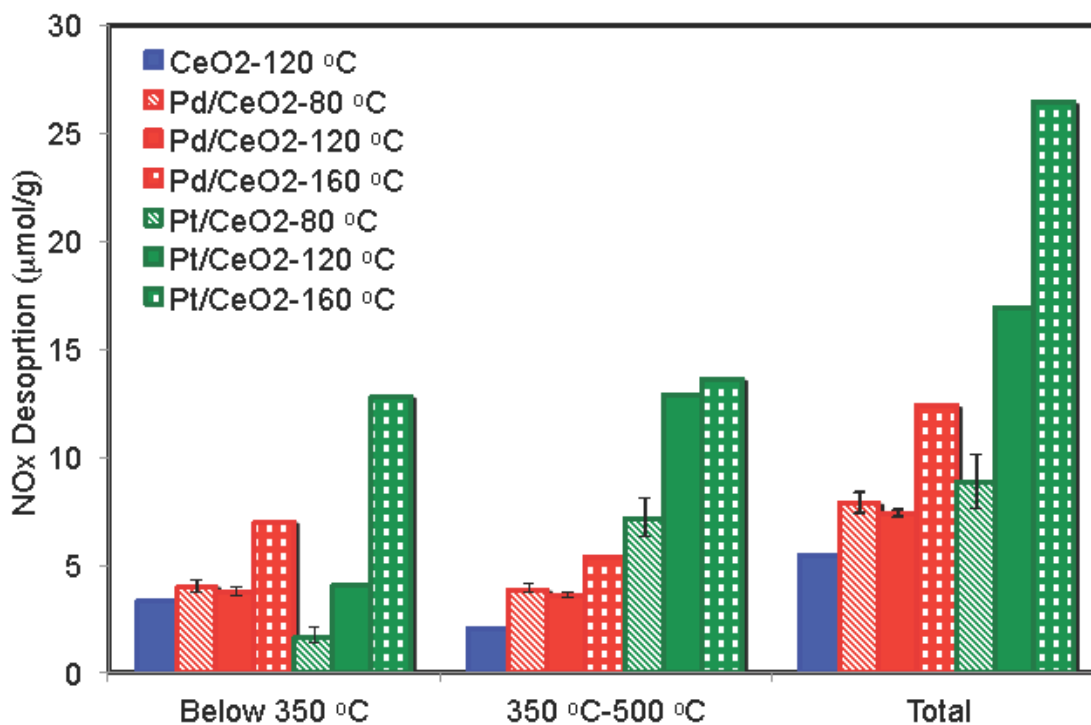


Figure 4.4. Effect of NO_x storage temperature on the amount of NO_x desorbed during TPD.

4.3.4. Effect of CO₂ and H₂O on NO_x adsorption/desorption.

Storage/desorption studies were also performed in the absence of CO₂ and H₂O at 120 °C for 5 min to facilitate a realistic comparison between microreactor data and DRIFTS spectra (vide infra). Figure 4.5 shows the measured NSE as a function of time, while Figure 4.6 shows the corresponding NDE data. Both catalysts stored more than double the amount of NO_x that was stored in the presence of CO₂ and water, indicating that CO₂ and water can competitively adsorb with NO_x [30]. For example, Pt/CeO₂ stored 83.9% of feed NO_x after one minute at 120 °C, the corresponding NSE value measured in the presence of CO₂ and H₂O being 41.3%.

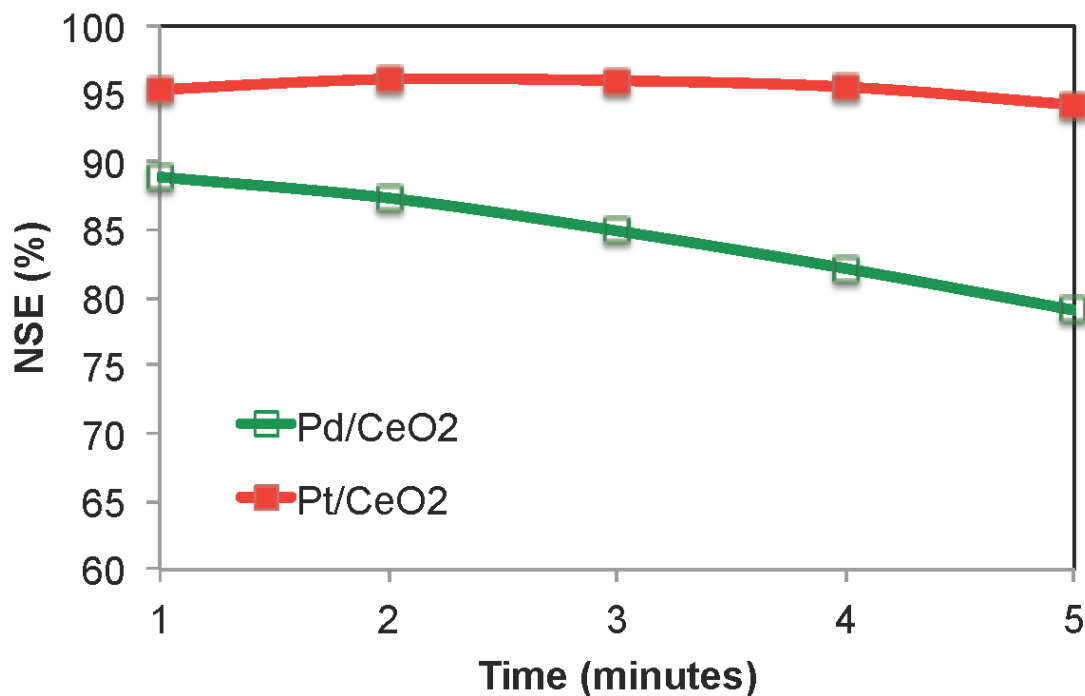


Figure 4.5. Comparison of NO_x storage efficiency at 120 °C in the absence of H₂O and CO₂.

According to the NDE data, Pd/CeO₂ again released significantly more NO_x at low temperatures (<300 °C) than Pt/CeO₂ (Fig. 4.6). However, NO_x desorption above 350 °C for Pd/CeO₂ was roughly double the amount of NO_x released below 350 °C, whereas the amount of high temperature and low temperature NO_x release in the presence of CO₂ and water was roughly equal (Fig. 4.3). The same pattern was observed for Pt/CeO₂, significantly more NO_x being released above 350 °C in the absence of CO₂ and water than in the presence of CO₂ and water. This is a notable result, suggesting that in the absence of water and CO₂ the formation of nitrates is preferred, resulting in a higher proportion of NO_x being stored as more thermally stable nitrate (*vide infra*). Indeed, in our previous study [19] of NO oxidation over Pt/CeO₂, addition of water to the feed resulted in a relative enhancement in the intensity of the nitrite bands present (relative to the nitrate bands) and also influenced the nature of the nitrate species formed, favoring the formation of nitrate species giving rise to an IR band at ~1550 cm⁻¹ as opposed to those associated with a band at ~1525 cm⁻¹. Overall it was concluded that the adsorption

of water on Pt/CeO₂ both reduces the number of NO_x adsorption sites and influences the nature of the adsorbed species, the data presented above being consistent with these earlier findings.

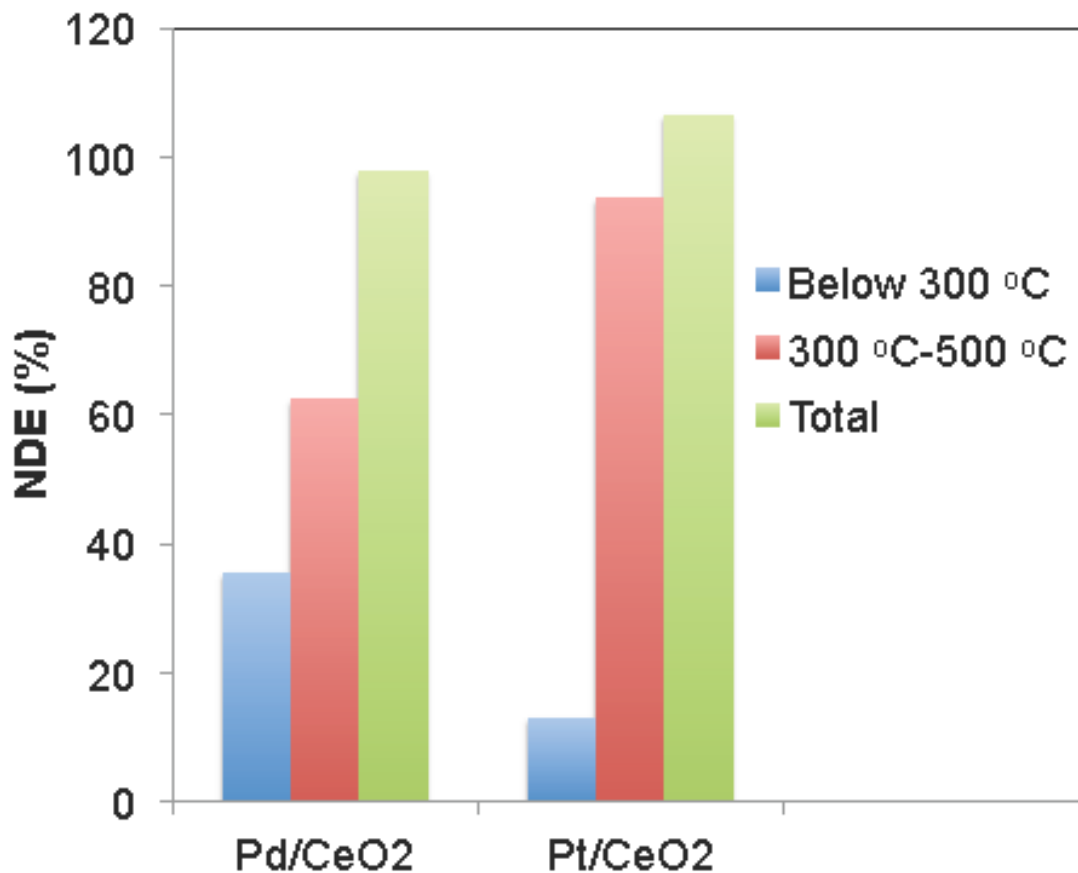


Figure 4.6. Comparison of NO_x desorption efficiency after storage 120 °C for 5 min in the absence of H₂O and CO₂.

4.3.5. Adsorption/desorption cycling.

For real world applications, a PNA would be cycled between ambient temperature (cold start) and an operating temperature at which some degree of NO_x desorption would occur. For a light duty diesel engine, typical operating temperatures generally fall in the range ~180-350 °C [5]. To simulate this, cycling experiments were performed for both Pt/CeO₂ and Pd/CeO₂ with NO_x storage at 120 °C for 5 min, followed by heating to 350

°C to induce thermal release of the stored NO_x. This was repeated 5 times. Figure 4.7 displays the measured NSE as a function of cycle number and Figure 4.8 summarizes the corresponding NDE data. In the case of Pt/CeO₂ a decrease in NSE was observed between the first and second storage phases, although the NSE decreased only marginally thereafter from one cycle to the next. For Pd/CeO₂ the NSE showed little variation, with only a slight decrease between the second and third cycles. Notably, both samples showed a progressive increase in NDE during ramping to 350 °C with increasing cycle number. This observation suggests that as cycling proceeds, strong adsorption sites are initially filled from which relatively little NO_x is released during thermal ramping. Consequently, as cycling proceeds, weak storage sites are increasingly utilized, from which NO_x is readily desorbed.

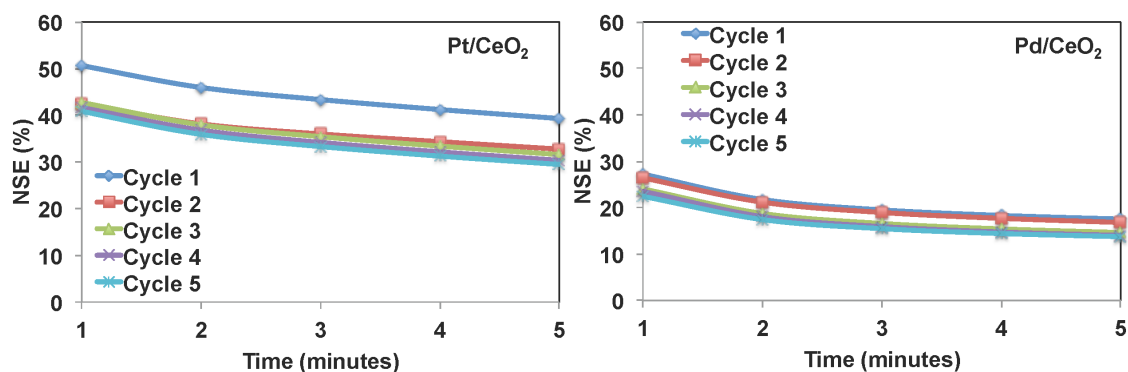


Figure 4.7. Comparison of NO_x storage efficiency during storage at 120 °C for 5 min for five consecutive adsorption-desorption cycles. Feed gas same as for Fig. 3.1.

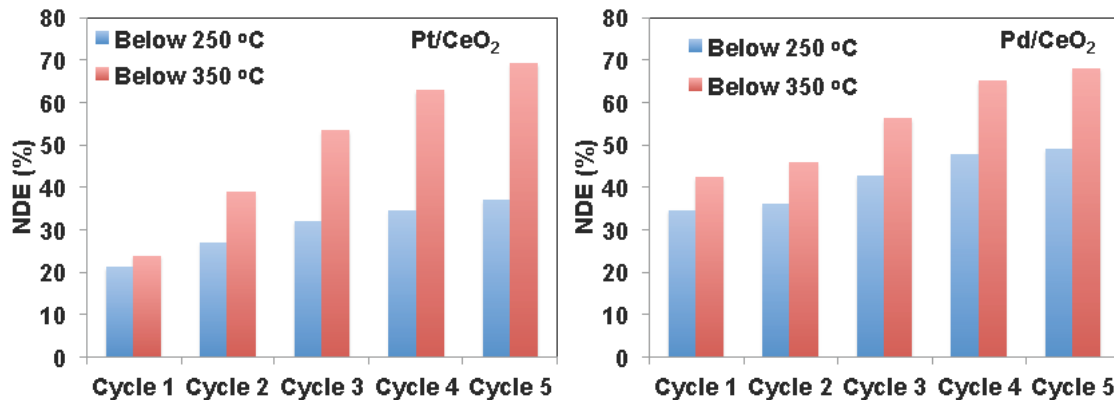


Figure 4.8. Comparison of NO_x desorption efficiency below 250 °C and 350 °C during TPD for five consecutive adsorption-desorption cycles.

4.3.6. DRIFTS measurements.

From the foregoing it is apparent that Pd/CeO₂ tends to release more NO_x below 350 °C during NO_x-TPD than its Pt analog (see Figures A.2.6 and A.2.7 for nitrite and nitrate species structures). In an effort to rationalize these results, DRIFT spectra were obtained for Pt/CeO₂ and Pd/CeO₂ catalysts during NO storage in the presence of O₂ at 100 °C for 30 min (Figure 4.9). During NO storage on Pt/CeO₂ strong absorption bands were observed corresponding to a bridging nitrate (1611 cm⁻¹) and monodentate nitrates at 1547 cm⁻¹ and 1522 cm⁻¹ [30-32]. An additional strong band at 1634 cm⁻¹ can be assigned to molecularly adsorbed NO₂ [33]. Weaker bands appeared at 1462, 1400, and 1313 cm⁻¹ corresponding to two types of monodentate nitrites as well as a bidentate nitrite species, respectively [31,32]. During the later stages of NO storage, a weak bidentate nitrite band also appeared at 1170 cm⁻¹ (which is paired with the band at 1313 cm⁻¹) [18-20].

Somewhat different results were obtained for Pd/CeO₂. During NO storage at 100 °C, a strong bidentate nitrite band rapidly formed at 1173 cm⁻¹ with a corresponding band at 1317 cm⁻¹, while bands due to monodentate nitrites appeared at 1430 and 1298 cm⁻¹. A strong band at 1633 cm⁻¹ (molecularly adsorbed NO₂) as well as weak nitrate bands at 1572 and 1532 cm⁻¹ also appeared early on. A corresponding weak nitrate band appeared at 1272 cm⁻¹ after 2 minutes [20]. With time the band at 1633 cm⁻¹ disappeared, while the

other nitrate bands simultaneously became more intense with additional nitrate bands appearing after 2 min at 1592, 1272, 1244, 1212 and 1007 cm^{-1} [19, 20, 30-32].

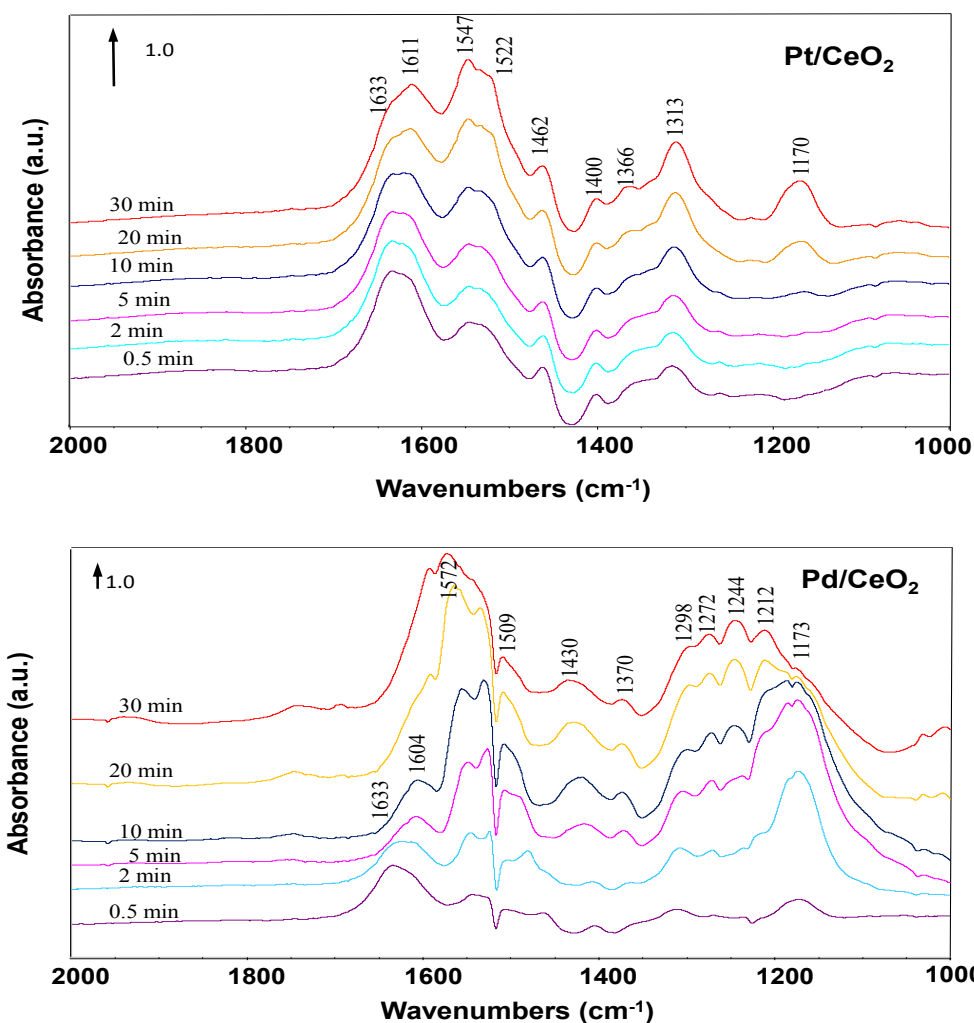


Figure 4.9. Evolution of surface species during NO_x storage at 100 °C. Feed: 300 ppm NO , 5% O_2 , and Ar balance. Top: Pt/CeO_2 ; bottom: Pd/CeO_2 .

DRIFT spectra acquired during subsequent TPD are shown in Figure 4.10. In the case of Pt/CeO_2 , raising the temperature to 300 °C resulted in the disappearance of the nitrite bands at 1459, 1310, and 1166 cm^{-1} . The bands at 1547 and 1514 cm^{-1} increased in intensity (with concomitant increases in the intensity of the related bands at 1227 and 1030 cm^{-1}), reaching their maximum intensity at 300 °C. Further increase of the temperature to 500 °C resulted in a gradual weakening of the intensity of these nitrate

bands. In comparison to Pt/CeO₂, the nitrite bands observed for the Pd/CeO₂ sample were removed at lower temperature. The monodentate nitrite band at 1431 cm⁻¹ disappeared by 200 °C. It should also be noted that the position and intensity of the nitrate bands remained almost unchanged until the temperature reached 450-500 °C, at which point the bands decreased in intensity. This suggests that for the Pd/CeO₂ sample the nitrite species which disappeared were not converted to nitrates, i.e., they underwent thermal decomposition.

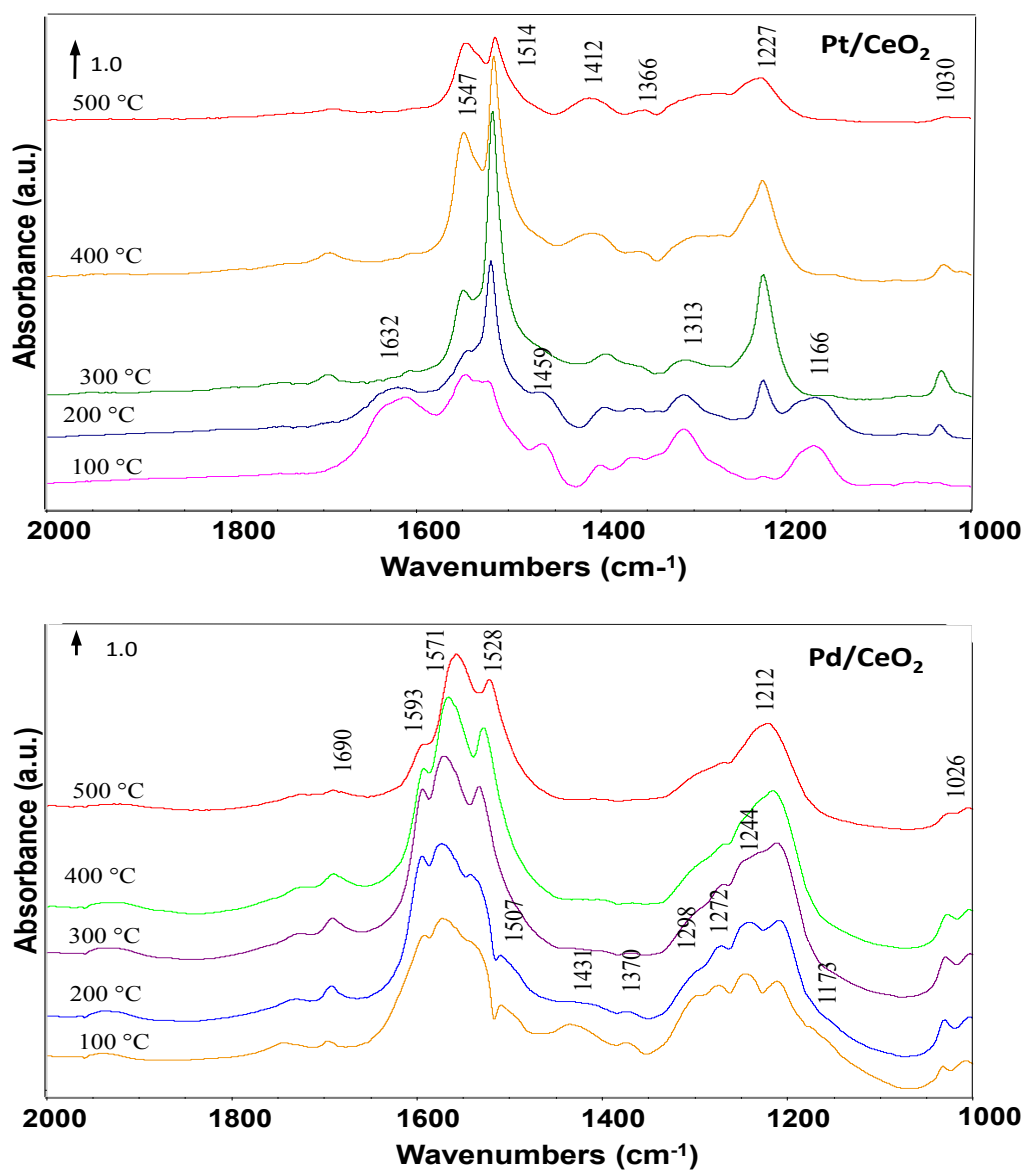
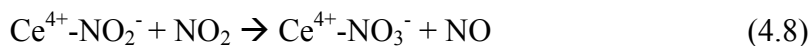
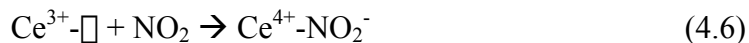
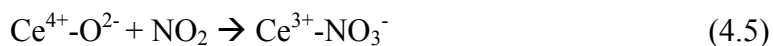
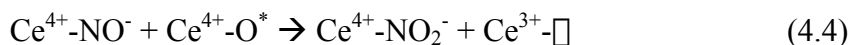
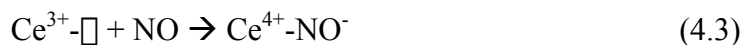
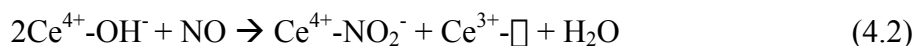
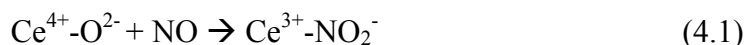


Figure 4.10. DRIFT spectra collected during NO_x-TPD. Feed: 300 ppm NO, 5% O₂, and Ar balance. Top: Pt/CeO₂; bottom: Pd/CeO₂.

The above DRIFTS results indicate that compared to Pt/CeO₂, Pd/CeO₂ stores relatively more NO as nitrites, particularly at short storage times. We attribute this behavior to the lower NO oxidation activity of Pd [28,29]. According to the literature nitrites can be formed via the interaction of NO with Ce⁴⁺ sites (eqns. 4.1 and 4.2) [17,34-36]. Moreover, recent studies suggest the involvement of oxygen vacancies in the formation of nitrites and nitrates [15-17], this being facilitated by electron and/or oxygen transfer on the catalyst surface. Specifically, nitrite can be formed on CeO₂ by the adsorption of NO on an oxygen vacancy (Ce³⁺-□) (eqn. 4.3) which is then oxidized by a neighboring lattice site (Ce⁴⁺-O*) to form a nitrite (Ce⁴⁺-NO₂⁻) (eqn. 4.4). Nitrates are formed by similar mechanisms through the adsorption of NO₂ (eqns. 4.5 -4.7).



The presence of Pt is not necessary for these reactions [15-17,34-36]; however, if present, Pt can fulfill several roles: Pt can chemisorb NO, which can then spill over onto the CeO₂ surface where the reaction depicted in eqns. (4.1) - (4.3) can occur, or, if oxidation of NO occurs on Pt, the formed NO₂ can react with the ceria surface to form nitrates according to eqns. (4.5) - (4.8); moreover, by dissociatively adsorbing O₂, Pt can act as a conduit for the spillover of O onto the ceria surface, resulting in nitrite oxidation to nitrate. Notably, the rates of NO oxidation and O₂ dissociation on Pt are likely to be related, as shown recently for Pd [37]. Indeed, the importance of O₂ dissociation as the sole kinetically relevant step in NO oxidation on Pd was demonstrated by the finding that the rate of ¹⁶O₂-¹⁸O₂ exchange was equal to the NO oxidation rate at a given value of the oxygen chemical potential. Moreover, the rate law for steady state NO oxidation on Pd

was the same as that for Pt, implying that the same kinetically relevant steps are involved. This suggests that both of the above Pt-mediated pathways for nitrate formation should be important. Given that Pd is an inferior NO oxidation catalyst compared to Pt, the formation of nitrate according to the pathways depicted in eqns. (4.5) - (4.7) is less likely, particularly at low temperatures. However, it should be noted that as temperature increases the rate of oxygen mobility likewise increases and hence the rate of nitrite to nitrate oxidation (according to eqn. (4.7)) would be expected to increase.

As indicated by the DRIFTS-TPD results presented above, nitrites are thermally less stable than nitrates, which explains why relatively more NO_x is desorbed at low temperature (<350 °C) for the Pd/CeO₂ catalyst compared to the high temperature release (350-500 °C). While Pt/CeO₂ stores more NO_x, Pd/CeO₂ is more desirable for PNA use due to its ability to store NO as nitrites rather than nitrates, allowing Pd/CeO₂ to release more NO_x below 350 °C.

4.4. Conclusions.

The NO_x storage and desorption properties of Pt/CeO₂ and Pd/CeO₂ were investigated using microreactor and DRIFTS measurements. Promotion of CeO₂ with 1 wt. % Pt and with 1 wt.% Pd increased the amount of NO_x storage compared to bare CeO₂, Pt/CeO₂ showing significantly higher NSE than Pd/CeO₂ at all temperatures. However, for NO_x stored at 80 °C and 120 °C, the use of Pd improved lower temperature NO_x desorption (< 350 °C) compared to the Pt analog. During NO_x storage and desorption cycling small decreases in NSE were initially observed for both samples, although stable NSE were achieved by the third adsorption-desorption cycle. Notably, both samples showed a progressive increase in NDE during ramping to 350 °C with increasing cycle number, suggesting that as cycling proceeds strong adsorption sites are initially filled from which relatively little NO_x is released during thermal ramping. Consequently, as cycling proceeds, weak storage sites are increasingly utilized, from which NO_x is readily desorbed. DRIFTS measurements indicated that NO_x was stored predominately as nitrates on Pt/CeO₂, while on the Pd sample primarily nitrites were formed; this difference is ascribed to the lower NO oxidation activity of Pd compared to Pt. Nitrite species were weakly bound on both the Pt- and Pd-containing samples,

typically being removed by 250 °C upon thermal ramping. The fact that NO_x is primarily stored as nitrites on Pd/CeO₂ therefore explains its high NDE below 350 °C.

5.1. Introduction.

Mitigation of cold start NO_x emissions is necessary for automotive companies to meet upcoming Tier 3 emission standards. This proves challenging in lean burn engines due to the necessary operating temperatures for current aftertreatment technology. Current lean exhaust systems use either Lean NO_x Trap (LNT) or Selective Catalytic Reduction (SCR) catalysts which require temperatures of at least 200 °C to perform efficiently. Slow decomposition rates of urea at low temperatures limit the use of urea-SCR catalysts below 200 °C. Urea decomposes through the release of NH₃ and isocyanic acid (HNCO) from urea. The isocyanic acid is then hydrolyzed to NH₃ and CO₂ [1-2]. Melamine and related compounds (formed by reaction of NH₃ with HNCO) can deposit on the SCR catalyst surface at low temperatures, resulting in catalyst deactivation [3]. To prevent this type of catalyst poisoning urea injection is typically ramped over the range ~150-200 °C, i.e. sub-stoichiometric amounts of urea are injected to minimize catalyst poisoning at the expense of unconverted NO_x (stoichiometric injection begins at ~200 °C) [4]. However, ramping urea injection limits the amount of NO_x that can be converted.

Researchers have suggested the use of Passive NO_x Adsorbers (PNAs) as a solution for the mitigation of NO_x slip during cold starts [5]. A Pt promoted γ -Al₂O₃ PNA, coupled with a urea-SCR catalyst, was first mentioned in a 2001 patent by Ford Motor Co. [6]. Further use of Pt/Al₂O₃ as a PNA has been studied by Ji et al [7] who observed that the addition of 1 wt% La to Al₂O₃ increased NO_x storage efficiency by increasing the number of NO_x storage sites. However, while the addition of La improved NO_x storage it did not benefit NO_x desorption below 250 °C, relatively more NO_x being desorbed at low temperatures for Pt/Al₂O₃ compared to Pt/La-Al₂O₃. DRIFTS data collected during NO_x-TPD measurements indicated that nitrites and weakly bound nitrate species were initially removed from the catalyst surfaces in both cases. The use of Ag/Al₂O₃ has been studied as a non-PGM alternative for alumina-based catalysts for low temperature NO_x storage, although the use of Ag requires that H₂ be present for NO oxidation and adsorption below 200 °C [8-9]. Recently, Pd/ZSM-5 has been reported by

Honda [10] to possess the ability to reduce NO_x and hydrocarbon (HC) emissions during cold starts as a NO_x trap three way catalyst (N-TWC).

Ceria-based systems are also being studied for their low temperature NO_x mitigation capabilities due to the anionic vacancies that can form in ceria's fluorite crystal structure [11-14] which have been found to facilitate NO_x adsorption [15-17]. Doping ceria has been found to increase the number of vacancies in the crystal lattice [18-19]. Rohart et. al. found that the use of rare earth oxides (Ce-Pr, Ce-La, Ce-Nd) in place of Ba in LNT catalysts resulted in substantially higher NO_x storage at low temperatures than their Ba counterparts. The Ce-Pr derivative stored over 90% of NO_x after 1 minute of storage at 250 °C, while Ce-La stored ~70% of NO_x, and the Ce-Nd catalyst stored less than 40%. These results paralleled catalyst ability to oxidize NO to NO₂ at 250 °C [20]. In a study by Wang et al., the addition of Nd, La, and Y to Pt/Ba/Ce_{0.6}Zr_{0.4}O₂-Al₂O₃ LNT catalyst was examined. The addition of La to Ce-Zr improved NO_x storage at 200 °C compared to the non-rare earth containing counterpart, while the addition of Y and Nd did not improve storage [21]. In a recent study NO_x storage capacity was found to improve when CeO₂ was incorporated into a Mn-Sn support to create Mn_{0.4}Sn_{0.5}Ce_{0.1} [22]. NO_x storage was evaluated at 100 °C, higher storage upon the addition of CeO₂ being attributed to the catalyst's ability to better oxidize NO to NO₂. Through XPS, NO_x storage, and H₂-TPR data Sun et al. were able to correlate increased oxidation activity to the presence of Sn-Ce interactions and surface defect oxygen species. Different metal ratios of Ce-Co-Cr-O containing catalysts were evaluated for NO_x storage by Cao et al. [23], who observed that storage was dependent on the Co³⁺ concentration. Higher Ce concentrations resulted in better dispersion of Co, thereby increasing Co/Cr interactions. As a result, NO oxidation was greatly enhanced, thus increasing NO_x storage.

Diffuse Reflectance Transform Infrared Fourier Spectroscopy (DRIFTS) been extensively used to understand NO_x storage and release on ceria. Phillipp et al. studied the adsorption of NO and O₂ on bare ceria at 50 °C, finding that NO is initially stored as a nitrite and further oxidizes to nitrates [24]. In a study looking at temperature affects of NO/O₂ adsorption on Pt/CeO₂, Ji et al. [25] observed the formation of nitrites at room temperature while storage at 200 °C resulted in predominately nitrate formation. Other

studies have also found that NO/O₂ adsorption on Pt/CeO₂ initially results in NO_x storage as nitrite, which then oxidizes to nitrate [26]. Similarly, in a 2012 patent by Johnson Matthey it is claimed that the use of Pd supported on CeO₂ as a PNA results in NO_x storage at nitrites, therefore avoiding the need for NO to be oxidized to NO₂ during storage [27]. In a report by Chen et al. [28], the diesel Cold Start Catalyst (dCSCTM) is reported to have the ability to store NO_x as nitrite over nitrate, making it easier to regenerate the catalyst's ability to store NO_x. The dCSCTM incorporates the previously mentioned PNA from Johnson Matthey along with a hydrocarbon trap. Jones et al. [29] reported the use of 1 wt.% Pt or Pd promoted CeO₂ as PNA catalysts. It was found that Pd preferentially stores NO_x as nitrites while Pt preferentially stores NO_x as nitrates. This is attributed to Pt's better oxidation capabilities compared to Pd. When Pd/CeO₂-ZrO₂-Pr₂O₃ was exposed to stoichiometric amounts of CO + HC + NO_x + O₂, Yang et al. [30] observed the formation of nitrite surface species on ceria-rich catalysts at 50 °C, while zirconia-rich catalysts favored the formation of nitrates. At higher Zr content the concentration of active oxygen species is increased, facilitating the oxidation of nitrites to nitrates.

Herein, we report the comparison of CeO₂ doped with Pr, Nd, Y, La, and Nd at different concentration levels for PNA use, as well as the comparison of doped CeO₂ when promoted with 1 wt.% Pt and Pd. NO_x storage and NO_x desorption efficiencies were determined at 120 °C, both in the presence and absence of CO₂ and H₂O, and catalyst ability to store and release NO_x upon repeated adsorption-desorption cycling was evaluated. DRIFTS measurements were utilized to understand the NO_x species present on the catalyst surface during NO_x storage and desorption.

5.2. Experimental Methods.

5.2.1. Catalyst preparation.

Mixed oxides, $\text{CeO}_2\text{-M}_2\text{O}_3$, were prepared by co-precipitation from aqueous $\text{Ce}(\text{NO}_3)_3 \cdot 6\text{H}_2\text{O}$ and $\text{Sm}(\text{NO}_3)_3 \cdot 6\text{H}_2\text{O}$, $\text{Y}(\text{NO}_3)_3 \cdot 6\text{H}_2\text{O}$, $\text{Nd}(\text{NO}_3)_3 \cdot 6\text{H}_2\text{O}$, $\text{Pr}(\text{NO}_3)_3 \cdot 6\text{H}_2\text{O}$, or $\text{La}(\text{NO}_3)_3 \cdot 6\text{H}_2\text{O}$ and calcined in air at 500°C for 3 h [31]. 1 wt% Pt or Pd was loaded onto the $\text{CeO}_2\text{-M}_2\text{O}_3$ by means of incipient wetness impregnation using aqueous solutions of $[\text{Pt}(\text{NH}_3)_4](\text{NO}_3)_2$ or $[\text{Pd}(\text{NO}_3)_2] \cdot x\text{H}_2\text{O}$. The resulting samples were calcined at 500°C for 3 h in a muffle furnace.

5.2.2. Catalyst Characterization.

X-ray powder diffraction analysis was conducted on a Phillips X'Pert diffractometer using Cu-K α radiation ($\lambda=1.540598 \text{ \AA}$). Diffractograms were recorded between 5° and 90° (2θ) with a step size of 0.02° . Brunauer-Emmett-Teller (BET) surface area and pore volume measurements were performed by nitrogen physisorption at -196°C using a Micromeritics Tri-Star 3000 system. Catalyst samples were outgassed overnight at 160°C under vacuum prior to measurements.

Pt and Pd dispersions were determined by means of pulsed CO chemisorption at -78°C using a Micromeritics AutoChem II Analyzer. Samples (250 mg) were loaded into the reactor and reduced in 10% H_2/Ar at 300°C for 10 min. In each case the sample was then purged with Ar for 20 min at the same temperature to remove residual H_2 and then cooled to -78°C prior to CO chemisorption. During the measurements 10 ml of CO was pulsed into the reactor every 2 min, the CO signal being monitored with a thermal conductivity detector (TCD). CO pulsing was terminated when the TCD signal reached a constant value, i.e., the precious metal sites were saturated with CO. Assuming a 1:1 ratio of CO to surface Pt and Pd, the metal dispersion was calculated based on the amount of CO adsorbed.

Temperature-programmed reduction (TPR) was performed using Micromeritics AutoChem II Analyzer. Ca. 150 mg of catalyst was loaded in the reactor and pretreated in 10% O_2/Ar at 500°C for 30 min. After cooling the sample to room temperature (RT) the cold trap was submerged in a dry ice and isopropanol bath at -78°C . Followed by TPR

being carried out in a 10% H₂/Ar flow with a ramp of 10 °C/min from RT to 900 °C. The H₂ signal during TPR was monitored using a TCD.

Raman spectra of the catalysts were recorded using a Jobin Yvon Horiba Raman dispersive spectrometer with a variable-power He–Ne laser source (632.8 nm), equipped with a confocal microscope with a 10x objective of long focal length. The spectrum of each sample was obtained as the average signal of two individual spectra of different areas of the sample. The acquisition time for each individual spectrum was 20 s. The detector was of the CCD cooled Peltier type.

X-ray photoelectron spectroscopy (XPS, K-ALPHA, Thermo Scientific) was used to analyze the surfaces of the catalysts. All spectra were collected using Al-K α radiation (1486.6 eV), monochromatized by a twin crystal monochromator, yielding a focused X-ray spot with a diameter of 400 μ m, at 3 mA \times 12 kV. The alpha hemi-spherical analyser was operated in the constant energy mode with a pass energy of 50 eV. Charge compensation was achieved with a low energy electron flood gun and low energy argon ions from a single source.

5.2.3. NO_x storage and desorption measurements.

NO_x storage and desorption efficiencies of the catalysts were determined in a quartz microreactor with a Pfeiffer ThermoStar GSD301 mass spectrometer as the detector. Prior to measurements samples (170 mg) were pretreated at 550 °C for 10 min under a flow of 5% O₂ in He (120 sccm) and then cooled to room temperature under flowing Ar. Samples were then equilibrated under a flow of 3.5% H₂O, 5.0% CO₂ and 5% O₂ (bal. He, 120 sccm) at the designated storage temperature; typically, this took 15 min, at which point the feed and effluent H₂O and CO₂ concentrations were equivalent. NO_x storage was initiated by adding 300 ppm NO to the feed. Storage experiments were conducted at 120 °C using a 5 min storage time. In all cases, a total flow rate of 120 sccm was used, corresponding to a gas hourly space velocity (GHSV) of ca. 30,000 h⁻¹. At the completion of the storage period the feed gas was switched to bypass mode and the NO flow was switched off. When the NO concentration had dropped to zero, the gas was re-directed to the reactor and temperature programmed desorption (TPD) was carried out to

study NO_x desorption behavior using a ramp rate at 10 °C/min from the storage temperature up to 500 °C.

To understand the effect of multiple storage-desorption cycles, cycling experiments were also performed. Catalyst pretreatment and NO_x storage were performed as described above (using a storage temperature of 120 °C), after which TPD was performed up to 350 °C at a ramp of 10 °C/min under the same lean feed gas with the exclusion of NO. Subsequently, the temperature was lowered to 120 °C for the next NO_x adsorption-desorption cycle. A total of five cycles were performed for both Pt/CeO₂ and Pd/CeO₂.

NO_x storage efficiency (hereafter denoted as NSE) is defined as the percentage of NO_x passed over the catalyst that is stored, while NO_x desorption efficiency (hereafter denoted as NDE) is defined as the percentage of stored NO_x desorbed during TPD, i.e.:

$$\text{NSE} = \left(1 - \frac{\int_0^t ([\text{NO}_x]_{\text{out}}) dt}{\int_0^t [\text{NO}]_{\text{in}} dt} \right) \times 100\%$$

$$\text{NDE} = \left(\frac{\int_{t(T_0)}^{t(T)} ([\text{NO}_x]_{\text{out}}) dt}{\text{NSE} \times t \times [\text{NO}]_{\text{in}}} \right) \times 100\%$$

in which t is the NO_x storage time; $[\text{NO}]_{\text{in}}$ is the inlet NO_x concentration during NO_x storage; $[\text{NO}_x]_{\text{out}}$ is the outlet NO_x concentration during either NO_x storage or the subsequent NO_x desorption period; $t(T_0)$ is the start time of NO_x-TPD corresponding to the NO_x storage temperature before the temperature is raised; $t(T)$ is the end time of NO_x-TPD corresponding to the desired NO_x desorption temperature.

5.2.4. DRIFTS Measurements.

DRIFTS measurements were performed to monitor the surface species involved in NO_x adsorption and desorption. Measurements were performed using a Nicolet 6700 IR spectrometer equipped with a Harrick Praying Mantis accessory and MCT detector. The reaction cell was sealed with a dome equipped with two ZnSe windows and one SiO₂ observation window. The temperature of the reactor cell was controlled and monitored by

a K-type thermocouple placed beneath the reaction chamber. For each DRIFT spectrum an average of 115 scans was collected (requiring ca. 1 min) with a resolution of 4 cm^{-1} . The spectrometer as well as the outside of the reaction cell were continuously purged with dry nitrogen to avoid diffusion of air into the system. Catalyst samples ($\sim 50\text{ mg}$) were pretreated in situ in 300 ppm NO_x for 1 h then reduced at $450\text{ }^\circ\text{C}$ for 15 min under 10% H_2 in order to remove carbonates, after which background spectra were collected (under Ar) in the range of $500\text{-}100\text{ }^\circ\text{C}$ at intervals of $50\text{ }^\circ\text{C}$. NO_x storage was carried out at $100\text{ }^\circ\text{C}$ for 30 min using a feed consisting of 5% O_2/Ar and 300 ppm NO (120 sccm). During NO_x storage, spectra were collected as a function of time. After 30 min of NO_x storage, TPD was performed in flowing 5% O_2/Ar flow (120 sccm), the temperature being raised from $100\text{ }^\circ\text{C}$ to $500\text{ }^\circ\text{C}$ at a rate of $10\text{ }^\circ\text{C}/\text{min}$. DRIFT spectra were recorded during TPD at intervals of $50\text{ }^\circ\text{C}$. Absorbance spectra were obtained by subtracting background spectra from the spectra collected during NO_x storage and desorption.

5.3. Results and Discussion.

5.3.1. Sample Characterization.

Analytical data for $\text{CeO}_2\text{-M}_2\text{O}_3$ ($M = \text{Pr, Sm, Y, La, Nd}$) samples (Table A.2.1.) promoted with 1 wt.% Pt or Pd or a 1:1 weight ratio of Pt and Pd (total metal loading of 1 wt.%) are collected in Tables 5.1 and 5.2. Ceria was doped with the second rare earth metal at concentrations of 5 mol% and 20 mol%. Henceforth, all samples are referred to as Pt or PdCe5M (5 mol% of M present) or Ce20M (20 mol% of M present). After calcination at $500\text{ }^\circ\text{C}$ powder X-ray diffractograms of the doped CeO_2 supports contained diffraction lines corresponding to (111), (200), (220), (311), (222), (400), (331), (420) and (422) crystal planes (Figures 5.1 and 5.2), characteristic of the fluorite crystal structure of CeO_2 . There was no evidence of phase segregation according to the XRD data, and diffraction angles shifted to lower values when doping CeO_2 due to the expansion of the lattice caused by the larger ions: Pr^{3+} (113 pm), Sm^{3+} (109.8 pm), Y^{3+} (104 pm), La^{3+} (117.2 pm), and Nd^{3+} (112.3 pm). The average diameters of the crystallites in the supports calculated using the Scherrer equation ranged from 8.9-13.4 nm. As the dopant concentration increased the lattice parameter (a) increased, corresponding to expansion of the lattice to accommodate the increased concentration of

the larger ions. However, the lattice parameter didn't increase with increasing concentration of Y^{3+} , indicating that Y forms a separate phase although it isn't detectable in the X-ray diffractogram. XRD data obtained on the 80Ce-20Pr sample series after aging did not indicate a loss in crystallinity or the occurrence of phase segregation (not shown).

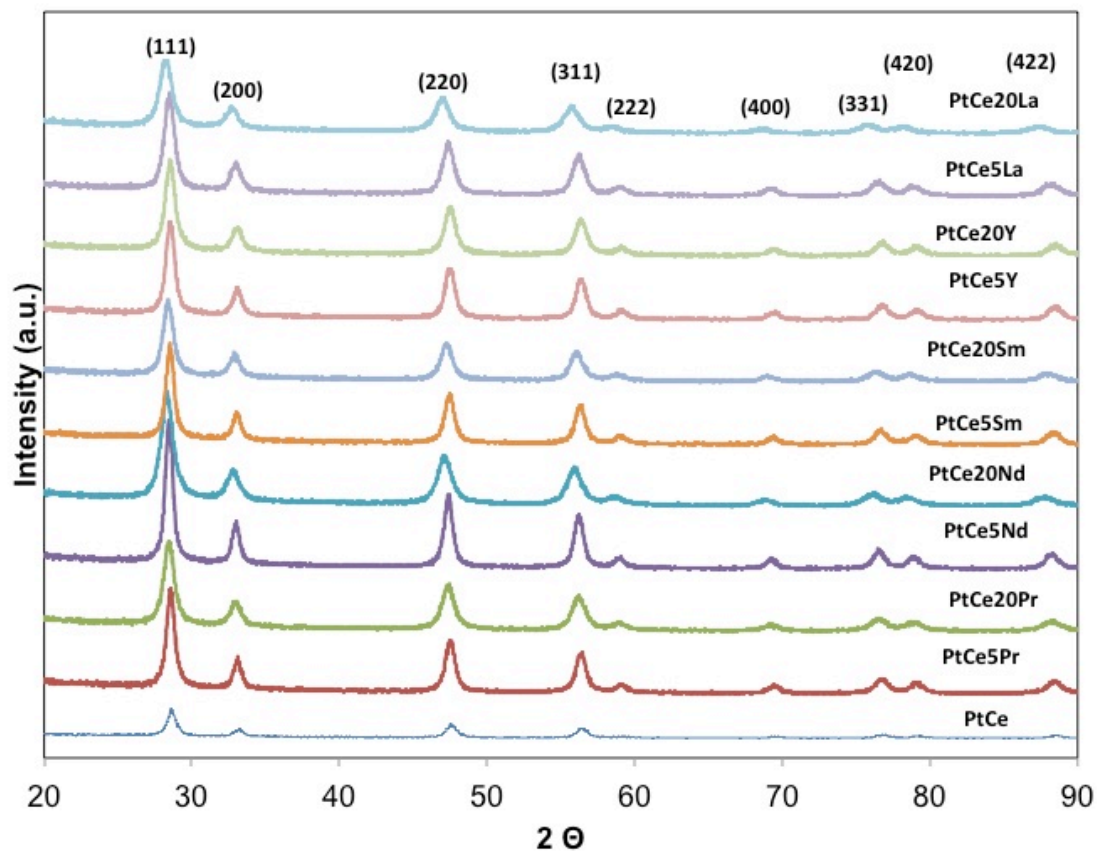


Figure 5.1. X-ray diffraction patterns of Pt-promoted $CeO_2-M_2O_3$ catalysts.

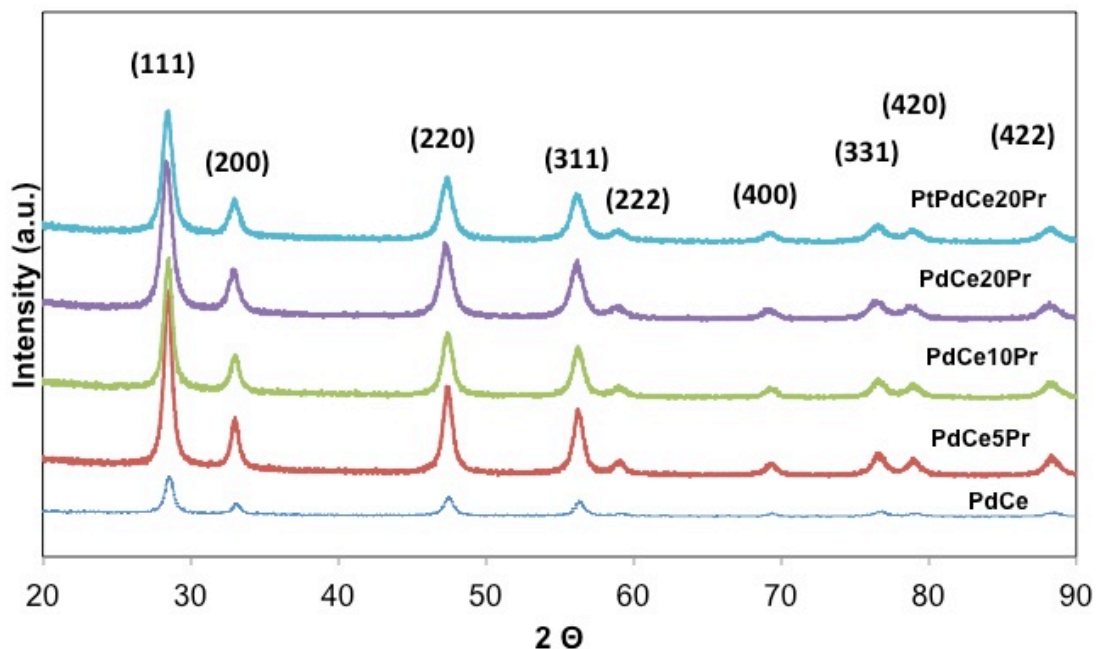


Figure 5.2. X-ray diffraction patterns of Pd- and Pt-Pd-promoted $\text{CeO}_2\text{-Pr}_2\text{O}_3$ catalysts.

From N_2 physisorption data BET surface areas as large as $86.3 \text{ m}^2/\text{g}$ (PtCe20Nd) and as small as $41.1 \text{ m}^2/\text{g}$ (PdCe10Pr) were obtained, this range being typical of doped CeO_2 prepared by co-precipitation methods [32]. CO chemisorption results for platinum-promoted mixed oxides in the fresh state indicated that Pt particle size (d_{metal}) increased with increasing concentration of dopant except in the case of Pr. With Pt promotion, increasing the Pr content from 5% to 20% resulted in a decrease in Pt particle size from 3.29 nm to 1.3 nm (Table 5.1). Larger Pt particle sizes with increased dopant concentrations for La, Y, Sm, and Nd suggest weaker interactions with Pt and therefore decreased Pt dispersions. The opposite trend is observed when promoting Ce-Pr mixed oxides with Pd, indicating that Pt has stronger interactions with the Ce-Pr surface than Pd. Upon increasing the Pr content from 5% to 20%, Pd particle sizes increased from 2.61 nm to 3.99 nm (Table 5.2). Consistent with the highly dispersed nature of the Pt and Pd in these samples, diffraction lines for Pt and Pd were not observed in their X-ray diffractograms. CO chemisorption data indicated that metal particle sizes increased after aging for all samples in the 80Ce-20Pr series. For example, CO chemisorption indicated

that PdCe20Pr had a Pd particle size of 3.99 nm in the fresh state, which increased to 8.30 nm after aging. BET surface area measurements also evidenced a decrease in support surface area after aging indicative of support sintering. The largest decrease in surface area was observed for PdCe20Pr, which decreased from 66.2 m²/g (fresh) to 18.9 m²/g (aged).

Table 5.1. Physical properties of Pt/CeO₂-M₂O₃ used in this work.

Catalyst	d _{support} (nm)		BET SA (m ² /g)		r _{pore} (nm)	V _{pore} (cm ³ /g)	d _{metal} (nm)		a (nm)
	Fresh	Aged	Fresh	Aged			Fresh	Aged	
PtCe	13.0	--	71.3	--	4.4	0.16	2.83	--	0.540
PtCe5Pr	13.2	--	67.0	--	3.8	0.13	3.29	--	0.540
PtCe10Pr	12.8	--	50.9	--	5.5	0.14	3.62	--	0.542
PtCe20Pr	10.0	13.9	65.9	24.1	3.4	0.11	1.30	4.98	0.544
PtCe5Y	12.1	--	65.8	--	3.2	0.12	3.30	--	0.542
PtCe20Y	10.8	--	62.1	--	2.1	0.07	6.66	--	0.542
PtCe5La	10.0	--	71.4	--	2.4	0.10	2.61	--	0.542
PtCe20La	9.4	--	57.6	--	4.6	0.13	4.42	--	0.546
PtCe5Sm	12.8	--	58.5	--	3.6	0.10	1.77	--	0.541
PtCe20Sm	10.0	--	55.2	--	2.3	0.06	7.22	--	0.544
PtCe5Nd	13.4	--	55.3	--	5.1	0.14	2.25	--	0.544
PtCe20Nd	8.9	--	86.3	--	5.5	.024	4.23	--	0.547

Table 5.2. Physical properties of Pd/CeO₂-Pr₂O₃ used in this work.

Catalysts	d _{support} (nm)		BET SA (m ² /g)		r _{pore} (nm)	V _{pore} (cm ³ /g)	d _{metal} (nm)		a (nm)
	Fresh	Aged	Fresh	Aged			Fresh	Aged	
PdCe	12.6	--	71.7	--	4.4	0.16	2.71	--	0.540
PdCe5Pr	12.4	--	70.0	--	3.8	0.13	2.61	--	0.543
PdCe10Pr	12.1	--	41.1	--	6.2	0.13	2.69	--	0.542
PdCe20Pr	10.0	14.9	66.2	18.9	3.4	0.24	3.99	8.30	0.546
PtPdCe20Pr	10.0	13.2	64.5	26.1	3.5	0.11	2.61	9.73	0.542

Raman analysis of the 80Ce-20Pr series, Figure 5.3, showed the presence of the typical F_{2g} mode of ceria's fluorite structure. Doping with Pr reduced the intensity of the F_{2g} band while creating vacancies as seen by the additional band observed at ~560 cm⁻¹. The lower Raman shift of the F_{2g} band with Pr doping (Figure 5.4) is attributed to the expansion of the unit cell in the presence of Pr³⁺, which is larger than Ce⁴⁺. Ce/Pr ratios of 2.6 as determined by XPS (summarized in Table 5.3) are below the nominal value of 4 in the case of PdCe20Pr and PtCe20Pr, suggesting a ceria-rich core with a Pr-rich surface. The opposite was observed for PtPdCe20Pr, which exhibited a Ce/Pr ratio of 15.8 indicating a Ce-rich surface with a Pr-rich core. Notably, the Ce³⁺ percentages determined by XPS were higher for PtCe and PdCe. This is attributed to Pr⁴⁺ reducing more easily than Ce⁴⁺; hence, Pr⁴⁺ reduction hinders Ce⁴⁺ reduction. In the case of PtPdCe20Pr the Ce³⁺ content was similar to that found for PtCe and PdCe due to the ceria-rich nature of the surface compared to the Pt- and PdCe20Pr samples. Ce/Pr ratios of aged samples in the Ce20Pr series as determined by XPS analysis are lower than the ratios found in the fresh state. This suggests that Pr diffuses to the surface during aging. For example, PdCe20Pr had a Ce/Pr ratio of 2.6 before aging, which decreased to 0.54 after aging (values summarized in Table 5.4). The amount of Ce³⁺ present after aging also increased which may be indicative of Ce-Pr phase segregation.

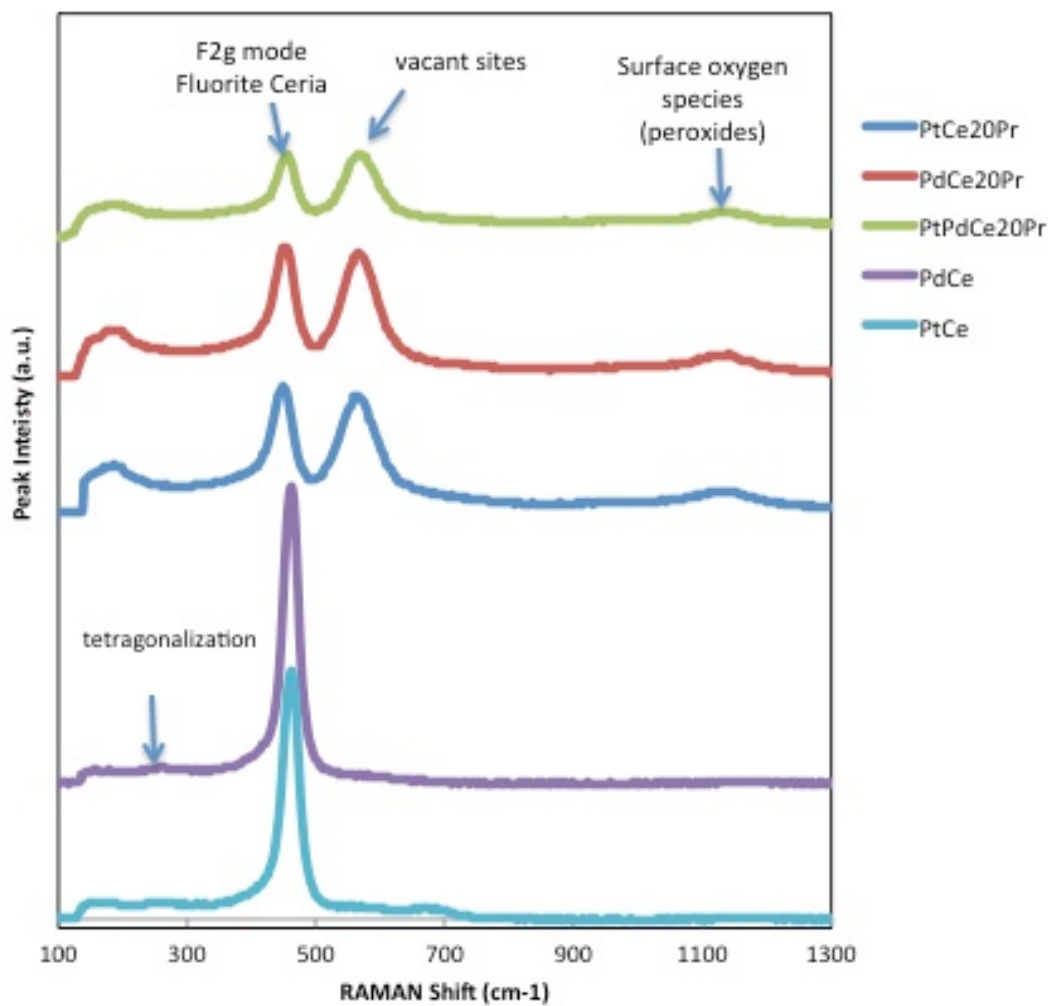


Figure 5.3. Raman analysis of undoped and Pr-doped CeO₂ catalysts.

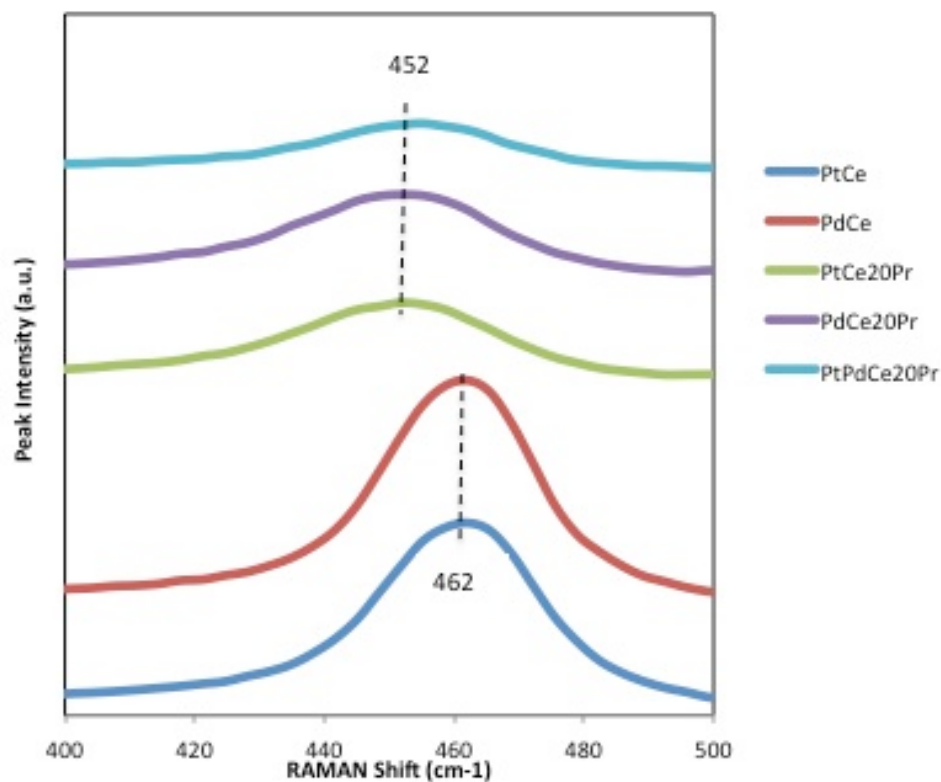


Figure 5.4. Effect of Pr doping on the Raman shift of the CeO₂ F_{2g} band.

Table 5.3. Atomic concentrations determined by XPS for fresh samples (*denotes nominal values).

Species	PtCe	PdCe	PtCe20Pr	PdCe20Pr	PtPdCe20Pr
C	30.5	35.29	33.12	49.02	63.4
Pt	0.27	--	0.15	--	0.1
Pd	--	0.62	--	0.43	0.1
O	48.9	45.39	47.36	36.69	29.7
Ce	20.33	18.71	14.04	10.05	6.3
Pr	--	--	5.33	3.82	0.4
Ce/Pr*	--	--	2.6 (4)	2.6 (4)	15.8 (4)
Ce ³⁺ (%)	36.8	33.2	25.6	26.7	34.9

Table 5.4. Atomic concentrations determined by XPS for aged samples (*denotes nominal values).

Species	PtCe20Pr	PdCe20Pr	PtPdCe20Pr
C	10.75	70.87	5.06
Pt	3.62	--	1.38
Pd	--	0.18	0.39
O	42.9	20.57	46.88
Ce	15.75	2.83	14.15
Pr	26.99	5.23	31.96
Ce/Pr*	0.58 (4)	0.54 (4)	0.44 (4)
Ce ³⁺ (%)	47.7	51.6	37.4

TPR data, shown in Figure 5.5, for the samples in the Ce20Pr series, indicate that Pt and Pd reduce at lower temperatures than the bulk support [33]. The addition of 1 wt% Pd lowers reduction temperatures the most. The reduction of PdO and the surface in close contact with Pd gives rise to a reduction peak at 103 °C. Reduction of PtO to metallic Pt, which again is accompanied by reduction of the Ce20Pr surface, occurs nearly 100 °C higher than that of Pd, reaching a maximum at 213 °C. PtPdCe20Pr displayed a reduction temperature of 111 °C, only slightly higher than the reduction of Pd on PdCe20Pr. Additionally, two broad reduction peaks were observed for the samples containing PGM, over the range 300-600 °C and 600-900 °C. These two reduction events can be attributed to Pr⁴⁺ and Ce⁴⁺ in the bulk, respectively [34]. Unpromoted Ce20Pr exhibits two surface reduction peaks at ~400 and 500 °C, likely Pr-rich and Ce-rich areas. It should also be noted that possible reduction of surface carbonates/hydroxides may contribute to reduction peaks in the 300-600 °C range for these various samples [35-38].

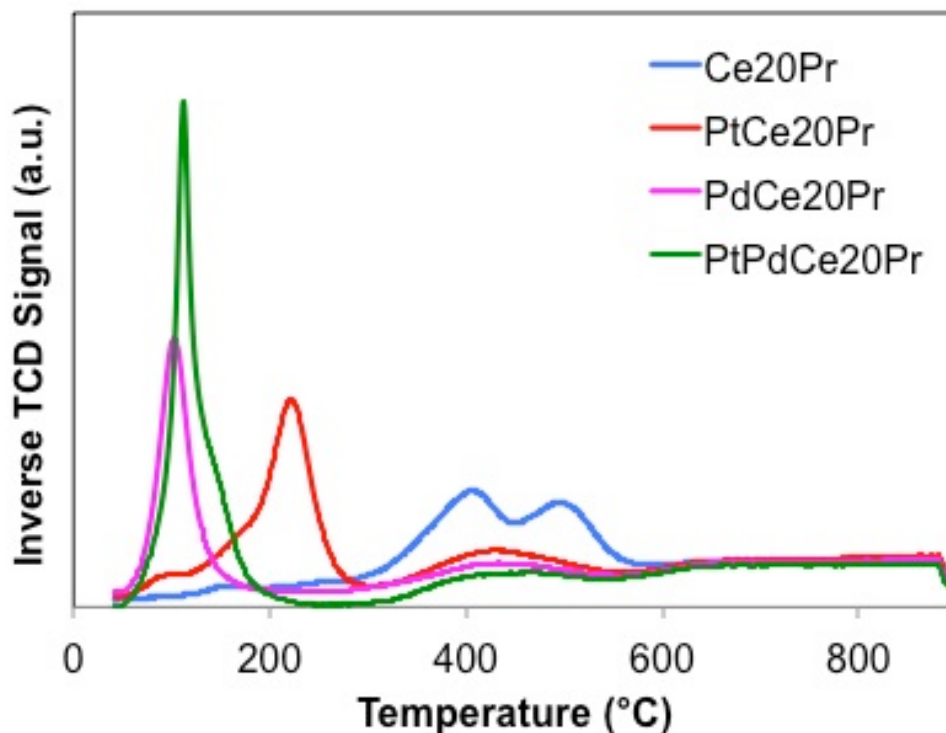


Figure 5.5. H₂-TPR profiles of fresh catalysts from the Ce20Pr series.

5.3.2. NSE and NDE for Pt-Promoted Catalysts.

A NO_x storage temperature of 120 °C was utilized during NO_x storage-desorption studies. For platinum-promoted catalysts, doping Ce with 5 mol% of Pr, Nd, or Sm increased NSE compared to PtCe only. However, doping Ce with La and Y didn't improve NSE. When the dopant concentration was increased to 20 mol%, NSE decreased in all cases except Pr (Figure 5.6). Indeed, increasing the amount of Pr increased NSE, while it severely hindered storage with Sm, Nd, Y, and La. Overall, utilizing 5% of the dopant in CeO₂ resulted in the following ordering of NSE: Pr>Nd>Sm>Ce>La,Y. (See Figure A.2.4. for absolute NSE data).

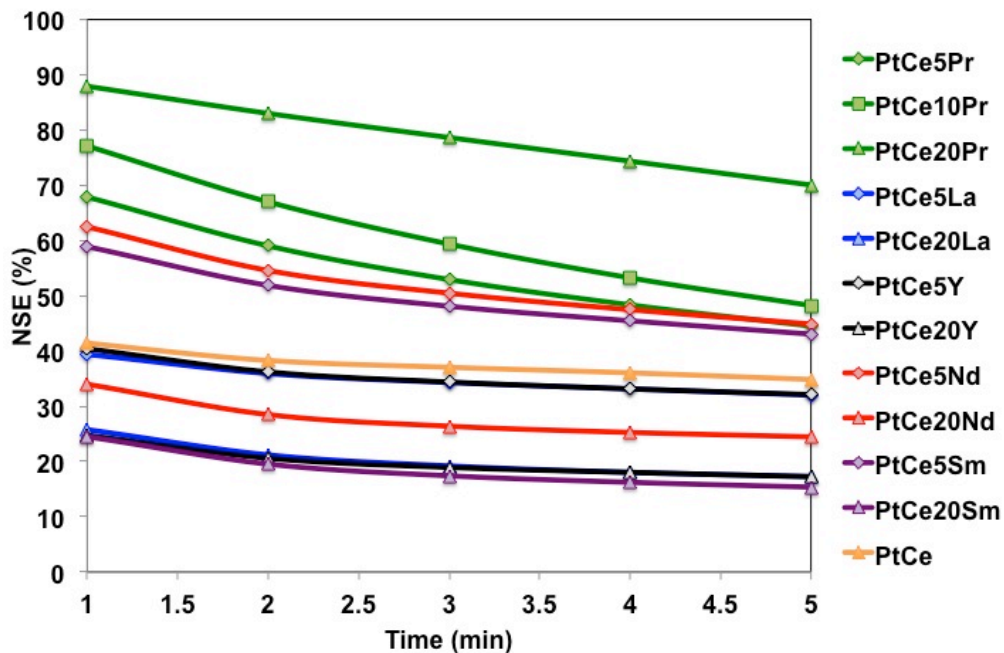


Figure 5.6. Comparison of NO_x storage efficiency at 120 °C for PtCe5-20M. Feed: 300 ppm NO, 5% O₂, 5% CO₂, 3.5% H₂O and He balance.

NO_x-TPD profiles for PtCe(5 or 20)M after NO_x storage at 120 °C for 5 minutes are displayed in Figure 5.7. Two different desorption ranges are evident for all catalysts: below 300 °C and 300-500 °C. Doping CeO₂ with 5 mol% of Y, La, Sm, and Pr shifted desorption peaks to higher temperatures compared to Pt/CeO₂, while doping with 5 mol% of Nd shifter desorption peaks to lower temperatures. Upon increasing dopant concentration from 5 mol% to 20 mol% desorption peaks shifted to higher temperatures with the exception of doping with Pr. Indeed, increasing the concentration of Pr from 5 mol% to 20 mol% shifted desorption peaks to lower temperatures. Relatively more NO_x was released below 300 °C for PtCe5Pr and PtCe20Pr compared to higher temperature release. Conversely, relatively more NO_x was released at temperatures surpassing 300 °C for CeO₂ doped with La, Y, Sm, and Nd.

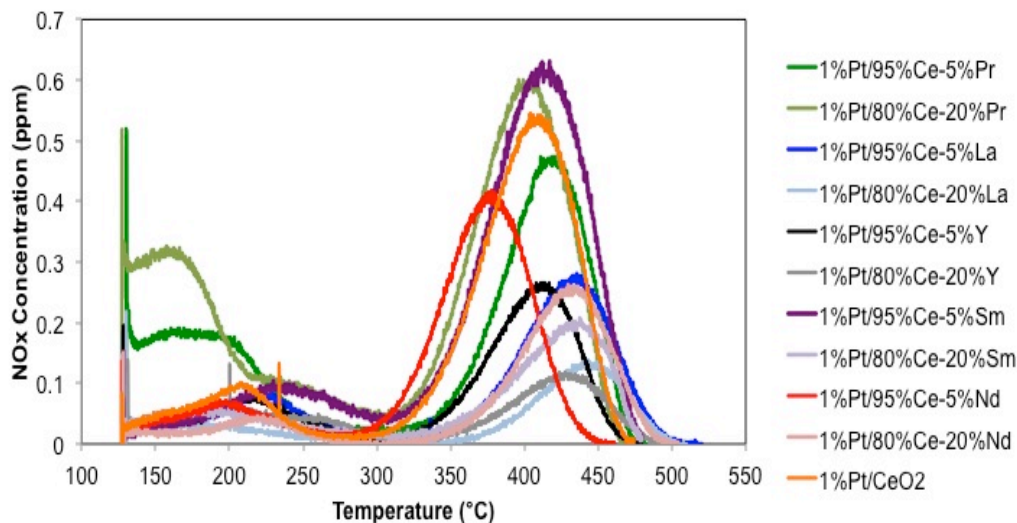


Figure 5.7. NO_x-TPD profiles of PtCe(5-20)M after NO_x storage at 120 °C for 5 minutes.

Figure 5.8 summarizes NDE for PtCe(5-20)M catalysts at temperatures <350 °C and 350-500 °C. In all cases but Pr, most NO_x was desorbed above 350 °C. The use of Pr greatly increased the amount of NO_x desorbed below 350 °C in both relative and absolute terms (Figure 5.9) compared to higher temperature desorption. Desorbing the majority of NO_x at lower temperatures is favorable since it makes it easier to regenerate the catalysts at typical diesel exhaust temperatures. Using Pr as a dopant in CeO₂ greatly benefited NSE and NDE, making it an interesting material for PNA applications. (See Figures A.2.5. and A.2.6. for triplicates of samples with more than 100% total NDE.)

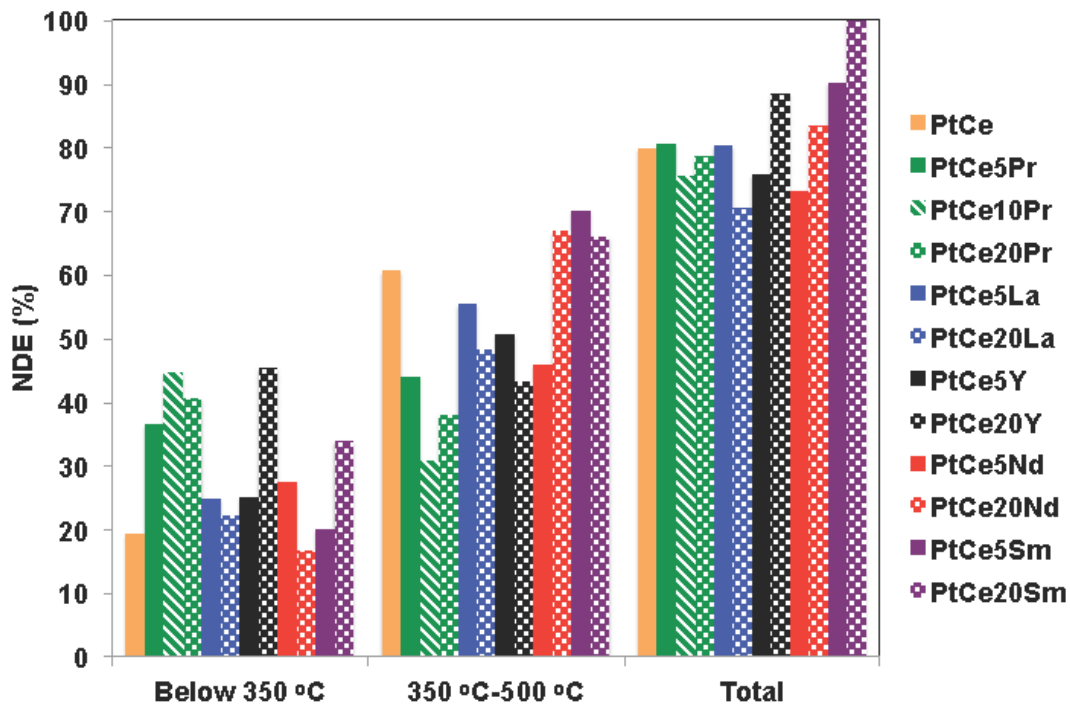


Figure 5.8. Comparison of NO_x desorption efficiency after storage at 120 °C for two different temperature ranges: < 350 °C and 350-500 °C.

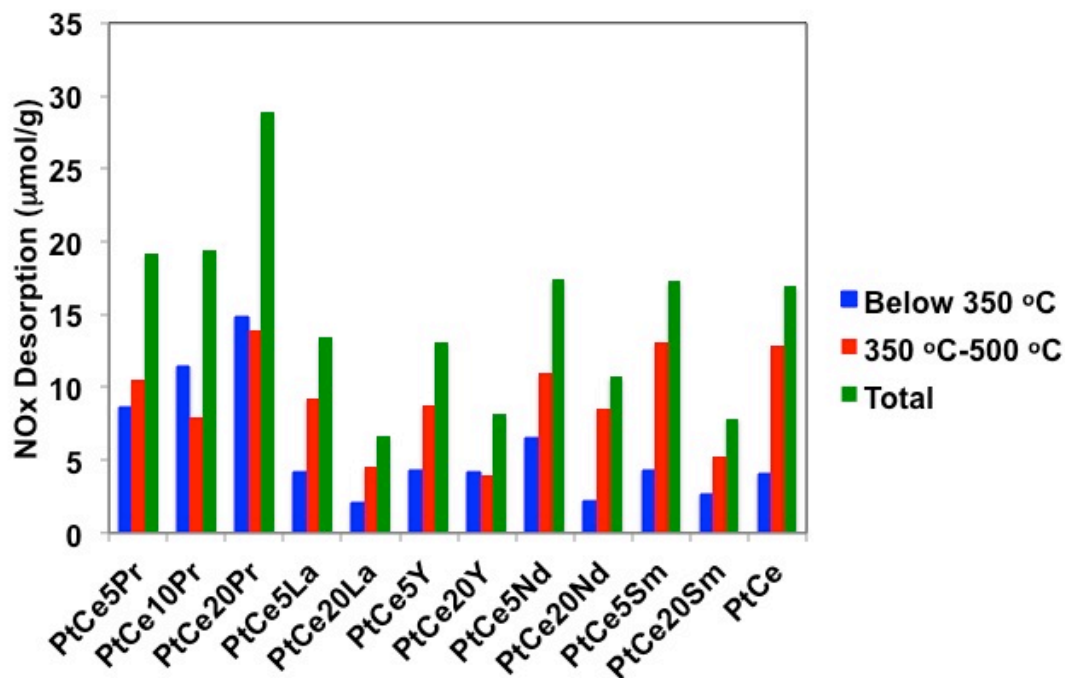


Figure 5.9. Comparison of amount of NO_x desorbed after storage at 120 °C for two different temperature ranges: < 350 °C and 350-500 °C.

5.3.3. NSE and NDE for Pd-Promoted Catalysts.

Previous studies have shown that the use of Pd instead of Pt for CeO₂ promotion results in storage of NO_x as predominantly thermally less stable nitrites as opposed to thermally more stable nitrates [27-29]. This is attributed to the superior activity of Pt for NO oxidation, NO₂ formation leading to storage as nitrate [39-40]. This was studied for the Ce(5-20)Pr supports in this work by promoting them with 1 wt% Pd and evaluating their NSE and NDE under the same conditions as the Pt-promoted catalysts. As seen in Figure 5.10 and similar to the Pt-promoted samples, higher concentrations of Pr resulted in higher NSE. While the incorporation of 10 mol% of Pr gave the highest NO_x release below 350 °C (the same results being observed for NO_x desorption in absolute values, see Figure 5.12) compared to high temperature release, the 20 mol% Pr sample stored more NO_x, making it the best catalyst for PNA applications overall (Figure 5.11). Similar to the TPD profiles for the PtCe(5-20)M samples, two desorption events were observed for PdCe(5-20)Pr. The first occurred below 300 °C with the second occurring in the range of

300-500 °C. Doping CeO₂ with Pr shifted desorption peaks to higher temperatures compared to undoped CeO₂ as for the platinum-promoted counterparts. Unlike the Pt-promoted samples, when the Pr content was increased from 5 mol% to 20 mol% the NO_x desorption peaks did not shift to lower temperatures. Rather, they shifted to higher temperatures (Figure 5.13).

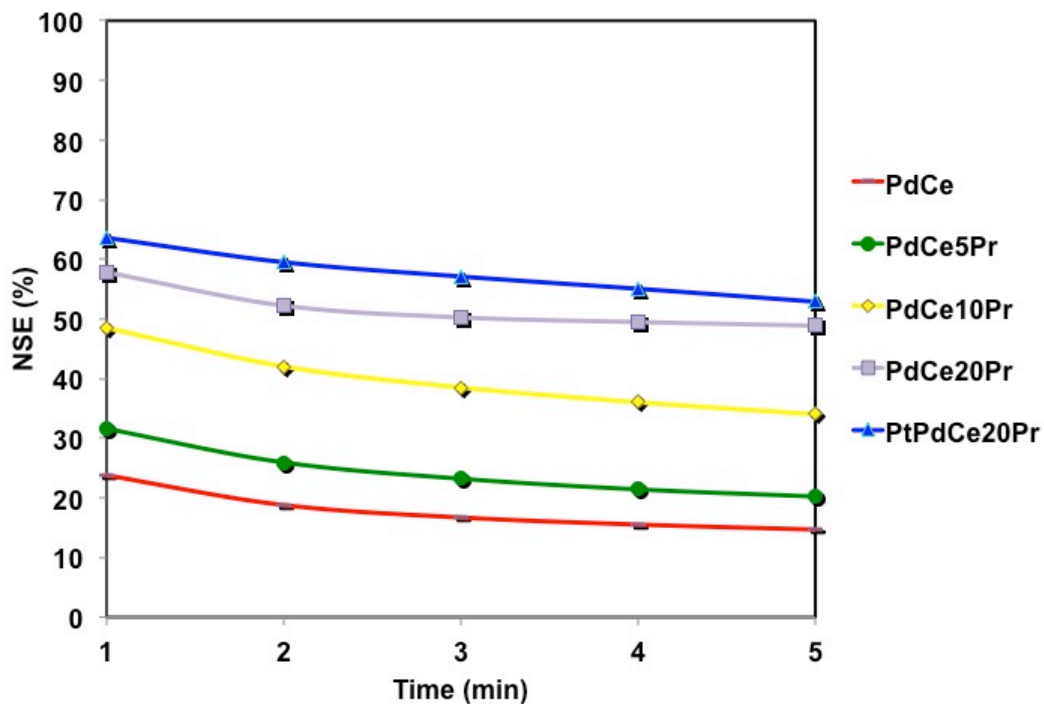


Figure 5.10. Comparison of NO_x storage efficiency at 120 °C for PtPd or PdCe5-20Pr.
 Feed: 300 ppm NO, 5% O₂, 5% CO₂, 3.5% H₂O and He balance.

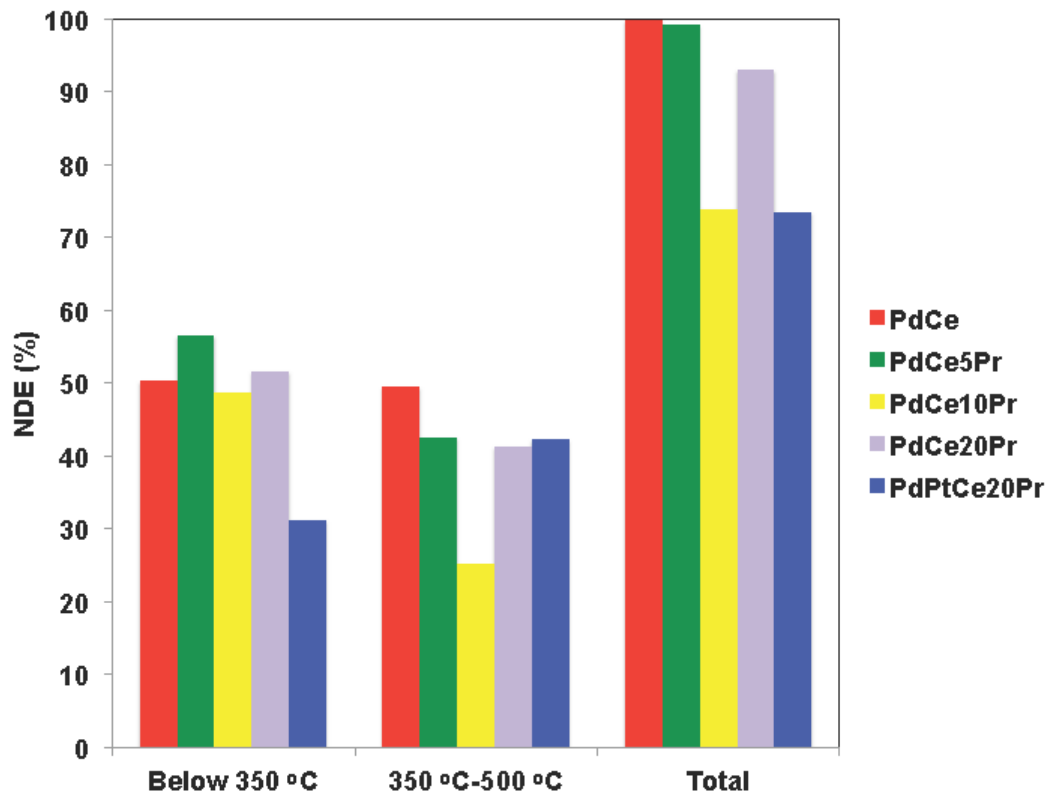


Figure 5.11. Comparison of NO_x desorption efficiency after storage at 120 °C for PdCePr catalysts at two different temperature ranges: < 350 °C and 350-500 °C.

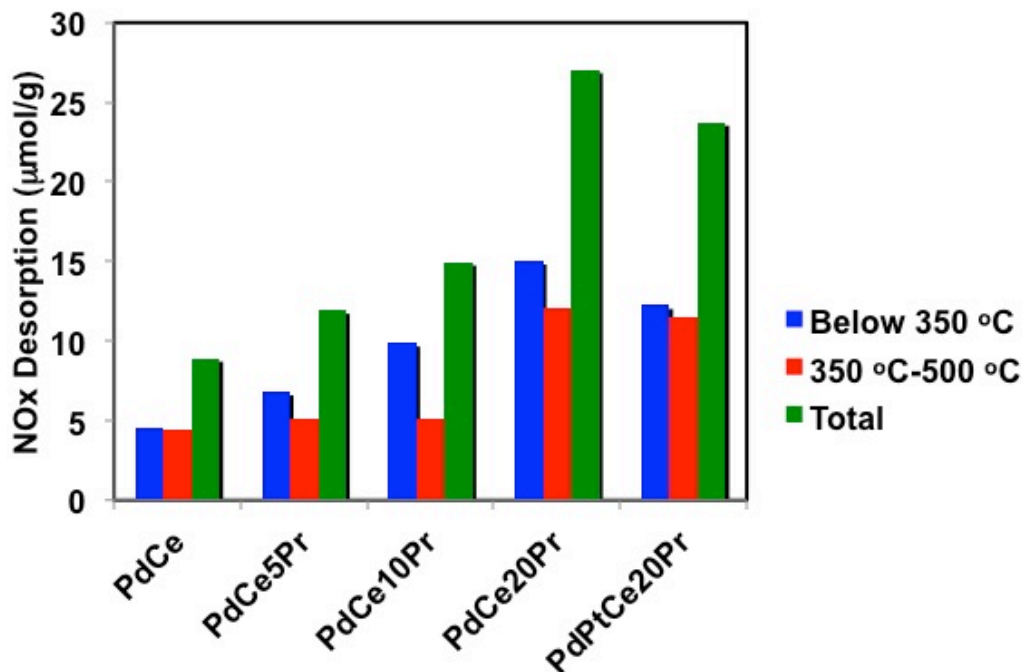


Figure 5.12. Comparison of amount of NO_x desorbed after storage at 120 °C for two different temperature ranges: < 350 °C and 350-500 °C.

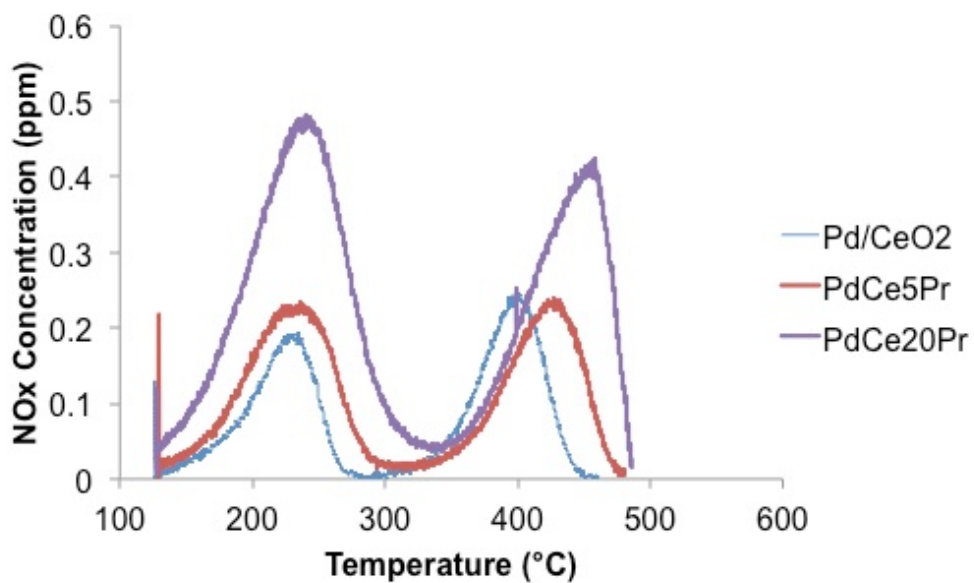


Figure 5.13. NO_x-TPD profiles of PdCe(5-20)Pr after NO_x storage at 120 °C for 5 minutes.

Compared to Pd, promotion with Pt resulted in a higher NSE at all concentrations of Pr. PtCe20Pr displayed an NSE 30% higher than that achieved for PdCe20Pr after 1 minute of storage at 120 °C. The largest difference in NSE between Pt- and Pd-promoted samples occurred when CeO₂ was doped with 5 mol% Pr. PtCe5Pr had an NSE 37% higher than that of PdCe5Pr. Although Pt-promotion resulted in higher NSE values, it was not as easy to regenerate the catalyst as compared to the same support promoted with Pd. Indeed, in all cases Pd-promoted Ce-Pr catalysts exhibited higher NDE below 350 °C compared to the Pt-promoted analogs. For example, PdCe20Pr released 13% more NO_x below 350 °C than PtCe20Pr.

To evaluate the use of Pt and Pd together, the Ce20Pr support was promoted with 0.5 wt% Pt and 0.5 wt% Pd. According to NSE and NDE measurements the presence of Pt and Pd resulted in catalyst behavior similar to that of the Pt-only promoted counterpart, showing lower NDE below 350 °C than PdCe20Pr and displaying a NSE of 63.6%, being lower than Pt (~88.0 %) but higher than Pd (57.8%) after the first minute. McCabe and co-workers found that utilizing Al₂O₃ promoted with Pt and Pd resulted in the catalyst behaving predominantly as its Pt only counterpart with regards to NO oxidation [41].

5.3.4. Cycling Studies.

Cycling studies were conducted to mimic the behavior of a PNA being repeatedly transitioned between ambient temperatures (e.g., cold start) and normal operating temperatures during which NO_x desorption occurs. Typical operating temperatures for a light duty diesel engine generally occur in the range ~180-350 °C [5]. To simulate this, cycling experiments were performed for the Ce20Pr series, NO_x storage being performed at 120 °C for 5 minutes, followed by heating to 350 °C to induce thermal release of stored NO_x. Five such cycles were performed. Figure 5.14 displays the measured NSE and the corresponding NDE as a function of cycle number for PtCe20Pr and PdCe20Pr. In the case of PtCe20Pr, a decrease in NSE was observed between the first and second storage phase, with only marginal changes from one cycle to the next thereafter. For PdCe20Pr NSE showed little variation, with only a slight difference between the third and fourth cycles. During temperature ramping to 350 °C both samples showed a

continued increase in NDE with continued cycling, more so for PdCe20Pr. This suggests that as cycling proceeds strong adsorption sites are initially filled from which relatively little NO_x is released during thermal ramping. Consequently, as cycling proceeds, weak storage sites are increasingly utilized, from which NO_x is readily desorbed. The increase in NDE from one cycle to the next when ramping to 350 °C was significantly more noticeable for PdCe20Pr, which further suggests that Pd preferentially stores NO_x as thermally less stable nitrites. The same pattern is observed when ramping to 250 °C in the case of Pd-only. Comparing the cycling performance of PtCe20Pr, PdCe20Pr and PtPdCe20Pr, Figure 5.15 shows that the sample containing both Pt and Pd behaves predominately as the Pt-only sample. PtPdCe20Pr has NSE similar to PtCe20Pr with the only significant change in NSE being between the first and second cycle. It is also observed that NDE for the first cycle is similar to that of PtCe20Pr by releasing significantly less NO_x than each subsequent cycle, while PdCe20Pr releases a similar amount of NO_x during the first cycle when compared to the other cycles.

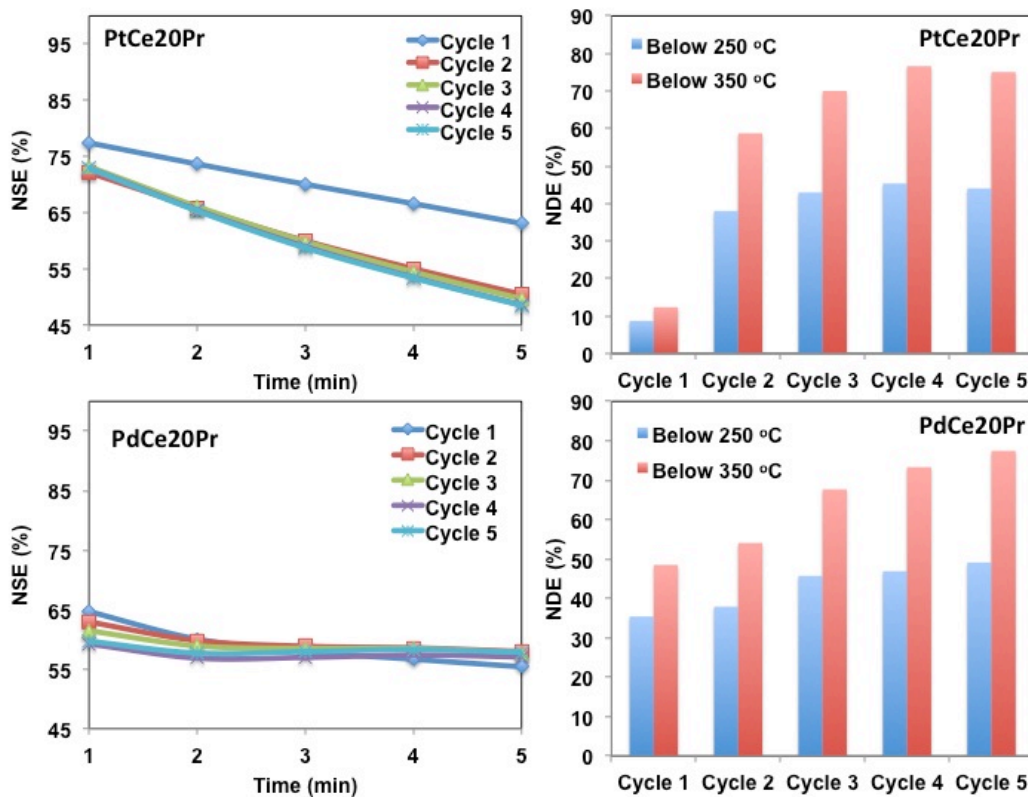


Figure 5.14. Comparison of NO_x storage efficiency at 120 °C for 5 minutes and NO_x desorption efficiency below 250 °C and 350 °C for five consecutive adsorption-desorption cycles for Pt and PdCe20Pr.

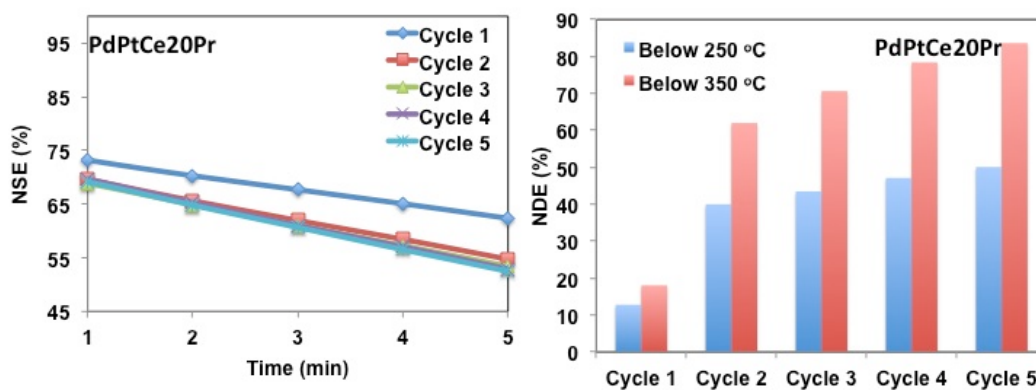


Figure 5.15. Comparison of NO_x storage efficiency storage at 120 °C for 5 minutes and NO_x desorption efficiency below 250 °C and 350 °C for five consecutive adsorption-desorption cycles for PdPtCe20Pr.

5.3.5. Aging Studies.

For real world applications, automotive catalysts need to be able to withstand high temperatures. During a typical DOC clean up the exhaust can reach temperatures up to 800 °C [5]. To test the Ce20Pr series' ability to withstand temperatures reached during a DOC clean off, the catalysts were aged at 750 °C for 16 hours under lean conditions (5% O₂, 5% CO₂, 3.5% H₂O with He balance). After aging, catalysts were cooled to room temperature and NO_x stored at 120 °C for 5 minutes followed by TPD. After aging NSE is severely hindered in all cases as displayed in Figure 5.16. PdCe20Pr displayed the worst NSE with the Pt containing counterparts having better NSE after aging. Although NSE significantly decreases after aging, the release of stored NO_x below 350 °C is greatly enhanced (Figure 5.17). BET analysis indicates a loss of catalyst surface area, although XRD data doesn't indicate any change in the structure of the support after aging, albeit the average diameter of the support particles slightly increased in size after aging as calculated using the Scherer equation. CO chemisorption also evidenced PGM sintering after aging, as indicated by increases in Pt and Pd particle sizes (summarized in Tables 5.1 and 5.2). All of the above indicates a loss in support surface area as well as evidence of PGM sintering, leading to the decrease in NSE after aging.

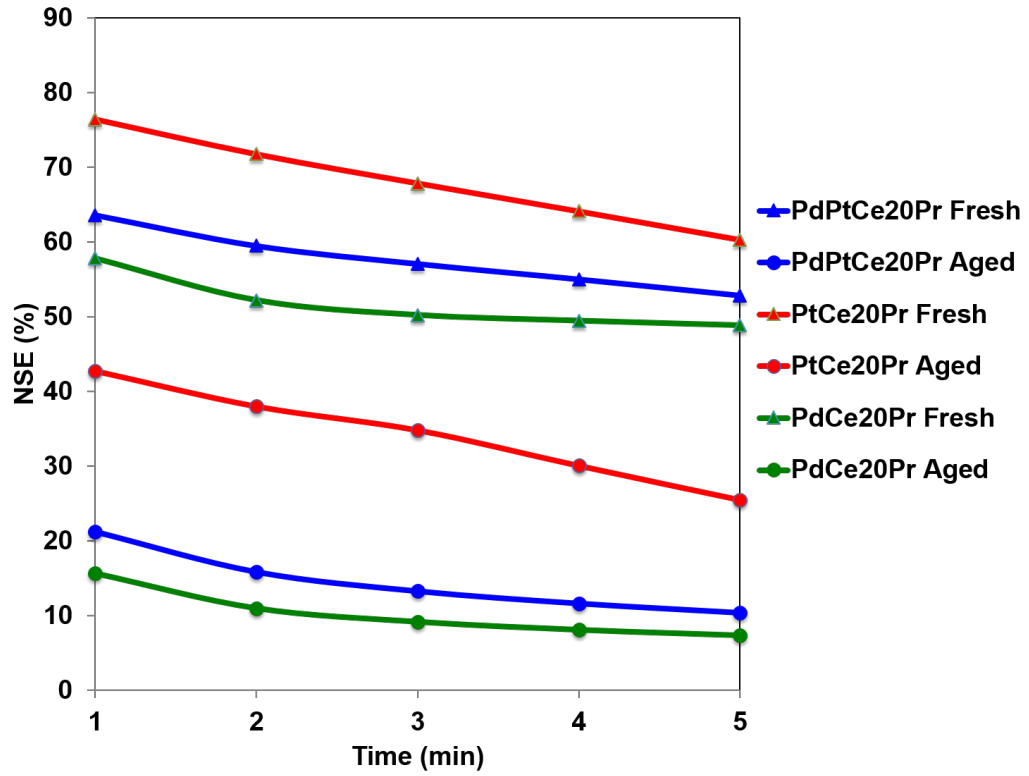


Figure 5.16. NSE comparison of Ce20Pr series after aging for 16 hours under lean conditions (5% CO₂, 5% O₂, and 3.5% H₂O with He balance).

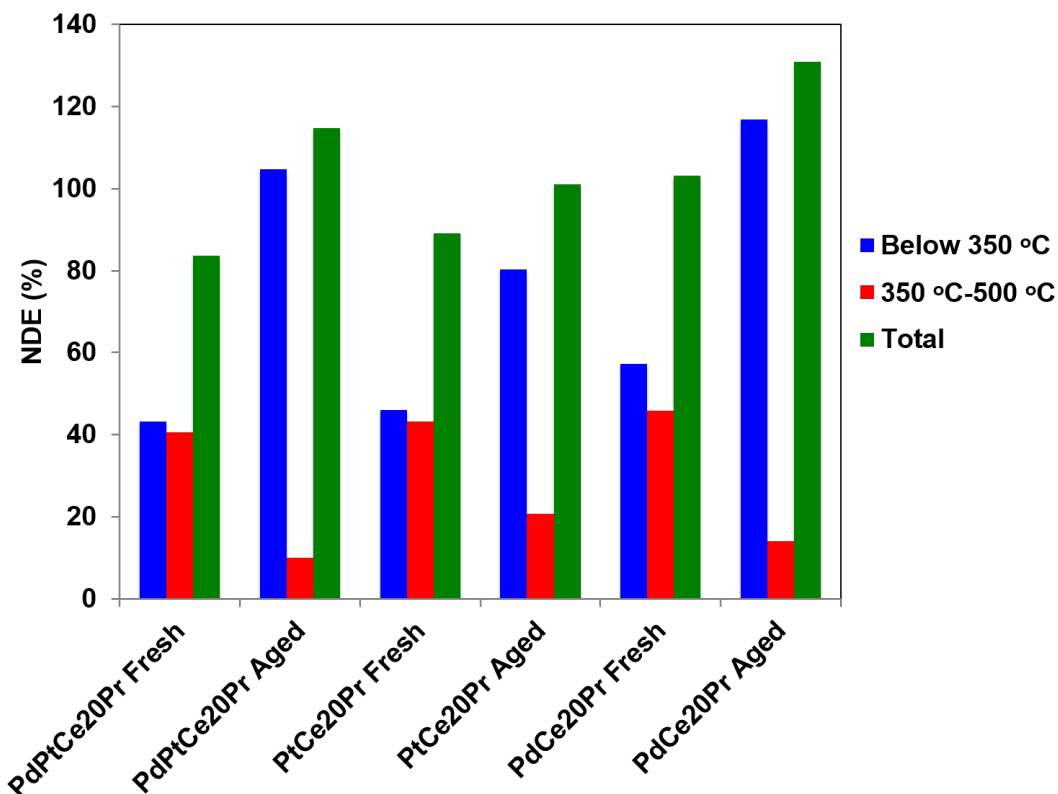


Figure 5.17. Comparison of NDE for Ce20Pr series after aging for 16 hours.

5.3.6. NSE and NDE in the absence of CO₂ and H₂O.

Storage/desorption studies were also performed in the absence of CO₂ and water at 120 °C for 5 min to facilitate a realistic comparison between microreactor data and DRIFTS spectra (vide infra). Figure 5.18 shows the measured NSE, while Figure 5.19 shows the corresponding NDE data. All of the catalysts in the Ce20Pr series that were promoted with Pd stored more NO_x in the absence of CO₂ and water. However, comparing NSE for PtCe20Pr in the presence and absence of CO₂ and water, roughly 88% of NO_x was stored at 120 °C after one minute in the presence of CO₂ and H₂O, while in their absence ~75% NSE was achieved after 1 minute. Previously it had been found that water competitively adsorbs with NO_x on CeO₂, reducing the number of absorption sites available for NO_x storage [45]. Comparing storage of NO_x in the presence and absence of CO₂ and water, the addition of 20 mol% Pr only increased storage by ~13% when storing NO_x in the absence of CO₂ and H₂O. The addition of Pr

appears to give CeO₂ the ability to tolerate water and carbon dioxide better compared to previously studied undoped CeO₂ catalysts [29]. Additionally, it was noted that NDE below 350 °C after storage without CO₂ and water in the feed was low (< 20%) suggesting that stored nitrites and nitrates possess enhanced stability when CO₂ and water are absent.

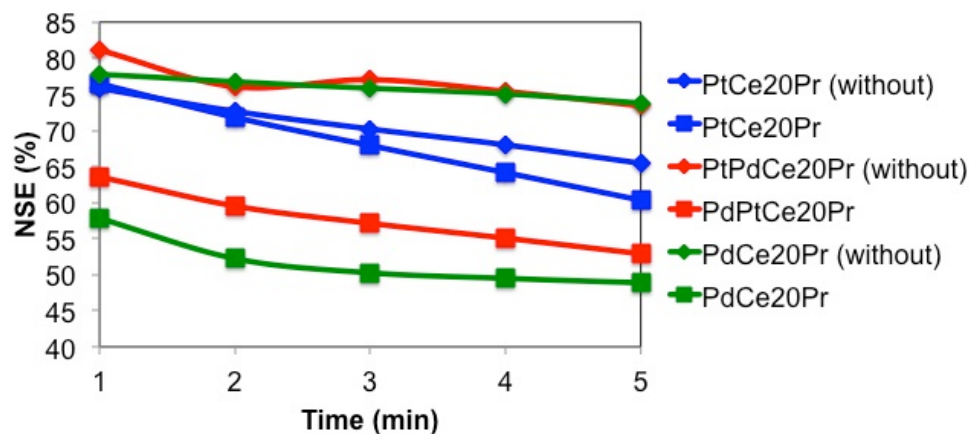


Figure 5.18. Comparison of NSE for Ce20Pr series measured without CO₂ and water in the feed.

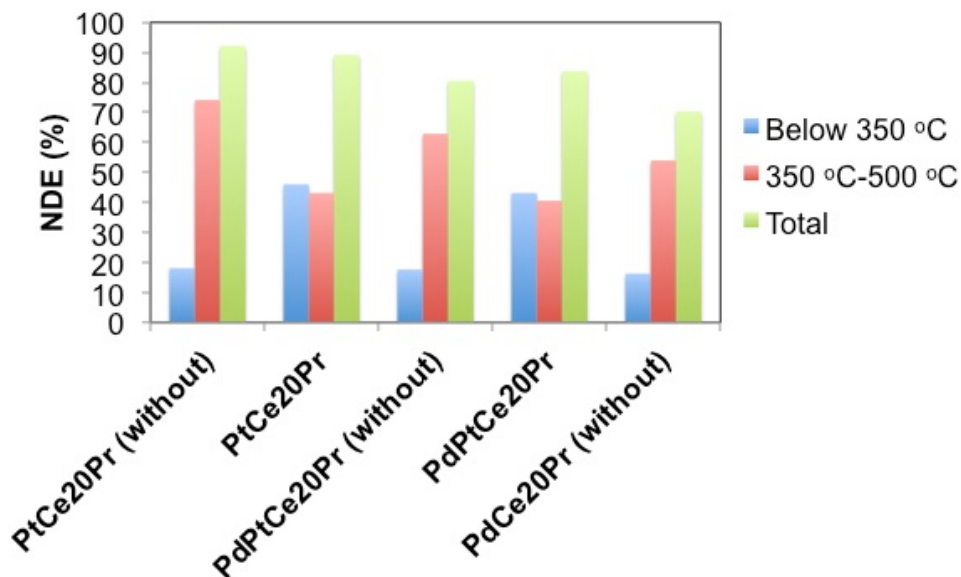


Figure 5.19. Comparison of NDE for Ce20Pr series without CO₂ and water in the feed.

5.3.7. DRIFTS Studies.

5.3.7.1. NO/O₂ Storage and Desorption.

From the information above it is evident that doping CeO₂ with Pr increases storage at 120 °C and desorption below 350 °C, while promotion with Pd increases low temperature NO_x release (<350 °C) compared to promotion with Pt. To understand these results DRIFT spectra of the Ce20Pr series were obtained during NO/O₂ storage at 100 °C (Figure 5.20). For PtCe20Pr, Figure 5.20a shows NO_x storage early on in the form of nitrates, evidenced by a band at 1606 cm⁻¹ corresponding to a bridging nitrate. Additionally, a band assigned to molecularly adsorbed NO₂ appeared at 1637 cm⁻¹ early on in the experiment, but disappeared after 10 minutes [42-44]. A chelating nitrite band was also observed after two minutes at 1166 cm⁻¹ [45-47]. Doping CeO₂ with Pr results in nitrite storage earlier than for undoped CeO₂ as previously reported [6]. Nitrate bands appeared after two minutes at 1564, 1275, 1212, 1060, and 1011 cm⁻¹ [42-47]. Moreover, a weak band assigned to NO storage on Pt was observed at 1747 cm⁻¹ and a nitrito nitrite band at 1415 cm⁻¹ grew in after 2 minutes [42].

Slightly different results were observed for PdCe20Pr. During the early stages of NO_x storage a strong chelating nitrite band was observed at 1167 cm⁻¹, together with a weaker nitrate band at 1583 cm⁻¹. Consistent with the lower NO oxidation activity of Pd compared to Pt, the presence of molecularly adsorbed NO₂ at 1637 cm⁻¹ wasn't observed for PdCe20Pr. Additionally the formation of a nitrito nitrite species was indicated by a band at 1417 cm⁻¹ after 30 seconds had elapsed (earlier than for PtCe20Pr). After 2 minutes nitrate bands grew in at 1567, 1269, and 1230 cm⁻¹. Subsequently, NO storage was observed on Pd (after ~10 min), evidenced by a band at 1745 cm⁻¹. In the case of PtPdCe20Pr, DRIFT spectra were similar to those of PtCe20Pr with the early formation of nitrates at 1562 and 1272 cm⁻¹, followed by nitrite formation after two minutes at 1155 cm⁻¹. An additional nitrate band associated with the band at 1562 cm⁻¹ grew in after two minutes at 1238 cm⁻¹, along with a nitrito nitrite band at 1415 cm⁻¹. Bands indicating storage on Pt and Pd were also present at 1798, 1744, and 1707 cm⁻¹ after 10 minutes.

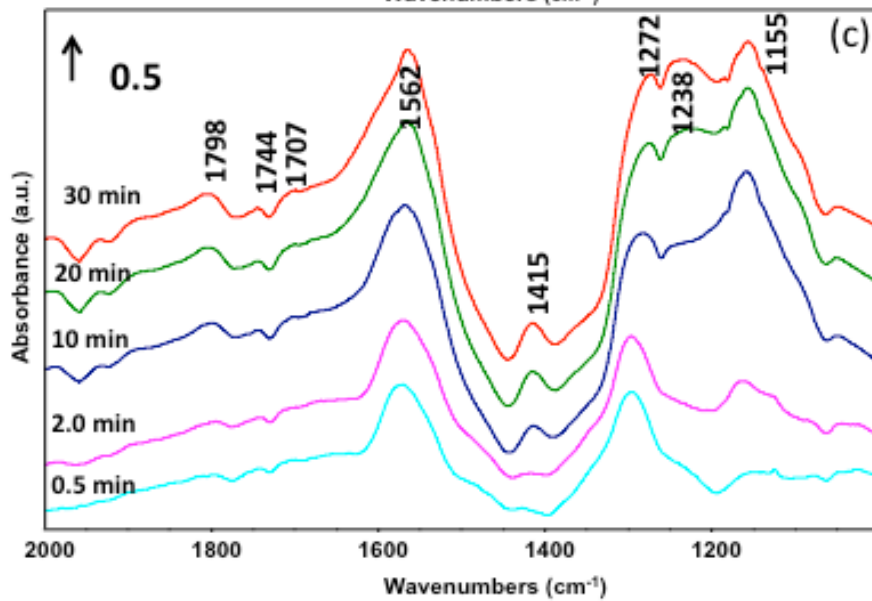
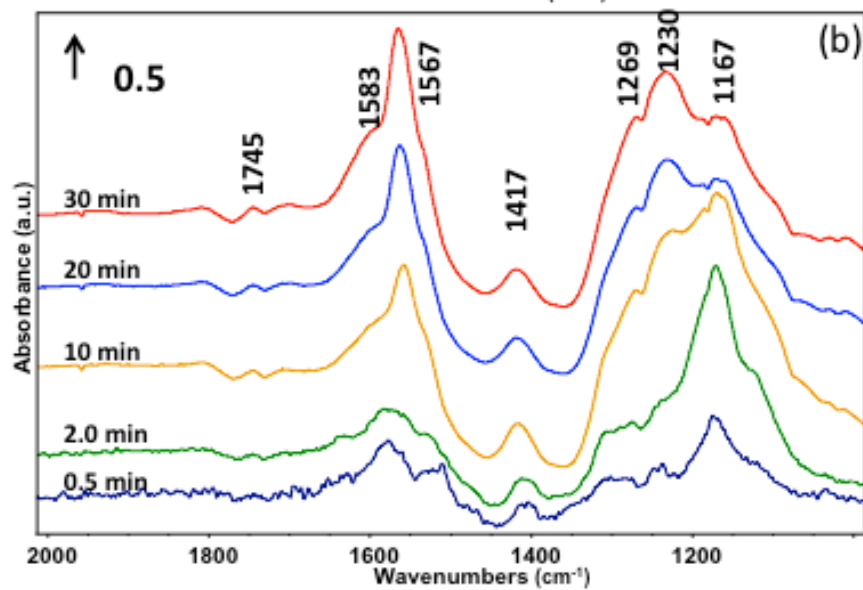
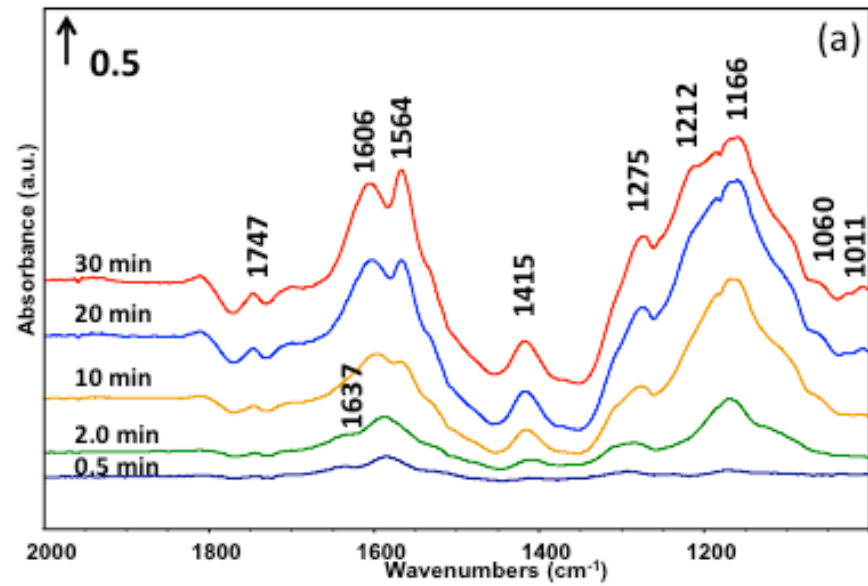


Figure 5.20. DRIFT spectra acquired during NO storage at 100 °C for (a) PtCe20Pr (b) PdCe20Pr and (c) PtPdCe20Pr. Feed: 300 ppm NO, 5% O₂, Ar balance.

During subsequent TPD, Figure 5.21a, increase of the temperature to 300 °C for PtCe20Pr resulted in the disappearance of the chelating nitrite at 1158 cm⁻¹. Simultaneously, bridging and monodentate nitrate bands appeared at 1607 and 1553 cm⁻¹, respectively, reaching their maximum values in the range 300-400 °C. The nitrito nitrite band at 1410 cm⁻¹ and Pt-NO band at 1741 cm⁻¹ decreased in intensity above 300 °C, disappearing by 500 °C. At 500 °C, the main bands remaining were the nitrate bands at 1235 and 1553 cm⁻¹. In the case of PdCe20Pr (Figure 5.21b), the evolution of the DRIFT spectra with temperature was very similar to the Pt analog, although NO stored on Pd (1743 cm⁻¹) was removed at slightly lower temperatures. Results for PtPdCe20Pr (Figure 5.21c) were similar to PtCe20Pr and PdCe20Pr. Again, nitrites at 1415 and 1155 cm⁻¹ were removed by 300 °C, with a continual increase in nitrate band intensity (1548 cm⁻¹), maximum intensity being reached at 300-400 °C. Above 400 °C the nitrate bands decreased in intensity, although monodentate nitrates still remained at 500 °C. From the obtained DRIFT spectra, it is concluded that Pd promotion results in storage of NO principally as nitrites that can be removed at low temperatures (< 300 °C). Promotion with Pt and equal mol % of Pt and Pd result in NO storage mostly as nitrates, which remain on the surface to at least 400 °C during TPD.

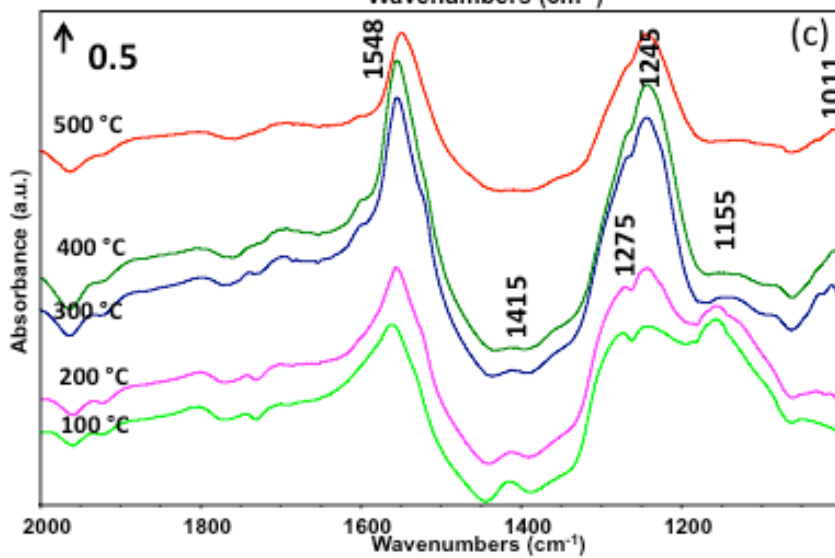
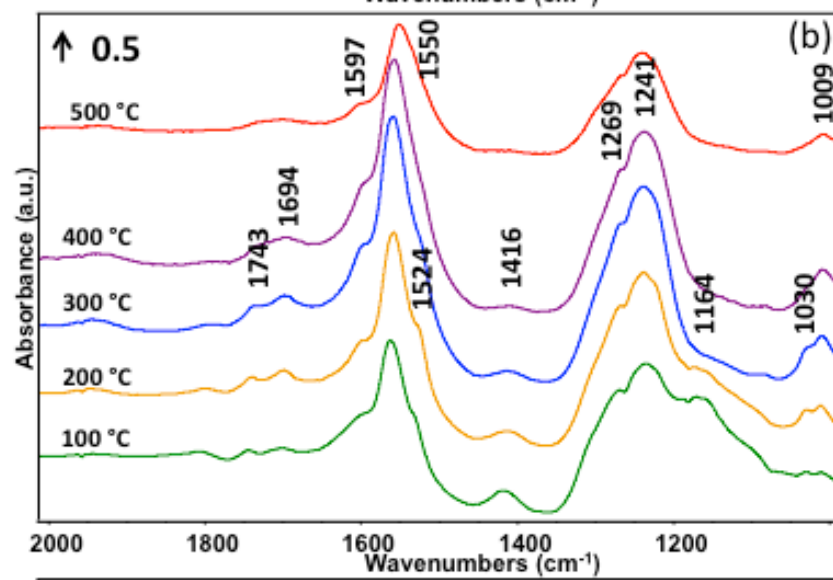
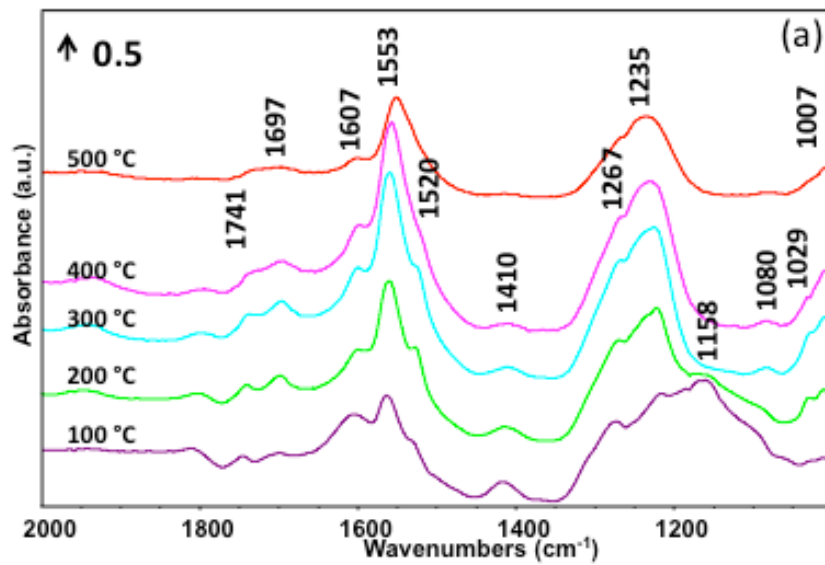


Figure 5.21. DRIFT spectra acquired during TPD after NO storage at 100 °C for (a) PtCe20Pr (b) PdCe20Pr and (c) PtPdCe20Pr. Feed: 300 ppm NO, 5% O₂, Ar balance.

5.4. Conclusions.

NO_x storage and desorption properties of CeO₂ doped with Pr, Y, Nd, Sm, and La at different concentrations were evaluated using microreactor and DRIFTS measurements. For Pt-promoted samples, doping CeO₂ with 5% Nd, Sm, and Pr resulted in an improvement of NSE, while doping with La and Y failed to improve NO_x storage. Pr proved to be the most promising dopant for increased NO_x storage at low temperatures, as indicated by the superior NSE obtained. With regard to catalyst regeneration, Pr-doped CeO₂ also proved to be the most promising material as confirmed by increased NO_x release below 350 °C. XPS analysis indicated that Pr⁴⁺ is reduced more readily than Ce⁴⁺, as evidenced by the higher concentration of Ce³⁺ present in undoped CeO₂ compared to that doped with Pr. Generation of lattice vacancies in Pr-doped CeO₂ appears to be particularly facile, as confirmed by Raman data, resulting in excellent NO_x storage properties. CeO₂ doped with 20 mol% Pr (the highest Pr loading examined) proved to be the most promising catalyst examined, although NSE was greatly decreased after hydrothermal aging. To a limited degree, the decreased NSE was countered by a large increase in NDE below 350 °C. Notably, NO_x storage on Pt- and Pd-promoted Ce20Pr was less affected by the presence of water and carbon dioxide than previously studied Pt/CeO₂ and Pd/CeO₂. Overall, doping with Pr was found to be promising for low temperature NO_x storage due to the ease of catalyst regeneration through NO_x release below 350 °C and the ability to store large quantities of NO_x at temperatures observed during cold starts.

Chapter 6. Doped CZO Catalysts for Passive NO_x Adsorber Applications.

6.1. Introduction.

Reducing NO_x emissions at low temperatures is challenging to automotive manufacturers due to the slow kinetics of NO_x reduction in this temperature regime (e.g., <200 °C). Manufacturers have the option of using either Lean NO_x trap (LNT) or Selective Catalytic Reduction (SCR) catalysts in current lean burn diesel aftertreatment systems, however they do not become operational until ~200 °C. Moreover, using urea-SCR catalysts at low temperatures has its own drawbacks due to the slow decomposition rates of urea. The decomposition of urea occurs through two steps: urea first decomposes to NH₃ and isocyanic acid (HNCO), which is followed by the hydrolysis of HNCO to NH₃ and CO₂ [1-2]. Lower operation temperatures (below 200 °C) can lead to accumulation of deposits of undecomposed urea on the catalyst surface, as well as side-products such as melamine which result from the reaction of HNCO with NH₃ [3]. These deposits on the SCR catalyst surface can cause catalyst deactivation. To prevent this from occurring manufacturers ramp urea injection at ~150-200 °C, but in doing so sub-stoichiometric amounts of urea are injected to minimize catalyst poisoning at the expense of unconverted NO_x (stoichiometric injection begins at 200 °C) [4]. This limits the amount of achievable NO_x conversion.

A 1998 patent suggested the use of Passive NO_x adsorbers (PNAs) to reduce NO_x emissions below 200 °C for stoichiometric gasoline vehicles [5]. A 2001 patent by Ford Motor Company first mentioned a PNA, Pt-promoted γ -Al₂O₃, coupled with a urea-SCR catalyst [6]. Ji et al. subsequently further researched the use of Pt/Al₂O₃ as a PNA catalyst [7]. They looked at the addition of 1 wt% La to Pt/Al₂O₃ and observed that the addition of La generated new NO_x storage sites. While the addition of La increased the amount of NO_x the catalyst was able to store, it did not benefit the amount of NO_x released below 250 °C when compared to the non-La containing counterpart which actually exhibited higher NO_x release below 250 °C. To further investigate this phenomenon, DRIFTS measurements were obtained. During NO_x-TPD, spectra indicated the presence of nitrites and weakly bound nitrate species that were removed from the

catalyst surface at low temperatures. Desorption above 250 °C was found to be mainly associated with the removal of nitrates.

General Motors researchers have also researched the use of an Al₂O₃ support without the use of precious metals. Studying Ag on Al₂O₃, they found that the use of Ag requires H₂ to be present for NO oxidation and adsorption below 200 °C [8-9]. Toyota reported the use of Ag/Al₂O₃-TiO₂ as a NO_x Storage Reduction (NSR) catalyst, finding that the addition of TiO₂ improved NO_x storage at 150 °C, while lowering necessary desulfation temperatures to 600 °C or lower [10]. Pd/ZSM-5 has been reported as a NO_x trap three way catalyst (N-TWC) by Honda [11]. The N-TWC catalyst was reported to have the ability to reduce NO_x and hydrocarbon (HC) emissions during cold starts, which have proven to be a problem in TWC catalysts.

Ceria is also a candidate material for PNA applications due to anionic vacancies in the crystal lattice [12-15] that have been found to facilitate NO_x adsorption [16-18]. Cordatos et al. observed that oxygen and NO were able to move freely between supported Pd and the CeO₂ support [19]. Moreover, doping ceria has been found to increase the number of vacancies in the crystal lattice [20-21]. Ceria doped with Pr, La, or Nd was used in place of the Ba phase in traditional LNT catalysts by Rohart et al. It was found that doping ceria greatly benefited NO_x storage at low temperatures compared to the Ba-containing LNT catalysts tested. Doping CeO₂ with Pr proved to result in the best storage at 250 °C after NO_x storage for one minute, resulting in a storage efficiency of 90%. In comparison, Ce-La stored ~70% of the NO_x fed, with the Ce-Nd catalyst storing less than 40%. The same trend was paralleled in catalyst ability to oxidize NO to NO₂ at 250 °C [22]. Wang et al. also explored the addition of Nd, La, and Y to Pt/Ba/Ce_{0.6}Zr_{0.4}O₂-Al₂O₃ LNT catalyst. They found that the addition of La to Ce-Zr improved NO_x storage at 200 °C, while the addition of Y and Nd did not improve storage [23].

Alternatively, several studies have been performed to evaluate the use of CeO₂ for low temperature NO_x storage without rare earth doping. Sun et al. recently studied Sn-Mn materials for their NO_x storage ability at 100 °C. Upon the addition of CeO₂, it was noted that NO_x storage increased. It was concluded that the addition of CeO₂ increased NO_x storage due to the ability of ceria to oxidize NO to NO₂. The presence of Sn-Ce interactions and increased concentrations of defect oxygen species on the catalyst surface

were also considered to be significant factors [24]. In a study by Cao et al. [25], it was observed that storage was dependent on the Co^{3+} concentration in Ce-Co-Cr-O catalysts. To achieve better dispersions of Co, high concentrations of Ce were needed which increased Co/Cr interactions. Increased Co/Cr interactions enhanced NO oxidation, thus increasing NO_x storage. Cu-Mn based catalysts were evaluated for NO_x reduction by non-thermal plasma (NTP) and temperature swing adsorption (TSA) utilizing waste heat from an engine [26]. A mixture of N_2 and NO_x is produced through TSA followed by reduction by NTP. Upon incorporation of the Cu-Mn catalyst a higher NTP energy efficiency was observed as well as increased NO_x conversion.

Recently, researchers at Ford have studied the use of Low Temperature NO_x Adsorbers (LTNAs). Theis et al. studied the effects of different ratios of Pt and Pd present on a catalyst support obtained from a commercial supplier [27]. All catalysts were aged prior to use. Catalysts that were Pt-only and Pt-rich had poor NO_x storage and NO oxidation activity during cold starts, whereas Pd-rich samples had superior ethene and NO_x storage. Stored NO_x was released predominantly as NO from Pd-rich samples, suggesting storage occurred in the form of nitrites. This improved the catalysts' ability to withstand SO_2 poisoning by reducing the amount of NO_x stored as nitrates, which strongly bind to SO_2 . Ford has also studied Pt and Pd on Al_2O_3 and ceria-zirconia (CZO) washcoats for low temperature NO_x storage and desorption under lean conditions [28]. Ethene was found to benefit NO_x storage below 100 °C for Pd/CZO after aging at 700 °C under lean conditions due to beneficial interactions between ethene and NO during simulated cold starts (not HC-SCR reactions—which were observed at higher temperatures). Pd/CZO was found to exhibit the best performance for NO_x storage, most NO_x being released below 400 °C, while minimal amounts of NO_2 and N_2O were formed.

Diffuse Reflectance Infrared Fourier Transform Spectroscopy (DRIFTS) has been frequently applied by researchers to understand how NO_x is stored and released on ceria-based catalysts. When storing NO and O_2 on CeO_2 at 50 °C, Philipp et al. noticed that NO initially stores as nitrites, which is followed by their oxidation to nitrates [29]. A study focusing on the effects of temperature on the adsorption of $\text{NO} + \text{O}_2$ on Pt/ CeO_2 found that at room temperature NO is stored as nitrites and is stored as nitrates at temperatures in excess of 200 °C [30]. Other researchers have observed the same

phenomenon, namely, that NO/O₂ initially adsorbs on Pt/CeO₂ as nitrites which are then oxidized to nitrates [31]. Researchers at Johnson Matthey have claimed that Pd/CeO₂ can store NO directly as nitrites, such that NO does not have to be oxidized to NO₂ during storage [32]. The diesel Cold Start Catalyst (dCSCTM), which incorporates the aforementioned PNA with a hydrocarbon trap, has been reported to store NO as nitrites making it easier to regenerate the catalyst. In a study of model catalysts by Jones et al. [33], it was found that Pd preferentially stores NO as nitrites, although Pt preferentially stores NO as nitrates due to Pt's superior oxidation activity over Pd. Pd/CeO₂-ZrO₂-Pr₂O₃ was studied by Yang et al. who observed the NO_x species present after exposure to stoichiometric amounts of CO + HC + NO_x + O₂ [34]. Ceria -rich catalysts formed nitrites at 50 °C, while zirconia-rich catalysts favored the formation of nitrates. They also found that higher Zr concentrations favored higher concentrations of surface oxygen species. This observation explains why Zr-rich catalysts favoring nitrate storage at 50 °C.

Herein, we report the comparison of 1 wt% Pd on ceria-zirconia doped with Pr (obtained from MEL Chemicals) for low temperature NO_x storage. Catalysts were evaluated for NO_x storage and NO_x desorption efficiencies at 120 °C, both in the presence and absence of CO₂ and H₂O. The catalysts' ability to store and release NO_x upon repeated adsorption-desorption cycling was also evaluated. DRIFTS measurements were obtained to understand the specific NO_x species present on the catalyst surface during NO_x storage and desorption.

6.2. Experimental Methods.

6.2.1. Catalyst preparation.

Mixed oxides, namely, CeO₂-ZrO₂ (CZO) doped with Pr and Pr₂O₃-ZrO₂ were obtained from MEL Chemicals. 1 wt.% Pd was loaded onto the mixed oxides by means of incipient wetness impregnation using aqueous solutions of Pd(NO₃)₂*xH₂O. The resulting samples were dried in a vacuum oven at 160 °C overnight and calcined at 500 °C for 3 h in a muffle furnace.

6.2.2 Catalyst Characterization.

X-ray powder diffraction analysis was conducted on a Phillips X'Pert diffractometer using Cu-K α radiation ($\lambda=1.540598 \text{ \AA}$). Diffractograms were recorded between 5° and 90° (2θ) with a step size of 0.02° . Brunauer-Emmett-Teller (BET) surface area and pore volume measurements were performed by nitrogen physisorption at -196°C using a Micromeritics Tri-Star 3000 system. Catalyst samples were outgassed overnight at 160°C under vacuum prior to measurements.

Pd dispersions were determined by means of pulsed CO chemisorption at -78°C using a Micromeritics AutoChem II Analyzer. Samples (250 mg) were loaded into the reactor and reduced in 10% H_2/Ar at 300°C for 10 min. In each case the sample was then purged with Ar for 20 min at the same temperature to remove residual H_2 and then cooled to -78°C prior to CO chemisorption. During the measurements 10 ml of CO was pulsed into the reactor every 2 min, the CO signal being monitored with a thermal conductivity detector (TCD). CO pulsing was terminated when the TCD signal reached a constant value, i.e., the precious metal sites were saturated with CO. Assuming a 1:1 ratio of CO to surface Pd, the metal dispersion was calculated based on the amount of CO adsorbed.

Temperature-programmed reduction (TPR) was performed using Micromeritics AutoChem II Analyzer. Ca. 150 mg of catalyst was loaded in the reactor and pretreated in 10% O_2/Ar at 500°C for 30 min. After cooling the sample to room temperature (RT) the cold trap was submerged in a dry ice and isopropanol bath at -78°C . Followed by TPR being carried out in a 10% H_2/Ar flow with a ramp of $10^\circ \text{C}/\text{min}$ from RT to 900°C . The H_2 signal during TPR was monitored using a TCD.

Raman spectra of the catalysts were recorded using a Jobin Yvon Horiba Raman dispersive spectrometer with a variable-power He-Ne laser source (632.8 nm), equipped with a confocal microscope with a 10x objective of long focal length. The spectrum of each sample was obtained as the average signal of two individual spectra of different areas of the sample. The acquisition time for each individual spectrum was 20 s. The detector was of the CCD cooled Peltier type.

X-ray photoelectron spectroscopy (XPS, K-ALPHA, Thermo Scientific) was used to analyze the surfaces of the catalysts. All spectra were collected using Al-K α radiation (1486.6 eV), monochromatized by a twin crystal monochromator, yielding a focused X-

ray spot with a diameter of 400 μm , at 3 mA \times 12 kV. The alpha hemi- spherical analyser was operated in the constant energy mode with a pass energy of 50 eV. Charge compensation was achieved with a low energy electron flood gun and low energy argon ions from a single source.

6.2.3. NO_x storage and desorption measurements.

NO_x storage and desorption efficiencies of the catalysts were determined in a quartz microreactor with a Pfeiffer ThermoStar GSD301 mass spectrometer as the detector. Prior to measurements samples (170 mg) were pretreated at 550 °C for 10 min under a flow of 5% O₂ in He (120 sccm) and then cooled to room temperature under flowing Ar. Samples were then equilibrated under a flow of 3.5% H₂O, 5.0% CO₂ and 5% O₂ (bal. He, 120 sccm) at the designated storage temperature; typically, this took 15 min, at which point the feed and effluent H₂O and CO₂ concentrations were equivalent. NO_x storage was initiated by adding 300 ppm NO to the feed. Storage experiments were conducted at 120 °C using a 5 min storage time. In all cases, a total flow rate of 120 sccm was used, corresponding to a gas hourly space velocity (GHSV) of ca. 30,000 h⁻¹. At the completion of the storage period the feed gas was switched to bypass mode and the NO flow was switched off. When the NO concentration had dropped to zero, the gas was re-directed to the reactor and temperature programmed desorption (TPD) was carried out to study NO_x desorption behavior using a ramp rate at 10 °C/min from the storage temperature up to 500 °C.

To understand the effect of multiple storage-desorption cycles, cycling experiments were also performed. Catalyst pretreatment and NO_x storage were performed as described above (using a storage temperature of 120 °C), after which TPD was performed up to 350 °C at a ramp of 10 °C/min under the same lean feed gas with the exclusion of NO. Subsequently, the temperature was lowered to 120 °C for the next NO_x adsorption-desorption cycle. A total of five cycles were performed for both Pt/CeO₂ and Pd/CeO₂.

NO_x storage efficiency (hereafter denoted as NSE) is defined as the percentage of NO_x passed over the catalyst that is stored, while NO_x desorption efficiency (hereafter denoted as NDE) is defined as the percentage of stored NO_x desorbed during TPD, i.e.:

$$\text{NSE} = \left(1 - \frac{\int_0^t ([\text{NO}_x]_{\text{out}}) dt}{\int_0^t [\text{NO}]_{\text{in}} dt} \right) \times 100\%$$

$$\text{NDE} = \left(\frac{\int_{t(T_0)}^{t(T)} ([\text{NO}_x]_{\text{out}}) dt}{\text{NSE} \times t \times [\text{NO}]_{\text{in}}} \right) \times 100\%$$

in which t is the NO_x storage time; $[\text{NO}]_{\text{in}}$ is the inlet NO_x concentration during NO_x storage; $[\text{NO}_x]_{\text{out}}$ is the outlet NO_x concentration during either NO_x storage or the subsequent NO_x desorption period; $t(T_0)$ is the start time of NO_x -TPD corresponding to the NO_x storage temperature before the temperature is raised; $t(T)$ is the end time of NO_x -TPD corresponding to the desired NO_x desorption temperature.

6.2.4. DRIFTS Measurements.

DRIFTS measurements were performed to monitor the surface species involved in NO_x adsorption and desorption. Measurements were performed using a Nicolet 6700 IR spectrometer equipped with a Harrick Praying Mantis accessory and MCT detector. The reaction cell was sealed with a dome equipped with two ZnSe windows and one SiO_2 observation window. The temperature of the reactor cell was controlled and monitored by a K-type thermocouple placed beneath the reaction chamber. For each DRIFT spectrum an average of 115 scans was collected (requiring ca. 1 min) with a resolution of 4 cm^{-1} . The spectrometer as well as the outside of the reaction cell were continuously purged with dry nitrogen to avoid diffusion of air into the system. Catalyst samples (~50 mg) were pretreated in situ in 300 ppm NO_x for 1 h then reduced at $450 \text{ }^\circ\text{C}$ for 15 min under 10% H_2 in order to remove carbonates, after which background spectra were collected (under Ar) in the range of $500\text{-}100 \text{ }^\circ\text{C}$ at intervals of $50 \text{ }^\circ\text{C}$. NO_x storage was carried out at $100 \text{ }^\circ\text{C}$ for 30 min using a feed consisting of 5% O_2/Ar and 300 ppm NO (120 sccm). During NO_x storage, spectra were collected as a function of time. After 30 min of NO_x storage, TPD was performed in flowing 5% O_2/Ar flow (120 sccm), the temperature being raised from $100 \text{ }^\circ\text{C}$ to $500 \text{ }^\circ\text{C}$ at a rate of $10 \text{ }^\circ\text{C}/\text{min}$. DRIFT spectra were recorded

during TPD at intervals of 50 °C. Absorbance spectra were obtained by subtracting background spectra from the spectra collected during NO_x storage and desorption.

6.3. Results and Discussion.

6.3.1. Sample Characterization.

Analytical data for CZO-Pr promoted with 1 wt.% Pd are collected in Table 1. Henceforth, all samples will be referred to as PdACeBZrCPr, where A is the concentration of Ce present, B is the concentration of Zr, and C is the concentration of Pr present in the catalyst. For previously studied CeO₂ doped with Pr₂O₃, it was found that a Ce/Pr mole ratio of 4 exhibited the best performance, thus supports with the same Ce/Pr ratio with Zr-rich or Zr-light concentrations were prepared. Additionally, mixed oxides containing differing concentrations of Pr and equal concentrations of Ce-Pr with ZrO₂ were prepared in order to show the effect of lowering the Ce/Pr mole ratio to 1. As shown in Figure 6.1, powder X-ray diffractograms of the doped CeO₂ supports display broad diffraction peaks. The Pd₆₄Ce₁₆Pr₂₀Zr sample showed typical diffraction peaks for the CeO₂ [35-36] fluorite structure with no evidence of separate ZrO₂ phases. The main two peaks characteristic of the fluorite structure, corresponding to the (111) and (220) planes, were observed at 28.5° and 32.6° respectively. However, the Pd₂₀Pr₈₀Zr, Pd₄₀Pr₆₀Zr, and Pd₁₆Ce₄Pr₈₀Zr samples showed typical diffraction peaks associated with the monoclinic crystal structure of ZrO₂ at 29.6° (111) and 34.0° (200) [37]. Pd₂₀Ce₂₀Pr₆₀Zr was the only sample with diffraction peaks associated with both CeO₂ fluorite structure and the ZrO₂ monoclinic structure. The average crystallite diameters of the supports calculated using the Scherrer equation ranged from 5.2 to 11.9 nm.

From N₂ physisorption data, BET surface areas as large as 112.5 m²/g (Pd₂₀Ce₂₀Pr₆₀Zr) and as small as 74.9 m²/g (Pd₂₀Ce₈₀Pr) were obtained, all of the samples displaying larger surface areas than PdCe₂₀Pr (discussed in Chapter 5). Doping Ce-Pr with Zr also increased pore radius (r_{pore}) and pore volumes (V_{pore}). Aging of Pd₆₄Ce₁₆Pr₂₀Zr resulted in a 50% loss in surface area, as summarized in Table 6.1. CO chemisorption indicates that Pd particle sizes were as small as 2.18 nm for Pd₁₆Ce₃Pr₈₀Zr and as large as 4.45 nm for Pd₂₀Ce₂₀Pr₆₀Zr. Pd particle sizes were similar to those obtained for CeO₂ mixed oxides, discussed in the previous chapter.

However, increasing the Pr content for samples without CeO₂ resulted in an increase in Pd size (3.43-3.95 nm). The same trend is observed when increasing CeO₂ content in samples that maintain a Ce/Pr of 4, while equal concentrations of Ce and Pr gave the largest Pd particle size. This suggests that increasing the content of Ce and Pr weakens interactions with Pd, resulting in the increased Pd particle size. As expected the lattice parameter (*a*) is significantly smaller for all Zr-containing samples due to the smaller diameter of Zr⁴⁺ (84 nm—ionic radii of Ce and Pr are greater than 100 nm). Additionally, *a* increases from 0.302 nm (Pd20Pr80Zr) to 0.305 nm (Pd40Pr60Zr) when increasing the content of Pr in Zr, indicating that the lattice is expanding to accommodate the additional Pr. The same finding was observed for other samples containing Ce, Pr, and Zr, i.e. *a* became larger as Zr content decreased. Consistent with the highly dispersed nature of Pd in these samples, diffraction lines for Pd was not observed in their X-ray diffractograms.

Table 6.1. Physical properties of fresh Pr-doped CeO₂ and CeO₂-ZrO₂ catalysts used in this work.

Catalyst	d _{support} (nm)		BET SA (m ² /g)		d _{pore} (nm)	V _{pore} (cm ³ / g)	Γ _{metal} (nm)		<i>a</i> (nm)
	Fresh	Aged	Fresh	Aged			Fresh	Aged	
PdCe20Pr	10.0	14.9	66.2	18.9	3.4	0.24	3.99	8.30	0.546
Pd20Pr80Zr	11.9	--	74.9	--	9.6	0.36	3.43	--	0.302
Pd40Pr60Zr	8.0	--	88.4	--	8.1	0.37	3.95	--	0.305
Pd16Ce4Pr80Zr	7.8	--	77.3	--	8.9	0.34	2.18	--	0.299
Pd20Ce20Pr60Zr	5.2	--	112.5	--	7.4	0.42	4.45	--	0.304
Pd64Ce16Pr20Zr	7.2	13.2	88.0	44.6	5.2	0.23	2.85	4.63	0.312

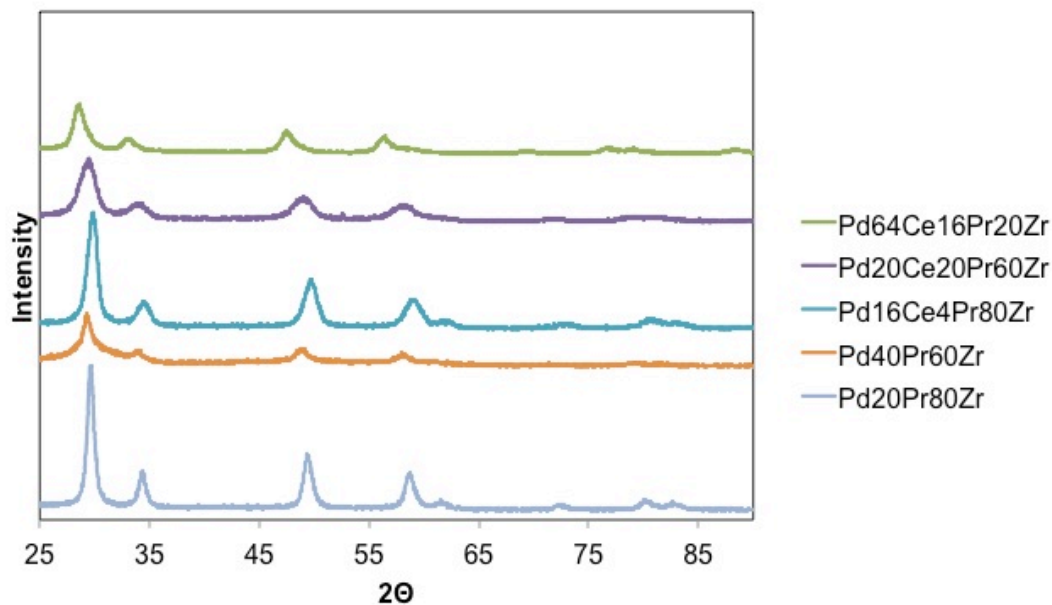


Figure 6.1. X-ray diffraction patterns of Pr-doped CeO_2 and $\text{CeO}_2\text{-ZrO}_2$ catalysts.

Raman spectroscopic analysis of fresh samples (PdCe, PdCe20Pr, Pd64Ce16Pr20Zr) indicates a decrease in the intensity of the bands associated with the ceria F_{2g} mode and the presence of oxygen vacancies when Pd-promoted CeO_2 is doped with Pr and/or Zr. This is attributed to the effects associated with the doping of CeO_2 previously discussed in Chapter 5. The presence of surface oxygen species/peroxides at 1151 cm^{-1} , was also detected through Raman spectroscopy [38-39]. A shift in ceria's F_{2g} mode towards lower wavenumber was observed upon doping with Zr and/or Pr (see Figure 6.2). This is attributed to the expansion of the unit cell to accommodate Pr^{3+} (larger than Ce^{4+}). The expected change of the F_{2g} band position upon Zr^{4+} doping (smaller than Ce^{4+}) would be towards higher Raman shifts, but this was not observed, indicating that the effect of Pr doping prevails with regard to that of Zr doping. Through XPS analysis, summarized in Table 6.2, it was concluded that doped samples were somewhat enriched in Zr and Pr due to Ce/Zr and Ce/Pr ratios being lower than the nominal values.

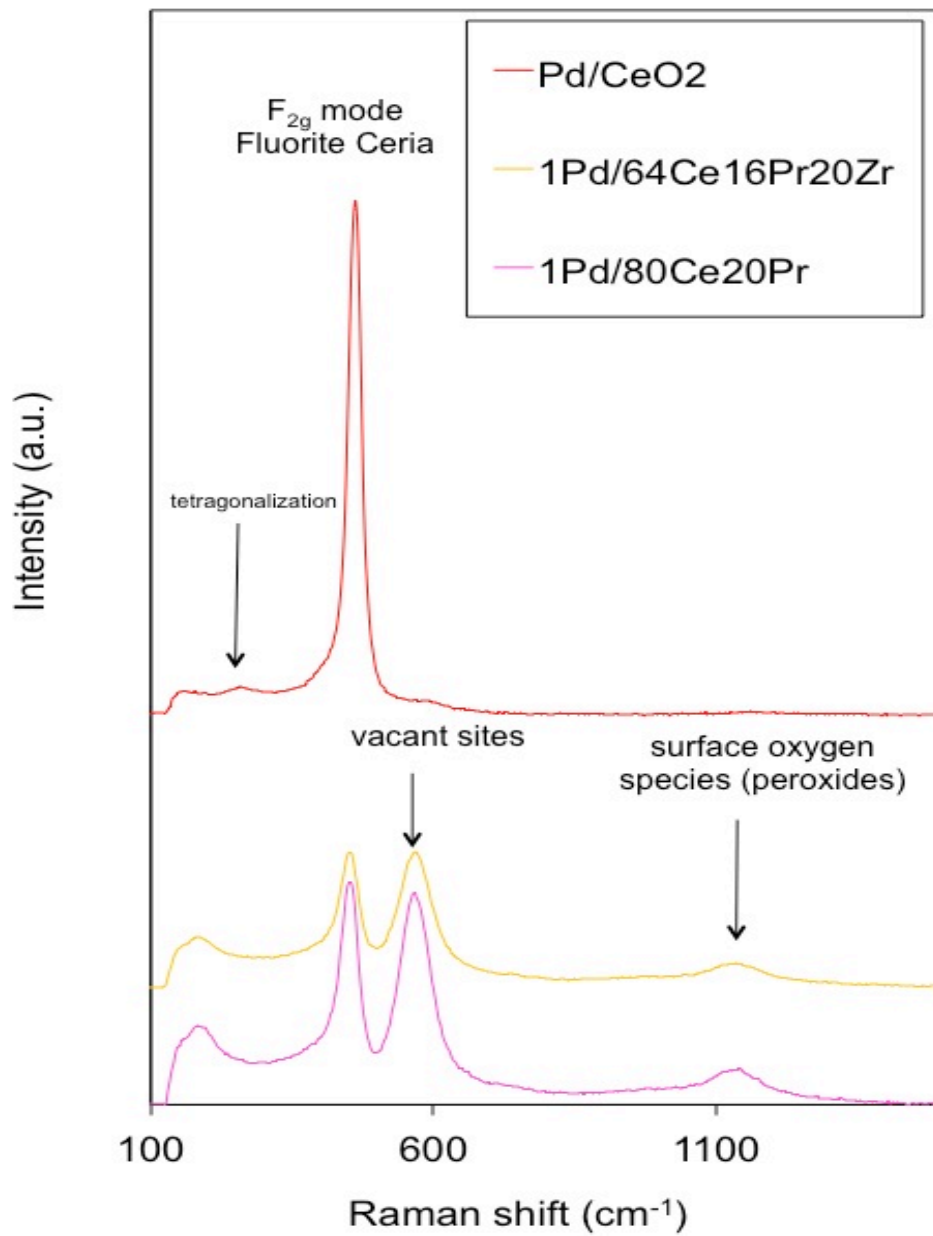


Figure 6.2. Raman analysis of Pr-doped CeO₂ and CeO₂-ZrO₂ catalysts.

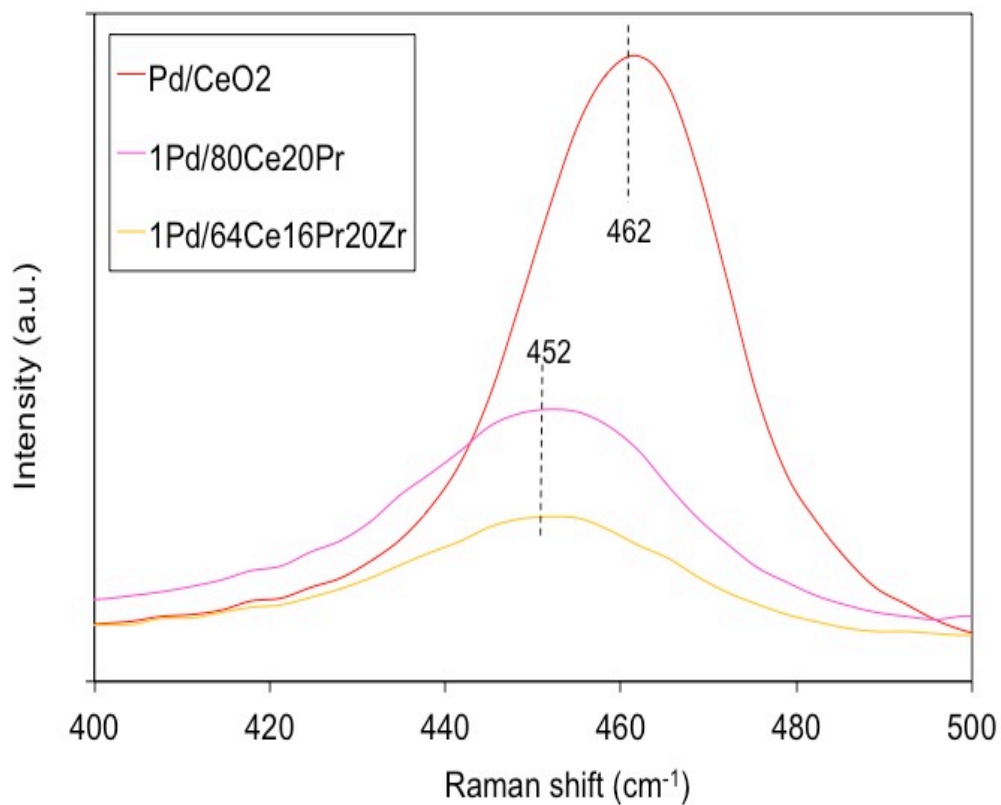


Figure 6.3. Effect of Pr doping on the Raman shift of the CeO₂ F_{2g} band.

Table 6.2. Atomic concentrations determined by XPS for fresh samples (*denotes nominal values).

Species	Pd64Ce16Pr20Zr	PdCe20Pr	PdCe
C	27.48	49.02	35.29
O	47.41	36.69	45.39
Pd	0.75	0.43	0.62
Ce	13.1	14.04	18.71
Pr	6.3	5.33	--
Zr	4.94	--	--
Ce ³⁺ (%)	30.1	25.9	33.2
Ce/Pr	2.1 (4)	2.6 (4)	--
Ce/Zr	2.7 (3.2)	--	--

Figure 6.4 compares TPR profiles of 64Ce16Pr20Zr to Ce20Pr. In both instances it is evident that PdO and the surface in close contact with Pd reduce at lower temperatures than the bulk support [40]. However, the PdO of Pd64Cr16Pr20Zr is appears to undergo reduction at room temperature, which is significantly lower than PdO on PdCe20Pr (103 °C). Additionally, a small reduction peak is observed at ~70 °C for Pd64Ce16Pr20Zr, possibly due to the reduction of PdO on ZrO₂ domains. PdCe20Pr also exhibits two reduction peaks in the ranges of 300-600 °C and 600-900 °C attributed to the bulk support. Most likely these correspond to Pr-rich and Ce-rich areas respectively as it has been shown that Pr⁴⁺ reduces more readily than Ce⁴⁺ [41]. Pd64Ce16Pr20Zr shows bulk reduction peaks at slightly different temperatures than those observed for PdCe20Pr: 235-630 °C and 630-900 °C. Unpromoted Ce20Pr has two reduction bands at ~400 and 500 °C which can be attributed to surface reduction, while those of unpromoted 64Cr16Pr20Zr are shifted to slightly higher temperatures at 430 °C and 540 °C. It should also be noted that reduction bands observed in the region 300-600 °C for all samples can also be attributed to carbonates or hydroxides [42-45].

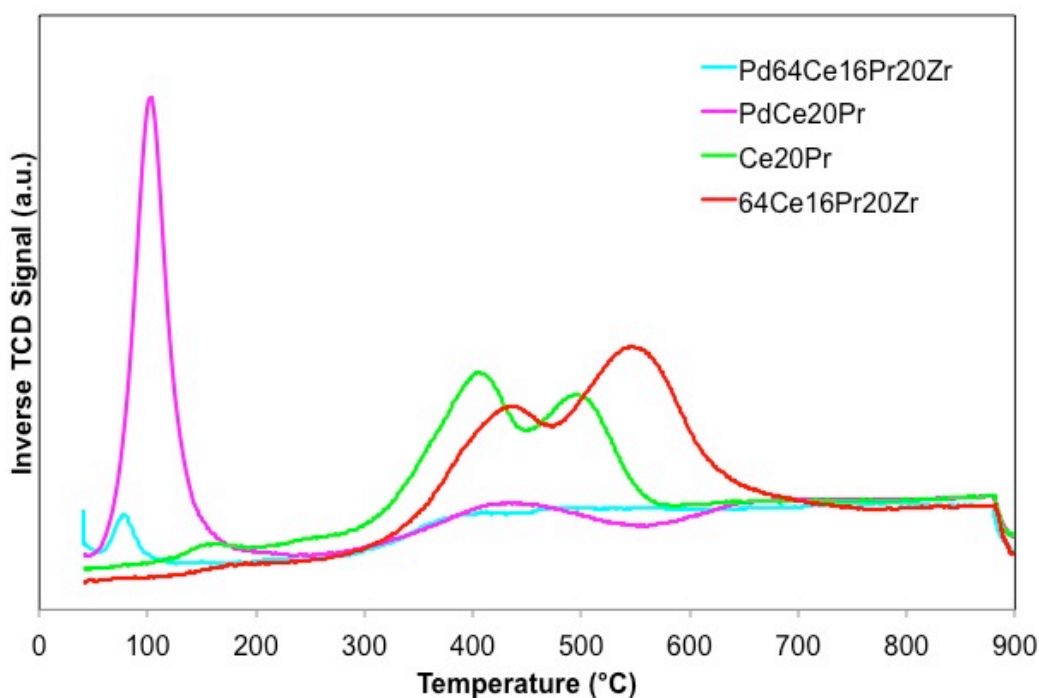


Figure 6.4. H₂-TPR profiles of fresh catalysts from the Ce20Pr and 64Ce16Pr20Zr series.

6.3.2. Effect of CeO₂ content on NSE.

Preventing NO_x slip at temperatures below 180 °C has become the major focus of emission control for automotive companies. It was reported by Ford Motor Company [46] that the exhaust temperature of a 4.4 L diesel engine reaches 60 °C within ~10 s during cold starts. However, to reach temperatures greater than 180 °C, ~180 seconds are required. For this reason, NO_x Storage Efficiency (NSE) was evaluated at 120 °C for all samples. Supports were promoted with 1 wt% Pd due to the benefit of low temperature (<350 °C) desorption as previously discussed. Figure 6.5 summarizes the NSE of the samples at 120 °C for 5 minutes of NO_x storage. For CeO₂-M₂O₃ mixed oxides, the best NSE was achieved by a catalyst with a molar Ce:Pr ratio of 4, as discussed in Chapter 5. Therefore, in order to assess the effect of doping with Zr, Pd₆₄Ce₁₆Pr₂₀Zr was prepared, which had an NSE of ~53% after 1 minute of storage under lean conditions, although this was lower than that achieved by PdCe₂₀Pr (~58%) at one minute. Lowering the concentration of CeO₂ and Pr₂O₃, while maintaining a Ce:Pr ratio of 4 to create Pd₁₆Ce₄Pr₈₀Zr, lowered NSE by ~10% at one minute. To evaluate the effects of equal concentrations of CeO₂ and Pr₂O₃ on NO_x storage, Pd₂₀Ce₂₀Pr₆₀Zr was utilized. Pd₂₀Ce₂₀Pr₆₀Zr exhibited the worst NSE of all the CeO₂ containing catalysts, indicating that an excess of CeO₂ needs to be present relative to Pr₂O₃ to obtain good NO_x storage efficiency. To evaluate the affects of Pr₂O₃ without the presence of CeO₂, Pd₂₀Pr₈₀Zr and Pd₄₀Pr₆₀Zr were prepared. Doping ZrO₂ with small amounts of Pr₂O₃ without CeO₂ present afforded an NSE comparable to that of Pd₁₆Ce₄Pr₈₀Zr. However, increasing the Pr₂O₃ concentration from 20 mol% to 40 mol% severely hindered NSE, making it the least appealing catalyst for NO_x storage. While increasing the concentration of Pr₂O₃ in CeO₂ benefited NSE as previously discussed in Chapter 5, it did not perform well without the presence of CeO₂. In summary, adding CeO₂ to Pr and Zr benefited NSE when the ternary oxide catalysts were Ce-rich, indicating that CeO₂ is necessary for NO_x storage and that doping CeO₂ with small quantities of Pr and potentially Zr can further increase storage efficiency.

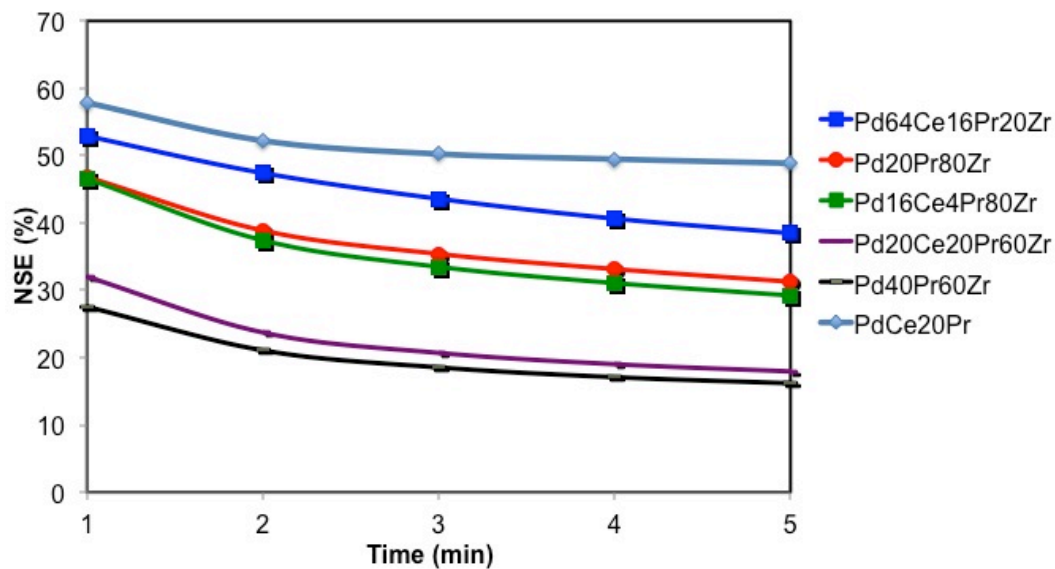


Figure 6.5. Comparison of NO_x storage efficiency at 120 °C for Pr-doped CeO₂ and CeO₂-ZrO₂ catalysts. Feed: 300 ppm NO, 5% O₂, 5% CO₂, 3.5% H₂O and He balance.

6.3.3. NO_x-TPD and NDE results.

As shown in Figure 6.6, the addition of Zr to Ce-Pr supports shifted desorption peaks above 350 °C to slightly lower temperatures compared to PdCe20Pr. However, in comparison Pr-Zr supports exhibited slightly higher desorption temperatures. Notably, Ce-rich catalysts released less NO_x below 350 °C compared to high temperature release, while Zr- and Pr-rich samples release relatively more NO_x at lower temperatures (Figure 6.7). The same trend is observed when evaluating NO_x Desorption Efficiencies (NDE) below 350 °C and 350-500 °C. Pd20P80Z and Pd40P60Z release the majority of stored NO_x below 350 °C, while the addition of Ce (Pd16C4P80Z) slightly increased release above 350 °C (in relative and absolute terms—see Figure 6.8) which continued to increase with CeO₂ content. Thus, as previously observed, Pr is beneficial to low temperature NO_x desorption, while the interaction of CeO₂ with Pr benefits NSE. However, when the CeO₂ content was increased to a high level (64 mol%), high temperature NO_x release increased. (See Figures A.2.5. and A.2.6. for triplicates of samples with initially more than 100% total NDE).

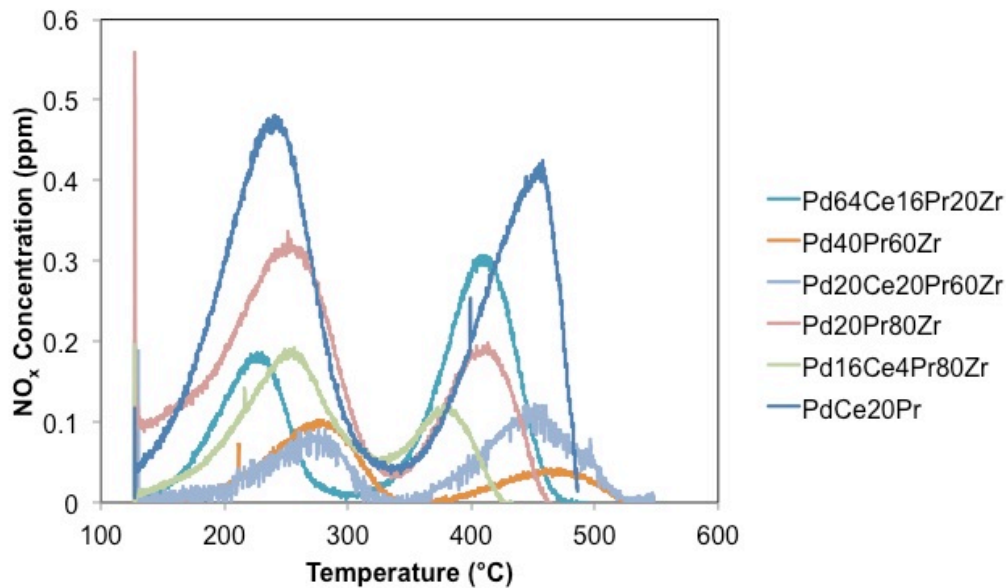


Figure 6.6. NO_x-TPD profiles of Pr-doped CeO₂ and CeO₂-ZrO₂ after NO_x storage at 120 °C for 5 minutes.

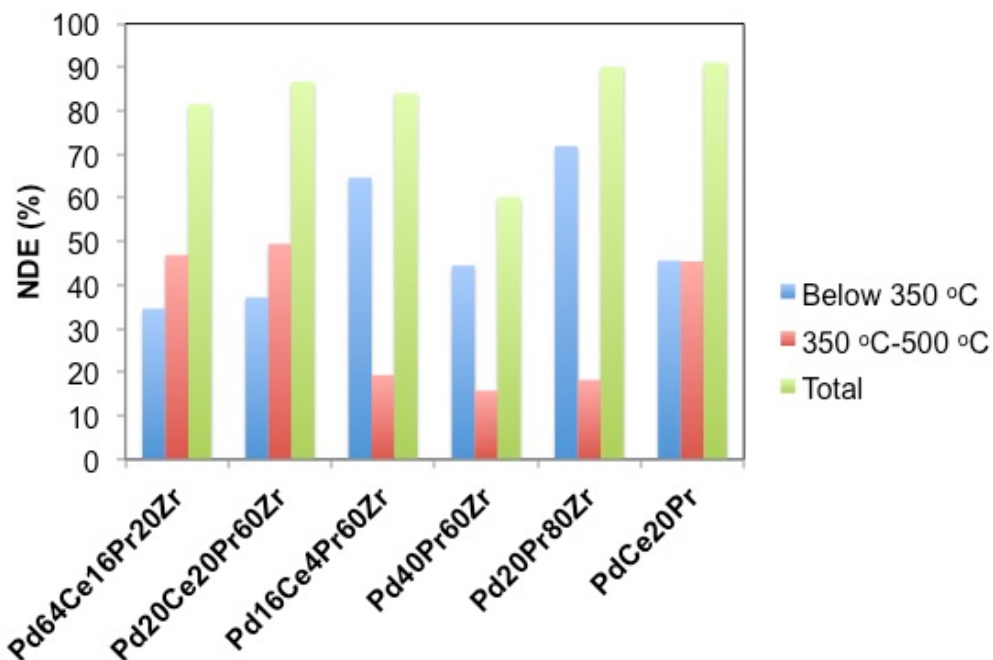


Figure 6.7. Comparison of NO_x desorption efficiency after storage at 120 °C for two different temperature ranges: < 350 °C and 350-500 °C.

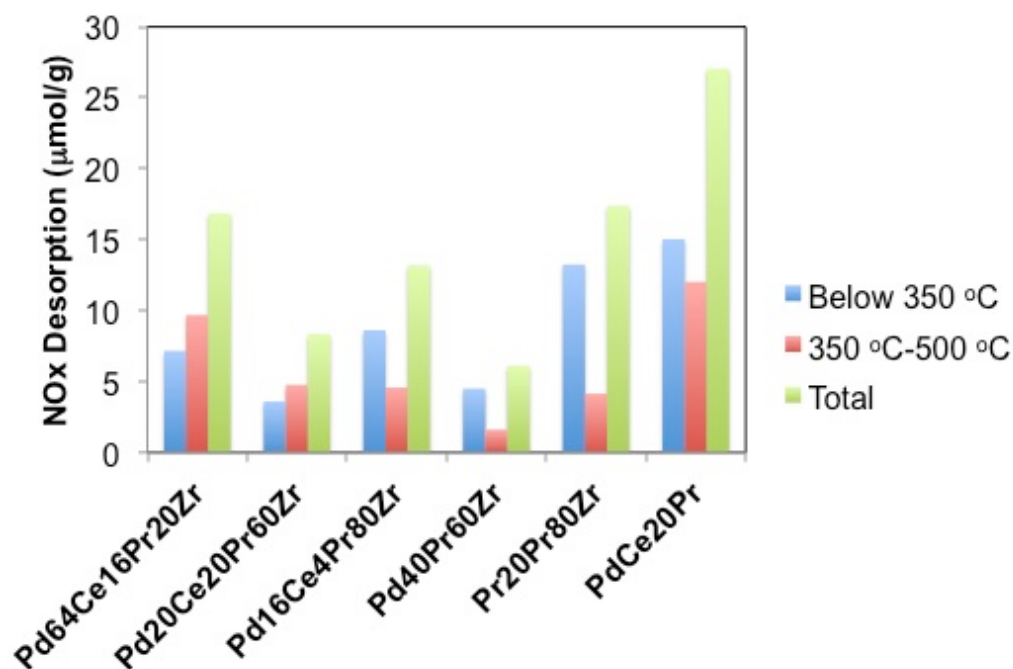


Figure 6.8. Comparison of amount of NO_x desorbed after storage at 120 °C for two different temperature ranges: < 350 °C and 350-500 °C.

6.3.4. Cycling Studies.

Actual use of PNA catalysts in exhaust aftertreatment systems would require that the catalyst be cycled between ambient temperatures (cold start) and standard operating temperatures (~180-350 °C for a light duty diesel engine) [47]. At normal operating temperatures some degree of NO_x desorption would occur. To test PdCe20Pr and Pd64Ce16Pr20Zr under these conditions, cycling experiments were performed involving NO_x adsorption at 120 °C for 5 minutes, followed by heating to 350 °C to induce thermal release of stored NO_x. This was repeated 5 times. During cycling of Pd64Ce16Pr20Zr, the NSE of the second cycle was higher than the first, indicating that one cycle is needed to stabilize the support with respect to NO_x storage (Figure 6.9). Little change in NSE was observed after the 3rd cycle for Pd64Ce16Pr20Zr. In contrast, PdCe20Pr requires longer to reach quasi-steady state conditions and doesn't reach a stable NSE until the 4th

cycle. Minimal differences are observed in NDE below 250 °C and 350 °C for both samples as shown in Figure 6.10. In both instances desorption below 250 °C reaches a near constant value after the 3rd cycle, while release below 350 °C continues to increase with each cycle due to incomplete desorption of stored NO_x from the previous cycle. Comparatively, Figure 6.11, displays a comparison of NO_x stored with NO_x desorbed with each cycle for Pd64Ce16Pr20Zr and PdCe20Pr. More NO_x is stored than released below 250 °C and 350 °C. With each cycle the total amount of NO_x released below 350 °C becomes closer to the amount stored, further suggesting that stored NO_x from previous cycles is being released with each cycle (i.e., approaching “steady-state” the surface is becoming saturate with NO_x).

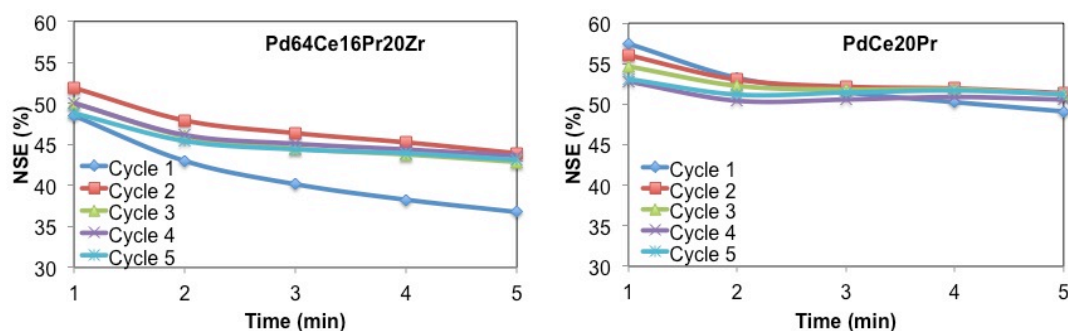


Figure 6.9. Comparison of NO_x storage efficiency at 120 °C for 5 minutes for five consecutive adsorption cycles for Pd64Ce16Pr20Zr and PdCe20Pr.

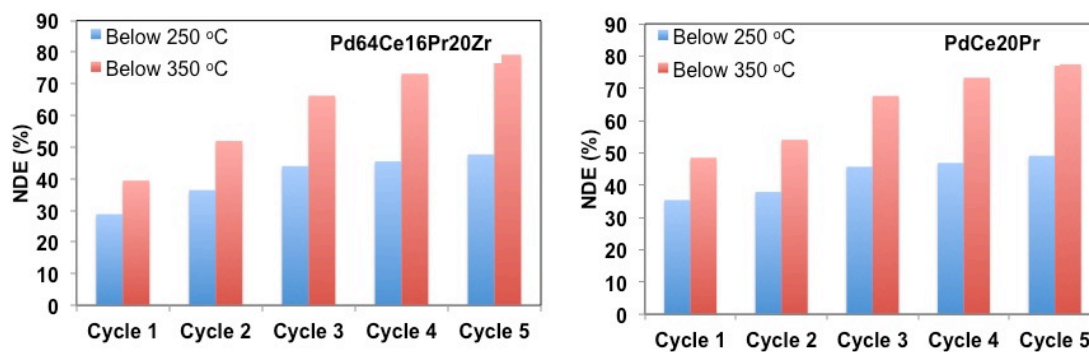


Figure 6.10. Comparison of NO_x desorption efficiency below 250 °C and 350 °C for five consecutive desorption cycles for Pd64Ce16Pr20Zr and PdCe20Pr.

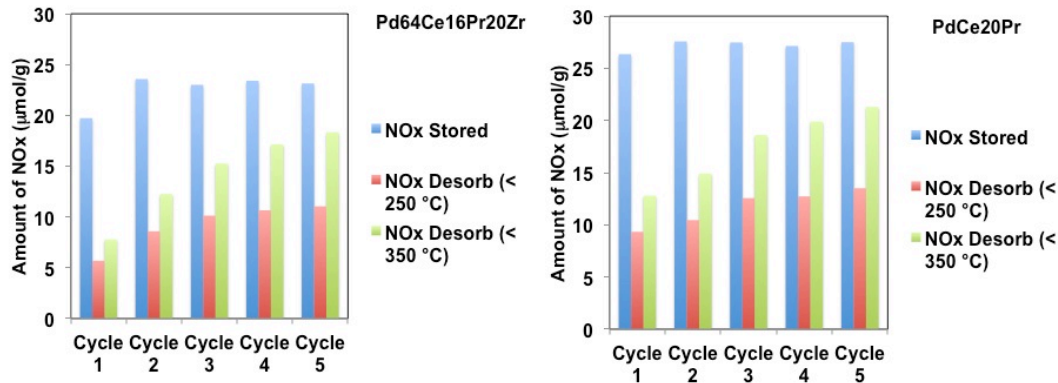


Figure 6.11. Comparison of NO_x storage and desorption with each cycle for Pd64Ce16Pr20Zr and PdCe20Pr.

6.3.5. Effect of Zr on Content Aging.

Aside from continued use, catalysts in aftertreatment systems need to be able to withstand high temperatures. Ford researchers found that exhaust temperatures can be as high as 800 °C during a DOC clean up [27]. Therefore, Pd64Ce16Pr20Zr was aged at 750 °C for 16 hours under lean conditions (5% O₂, 5% CO₂, 3.5% H₂O with He balance) and compared to PdCe20Pr after aging to gauge the effect of Zr doping on catalyst ability to withstand high temperatures. After aging, catalysts were cooled to room temperature and NO_x stored at 120 °C for 5 minutes followed by TPD. Figure 6.12 displays the NSE comparison of PdCe20Pr and Pd64C16P20Z before and after aging. It is evident that NO_x storage is severely hindered by aging for both catalysts. However, Pd64Ce16Pr20Zr stores almost 10% more NO_x after aging than PdCe20Pr (at all storage times), thus suggesting that the addition of Zr improves the catalyst's ability to withstand deactivation at high temperatures. NO_x desorption after aging significantly increases below 350 °C in both cases (see Figure 6.13). Overall, Pd64Ce16Pr20Zr maintains better storage after aging than PdCe20Pr, while the NDE below 350 °C is similar for the two aged catalysts. Cumulatively Pd64Ce16Pr20Zr releases more NO_x than PdCe20Pr after aging (Figure 6.14). This is consistent with the fact that Zr stabilizes the lattice, as confirmed by the lower decrease in surface area after aging for Pd64Ce16Pr20Zr. Indeed, Pd64Ce16Pr20Zr lost roughly half of its surface area after aging, while PdCe20Pr lost more than 3 times its original surface area (summarized in Table 6.1).

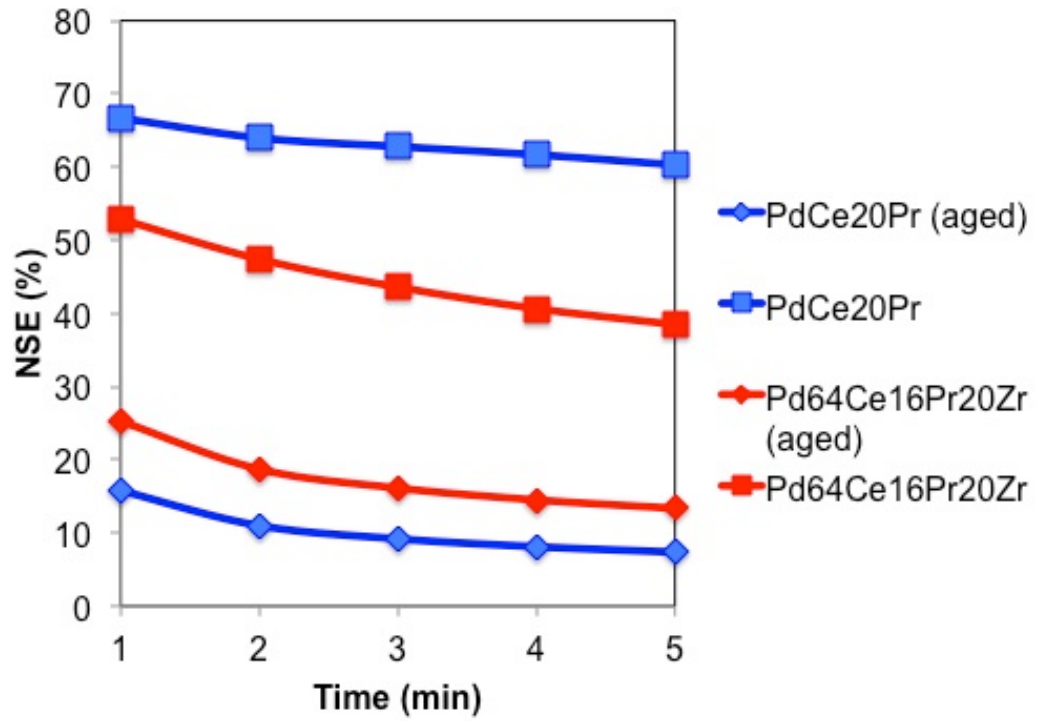


Figure 6.12. NSE comparison of PdCe20Pr and Pd64Ce16Pr20Zr after aging for 16 hours under lean conditions (5% CO₂, 5% O₂, and 3.5% H₂O with He balance).

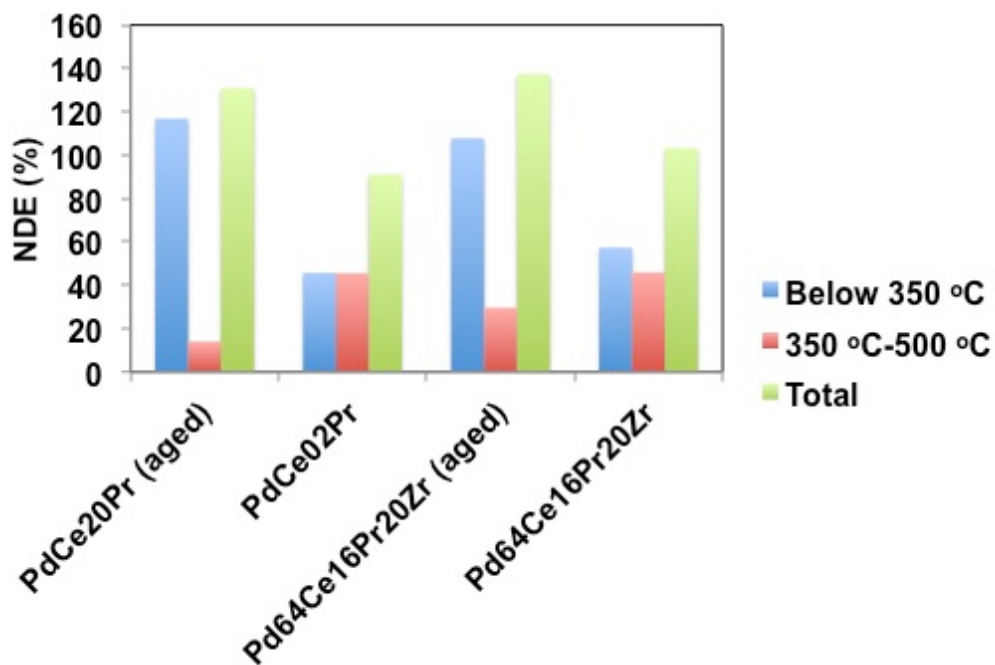


Figure 6.13. Comparison of NDE for PdCe20Pr and Pd64Ce16Pr20Zr after aging for 16 hours.

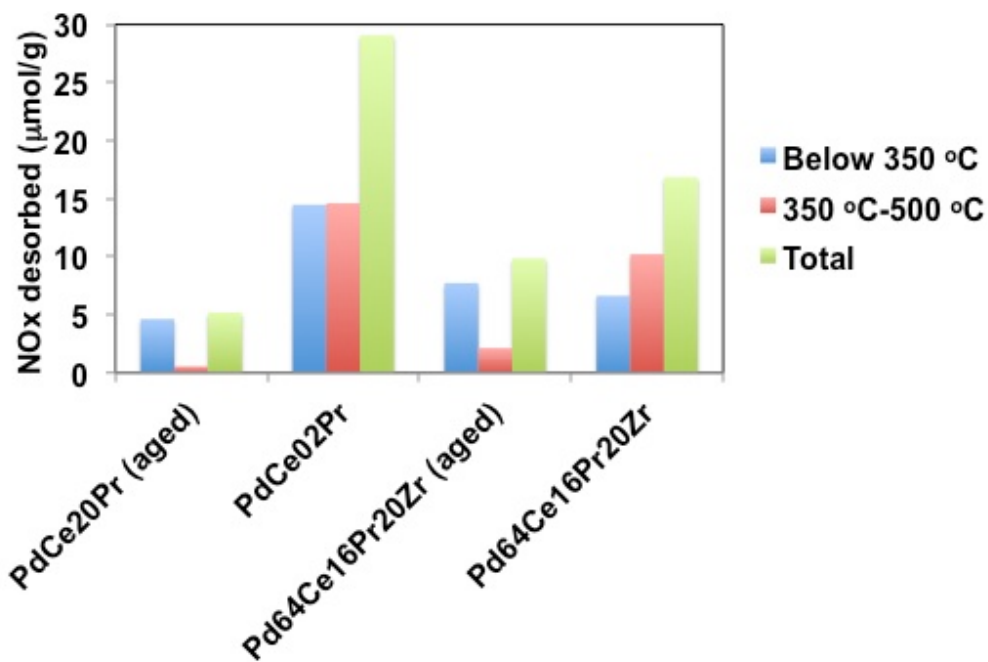


Figure 6.14. Cumulative NO_x release of fresh and aged PdCe20Pr and Pd64Ce16Pr20Zr.

6.3.6. Affects of CO₂ and H₂O on NSE and NDE.

It has been previously reported that CO₂ and water competitively adsorb with NO_x on CeO₂ [29]. Therefore, the effects of CO₂ and water on NO_x storage were evaluated for fresh Pd64Ce16Pr20Zr and PdCe20Pr (Figure 6.15). The same conditions were used for NO_x storage as previously described in section 6.2.3 without CO₂ and water in the feed. In the previous chapter it was reported that the addition of Pr to PdCe improved ceria's ability to withstand deactivation by water and CO₂. Comparing PdCe20Pr and Pd64Ce16Pr20Zr without water and carbon dioxide present, it was found that unlike PdCe20Pr, Pd64Ce16Pr20Zr exhibited a much higher NSE. For both catalysts, NDE for NO storage without water and CO₂ in the feed was significantly lower below 350 °C than that observed in the presence of CO₂ and water (Figure 6.16). This further confirms that water and CO₂ can adsorb on strong adsorption sites in the catalysts.

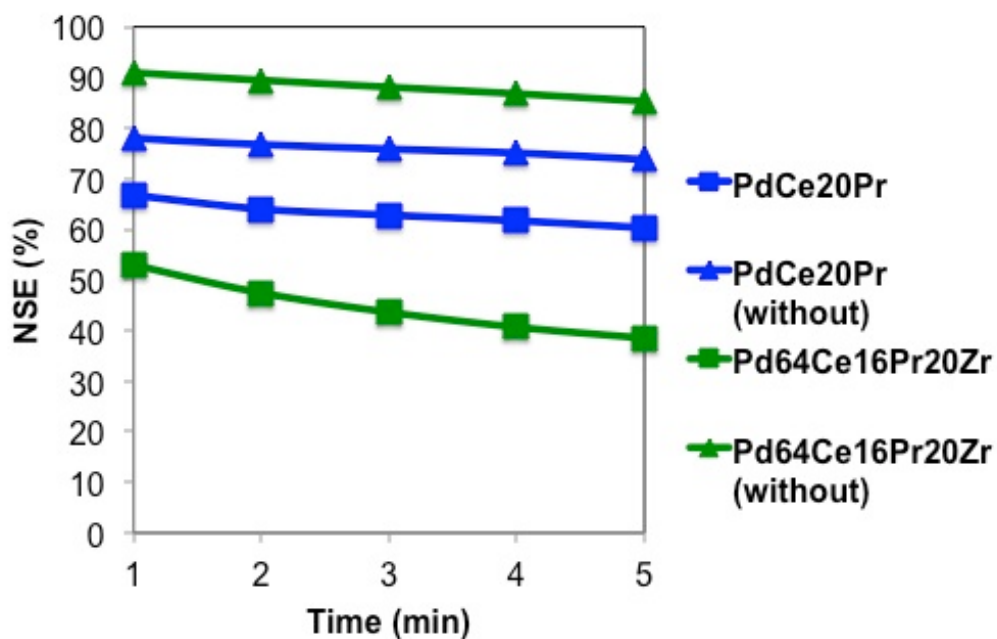


Figure 6.15. Comparison of NSE for PdCe20Pr and Pd64Ce16Pr20Zr measured with and without CO₂ and water in the feed.

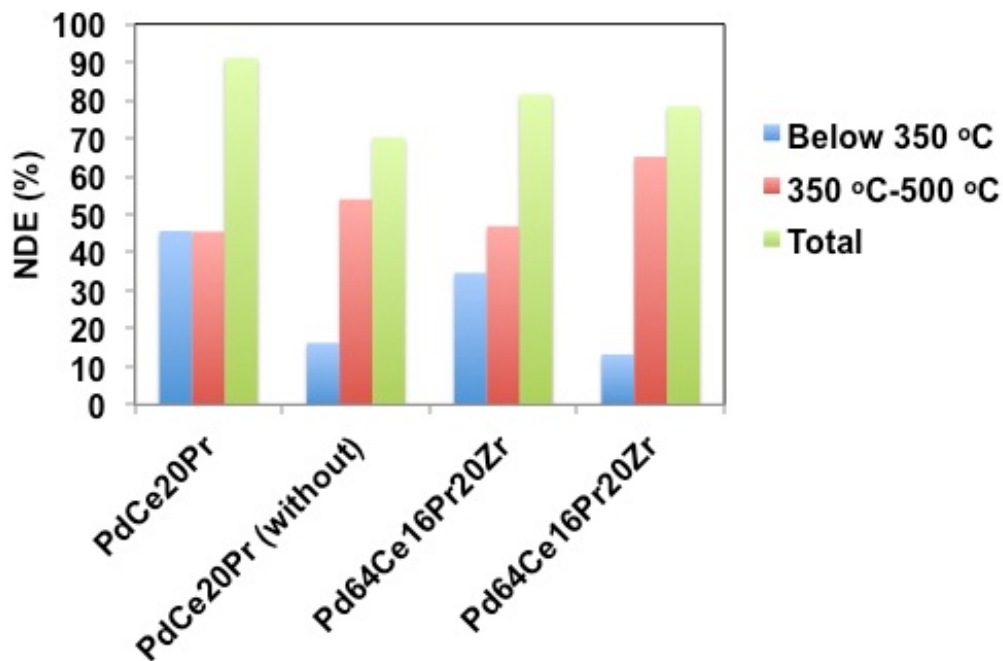


Figure 6.16. Comparison of NDE for PdCe20Pr and Pd64Ce16Pr20Zr with and without CO₂ and water in the feed.

6.3.7. DRIFTS Studies.

6.3.7.1. NO/O₂ Storage and Desorption.

The above indicates that Pd64Ce16Pr20Zr yields the best NSE at low temperatures, although lower than PdCe20Pr. To understand which NO_x species are present during adsorption and desorption, DRIFT spectra for Pd64Ce16Pr20Zr were obtained for NO/O₂ storage at 100 °C for 30 minutes, Figure 6.17. After 30 seconds of NO_x storage a strong chelating nitrite band [29-31] and nitrito nitrite band [48] are observed at 1174 cm⁻¹ and 1424 cm⁻¹ respectively. Little to no nitrates are detected after 30 seconds of storage. In contrast, PdCe20Pr displays a weak band associated with molecularly adsorbed NO₂ at 1637 cm⁻¹ that is absent in Pd64Ce16Pr20Zr (previously discussed in Chapter 5). Several nitrate bands appear after two minutes at 1609, 1565, 1252, and 1018 cm⁻¹ [29-31, 49-50]. The nitrate band at 1609 cm⁻¹ was absent in storage spectra for PdCe20Pr. NO_x storage on Pd (~1747 cm⁻¹) was not observed for Pd64Ce16Pr20Zr as for PdCe20Pr. All bands continue to grow in intensity as time advances.

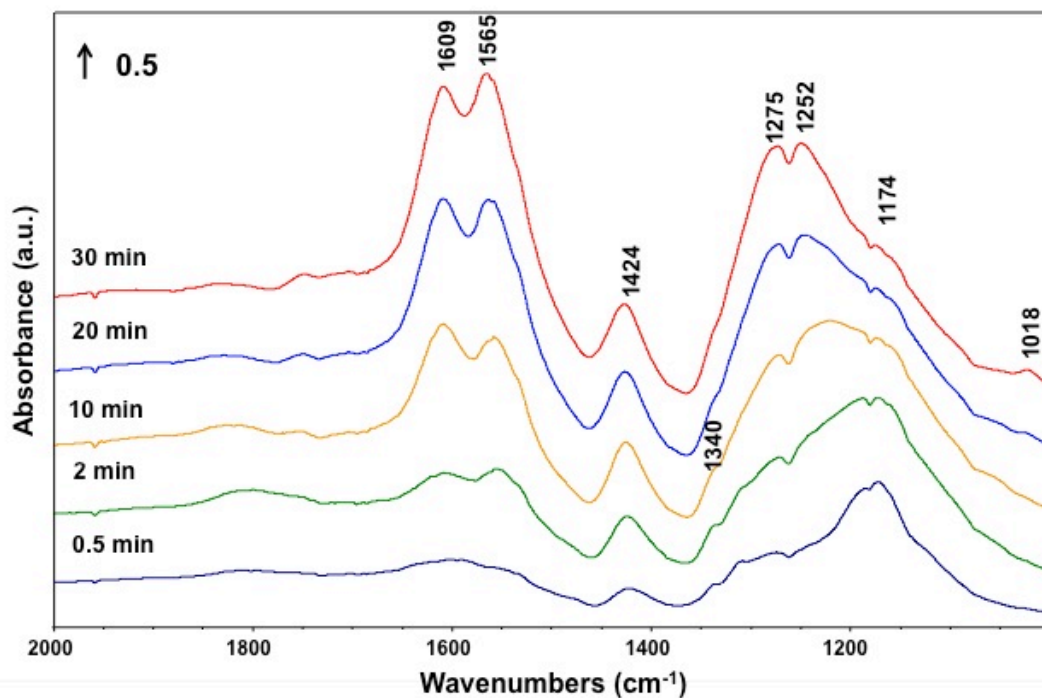


Figure 6.17. DRIFT spectra acquired during NO storage at 100 °C for Pd₆₄Ce₁₆Pr₂₀Zr.
Feed: 300 ppm NO, 5% O₂, Ar balance.

DRIFT spectra obtained during TPD for Pd₆₄Ce₁₆Pr₂₀Zr are shown in Figure 6.18. Like PdCe₂₀Pr, the chelating nitrite band at 1164 cm⁻¹ disappears by 300 °C. The nitrito nitrite band at 1421 cm⁻¹ decreases in intensity with ramping of the temperature to 500 °C. Nitrate bands at 1032 and 1009 cm⁻¹ reach a maximum intensity at 300 °C and begin to diminish above 300 °C. While nitrites disappear by 500 °C, nitrates remain at 1611, 1556, 1535, 1266, 1243, and 1009 cm⁻¹. Desorption behavior of Pd₆₄Ce₁₆Pr₂₀Zr is very similar to that observed for PdCe₂₀Pr, only adsorption spectra display significant differences.

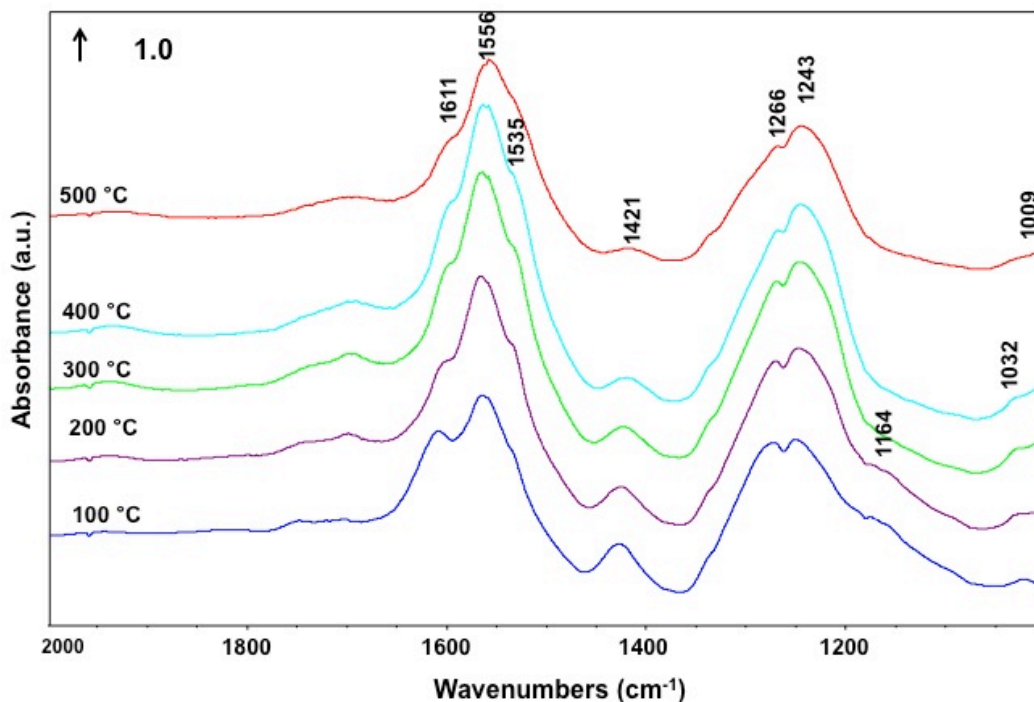


Figure 6.18. DRIFT spectra acquired during TPD after NO storage at 100 °C for Pd64Ce16Pr20Zr. Feed: 300 ppm NO, 5% O₂, Ar balance.

6.4. Conclusions.

NO_x storage was not benefited by the addition of Zr compared to previously studied binary systems (in the fresh state). Increasing CeO₂ content in the ternary systems was found to increase high temperature NO_x desorption due to increased oxygen mobility with increased CeO₂ concentration. Additionally, the reduction of PdO at room temperature for Pd64Ce16Pr20Zr and increased NO_x desorption above 350 °C further confirm that increased CeO₂ content of the ternary mixed oxides increases oxygen mobility. Pr-Zr supports had low NSE, but the low NSE was partially compensated by greatly increased NO_x release below 350 °C. Equal concentrations of Pr and CeO₂ in the Ce-Pr-Zr system resulted in nearly the lowest NSE amongst all supports evaluated, thus indicating that the optimal Ce/Pr mole ratio is 4. Pd64Ce16Pr20Zr was found to be the best catalyst among those provided by MEL chemicals. Although NSE was lower than that observed for PdCe20Pr, the addition of Zr increased catalysts ability to withstand

high temperatures as observed when tested after hydrothermal aging at 750 °C for 16 hours under lean conditions. As previously observed, a large portion of stored NO_x on aged catalysts was released below 350 °C. With increased stability after hydrothermal aging and enhanced low temperature desorption below 350 °C, Pd₆₄Ce₁₆Pr₂₀Zr proved to be the most promising catalyst evaluated for PNA applications.

Chapter 7. Significant Findings and Recommendations.

The primary goal of this dissertation was to evaluate and improve ceria-based catalysts for low temperature NO_x storage to mitigate cold start NO_x slip. The drive for research focused on reducing NO_x emissions during cold starts for diesel engines is due to evolving and more stringent emission regulations set forth in the United States by the EPA. A second objective was to study structural changes in aged LNT and SCR catalysts using electron microscopy. The methodology for achieving these goals was as follows:

- Investigation of morphology changes between fresh and aged LNT and SCR catalysts after simulated road aging utilizing TEM, STEM, and EDS.
- Study of model ceria catalysts for NO_x storage and desorption behavior at selected storage temperatures (80 °C, 120 °C, and 160 °C) for 5 minutes.
- Evaluation of the role of Pt and Pd in NO_x storage and desorption behavior as well as the role of ceria dopants in both the fresh and aged state.
- Study of NO_x storage and desorption mechanisms of PNA catalysts utilizing DRIFTS.

7.1. Significant Findings.

7.1.1. Electron Microscopy of LNT and SCR Catalysts.

- Simulated road aging led to the accumulation of sulfur on Pt in the LNT catalyst as well as sintering of Pt particles.
- Aging of Cu-CHA SCR catalyst led to the migration of Cu²⁺ (originally present on the ion exchange sites in the zeolite) to the surface to form CuO nanoparticles.
- Zr-rich areas observed in both the fresh and aged SCR catalyst did not display structural changes after aging.

7.1.2. NO_x Storage and Desorption Behavior of Model Ceria Catalysts.

- Promotion with Pt increased NO_x storage, however, the majority of NO_x is released at temperatures above 350 °C making it harder to regenerate the catalyst during normal operation.

- Promotion with Pd decreased NO_x storage, however, the loss of storage with the use of Pd is to some degree compensated by the increase in low temperature (< 350 °C) NO_x release.
- Evaluation of NO_x storage at three temperatures revealed that increasing storage temperature increased NO_x storage. For NO_x stored at 80 and 120 °C, Pd/CeO₂ gave higher low temperature NO_x desorption in absolute terms compared to Pt/CeO₂.
- Adsorption-desorption cycling studies revealed that NSE stabilized after the third cycle and NDE continued to increase below 350 °C with continued cycling. This indicates that with each cycle weak storage sites are increasingly used for which NO_x readily desorbs.
- DRIFT spectra indicate that NO_x is preferentially stored as thermally stable nitrates for platinum-promoted materials while palladium promotes NO_x storage as thermally labile nitrites. Platinum, being a better oxidation catalyst than palladium, tends to store NO_x as nitrates.

7.1.3. Effects of NO_x Storage Behavior upon Doping CeO₂ with Rare Earth Oxides.

- Doping ceria with Pr generates oxygen vacancies as well as surface oxygen species according to Raman analysis.
- Doping with Pr, Sm, and Nd benefited NSE compared to undoped CeO₂, while doping with Y, and La did not.
- Pr proved to be the most promising dopant for increased NO_x storage at low temperatures as indicated by the superior NSE obtained. This is attributed to the fact that Pr⁴⁺ reducing more easily than Ce⁴⁺ as indicated by XPS data.
- Doping with Pr increased NO_x release below 350 °C (making it easier to regenerate the catalyst).
- Pt- and Pd-promoted Ce₂₀Pr were found to have a lower change in NSE when NO_x is stored in the presence and absence of CO₂ and H₂O compared to model catalysts described in Chapter 4. Thus doping CeO₂ with Pr makes the support more resilient to the effects of CO₂ and H₂O, which has been shown to competitively adsorb on CeO₂ with NO_x.

- Overall, doping with Pr was found to be promising due to increased NSE at low temperatures, ease of catalyst regeneration, and resistance to deactivation in the presence of water and CO₂.

7.1.4. Doping Ce-Pr mixed oxides with ZrO₂.

- Zirconia-rich supports had lower NSE compared to ceria-rich supports.
- Binary systems, Pr-Zr, exhibit lower NSE than the ternary systems, Ce-Pr-Zr, indicating that CeO₂ is necessary to achieve high NSE at low temperatures.
- Increasing CeO₂ content increased high temperature NO_x release due to increased NO oxidation activity with increasing CeO₂ content (i.e., oxygen mobility increases with CeO₂ content.)
- The addition of ZrO₂ benefited catalyst storage by stabilizing the support, with the consequence that Pd₆₄Ce₁₆Pr₂₀Zr showed a smaller decrease in NSE after aging compared to PdCe₂₀Pr.

7.2. Suggestions for Future Work.

Although the work presented here suggests ceria doped with praseodymium to be promising for PNA applications, more research is needed if this is to become a commercially viable technology. Ceria doped with 20% Pr was identified as the most promising material for PNA applications, however, after aging the catalyst displayed significantly lower NO_x storage activity than in the fresh state. Current diesel aftertreatment systems must be able to withstand high temperatures that may be experienced during a DPF clean up. Due to these high temperature demands on the catalyst, further development is needed to improve the stability of these materials without compromising NO_x storage and catalyst regeneration abilities.

In depth reactor studies are needed to understand catalyst activity after exposure to sulfur as well as hydrocarbons. Exposure to sulfur is inevitable in diesel aftertreatment systems, therefore it is imperative for PNA catalysts to withstand sulfur poisoning.

A reactor system with the ability to measure N_2O evolution during NO_x desorption would be beneficial, as N_2O has a larger contribution to the greenhouse effect than CO_2 . Hence, it is important to ensure that N_2O is not generated over the PNA during NO_x storage or desorption.

With regard to the study of NO_x storage and desorption mechanisms, the ability to acquire DRIFT spectra with water present in the feed gas would be beneficial for identifying the NO_x species present during NO_x storage and desorption under realistic conditions.

Lastly, studies of a PNA coupled to a urea-SCR catalyst, operating with feed gas from a diesel engine, would lend significant insight as to the performance of the PNA in a vehicle.

Appendix – List of Abbreviations.

A-DOC: advanced-diesel oxidation catalyst.

BET: Brunnauer-Emmett-Teller.

CAA: clean air act.

CO: carbon monoxide.

CZO: ceria-zirconia oxide.

dCSCTM: diesel Cold Start Catalyst.

DOC: diesel oxidation catalyst.

DPF: diesel particulate filter.

DRIFTS: diffuse reflectance infrared Fourier transform spectroscopy.

EPA: Environmental Protection Agency.

FTP-75: federal test procedure mimicking urban driving.

GHSV: gas hourly space velocity.

GM: General Motors.

GVWR: gross vehicle weight ratio.

HC: hydrocarbon.

HC-SCR: selective catalytic reduction catalyst utilizing hydrocarbons as the reductant.

HNO₃: nitric acid.

HT: high temperature.

ICP: inductively coupled plasma.

LDV: light duty vehicle.

LNT: lean NO_x trap.

LT: low temperature.

LTNA: low temperature NO_x adsorber.

MS: mass spectrometry.

N₂: nitrogen gas.

NDE: NO_x desorption efficiency.

N₂O: nitrous oxide.

NH₃-SCR: selective catalytic reduction of NO_x with ammonia reductants.

NMOG: non-methane organic gases.

NO_x: nitrogen oxides (NO and NO₂).

NSE: NO_x storage efficiency.

NTP-TSW: Non-thermal plasma-temperature swing adsorption.

N-TWC: NO_x-trap three way catalyst.

O₃: atmospheric gas ozone.

PBA: platinum promoted barium-alumina.

PBAC: platinum promoted barium-alumina-ceria.

PdACeBPrCZr: palladium promoted ceria-zirconia-praseodymium with A being the mol % of Ce, B the mol % of Pr, and C the mol % of Zr present.

PdCe[X]M: palladium promoted ceria doped with [X] quantity (X = 5, 10, or 20 mol.%) of dopant M (M=La, Y, Sm, Nd, or Pr).

PGMs: platinum group metals (Ru, Rh, Pd, Os, Ir, Pt).

PM: particulate matter.

PNA: passive NO_x adsorber.

PtCe[X]M: platinum promoted ceria doped with [X] quantity (X = 5, 10, or 20 mol.%) of dopant M (M=La, Y, Sm, Nd, or Pr).

SC03: supplemental federal test procedure mimicking urban driving with the use of air conditioning.

SCR: selective catalytic reduction.

TCD: thermal conductivity detector.

TPD: temperature programmed desorption.

TPR: temperature programmed reduction.

TWC: three-way catalyst.

US06: supplemental federal test procedure simulating high speed driving.

VOC: volatile organic compounds.

XPS: X-ray photoelectron spectroscopy.

XRF: X-ray fluorescence.

Appendix A.2. Supplemental Figures and Graphs.

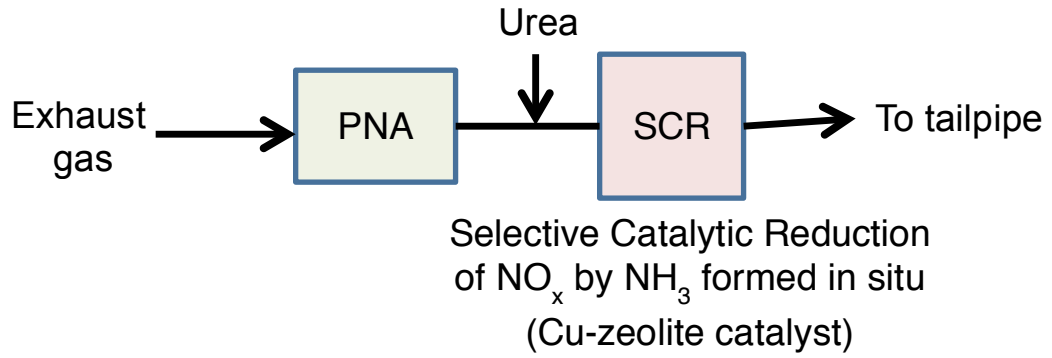


Figure A.2.1. NO_x emissions are stored on the PNA until the downstream SCR catalyst has reached operational temperatures ($>180^\circ\text{C}$).

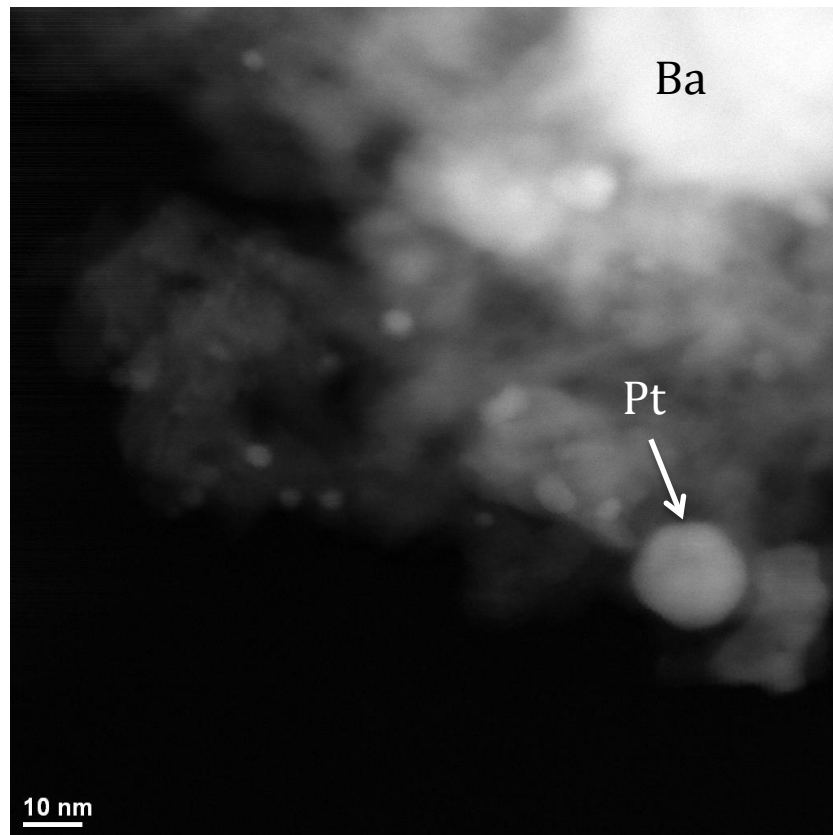


Figure A.2.2. STEM image of aged LNT catalyst displaying Pt particle with a size of 27 nm.

Catalyst Preparation

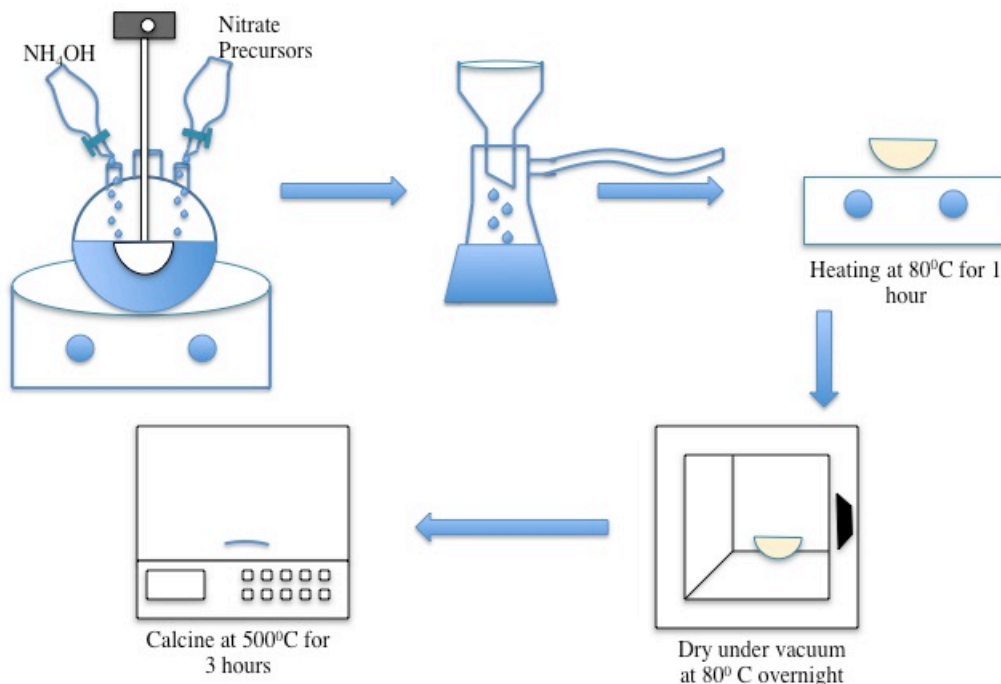


Figure A.2.3. Co-precipitation procedure utilized to make $\text{CeO}_2\text{-M}_2\text{O}_3$ supports. Nitrate precursors were combined with Ammonium hydroxide (NH_4OH) and allowed to stir over night to precipitate. Followed by vacuum filtration and heating of the catalyst in air for 1 hour at 80°C after which the catalyst is placed in a vacuum oven to completely drive over night at 80°C . Once the catalyst is completely dry it is calcined in a muffle furnace at 500°C for 3 hours to remove nitrates.

Table A.2.1. BET surface area (SA) of catalyst supports prepared at the University of Kentucky Center for Applied Energy Research and support diameters as determined by x-ray diffraction.

Support	BET SA (m^2/g)	Support diameter (nm)
CeO_2	76.6	13.2
Ce5Pr	66.5	11.7

Ce20Pr	83.7	10.1
Ce5La	59.2	11.7
Ce20La	66.5	11.7
Ce5Y	67.8	11.9
Ce20Y	64.2	11.7
Ce5Sm	61.7	13.2
Ce20Sm	54.9	11.4
Ce5Nd	61.2	13.9
Ce20Nd	80.9	8.9

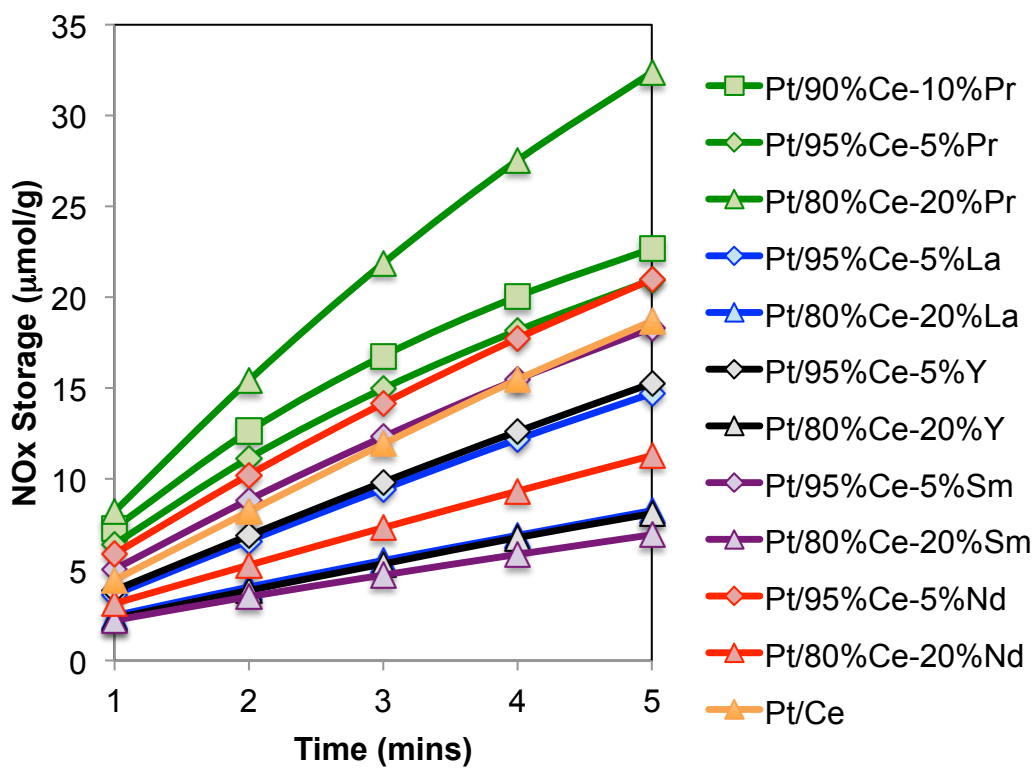


Figure A.2.4. Total amount of NO_x released (mmol) per gram of catalysts follows the same trend as NSE data for PtCeXM. Increasing Pr content increases NO_x storage, but decreases storage when increasing the content of Y, La, Nd, and Sm.

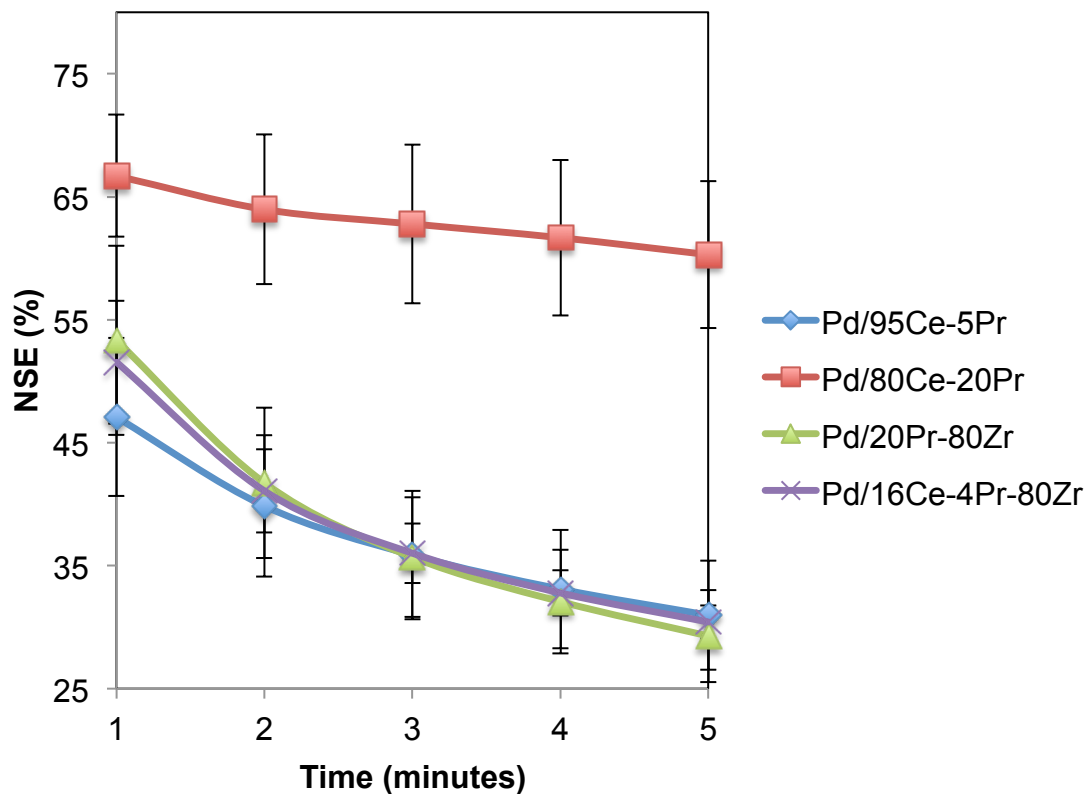


Figure A.2.5. NSE at 120 °C for 5 minutes were performed in triplicates for catalysts that had initial NDE greater than 100%. Percent error was found to be largest for Pd/20Pr-80Zr at 1 minute with a percent error of 7.70% and smallest for Pd/16Ce-4Pr-80Zr at one minute with a percent error of 5.00%.

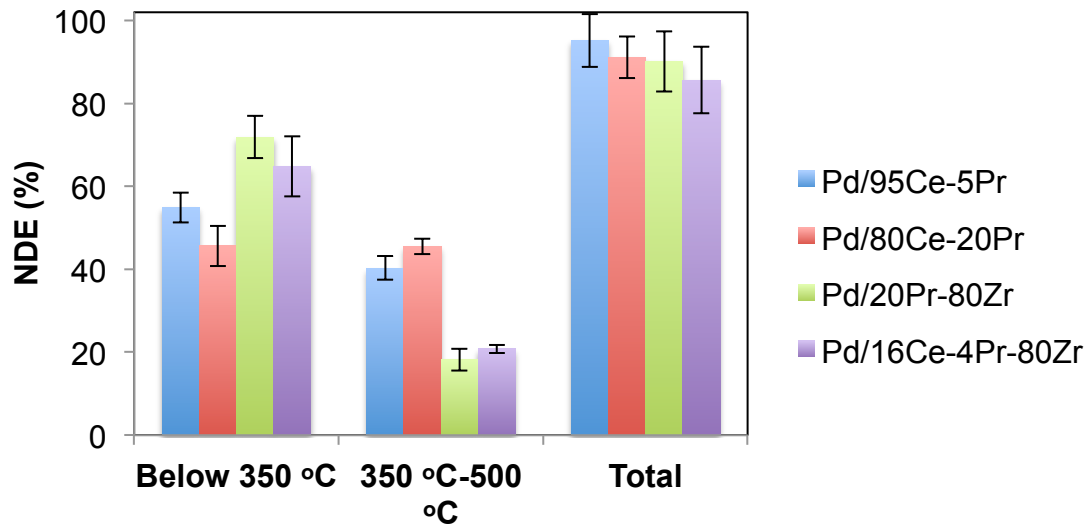


Figure A.2.6. NDE of storage performed in triplicates at 120 °C for 5 minutes indicated that Pd/16Ce-4Pr-80Ze had the largest total NDE percent error of 8.07% and Pd/80Ce-20Pr had the smallest total NDE percent error of 5.00%.

Nitrite Storage

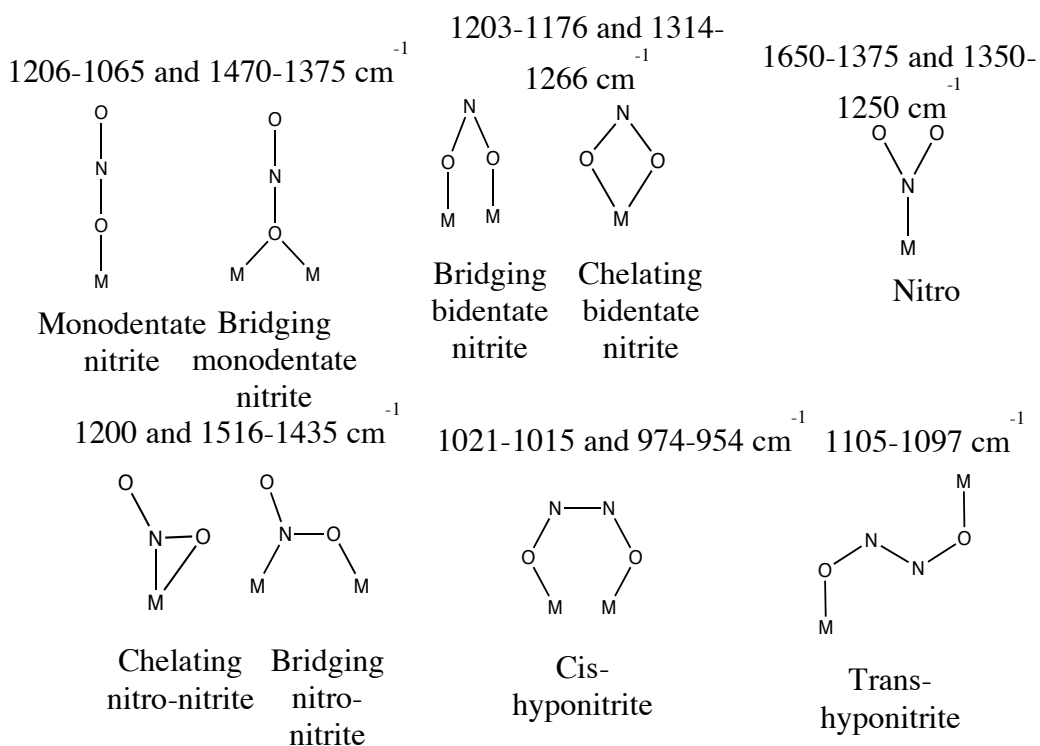


Figure A.2.7. Nitrite species that may appear on the catalyst surface during NO_x storage and the band ranges.

Nitrate Storage

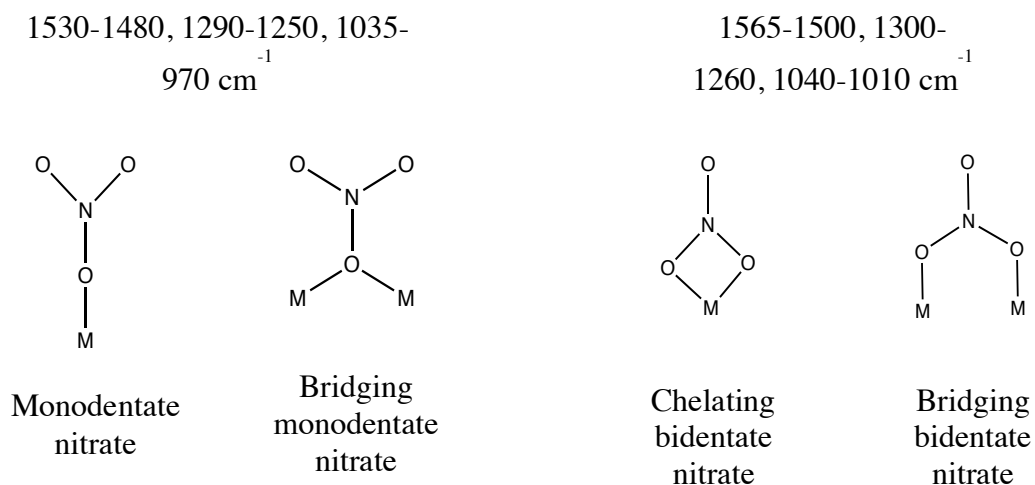


Figure A.2.8. Nitrate species that may appear on the catalyst surface during NO_x storage and the band ranges.

BIBLIOGRAPHY

Chapter 1

- [1] "Air Quality Management In The United States." National Academic Press: Washington, D.C., 2004, p. 133-173.
- [2] Easterling, Vencon G., "The Effects of Ceria Addition on Aging and Sulfation of Lean NO_x Traps for Stand Alone and LNT-SCR Applications" (2013). Thesis and Dissertations--Chemical and Materials Engineering. Paper 17. http://uknowledge.uky.edu/cme_etds/17
- [3] Delmas, R., Serca, D., Jambert, C. Nutrient Cycling in Agroecosystems. 1997, 48, 51-60.
- [4] Nitrogen Oxide Emissions. [https://www.colorado.gov/pacific/sites/default/files/AP_PO_NOx-Emissions-Fact-Sheet%20\(1\).pdf](https://www.colorado.gov/pacific/sites/default/files/AP_PO_NOx-Emissions-Fact-Sheet%20(1).pdf) (accessed March 22, 2016).
- [5] Nitrogen Oxides. <http://people.oregonstate.edu/~muirp/whatisit.htm> (accessed March 17, 2016).
- [6] The Plain English Guide to The Clean Air Act; EPA-456/K-07-001; Environmental Protection Agency: Research Triangle Park, NC, 2007.
- [7] Klein, C. The Killer Fog That Blanketed London, 60 Years Ago. <http://www.history.com/news/the-killer-fog-that-blanketed-london-60-years-ago> (accessed March 17, 2016).
- [8] Hopey, D., Templeton, D. In 1948, Smog Left Deadly Legacy in Donora. <http://www.post-gazette.com/news/health/2010/12/12/In-1948-smog-left-deadly-legacy-in-Donora/stories/201012120248> (accessed April 13, 2016).
- [9] Rani, B., Singh, U., Chuhan, A.K., Sharma, D., Maheshwari, R. Photochemical Smog Pollution and Its Mitigation Measures. J. Adv. Scient. Res., 2011, 2, 28-33.
- [10] Environmental Pollution Control-Nitrogen Oxides Reduction. http://www.sp.edu.sg/greenpage/Green_Projects/gproject_cls5.html (accessed March 17, 2016).
- [11] Learning About Acid Rain. EPA 430-F-08-002; Environmental Protection Agency: Washington, D.C., 2008.
- [12] pH: Water Properties. <http://water.usgs.gov/edu/ph.html> (accessed March 23, 2016).
- [13] Casiday, R., Frey, R. Acid Rain: Inorganic Reactions Experiment. Department of Chemistry, Washington University, St. Louis, MO.
- [14] Nitrous Oxide Emissions. <https://www3.epa.gov/climatechange/ghgemissions/gases/n2o.html> (accessed March 17, 2016).
- [15] IPCC. 2013. Climate Change 2013: The Physical Science Basis. Contribution of Working Group I to the Fifth Assessment Report of the Intergovernmental Panel on Climate Change [Stocker, T.F., Qin, D., Plattner, G.-K., Tignor, M., Allen, S.K., Boschung, J., Nauels, A., Xia, T., Bex, V., Midgley, P.M. (eds.)]. Cambridge University Press, Cambridge, United Kingdom and New York, NY, USA. http://www.climatechange2013.org/images/report/WG1AR5_TS_FINAL.pdf
- [16] Greenhouse Gases. <https://www3.epa.gov/climatechange/kids/basics/today/greenhouse-gases.html> (accessed March 17, 2016).

- [17] Overview of Greenhouse Gases.
<https://www3.epa.gov/climatechange/ghgemissions/gases/n2o.html> (accessed March 17, 2016).
- [18] Gerard, D., Lave, L.B. *Tech. Fore. Soc. Change.* 2005, 72, 761-778.
- [19] Cornell University Law School. <http://www.law.cornell.edu/uscode/text/42/7521> (accessed June 25, 2013).
- [20] Samuel, S., Austin, L., Morrey, D. J. *Automobile Engineering.* 2002, 216, 555-564.
- [21] Emission Test Cycles: FTP-75.
<https://www.dieselnet.com/standards/cycles/ftp75.php> (accessed on March 17, 2016).
- [22] STFP-US06. https://www.dieselnet.com/standards/cycles/ftp_us06.php (accessed March 17, 2016).
- [23] Emission Test Cycles: SFTP-SC03.
https://www.dieselnet.com/standards/cycles/ftp_sc03.php (accessed March 17, 2016).
- [24] Faiz, A., Weaver, C. S., Walsh, M. P. *Air Pollution From Motor Vehicles: Standards and Technologies for Controlling Emissions*, The World Bank: Washington, D.C., 1996, p 1-24.
- [25] Bertelsen, B.I. *Top. Catal.* 2001, 16, 15-22.
- [26] Cars and Light-Duty Trucks-Tier 2.
https://www.dieselnet.com/standards/us/ld_t2.php (accessed March 17, 2016).
- [27] Cars and Light-Duty Trucks-Tier 3.
https://www.dieselnet.com/standards/us/ld_t3.php (accessed March 17, 2016).
- [28] Worcester Polytechnic Institute. <http://www.wpi.edu/about/history/catalytic.html> (accessed June 25, 2013).
- [29] Harold, M.P. *Current Opinion in Chemical Engineering.* 2012, 1, 303-311.
- [30] Gulati, S.T. In *Structured Catalysts and Reactors*; Cybulski, A.; Moulijn, J.A., Eds.; CRC Press: Boca Raton, 2006; pp. 21-70.
- [31] Twigg, M.V. *Appl. Catal B: Env.* 2007, 70, 2-15.
- [32] Gulati, S. and Reddy, K. SAE Technical Paper 930165, 1993, doi:10.4271/930165.
- [33] Bagley, A.D. U.S. Patent 3,905,743, September 16, 1975.
- [34] Harold, M.P. *Current Opinion in Chemical Engineering.* 2012, 1, 303-311.
- [35] Heck, R.M., Farrauto, R.J., Gulati, S. *Catalytic Air Pollution Control: Commercial Technology*, 2nd ed., John Wiley & Sons, Inc.:New york, 2002, p 186-262.
- [36] Russell, A., Epling, W.S. *Catal. Review.* 2011, 53, 337-423.
- [37] Konstandopoulos, A.G., Kostoglou, M., Skaperdas, E., Papioannou, E., Zarvalis, D., Kiadopoulou, E. (2000) SAE 2000-01-1016.
- [38] Zhang, L.; Pierce, J.; Leung, V.; Wang, D.; Epling, W.S. *J. Phys. Chem.* 2013, 117, 8282-8289.
- [39] Sivachandiran, L.; Thevent, F.; Gravejat, P.; Rousseau, A. *Appl. Catal. B: Env.* 2013, 142-143, 196-204.
- [40] Takahashi, N.; Shinjoh, H.; Suzuki, T. *Catal. Today.* 1996, 27, 63-69.
- [41] Kabin, K.S.; Muncrief, R.L.; Harold, M.P. *Catal. Today.* 2004, 96, 79-89.
- [42] Epling, W.S.; Campbell, L.E.; Yezerets, A.; Currier, N.W.; Parks, J.E. *Catalysis Reviews*, 2004, 46, 163-245.

- [43] Cohn, G., Steele, D., Anderson, H. Nitric Acid Tail Gas Abatement, U.S. Patent 2,975,025 (1961).
- [44] Heck, R. M., Farrauto, R. J., Gulati, S. T. Catalytic Air Pollution Control: Commercial Technology, John Wiley & Sons, Inc: New York, 2002, p 306-333.
- [45] Heck, R., Bonacci, J., Chen, J. "Catalytic air pollution controls—comercial development of selective catalytic reduction of NO_x," paper 87-523, 80th Annual Meeting of APCA (June 21-26, 1987), New York.
- [46] Bosch, H., Janssen, K. "Catalytic reduction of nitric oxides—a review of the fundamentals and technology," Catal. Today. 1998, 2, 369-521.
- [47] Heck, R., Chen, J., Speronello, B., Morris, L. "Family of versatile catalyst technologies for NO_x removal in power plant applications," ACS Symp. Series. 1994, 552, 215-223.
- [48] Byrne, J., Chen, J., Speronello, B. "Selective catalytic reduction of NO_x using zeolites for high temperature applications," Catal. Today. 1992, 13, 33-42.
- [49] Lambert, C.; Cavataio, G.; Cheng, Y.; Dodson, D.; Girard, J.; Laing, P.; Patterson, J.; Williams, S.; Urea SCR and DPF System for Tier 2 Diesel Light-Duty Trucks. In Diesel Engine-Efficiency and Emissions Research, Detroit, MI, August 20-24, 2006.
- [50] Diesel Net. <http://www.dieselnet.com/standards/cycles/ftp75.php> (accessed January 23, 2014).
- [51] Diesel Net. http://www.dieselnet.com/standards/us/ld_t2.php (accessed Jan 22, 2014).
- [52] Environmental Protection Agency. Control of Air Pollution From Motor Vehicles: Tier 3 Motor Vehicle Emission and Fuel Standards; Proposed Rule. Fed. Regist. 2013, 78, 29816-30191.
- [53] EPA Proposes Tier 3 Tailpipe and Evaporative Emission Vehicle Fuel Standards; EPA-420-F-13-018A; United States Department of Environmental Protective Services, Office of Transportation and Air Quality, U.S. Government Printing Office: Washington, DC, 2013.

Chapter 2

- [1] Guo, G., Dodson, D., Warner, J., Ruona, W., Lambert, C. SAE 2012-01-0371.
- [2] Majewski, W.A. SCR Systems for Mobile Engines. https://www.dieselnet.com/tech/cat_scr_mobile.php (accessed May 6, 2016).
- [3] Cole, J.A., Energy and Environmental Research Corporation. U.S. Patent 5,800,793, September 1, 1998.
- [4] Jarvis, M., Adams, K.M., Ford Global Technologies. U.S. Patent 6,182,443, February 6, 2001.
- [5] Gonze, E.V., Paratore, M.J., Bedford, J.C. GM Global Technology Operations. US Patent Application 2012/0117947, November 15, 2010.
- [6] Melville, J.E., Brisley, E.J., Keane, O., Phillips, P.R., Mountstevens, E.H. US Patent 8,105,559, 2012.
- [7] Chen, H.Y., Shadab, M., Weigert, E., Camm, K., Ballinger, T., Cox, J., Blakeman, P. SAE Paper No. 2013-01-0535.
- [8] Henry, C., Langenderfer, D., Yezerets, A., Ruth, M., Chen, H.Y., Hess, H., Naseri, M. Passive Catalytic Approach to Low Temperature NO_x Emission Abatement. In Diesel Engine-Efficiency and Emissions Research, Detroit, MI, October 3-6, 2011.

- [9] Skorodumova, N.V., Simak, S.I., Lundqvist, B.I., Abrikosov, I.A., Johansson, B. *Phys. Rev. Lett.* 2002, 89, 166601-1-166601-4.
- [10] Mamontov, E., Egami, T. *J. Phys. Chem.* 2000, 104, 11110-11116.
- [11] Hartridge, A., Ghanashyam-Krishna, M., Bhattacharya, A.K. *J. Phys. Chem. Solids.* 1998, 59, 859-866.
- [12] Griffiths, T.R.; Hubbard, H.V.S.A.; Davies, M.J. *Inorg. Chim. Acta.* 1994, 225, 305-317.
- [13] Sanchez, M.G., Gazquez, J.L. *J. Catal.* 1987, 104, 120.
- [14] Cordatos, H., Gorte, R.J. *J. Catal.* 1996, 159, 112-118.
- [15] Shi, C.; Ji, Y.; Graham, U.M.; Jacobs, G.; Crocker, M.; Zhang, Z.; Wang, Y. *Toops, T.J. Appl. Catal. B.* 2012, 119-120, 183-196.
- [16] Piacentini, M.; Maciejewski, M.; Baiker, A. *Appl. Catal. B.* 2007, 72, 105-117.
- [17] Le Phuc, N.; Corbos, E.C.; Courtois, X.; Can, F.; Marecot, P., Duprez, D. *Appl. Catal. B.* 2009, 93, 12-21.
- [18] Lin, H.Y.; Wu, C.J.; Chen, Y.W.; Lee, C.H. *Ind. Eng. Chem. Res.* 2006, 45, 134-141.
- [19] Belliere-Baca, V.; Harle, V.; Pitois, C.; Rohart, E.; Allain, M. SAE Technical Paper No. 2007-01-1241.
- [20] Diwell, A.F.; Rajaram, R.R.; Shaw, H.A.; Truex, T.J. *Stud. Surf. Sci. Catal.* 1991, 71, 139-152.
- [21] Ji, Y.; Toops, T.J.; Crocker, M. *Catal. Lett.* 2009, 127, 55-62.
- [22] Easterling, V.; Ji, Y.; Crocker, M.; Ura, J.; Theis, J.R.; McCabe, R.W. *Catal. Today.* 2010, 151, 338-346.
- [23] Ji, Y.; Toops, T.J.; Graham, U.M.; Jacobs, G.; Crocker, M. *Catal. Lett.* 2006, 110, 29-37.
- [24] Ji, Y.; Toops, T.J.; Crocker, M. *Catal Lett.* 2007, 119, 257-264.
- [25] Ji, Y.; Choi, J.-S.; Toops, T.J.; Crocker, M.; Naseri, M. *Catal. Today.* 2008, 136, 146-155.
- [26] Rohart, E.; Belliere-Baca, V.; Yokota, K.; Harle, V.; Pitois, C. *Top. Catal.* 2007, 42-43, 71-75.
- [27] Yuvaraj, S., Fan-Yuan, L., Tsong-Huei, C., Chuin-Tih, Y. *J. Phys. Chem. B.* 2003, 107, 1044-1047.
- [28] Stem, K.H. *J. Phys. Chem. Ref. Data.* 1972, 1, 747-772.
- [29] Mu, J., Perlmutter, D.D. *Thermochimica Acta.* 1981, 56, 253-260.
- [30] Melnikov, R., Nascimento, V.A., Consolo, L.Z.Z., Silva, A.F. *J. Therm. Anal. Calorim.* 2013, 111, 115-119.
- [31] Arean, C.O., Andez-Colinas, J.M.F., Arjona, A.M., Villa-Garcia, M.A. *J. Chem. Tech. Biotech.* 1982, 32, 882-887.
- [32] Patil, K.C., Gosavi, R.K., Rao, C.N.R. *Inorganica. Chimica. Acta.* 1967, 1, 155-160.
- [33] Stern, K.H. "Thermal Decomposition of Inorganic Salts and Oxyanions." CRC Press: Boca Raton, FL, 2001, p 135-181.
- [34] Wang, X.; Chen, Z.; Wang, Y.; Wang, R. *ChemCatChem.* 2014, 6, 237-244.
- [35] Stakheev, A.Y., Mashkovsky, I.S., Bragina, G.O., Baeva, G.N., Telegina, N.S., Malmstrøm Larsen, K., Kustov, A.L., Thøgersen, J.R. *Top. Catal.* 2016, doi 10.1007/s11244-016-0571-5.

- [36] Giménez-Mañogil, J., Guillén-Hurtado, N., Fernández-García, S., Chen, X. W., Calvino-Gámez, J.J., García-García, A. *Top. Catal.* Doi. 10.1007/s11244-016-0591-1.
- [37] Huang, H.Y., Yang, R.T. *Langmuir.* 2001, 17, 4997-5003.
- [38] Yoshida, K., Kuwahara, T., Kuroki, T., Okubo, M. *J. Haz. Mat.* 2012, 231-232, 18-25.
- [39] Sun, X., Qu, R., Lei, Y., Bai, B., Chang, H., Peng, Y., Su, W., Zhang, C., Li, J. *Catal. Today.* 2015, 258, 556-563.
- [40] Cao, Y., Wei, C. *Asia-Pac. J. Chem. Eng.* 2016, doi:10.1002/apj.1967.
- [41] Theis, J.R., Lambert, C.K. *Catal. Today.* 2015, 258, 367-377.
- [42] Theis, J.R. *Catal. Today.* 2016, <http://dx.doi.org/10.1016/j.cattod.2016.01.032>.
- [43] Ji, Y., Bai, S., Crocker, M. *Appl. Catal. B.* 2015, 170-171, 283.
- [44] Millo, F., Vezza, D. SAE 2012-01-0373.
- [45] Tsukamoto, Y., Nishiok, H., Imai, D., Sobue, Y., Takagi, N. SAE 2012-01-0370.
- [46] Ren, A., Schmeig, S.J., Koch, C.K., Qi, G., Li, W. *Catal. Today* 2015, 258, 378-385.
- [47] Koch, C.K. (2013) U.S. Patent Application 2013/0294990.
- [48] Murata, Y., Morita, T., Wada, K., Ohno, H. SAE 2015-01-1002.
- [49] Luo, J.-Y.; Epling, W.S.; Qi, G.; Li, W. *Catal. Lett.* 2012, 142, 946-958.
- [50] Philipp, S.; Drochner, A.; Kunert, J.; Vogel, H.; Theis, J.; Lox, E.S. *Top. Catal.* 2004, 30/31, 235-238.
- [51] Symalla, M.O.; Drochner, A.; Vogel, H.; Philipp, S.; Gobel, U.; Muller, W. *Top. Catal.* 2007, 42-43, 199-202.
- [52] Yang, X., Yang, L., Ling, S., Zhou, R. *J. Haz. Mat.* 2015, 285, 182.
- [53] Auvray, X., Olsson, L. *Appl. Catal. B: Env.* 2015, 168-169, 342.
- [54] Ji Y, Toops, T.J., Pihl, J.A., Crocker, M. *Appl. Catal. B: Env.* 2009, 91, 329.
- [55] Levasseur A, Ebrahim AM, Bandosz TJ (2011) *Langmuir.* 2011, 27, 9379.
- [56] Atribak, I., Azambre, B., Bueno-López, A., García-García, A. *Appl. Catal. B: Env.* 2009, 92, 126.
- [57] Hernández-Giménez, A.M., dos Santos Xavier, L.P., Bueno-López, A. *Appl. Catal. A: Gen.* 2013, 462-463, 100.
- [58] Weiss, B.M., Iglesia, E. *J. Catal.* 2010, 272, 74.
- [59] Yu, J., Si, Z., Chen, L., Wu, X., Weng, D. *Appl. Catal. B: Env.* 2015, 163, 223.

Chapter 3

- [1] Wang, J.; Ji, Y.; He, Z.; Crocker, M.; Dearth, M.; McCabe, R.W. *Appl. Catal. B.* 2012, 111-112, 562-570.
- [2] Xu, L.; McCabe, R.; Tennison, P.; Jen, H.-W. SAE Technical Paper 2011-01-0308, 2011.
- [3] Wang, J.; Crocker, M. *Catal Lett.* 2012, 142, 1167-1174.
- [4] Slunder, C.S.; Storey, J.M.E.; Lewis, S.A.; Lewis, L.A. Low Temperature Urea Decomposition and SCR Performance; SAE Technical Paper 2005-01-1858; 2005.
- [5] Epling, W.S.; Campbell, L.E.; Yezerets, A.; Currier, N.W.; II Parks, J.E. *Catal. Rev.* 2004, 46, 163-245.
- [6] Kim, D.H.; Chin, Y.-H.; Muntean, G.G.; Yezeretz, A.; Currier, N.W.; Epling, W.S.; Chen, H.-Y.; Hess, H.; Pedem C.H.F. *Ind. Eng. Chem. Res.* 2006, 45, 8815-8821.

- [7] Ji, Y.; Fisk, C.; Easterling, V.; Graham, U.; Poole, A.; Crocker, M.; Choi, J.-S.; Partridge, W.; Wilson, K. *Catal. Today*. 2010, 151, 362-375.
- [8] Ji, Y.; Easterling, V.; Graham, U.; Fisk, C.; Crocker, M.; Choi, J.-S. *Appl. Catal. B*. 2011, 103, 413-427.
- [9] Fickel, D.W.; D'Addio, E.; Lauterbach, J.A.; Lobo, R.F.; *Appl. Catal. B*. 2011, 102, 441-448.
- [10] Kwak, J.H.; Tran, D.; Burton, S.D.; Szanyi, J.I Lee, J.H.; Peden, C.H.F. *J. Catal.* 2012, 287, 203-209.
- [11] Levasseur, B.; Ebrahim, A.M.; Bandosz, T.J. *Langmuir*. 2011, 27, 9379-9386.
- [12] Xu, L., McCabe, R., Ruona, W., Cavataio, G. SAE 2009-01-0285.
- [13] Ji, Y., Fisk, C., Easterling, V., Graham, U., Poole, A., Crocker, M., Choi, J.-S., Partridge, W., Wilson, K. *Catal. Today*. 2010, 151, 362.
- [14] Wang, J.; Ji, Y.; Jacobs, G.; Jones, S.; Kim, D.J.; Crocker, M. *App. Catal. B: Env.* 2014, 148-149, 51-61.
- [15] Schmeig, S.J.; Oh, S.H.; Kim, C.H.; Brown, D.B.; Lee, J.H.; Peden, C.H.F.; Kim, D.H. *Catal. Today*. 2012, 184, 252-261.

Chapter 4

- [1] Koebel M, Strutz EO (2003) *Ind Eng Chem Res* 42:2093.
- [2] Slunder CS, Storey JME, Lewis SA, SAE Technical Paper 2005-01-1858.
- [3] Fang HL, DaCosta HFM (2003) *Appl Catal B: Env* 46:17.
- [4] Lambert C. (Ford Motor Co.), personal communication.
- [4] Theis J, Lambert C (2015) *Catal Today* 258:367.
- [5] Jarvis M, Adams KM (2001) U.S. Patent 6,182,443.
- [6] Ji Y, Bai S, Crocker M (2015) *Appl Catal B: Env* 170-171:283.
- [7] Ren A, Schmiege SJ, Koch CK, Qi G, Li W (2015) *Catal Today* 258:378.
- [8] Koch CK, W (2013) U.S. Patent Application 2013/0294990.
- [9] Murata Y, Morita T, Wada K, Ohno H, SAE 2015-01-1002.
- [10] Skorodumova NV, Simak SI, Lundqvist BI, Abrikosov IA, Johansson B (2002) *Phys Rev Lett* 89:166601-1.
- [11] Mamontov E, Egami T, Brezny R, Koranne, M, Tyagi, S (2000) *J Phys Chem B* 104:11110.
- [12] Hartridge A, Ghanashyam-Krishna M, Bhattacharya AK (1998) *J Phys Chem Solids* 59:859.
- [13] Griffiths TR, Hubbard HVSA, Davies MJ (1994) *Inorg Chim Acta* 225:305.
- [14] Yu J, Si Z, Chen L, Wu X, Weng D (2015) *Appl Catal B: Env* 163:223.
- [15] Le Phuc N, Corbos EC, Courtois X, Can F, Marecot P, Duprez D (2009) *Appl Catal B: Env* 93:12.
- [16] Levasseur A, Ebrahim AM, Bandosz TJ (2011) *Langmuir* 27:9379.
- [17] Philipp S, Drochner A, Kunert J, Vogel H, Theis J, Lox ES (2004) *Top Catal* 30/31:235.
- [18] Ji Y, Toops TJ, Graham UM, Jacobs G, Crocker M (2006) *Catal Lett* 110:29.
- [19] Luo JY, Epling WS, Qi G (2012) *Catal Lett* 142:946.
- [20] Melville JE, Brisley EJ, Keane O, Phillips PR, Mountstevens EH (2012) US Patent 8,105,559.

- [21] Chen HY, Shadab M, Weigert E, Camm K, Ballinger T, Cox J, Blakeman P, SAE Paper No. 2013-01-0535.
- [22] Yang X, Yang L, Lin S, Zhou R (2015) *J Haz Mat* 285:182.
- [23] Kubsh JE, Rieck JS, Spencer ND (1991) *Stud Surf Sci Catal* 71:125.
- [24] de Rivas B, Guillen-Hurtado N, Lopez-Fonseca R, Coloma-Pascual F, Garcia-Garcia A, Gutierrez-Ortiz JI, Bueno-Lopez A (2012) *Appl Catal B: Env* 121-122:162.
- [26] Guo G, Dobson J, Warner J, Ruona W, Lambert C, SAE Technical Paper 2012-01-0371.
- [27] Graham GW, Jen H-W, Ezekoye, O, Kudla RJ, Chun W, Pan XQ, McCabe RW (2007) *Catal Lett* 116:1.
- [28] Salasc S, Skoglundh M, Fridell E (2002) *Appl Catal B: Env* 36:145.
- [29] Auvray X, Olsson L (2015) *Appl Catal B: Env* 168-169:342.
- [30] Ji Y, Toops TJ, Pihl JA, Crocker M (2009) *Appl Catal B: Env* 91:329.
- [31] Hadjiivanov KI (2000) *Catal Rev Sci Eng* 42:71.
- [32] Pozdnyakov DV, Filimonov VN (1973) *Kinet Catal* 14:655.
- [33] Huang W, Shi J (2015) *Appl Catal A: Gen* 507:65-74.
- [34] Filtschew A, Stranz D, Hess, C (2013) *Phys Chem Chem Phys* 15:9066.
- [35] Atribak I, Azambre B, Bueno-López A, García-García A (2009) *Appl Catal B: Env* 92:126.
- [36] Hernández-Giménez AM, dos Santos Xavier LP, Bueno-López A (2013) *Appl Catal A: Gen* 462-463:100.
- [37] Weiss BM, Iglesia E (2010) *J Catal* 272:74.

Chapter 5

- [1] Koebel M, Strutz EO (2003) *Ind. Eng. Chem. Res.* 42:2093.
- [2] Slunder CS, Storey JME, Lewis SA, SAE Technical Paper 2005-01-1858.
- [3] Fang HL, DaCosta HFM (2003) *Appl. Catal. B.* 46:17.
- [4] Lambert C. (Ford Motor Co.) personal communication.
- [5] Theis J., Lambert C. *Catal. Today.* 2015, 258, 367.
- [6] Jarvis, M., Adams, K.M. (2001) U.S. Patent 6,182,443.
- [7] Ji, Y., Bai, S., Crocker, M. *Appl. Catal. B.* 2015, 170-171, 283.
- [8] Ren, A., Schmeig, S.J., Koch, C.K., Qi, G., Li, W. *Catal. Today* 2015, 258, 378-385.
- [9] Koch, C.K. (2013) U.S. Patent Application 2013/0294990.
- [10] Murata, Y., Morita, T., Wada, K., Ohno, H. SAE 2015-01-1002.
- [11] Skorodumova, N.V., Simak, S.I., Lundqvist, B.I., Abrikosov, I., Johansson, B. *Phys. Rev. Lett.* 2002, 104, 11110.
- [12] Mamontov, E., Egami, T., Brezny, R., Koranne, M., Tyagi, S. *J.Phys. Chem. B.* 2002, 89, 166601-1.
- [13] Hartridge, A., Ghanashyam-Krishna, M., Bhattacharya, A.K. *J. Phys. Chem. Solids.* 1998, 59, 859.
- [14] Griffiths, T.R., Hubbards, H.V.S.A., Davies, M.J. *Inorg. Chim. Acta.* 1994, 225, 305.
- [15] Yu, J., Si, Z., Chen, L., Wu, X., Weng, D. *Appl. Catal. B.* 2015, 163, 223.
- [16] Le Phuc, N., Corbos, E.C., Courtois, X., Can, F., Marecot, P., Duprez, D. *Appl. Catal. B.* 2009, 93, 12.
- [17] Levasseur, A., Ebrahim, A.m., Bandosz, T.J. *Langmuir.* 2011, 27, 9379.

- [18] Hong, S., Virkar, A. J. *Am. Ceram. Soc.* 1998, 78, 433-439.
- [19] Glushkova, V., Hanic, F., Sazonova, L., *Ceramurgia Int.* 1987, 4, 176-178.
- [20] Rohart, E., Belliere-Baca, V., Yokota, K., Harle, V., Pitois, C. *Top. Catal.* 2007, 42-43, 71-75.
- [21] Wang, X., Chen, Z., Wang, Y., Wang, R. *ChemCatChem.* 2014, 6, 237-244.
- [22] Sun, X., Qu, R., Lei, Y., Bai, B., Chang, H., Peng, Y., Su, W., Zhang, C., Li, J. *Catal. Today.* 2015, 258, 556-563.
- [23] Cao, Y., Wei, C. *Asia-Pac. J. Chem. Eng.* 2016, doi:10.1002/apj.1967.
- [24] Philipp, S., Drochner, A., Kunert, J., Vogel, H., Theis, J., Lox, E.S. *Top. Catal.* 2004, 30/31, 235.
- [25] Ji, Y., Toops, T.J., Graham, U.M., Jacobs, G., Crocker, M. *Catal. Lett.* 2006, 110, 29.
- [26] Luo, J.Y., Epling, W.S., Qi, G. *Catal Lett.* 2012, 142, 946.
- [27] Melville, J.E., Brisley, E.J., Keane, O., Phillips, P.R., Mountstevens, E.H. *US Patent* 8,105,559, 2012.
- [28] Chen, H.Y., Shadab, M., Weigert, E., Camm, K., Ballinger, T., Cox, J., Blakeman, P. *SAE Paper No.* 2013-01-0535.
- [29] Jones, S., Ji, Y., Crocker, M. *Catal. Lett.* 2015, 146, 909-917.
- [30] Yang, X., Yang, L., Ling, S., Zhou, R. *J. Haz. Mat.* 2015, 285, 182.
- [31] de Rivas B., Guillen-Hurtado N., Lopez-Fonseca R., Coloma-Pascual F., Garcia-Garcia A., Gutierrez-Ortiz J.I., Bueno-Lopez, A. *Appl. Catal. B: Env.* 2012, 121-122, 162-170.
- [32] Rivas, B., Guillen-Hurtado, N., Lopez-Fonseca, R., Coloma-Pascual, F., Garcia-Garcia, A., Guitierrez-Ortiz, J.I., Bueno-Lopez, A. *Appl. Catal. B.* 2012, 121-122, 162.
- [33] Silvestre-Albero, J., Rodriguez-Reinoso, F., Sepulveda-Escribano, A. *J. Catal.* 2002, 210, 127-136.
- [34] Krishna, K., Bueno-Lopez, A., Makkee, M., Moulijin, J.A. *Appl. Catal. B.* 2007, 75, 189.
- [35] Zotin, F.M.Z., Tournayan, L., Varloud, J., Perrichon, V., Frety, R. *Appl. Catal. A.* 1993, 98, 99-114.
- [36] Fornasiero, P., DiMonte, R., Rao, G.R., Kaspar, J., Meriani, S., Trovarelli, A., Graziani, M. *J. Catal.* 1995, 151, 168-177.
- [37] Trovarelli, A. (ed.) *Catalysis by Ceria and Related Materials*, Catalysis Science Series, vol. 2, Imperial College Press, 2002, pp. 51-83.
- [38] Bernal, S., Calvino, J.J., Cifrendo, G.A., Gatica, J.M., Perez Omil, J.A., Pintado, J.M. *J. Chem. Soc., Faraday Trans.* 1993, 89, 3499-3505.
- [39] Auvray X, Olsson L (2015) *Appl Catal B: Env* 168-169:342.
- [40] Salasc S, Skoglundh M, Fridell E (2002) *Appl Catal B: Env* 36:145.
- [41] Graham, G.W., Jen, H.-W., Ezekoye, O., Kudla, R.J., Chun, W., Pan, X.Q., and McCabe, R.W. *Catal. Lett.* 2007, 116, 1-8.
- [42] Ji, Y., Toops, T.J., Pihl, J.A., Crocker, M. *Appl. Catal. B.* 2009, 91, 329.
- [43] Hadjiivanov, K.I. *Catal. Rev. Sci. Eng.* 2000, 42, 71.
- [44] Pozdnyakov, D.V., Filimonov, V.N. *Kinet. Catal.* 1973, 14, 655.
- [45] Philipp, S., Drochner, A., Kunert, J., Vogel, H., Theis, J., Lox, E.S. *Top. Catal.* 2004, 30/31, 235.

- [46] Ji, Y., Toops, T.J., Graham, U.M., Jacobs, G., Crocker, M. *Catal. Lett.* 2006, 110, 29.
- [47] Luo, J.Y., Epling, W.S., Qi, G. *Catal. Lett.* 2012, 142, 946.
- Chapter 6
- [1] Koebel M, Strutz EO (2003) *Ind. Eng. Chem. Res.* 42:2093.
- [2] Slunder CS, Storey JME, Lewis SA, SAE Technical Paper 2005-01-1858.
- [3] Fang HL, DaCosta HFM (2003) *Appl. Catal. B.* 46:17.
- [4] Lambert C. (Ford Motor Co.) personal communication.
- [5] Cole, J.A., Energy and Environmental Research Corporation. U.S. Patent 5,800,793, September 1, 1998.
- [6] Jarvis, M., Adams, K.M. (2001) U.S. Patent 6,182,443.
- [7] Ji, Y., Bai, S., Crocker, M. *Appl. Catal. B.* 2015, 170-171, 283.
- [8] Ren, A., Schmeig, S.J., Koch, C.K., Qi, G., Li, W. *Catal. Today.* 2015, 258, 378-385.
- [9] Koch, C.K. (2013) U.S. Patent Application 2013/0294990.
- [10] Tsukamoto, Y., Nishiok, H., Imai, D., Sobue, Y., Takagi, N. SAE 2012-01-0370.
- [11] Murata, Y., Morita, T., Wada, K., Ohno, H. SAE 2015-01-1002.
- [12] Skorodumova, N.V., Simak, S.I., Lundqvist, B.I., Abrikosov, I., Johansson, B. *Phys. Rev. Lett.* 2002, 104, 11110.
- [13] Mamontov, E., Egami, T., Brezny, R., Koranne, M., Tyagi, S. *J. Phys. Chem. B.* 2002, 89, 166601-1.
- [14] Hartridge, A., Ghanashyam-Krishna, M., Bhattacharya, A.K. *J. Phys. Chem. Solids.* 1998, 59, 859.
- [15] Griffiths, T.R., Hubbards, H.V.S.A., Davies, M.J. *Inorg. Chim. Acta.* 1994, 225, 305.
- [16] Yu, J., Si, Z., Chen, L., Wu, X., Weng, D. *Appl. Catal. B.* 2015, 163, 223.
- [17] Le Phuc, N., Corbos, E.C., Courtois, X., Can, F., Marecot, P., Duprez, D. *Appl. Catal. B.* 2009, 93, 12.
- [18] Levasseur, A., Ebrahim, A.m., Bandosz, T.J. *Langmuir.* 2011, 27, 9379.
- [19] Cordatos, H., Gorte, R.J. *J. Catal.* 1996, 159, 112-118.
- [20] Hong, S., Virkar, A. *J. Am. Ceram. Soc.* 1998, 78, 433-439.
- [21] Glushkova, V., Hanic, F., Sazonova, L., *Ceramurgia Int.* 1987, 4, 176-178.
- [22] Rohart, E., Belliere-Baca, V., Yokota, K., Harle, V., Pitois, C. *Top. Catal.* 2007, 42-43, 71-75.
- [23] Wang, X., Chen, Z., Wang, Y., Wang, R. *ChemCatChem.* 2014, 6, 237-244.
- [24] Sun, X., Qu, R., Lei, Y., Bai, B., Chang, H., Peng, Y., Su, W., Zhang, C., Li, J. *Catal. Today.* 2015, 258, 556-563.
- [25] Cao, Y., Wei, C. *Asia-Pac. J. Chem. Eng.* 2016, doi:10.1002/apj.1967.
- [26] Yoshida, K., Kuwahara, T., Kuroki, T., Okubo, M. *J. Haz. Mat.* 2012, 231-232, 18-25.
- [27] Theis, J.R., Lambert, C.K. *Catal. Today.* 2015, 258, 367-377.
- [28] Theis, J.R. *Catal. Today.* 2016, <http://dx.doi.org/10.1016/j.cattod.2016.01.032>.
- [29] Philipp, S., Drochner, A., Kunert, J., Vogel, H., Theis, J., Lox, E.S. *Top. Catal.* 2004, 30/31, 235.
- [30] Ji, Y., Toops, T.J., Graham, U.M., Jacobs, G., Crocker, M. *Catal. Lett.* 2006, 110, 29.
- [31] Luo, J.Y., Epling, W.S., Qi, G. *Catal Lett.* 2012, 142, 946.

- [32] Melville, J.E., Brisley, E.J., Keane, O., Phillips, P.R., Mountstevens, E.H. US Patent 8,105,559, 2012.
- [33] Jones, S., Ji, Y., Crocker, M. Catal. Lett. doi:10.1007/s10562-016-1704-y.
- [34] Yang, X., Yang, L., Ling, S., Zhou, R. J. Haz. Mat. 2015, 285, 182.
- [35] Atribak, I., Azambre, B., Bueno-Lopez, A., Garcia-Garcua, A. Appl. Catal. B. 2009, 92, 126-137.
- [36] Serrano-Ruiz, J.C., Luettich, J., Sepulveda-Escribano, A., Rodriguez-Reinoso, F. J. Catal. 2006, 241, 45-55.
- [37] Shi, F., Li, Y., Wang, H., Zhang, Q. Prog. Nat. Sci.: Mat. Int. 2012, 22, 15-20.
- [38] Luo, M.-F., Yan, Z.-L., Jin, I.-Y. J. Mol. Catal. A:Chem. 2006, 260, 157.
- [39] Rico-Pérez, V., Salinas-Martínez de Lecea, C., Bueno-López, A. Appl. Catal. A: Gen. 2014, 472, 134-142.
- [40] Silvestre-Albero, J., Rodriguez-Reinoso, F., Sepulveda-Escribano, A. J. Catal. 2002, 210, 127-136.
- [41] Krishna, K., Bueno-Lopez, A., Makkee, M., Moulijin, J.A. Appl. Catal. B. 2007, 75, 189.
- [42] Zotin, F.M.Z., Tournayan, L., Varloud, J., Perrichon, V., Frety, R. Appl. Catal. A. 1993, 98, 99-114.
- [43] Fornasiero, P., DiMonte, R., Rao, G.R., Kaspar, J., Meriani, S., Trovarelli, A., Graziani, M. J. Catal. 1995, 151, 168-177.
- [44] Trovarelli, A. (ed.) Catalysis by Ceria and Related Materials, Catalysis Science Series, vol. 2, Imperial College Press, 2002, pp. 51-83.
- [45] Bernal, S., Calvino, J.J., Cifrendo, G.A., Gatica, J.M., Perez Omil, J.A., Pintado, J.M. J. Chem. Soc., Faraday Trans. 1993, 89, 3499-3505.
- [46] Guo G., Dobson J., Warner J., Ruona W., Lambert C. SAE 2012-01-0371.
- [47] Theis, J., Lambert, C. Catal. Doi:10.1016/j.cattod.2015.01.031.
- [48] Ji, Y., Toops, T.J., Pihl, J.A., Crocker, M. Appl. Catal. B. 2009, 91, 329.
- [49] Hadjiivanov, K.I. Catal. Rev. Sci. Eng. 2000, 42, 71.
- [50] Pozdnyakov, D.V., Filimonov, V.N. Kinet. Catal. 1973, 14, 655.

VITA

Samantha Jones.

Personal Information.

Place of birth: Bristol, TN.

Education.

Emory & Henry College.
Emory, VA.
Bachelor of Science Degree in Chemistry (2011).

University of Kentucky.
Center for Applied Energy Research / Department of Chemistry.
Lexington, KY U.S.A.
Doctoral studies (2011-2016).
Advisor: Prof. Mark Crocker. Co-advisor: Prof. Jack Selegue.

Grants

Corrosion of Porous Glassy Films, awarded by the Virginia Foundation of Independent Colleges, summer 2009, \$2,000.

Awards, Honors, and scholarships.

Richard J. Kokes Travel Award program NACS, 24th NAM
Pittsburgh, PA (2015).

University of Kentucky Graduate School.
Teaching Assistantship (2011-2013, 2016).

University of Kentucky Center for Applied Energy Research.
Research Assistantship (2013-2015, 2016).

North American Catalysis Society (2013-present).

Junior League of Lexington, KY.
Provisional Member (2014).
Active Member (2015-present).
Holly Day Markey Decorations Chair/Board member (2015).
Community, Education, & Research Committee (2016).

Americorp, Emory & Henry College.

Two year service commitment in the amount of 900 hours of community service for an education award in the amount of \$2500 to be used for student loan repayment (2008-2010).

Publications.

1. Samantha Jones, Yaying Ji, Mark Crocker. Ceria-based Catalysts for Low Temperature NO_x Storage and Release. *Catalysis Letter*. Volume 146, 2016. Pages 909-917.
2. Ryan Loe, Eduardo Santillan-Jimenez, Tonya Morgan, Lilia Sewell, Yaying Ji, Samantha Jones, Mark A. Isaacs, Adam F. Lee, Mark Crocker. Effect of Cu and Sn Promotion on the Catalytic Deoxygenation of Model and Algal Lipids of Fuel-like Hydrocarbons over Supported Ni Catalysts. *Applied Catalysis B: Environmental*. Volume 191, 2016. Pages 147-156.
3. Jin Wang, Yaying Ji, Gary Jacobs, Samantha Jones, Dae J. Kim, Mark Crocker. Effect of aging on NO_x reduction in coupled LNT-SCR systems. *Applied Catalysis B: Environmental*. Volume 148-149, 2014. Pages 51-61.

Professional Conference proceedings (Poster/Oral).

1. Samantha Jones, Yaying Ji, Mark Crocker. CeO₂-M₂O₃ Passive NO_x Adsorbers for Cold Start Applications, presented at the SPARK Soiree & Bluegrass Showcase of Entrepreneurs and University Researchers at Copper Roux in Lexington, KY, May 25, 2016. Poster.
2. Samantha Jones, Yaying Ji, Mark Crocker. CeO₂-M₂O₃ Passive NO_x Adsorbers for Cold Start Applications, presented at the Regional Innovative Energy Forum at The University of Kentucky in Lexington, KY, April 21, 2016. Poster.
3. Samantha Jones and Mark Crocker. CeO₂-M₂O₃ Passive NO_x Adsorbers for Cold Start Applications, presented at the Cross-Cut Lean Exhaust Emissions Reduction Simulations Workshop in Ann Arbor, MI, April 6-8, 2016. Oral.
4. Samantha Jones, Yaying Ji, Mark Crocker. CeO₂-based Passive NO_x Adsorbers for Low Temperature Applications, presented at the 24th Meeting of the North American Catalysis Society in Pittsburgh, PA, June 14-19, 2015. Poster.
5. Samantha Jones, Yaying Ji, Mark Crocker. CeO₂-based Passive NO_x Adsorbers for Low Temperature Applications, presented at the Cross-Cut Lean Exhaust Emissions Reduction Simulations Workshop in Dearborn, MI, April 27-29, 2015. Poster.